SLAC-399
UC-414
(E)

Measurement of the Bottom Hadron Lifetime at the Z^0 Resonance

Donald Hideo Fujino

Stanford Linear Accelerator Center
Stanford University, Stanford, CA 94309

June 1992

Prepared for the Department of Energy
under contract number DE-AC03-76SF00515

Printed in the United States of America. Available from the National Technical Information Service, U.S. Department of Commerce, 5285 Port Royal Road, Springfield, Virginia 22161

---

*Ph.D. Thesis

Abstract

We have measured the bottom hadron lifetime from $b\bar{b}$ events produced at the Z^0 resonance. Using the precision vertex detectors of the Mark II detector at the Stanford Linear Collider, we developed an impact parameter tag to identify bottom hadrons. The vertex tracking system resolved impact parameters to 30 μm for high momentum tracks, and 70 μm for tracks with a momentum of 1 GeV. We selected B hadrons with an efficiency of 40% and a sample purity of 80%, by requiring there be at least two tracks in a single jet that significantly miss the Z^0 decay vertex.

From a total of 208 hadronic Z^0 events collected by the Mark II detector in 1990, we tagged 53 jets, of which 22 came from 11 double-tagged events. The jets opposite the tagged ones, referred as the "untagged" sample, are rich in B hadrons and unbiased in B decay times. The variable $\Sigma\delta$ is the sum of impact parameters from tracks in the jet, and contains vital information on the B decay time.

We measured the B lifetime from a one-parameter likelihood fit to the untagged $\Sigma\delta$ distribution, obtaining

$$\tau_b = 1.53^{+0.55}_{-0.45} \pm 0.16 \text{ ps}$$

which agrees with the current world average. The first error is statistical and the second is systematic. The systematic error was dominated by uncertainties in the track resolution function. As a check, we also obtained consistent results using the $\Sigma\delta$ distribution from the tagged jets and from the entire hadronic sample without any bottom enrichment.

I do not know what I may appear to the world, but to myself
I seem to have been only like a boy playing on the sea-shore,
and diverting myself in now and then finding a smoother
pebble or a prettier shell than ordinary, whilst the great
ocean of truth lay all undiscovered before me.

– Sir Isaac Newton

Acknowledgments

My years at Stanford University have been extremely rewarding, and I owe a hearty thanks to a great number of individuals. First, I would like to thank my advisor, John Jaros, for his guidance, sage advice, and encouragement during my career as a graduate student. I am still far from having all the necessary skills and fastidiousness in physics research, but I've come a long ways in the past eight years. I have also learned a great deal from the wisdom and expertise of Vera Luth, Morris Swartz, Ken Hayes, and Jonathan Dorfan. The vertex detector "gang" spent endless days and nights ensuring that the vertex chambers ran smoothly and the physics analysis was well thought out. Special thanks to Dale Koetke, Bob Jacobsen, Bruce Schumm, and Steve Wagner for a job well done. I would also like to thank the rest of the Mark II collaborators, too numerous to be mentioned individually, for providing a stimulating atmosphere in particle physics.

My physics buddies, Phil Burrows, Rahim Esmailzadeh, Lonnie Hordon, Ed Lu, Doug Mercer, and Kianoosh Nagshineh, were always eager to discuss the latest-breaking news in science, but would just as easily rip off their physics hats and head to the local pub or coffee house, where our conversations would invariably digress from the lofty to the bawdy. Scarcely a week could pass without shedding new light on a real dilemma in physics – the gender issue.

My friends from the good old days at Manzanita are especially dear to me and have kept me sane throughout the years. The many BBQ's and dinners, freshly baked cookies (my nose could always sniff them from a distance), the whip cream fights and water fights, trips to the City, Friday volleyball and weekend tennis – all these and many more. Laura Chen, John Downie, Suzi Gerlach-Downie, Carrie Fordham, and Elaina Kyrouz, I couldn't have made it without all of you. It's hard to believe that we lived in those fragile metal boxes for all those years.

My friends at Breakers always provided good food and good company. They taught me the fine art of cooking for fifty, when at first I could scarcely peel potatoes. I leave you with a collection of my favorite recipes – the ones with greasy stains are the best. Special thanks to my cohorts in gastronomical experimentation, Bob Bauch, Rafael Guzman, Christa Knebel, and Sanjay Mani.

I would also like to thank the many friends in JACL who made me more aware of my heritage and showed me there is more to life than just physics. Many thanks to my roommate, G. E. Light, for putting up with me in my frantic final months, and to Emilie Ito for the warmth she has shared with me.

Finally, I would like to thank my family for their continued support and encouragement throughout my seemingly endless years in college. They no longer have to worry that I am a starving student. I've now joined the ranks of the starving post-docs.

Most of all, I would like to thank my dad, who instilled in me the yearning and curiosity for science. I can still remember vividly when I was ten, the night he spent hours with me setting up my brand-new telescope and sharing the wonders of the rings of Saturn.

I dedicate this thesis to the memory of my father. I'm sure he is very proud.

Table of Contents

Chapter

List of Tables

List of Figures

The pure and simple truth is rarely pure and never simple.

– Oscar Wilde

1 Introduction

This thesis presents a measurement of the bottom hadron lifetime using a novel technique for identifying B hadrons, which are produced in electron-positron collisions at the Z^0 resonance by the Stanford Linear Collider (SLC). The Mark II detector at the SLC observes Z^0 boson decays and has a considerably better tracking resolution than earlier versions of the detector at the SPEAR and PEP storage rings. With the aid of two high precision vertex detectors, the Mark II was able to resolve tracks from B decays, since these tracks were typically inconsistent with coming from the Z^0 decay vertex. An impact parameter tag that requires at least two tracks in a jet to have a significant impact parameter can cleanly and efficiently identify B hadrons.

Our data consists of Z^0 decay events collected in 1990. We measured the B hadron lifetime using the jets opposite our tagged sample, since these jets represent a sample of B hadrons with high purity and unbiased decay times. The $\Sigma\delta$ distribution, which is the sum of track impact parameters in the jet, contains vital information on the lifetime. This method is complementary to past measurements which rely on high P_T leptons both to tag $b\bar{b}$ events and measure the B lifetime.

In this chapter, we will discuss the theoretical considerations salient to our measurement. The Standard Model is discussed briefly, followed by a description of the production and decay of B hadrons at the Z^0 resonance. Next, we introduce general techniques for measuring the B lifetime and list the results from prior experiments. We conclude by discussing the theoretical and experimental limits on differences between the charged and neutral B meson lifetimes.

1.1 The Standard Model

Our current understanding of elementary particle physics postulates that the fermions known as quarks and leptons are the fundamental particles in nature. These quarks and leptons can be packaged into three nearly identical families or generations that differ only in their masses (see Table 1). The first family of particles (up quark, down quark, electron, and electron neutrino) are the building blocks of matter which predominate in nature. For instance, protons are made up of three quarks (*uud*) and neutrons are composed of a slightly different combination (*udd*). Evidence for the second and third generation of particles emerged through their observations in cosmic ray and accelerator experiments

Interactions between these particles occur via four principal forces: gravity, electromagnetism, the strong force, and the weak force. These four forces have widely different strengths and spatial ranges as seen in Table 2. All forces have a particle-like nature that can be traced to fundamental bosons. The photon is a massless boson which mediates the electromagnetic force and couples to all particles that possess an electric charge. The weak force is responsible for certain types of radioactive decay and is transmitted by three massive vector bosons: the W^+, W^-, and Z^0 boson. They interact with all fermions that carry a weak charge. The strong force binds the quarks together inside protons and neutrons, and is mediated by eight massless gluons. A complex manifestation of the strong force, akin to Van der Waals forces in electromagnetism, causes the protons and neutrons to adhere in the nucleus. Gravity is the weakest force and plays no significant role in high energy physics interactions.

One of the goals in physics is to unify these underlying forces in the universe. We hope to describe these seemingly disparate phenomena as a result of a grander, more inclusive theory. Just as Maxwell unified electricity and magnetism at the end of the 19th century, Weinberg, Glashow, and Salam in the 1970's unified the theories of electromagnetism and weak interactions into a single theory. At low energies, the weak force is negligible compared to electromagnetism. But at energies above the mass of the W and Z^0, they become relatively comparable in strength. Weinberg, Glashow, and Salam theorized that the forces obey an underlying $SU(2)_L \otimes U(1)$ gauge symmetry which breaks down at low energies due to the non-zero vacuum expectations of a scalar Higgs field. The spontaneous

Table 1 The fundamental fermions in particle physics. The top quark and the tau neutrino have not been discovered to this date.

	QUARKS			LEPTONS		
	Flavor	**Charge**	**Mass**	**Flavor**	**Charge**	**Mass**
1st Generation	down (d)	-1/3	0.3 GeV	e	-1	0.511 MeV
	up (u)	+2/3	0.3 GeV	ν_e	0	< 17 eV
2nd Generation	strange (s)	-1/3	0.5 GeV	m	-1	0.106 GeV
	charm (c)	+2/3	1.5 GeV	n_m	0	< 270 KeV
3rd Generation	bottom (b)	-1/3	5.0 GeV	t	-1	1.784 GeV
	top (t)	+2/3	>87 GeV	n_t	0	< 35 MeV

Table 2 Fundamental forces and their mediating bosons. All bosons except for the graviton have been verified.

Force	Boson	Spin	Mass (GeV)	Range (cm)
electromagnetism	photon	1	0	∞
weak	$W^\pm$, Z^0	1	M_W=80.6 M_Z=91.2	10^{-16}
strong/nuclear	gluons	1	0	10^{-13}
gravity	graviton	2	0	∞

symmetry breaking predicts not only the masses of the γ, Z^0, and $W^\pm$ particles but also their couplings to quarks and leptons.

The strong interaction is described by the theory of quantum chromodynamics (QCD), whose force particles obey an $SU(3)_{color}$ gauge symmetry. Quarks possess one of three color charges: red, green, or blue. The gluons themselves also carry a color charge which allows gluon self-interactions. This feature causes the color flux lines to be constrained to a tubelike region, rather than fanning out in three dimensions as in electromagnetism. The force between two colored objects increases linearly with distance and prevents free quarks from existing in nature. All quarks are compelled to form colorless objects, analogous to the formation of electrically neutral atoms from charged particles. Quarks coalesce into either colorless baryons (qqq) or mesons $(q\bar{q})$.

The combined theories of QCD and electroweak interactions form the basis of the Standard Model, which describes the interactions of quarks, leptons, and the fundamental force particles. The Standard Model was confirmed with the discovery of the W and Z^0 bosons at CERN in 1983.† In the past few years, SLAC and CERN have constructed Z^0 factories which have produced over one million Z^0 bosons.

1.2 Decays of the Z^0 Boson

Colliding beams of electrons and positrons can annihilate and produce fermion-antifermion pairs. At low center of mass energies, this interaction is mediated by a virtual photon. Figure 1 illustrates the tree-level Feynman diagram of an e^+e^- annihilation into a fermion-antifermion pair. The relative production of quarks and leptons depends on the electric charge of the fermion Q_f. The cross section for $e^+e^- \to f\bar{f}$, above threshold and resonant production, falls sharply with the center of mass energy

$$\sigma(e^+e^- \to f\bar{f}) = \frac{4\pi\alpha^2}{3s} C_f Q_f^2 \tag{1}$$

where $\alpha \approx 1/137$ is the electromagnetic fine structure constant, $\sqrt{s}$ is the center of mass energy, and C_f is the color factor: 3 for quarks and 1 for leptons.

When the center of mass energy of the colliding beams is near the Z^0 mass, the cross section rises rapidly by about a thousand-fold due to the resonant production of the Z^0 boson (Figure 2). The Z^0 will decay into any quark or lepton pair ($q\bar{q}$, l^+l^-,

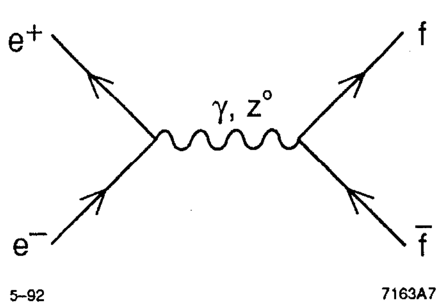

Figure 1 Feyman diagram of a tree-level e^+e^- annihilation through a virtual gamma or Z^0 into a fermion-antifermion pair.

---

† CERN is the European high energy physics laboratory in Geneva, Switzerland.

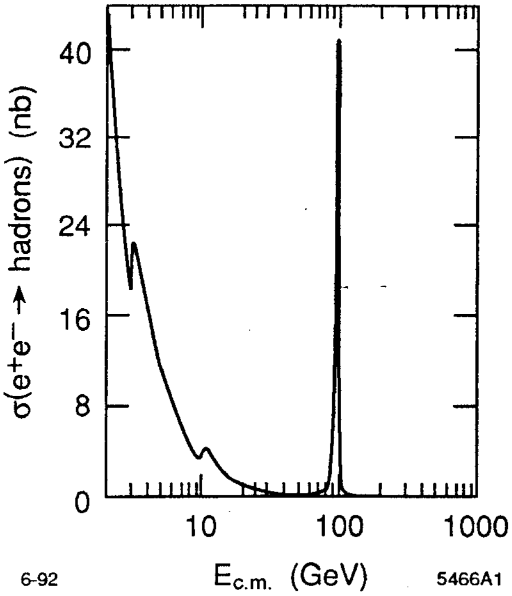

Figure 2 The cross section of e^+e^- annihilation into hadrons as a function of the center of mass energy. The Z^0 resonance occurs at 91 GeV. The rise in cross section at 3 GeV and 10 Gev corresponds to threshold production of charm and bottom hadrons, respectively.

or $\nu\bar{\nu}$) that is kinematically possible. The lineshape of the tree-level cross section $e^+e^- \to Z^0 \to f\bar{f}$ is described by the relativistic Breit-Wigner resonance

$$\sigma_{f\bar{f}}(s) = \frac{12\pi}{M_Z^2} \cdot \frac{s\Gamma_{ee}\Gamma_{f\bar{f}}}{(s-M_Z^2)^2 + s^2\Gamma_Z^2/M_Z^2} \tag{2}$$

where we have ignored contributions from initial state radiation. The total decay width of the Z^0 resonance (Γ_Z) is the sum of the partial decay widths of all available fermions. The partial width $\Gamma_{f\bar{f}}$ depends on the weak charge of the fermion, specified by the axial (a_f) and vector (v_f) coupling constants to the Z^0, and can be written as

$$\Gamma(Z^0 \to f\bar{f}) = \frac{G_F M_Z^3}{24\sqrt{2}\pi} C_f(a_f^2 + v_f^2) \tag{3}$$

Table 3 Axial and vector coupling constants of fermions to the Z^0 boson. The partial and relative decay rate into fermion-antifermion pairs.

Fermion	a_f	v_f	Γ_f (MeV)	%
ν_e, ν_μ, ν_τ	1	1	166	7%
e, μ, τ	–1	-0.08	83	3%
u, c	1	0.39	297	12%
d, s, b	–1	-0.69	383	15%
Hadronic (*udscb*)			1740	73%
Total			2490	100%

where G_F is the Fermi constant. The fermionic coupling constants are functions of the weak isospin, T_{3f}, and the Weinberg angle, θ_W, which describes the degree of mixing between the $U(1)$ and the $SU(2)_L$ neutral gauge bosons.

$$\begin{aligned} v_f &= 2T_{3f} - 4Q_f \sin^2\theta_W \\ a_f &= 2T_{3f} \end{aligned} \tag{4}$$

Table 3 summarizes the axial and vector couplings, the partial decay widths, and the percentage of Z^0 bosons which decay into each type of quark and lepton. Bottom quarks are produced in roughly 22% of all hadronic decays of the Z^0.

1.3 Fragmentation

Current theoretical prejudices assert that free quarks do not exist in nature. Instead, quarks produced in $Z^0 \to q\bar{q}$ decays must eventually transform themselves into stable hadrons in a process called fragmentation. Because the strong coupling constant α_s is no longer small at energy scales as low as 1 GeV, the fragmentation process cannot be predicted by perturbative QCD, but must instead be explained by phenomenological models. A popular model is the string fragmentation model.[84] Because of the three-gluon coupling, the color flux lines do not spread out in all space, as does electromagnetism, but instead is confined to a thin tubelike region. Hence, as the two bare quarks race apart from each other, the color potential energy will increase like a stretched elastic string. This string can snap and effectively shorten itself by producing a real $q\bar{q}$ pair out of the vacuum. The fragmentation process continues until there is insufficient energy in the string to produce more quark pairs. These additional quarks "dress" the bare parent quark and form a jet of hadrons that emerge in a narrow cone about the direction of the parent quark.

We can characterize the fragmentation process by defining the parameter

$$z \equiv \frac{(E + P_{\parallel})_{\text{hadron}}}{(E + P_{\parallel})_{\text{quark}}} \tag{5}$$

which is the fraction of energy and momentum parallel to the quark direction that is carried away by the primary hadron in the lab frame. The quark energy is not necessarily equal to the beam energy because the quark can radiate hard gluons to form three jet events. Initial state radiation on the Z^0 pole is negligible because falling off the Z^0 peak incurs a high penalty in rate loss.

The fragmentation for light quarks (*uds*) is well described by the Lund symmetric function

$$D(z) \propto \frac{1}{z}(1-z)^{A} \exp(-Bm_T^2/z) \tag{6}$$

where $m_T \equiv \sqrt{p_T^2 + m^2}$ is the transverse mass of the hadron, p_T is the momentum of the hadron transverse to the quark parton direction, and A and B are flavor-independent parameters which we have tuned to the data collected at the PEP storage ring at a center of mass energy of 29 GeV. [70] The LUND model creates a momentum spectrum that is too hard for heavy quark production. A better parametrization for charm and bottom is given by the Peterson fragmentation function [71]

$$D(z) \propto \frac{1}{z}\left(1 - \frac{1}{z} - \frac{\varepsilon_Q}{1-z}\right)^{-2} \tag{7}$$

whose only parameter is $\varepsilon_Q \sim (m_u/m_Q)^2$.

The parameter z is experimentally difficult to measure due to uncertainties in the denominator of Eqn. (5). Instead, the quantity x_E, defined as the hadron energy divided by the beam energy, is experimentally more accessible. B hadrons carry away an average of 70% of the beam energy. Charm hadrons produce a softer momentum spectrum and carry away only about 50% of the beam energy. The details of the fragmentation parameters are postponed until Section 3.1. Figure 3 illustrates the fragmentation function for strange, charm, and bottom hadrons. The momentum spectrum is stiffest for bottom hadrons.

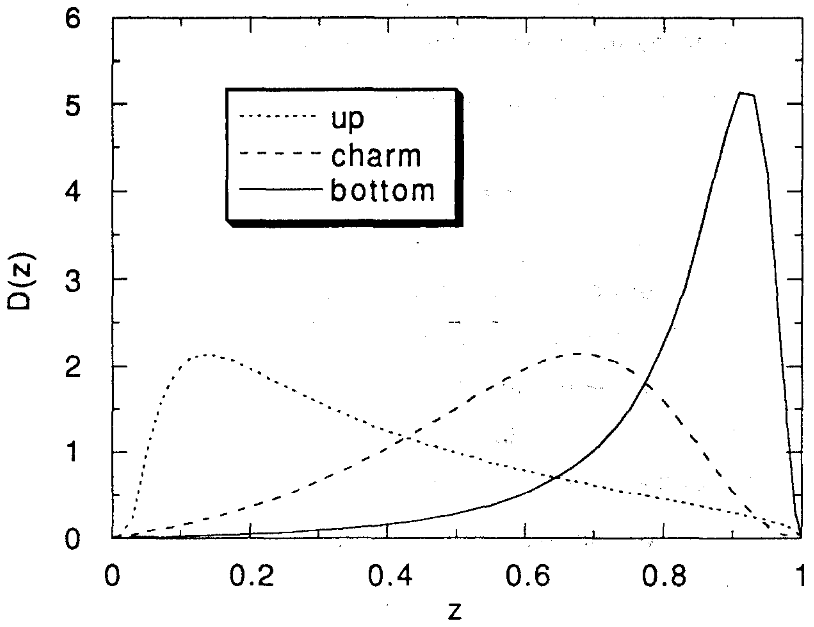

Figure 3 Quark parton fragmentation function. *uds* quark events use the Lund symmetric function, while charm and bottom events use the Peterson fragmentation function.

1.4 Bottom Hadron Decay

After the fragmentation process, the Z^0 event will continue to evolve with the decay of heavy hadrons into lighter flavors. These transitions must occur via weak interactions because electromagnetic and strong forces conserve the quark flavor. In the electroweak theory, the quark flavors are grouped into three generations of doublets. Quarks can transform into their doublet partner through the emission of a $W^{\pm}$ boson. If mixing did not exist between generations, then the only allowed transitions would be

$$\begin{array}{c} d \leftrightarrow u \\ s \leftrightarrow c \\ b \leftrightarrow t \end{array} \qquad (8)$$

Charm and top quarks would be able to decay into their lighter partner, whereas strange and bottom quarks would be energetically constrained to be stable.

However, inter-generational decays do occur, because the mass eigenstates for quarks are not identical to the weak eigenstates, although the decays occur at a suppressed rate compared to intra-generational decays of charm and top. For instance, the flavor content of the lower component in the third-generation, weak isodoublet is primarily bottom, but it also contains a small admixture of strange and down. The Cabibbo-Kobayashi-Maskawa (CKM) matrix [54] is a 3x3 unitary matrix that describes the mixing between the mass eigenstates $\begin{bmatrix} d & s & b \end{bmatrix}$ and the weak eigenstates $\begin{bmatrix} d' & s' & b' \end{bmatrix}$.

$$\begin{bmatrix} d' \\ s' \\ b' \end{bmatrix} = \begin{bmatrix} V_{ud} & V_{us} & V_{ub} \\ V_{cd} & V_{cs} & V_{cb} \\ V_{td} & V_{ts} & V_{tb} \end{bmatrix} \begin{bmatrix} d \\ s \\ b \end{bmatrix} \tag{9}$$

The CKM matrix is rich in structure with three arbitrary angles: θ_{12}, θ_{23}, and θ_{13}, that express the degree of mixing between the three generations of quarks and provide a mechanism for $s \to u$, $c \to d$, $b \to c$, and $b \to u$ transitions. It can also have one complex phase, which provides a potential source of CP violation. The diagonal terms of the CKM matrix are near unity; the off-diagonal terms are small but nonzero. Hence, B hadrons can decay via the transitions $b \to c$ and $b \to u$ with an amplitude proportional to the CKM elements V_{cb} and V_{ub}, respectively, albeit at a rate slower than the predicted top decay rate $t \to b$ due to the smallness of quark mixing. We shall see that $V_{cb} >> V_{ub}$, and so $b \to c$ decays dominate.

1.4.1 The Spectator Quark Model

The spectator quark model describes B hadron decays by treating the b quark as a free particle that decays via a tree-level charged weak current. The light anti-quark in B^0, B^-, B_s mesons and the diquark in Λ_b baryons are called spectator quarks and are postulated to have a negligible role in the decay process, hence all B hadrons are expected to have the same lifetime. Figure 4 illustrates a B^0 meson decay. The charm quark and the spectator quark, $\bar{d}$, form a color singlet, while the virtual W (denoted by W^*) collapses into a second $q_i\bar{q}_j$ color singlet or a $l\bar{\nu}_l$ pair. Each color singlet system hadronizes independently.

In the spectator model, the total B decay rate Γ_B has the same form as the muon decay rate $\Gamma(\mu \to e\nu\nu)$ except for a few minor modifications.[53]

$$\begin{aligned} \Gamma_B &= N_W |V_{cb}|^2 \cdot \frac{G_F^2 m_b^5}{192\pi^3} \\ &= \{N_W |V_{cb}|^2 \left(\frac{m_b}{m_\mu}\right)^5\} \cdot \Gamma(\mu \to e\nu\nu) \end{aligned} \tag{10}$$

The B decay rate scales with N_W, the number of final states available to the virtual W. The amplitude depends on the CKM matrix element V_{cb}, which is unity for muon

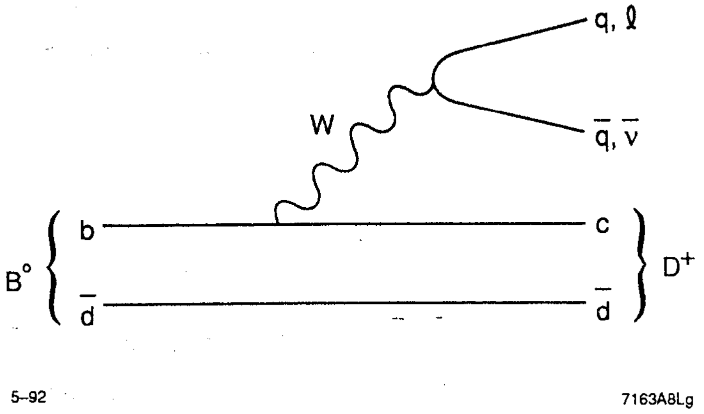

Figure 4 Decay of a B^0 meson. According to the spectator model, the spectator quark has no influence in the decay of the b quark.

decay since there is no lepton mixing. Even if neutrino mixing does occur, the decay rate remains unchanged since we sum over all ν states. For the present, we are ignoring the decay rate contribution from $b \to u$ transitions since $V_{ub} << V_{cb}$. Finally, Γ_B is much larger than the muon decay rate because of the difference in mass between the muon and the bottom quark.

Naively, if we consider only the color factor then

$$\Gamma_B (W^* \to \bar{u}d : \bar{c}s : \bar{\nu}_e e : \bar{\nu}_\mu \mu : \bar{\nu}_\tau \tau) = 3 : 3 : 1 : 1 : 1$$

where Γ_B is in units of $|V_{cb}|^2 G_F^2 m_b^5 / (192\pi^3)$. The semileptonic branching fraction is just the probability that the virtual W will collapse into an $l\bar{\nu}$ pair and is $\frac{1}{9}$ = 11% for each lepton flavor.

1.4.2 Corrections to the Spectator Model

We can extend the naive spectator model by introducing three corrections:

- Phase space suppression factor.
- Soft gluon radiation.
- Hard gluon exchanges.

Since the charm mass is not negligible compared to the B mass, a phase space suppression factor must be incorporated into the partial decay widths. The factor for a three-body decay $b \to q f_1 \bar{f}_2$ can be written as [45][44]

$$I(\varepsilon_q, \varepsilon_1, \varepsilon_2) = 12 \int_{(\varepsilon_q+\varepsilon_1)^2}^{(1-\varepsilon_2)^2} \frac{dx}{x} [x - \varepsilon_q^2 - \varepsilon_1^2]\,[1 + \varepsilon_2^2 - x] \\ \times \sqrt{[x - (\varepsilon_q - \varepsilon_1)^2]\,[x - (\varepsilon_q + \varepsilon_1)^2]\,[(1+\varepsilon_2)^2 - x]\,[(1-\varepsilon_2)^2 - x]} \tag{11}$$

where $\varepsilon_q \equiv m_q/m_b$, $\varepsilon_1 \equiv m_{f_1}/m_b$, and $\varepsilon_2 \equiv m_{f_2}/m_b$. The phase space factor reduces to $I(0,0,0) = 1$ for massless fermions and

$$I(\varepsilon, 0, 0) = 1 - 8\varepsilon^2 - 24\varepsilon^4 \ln\varepsilon + 8\varepsilon^6 - \varepsilon^8 \tag{12}$$

if we include the charm mass. Using quark masses of m_b=5 GeV and m_c=1.6 GeV, the phase space factor is 0.48. The $\bar{c}s$ and $\bar{\nu}_\tau\tau$ states are even further suppressed. The total decay rate is three times smaller than the naive estimate. Also, the semileptonic branching fraction will increase slightly to 16% (refer to Table 4).

The soft gluon radiative correction corresponds to two additional Feynman diagrams that are order α_s extensions of the tree-level decay, where α_s is the strong coupling constant (Figure 5). The first diagram renormalizes the $b \to c$ vertex due to one-loop gluon corrections, while the second diagram reflects the emission of real gluons. Both diagrams are needed to cancel the infrared divergence from soft colinear gluons. Nonleptonic B decays have an additional QCD vertex correction for the $q\bar{q}$ system from the W current. This factor is identical to the first order QCD vertex correction for $Z^0 \to q\bar{q}$. The modification to the B decay width for an individual mode can be written as [45][46]

$$\Gamma_B \to \Gamma_B \cdot \left(1 - \frac{2\alpha_s}{3\pi} f(\varepsilon_q)\right) \tag{13}$$

where $\varepsilon_q = m_q/m_b$. For $b \to c$ transition we use $\alpha_s(m_b) = 0.20$, $f_{sl}(\varepsilon_c) = 2.4$, and $f_{nl}(\varepsilon_c) = 0.9$, which results in a soft gluon correction of –10% and –4% for semileptonic (*sl*) and nonleptonic (*nl*) decays, respectively.

The third modification to the naive spectator model accounts for the color-suppressed diagram shown in Figure 6. As stated above, the charm quark will usually form a color singlet with the spectator quark. However, a hard gluon exchange between the quark lines can rearrange the color indices such that the $\bar{u}d$ pair from the charged W current no longer forms a color singlet. The new color singlets are $c\bar{u}$ and $\bar{q}d$. Since the color singlet $c\bar{u}$ is electrically neutral, the QCD

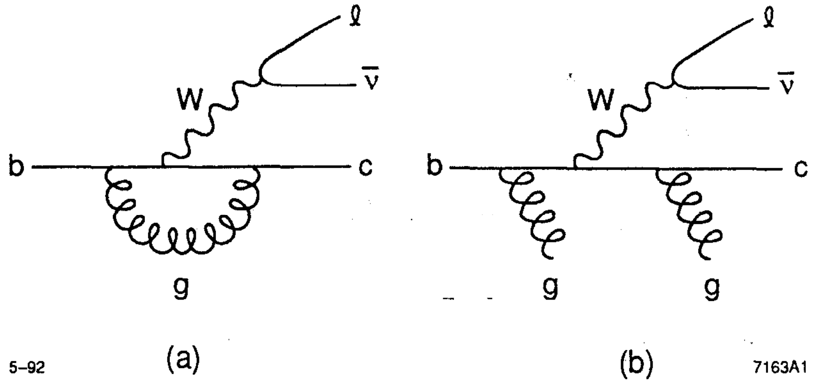

Figure 5 *Soft gluon radiative corrections to the B hadron decay rate:* (a) One-loop gluon correction to the *W* vertex, and (b) bremsstrahlung of soft gluons.

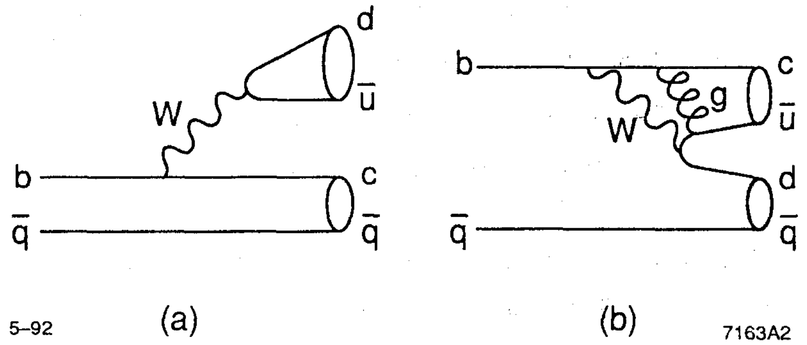

Figure 6 Hard gluon corrections to the *B* decay rate: (a) The color-favored diagram shows the usual color singlets. (b) In the color-suppressed diagram, a hard gluon is exchanged between quark lines and rearranges the color indices to form an alternate set of color singlets.

correction induces an effective neutral current, $b \to d$. This modifies the normal color factor value of 3 to the quantity $2c_+^2 + c_-^2$ where $c_\pm$ corresponds to the symmetric and antisymmetric combination of the color-allowed and the color-suppressed diagrams. The coefficients $c_\pm$ can be expressed as [43]

$$\begin{aligned} c_+ &= 1 - \frac{\alpha_s}{2\pi} \ln\left(\frac{m_W^2}{\mu^2}\right) \\ c_- &= 1 + \frac{\alpha_s}{\pi} \ln\left(\frac{m_W^2}{\mu^2}\right) \end{aligned} \tag{14}$$

If we turn off strong interactions, then $c_+ = c_- = 1$, and the color factor is 3. But if we renormalize $c_\pm$ at the B mass scale, then $c_+ \approx 0.85$, $c_- \approx 1.4$. The hadronic decay modes are enhanced by 13%. Since the semileptonic modes are not affected by hard gluon exchange, this effect will reduce the semileptonic branching fraction to 14%.

Even with these corrections to the naive spectator model, the theoretical semileptonic branching fraction differs from the current experimental value of $\mathrm{Br}\,(B \to Xl\nu) \approx 11\%$. The spectator model fails to describe the nonleptonic decay rate for several reasons. QCD interactions are only marginally perturbative at the bottom mass scale. Hence, gluon exchanges between the $b\bar{c}$, $\bar{u}d$, and spectator quark lines are only crudely approximated by the soft and hard gluon interactions described above. Also, the spectator quark does not necessarily play a passive role in nonleptonic decays, as will be discussed in Section 1.8.

The spectator model describes the semileptonic B decays with much greater success. The $l\bar{\nu}$ system is decoupled from the quark lines, and so the variety of QCD interactions is simplified tremendously. The inclusive semileptonic B decay rate $\Gamma_{sl}(B \to X_c l\bar{\nu})$ can be expressed as

$$\Gamma_{sl} = |V_{cb}|^2 \cdot \frac{G_F^2 m_b^5}{192\pi^3} \cdot I(\varepsilon_c, 0, 0) \cdot \left(1 - \frac{2\alpha_s}{3\pi} f_{sl}(\varepsilon_c)\right) \qquad (15)$$

Table 4 Partial decay rates of B hadrons, including phase space and QCD corrections, in units of $|V_{cb}|^2 G_F^2 m_b^5/(192\pi^3)$. The W^* denotes the virtual W in the B decay.

B Decay Channel	Naive Spectator	Phase space	add Soft gluons	add Hard gluons
$\Gamma(W^* \to e\bar{\nu})$	1	0.48	0.43	0.43
$\Gamma(W^* \to \mu\bar{\nu})$	1	0.48	0.43	0.43
$\Gamma(W^* \to \tau\bar{\nu})$	1	0.15	0.14	0.14
$\Gamma(W^* \to \bar{u}d)$	3	1.50	1.38	1.56
$\Gamma(W^* \to \bar{c}s)$	3	0.45	0.43	0.49
Total Γ_B	9	3.00	2.81	3.05
$\mathrm{Br}\,(b \to Xl\bar{\nu})$	11%	16%	15%	14%

Nevertheless, Γ_{sl} depends on the fifth power of the bottom quark mass, which is theoretically known to far less accuracy than either the B^0 or B^+ meson mass. Turning the equation around, the value of the CKM element V_{cb}, computed from the measured semileptonic decay rate, is limited by the theoretical uncertainty in the b quark mass.

In recent years several models have been developed to bridge the gap between calculable heavy quark decays and insoluble heavy meson decays. The ACM model by Altarelli *et al.* [48] is a quasi-free quark model which accommodates certain QCD corrections, which effectively softens the lepton spectrum. The spectator quark is assumed to travel with a Fermi momentum, which is gaussianly distributed with an average value of P_F. The b quark mass can be expressed in terms of the B meson mass of m_B=5.280 GeV, the spectator quark mass (m_{sp}), and the Fermi momentum. The ACM model has three free parameters: P_F, $\varepsilon_c = m_c/m_b$, and m_{sp}, which are determined from a fit to the lepton momentum spectrum. Hence, the expression for Γ_{sl} is completely void of the explicit m_b^5 dependence.

Other models predict exclusive semileptonic B meson decay rates into $Dl\bar{\nu}$, $D^*l\bar{\nu}$, or $D^{**}l\bar{\nu}$. The Isgur-Scora-Grinstein-Wise (ISGW),[49] Wirbel-Bauer-Stech (WBS),[50] and Körner-Schuler (KS) [51] models describe the exclusive decays in terms of form factors and the mass of the B^0 or B^+ meson. For instance, the decay $B \rightarrow Dl\bar{\nu}$ can be characterized by a single form factor, whereas the decay $B \rightarrow D^*l\bar{\nu}$ requires three non-negligible form factors since the D^* meson has three polarization states, namely the longitudinal and transverse polarization states. These models use different functions for the form factors and different normalization schemes. The ISGW model uses a non-relativistic wave function to describe the valence quarks in the hadron and normalizes the form factors at the maximum allowed q^2, which corresponds to a zero recoil of the D meson in the B rest frame. The form factors are maximal at q^2_{max} since the B and D wave functions have the greatest overlap. The WBS and the KS models describe only the D and D* modes. They use a relativistic wave function and normalize the form factors at q^2=0. All these models remove the explicit dependence on the fifth power of the b quark mass, and so the CKM elements can be determined with much greater accuracy. Nevertheless, the models all give slightly different relationships between V_{cb} and Γ_{sl}.

The Heavy Quark Effective Theory [52] (HQET) is not a model, but a theory which predicts relative rates of certain heavy quark exclusive decay rates. HQET has been most successful at describing exclusive semileptonic decays when the resulting D or D^* meson has low momentum recoil. The theory uses spin and heavy flavor symmetry to relate the 45 form factors in the four processes, $B^{(*)} \to D^{(*)} l\bar{\nu}$, in terms of a single universal form factor. Thus, extracting the CKM elements from the form factors is greatly simplified.

1.5 The B Lifetime

The B lifetime is equal to the reciprocal of its total decay rate, Γ_b. Unfortunately, Γ_b is difficult to compute theoretically because of the complexity of its hadronic decay modes from QCD corrections and non-spectator model contributions. The lifetime can be alternatively expressed in terms of the semileptonic branching fraction $\mathrm{Br}(B \to Xl\nu)$, which has been measured extensively (see Table 18 on page 89), and the semileptonic decay rate Γ_{sl}, which is theoretically better understood.

$$\tau_b = \frac{1}{\Gamma_b} = \frac{Br(B \to Xl\nu)}{\Gamma_{sl}} = \frac{192\pi^3}{G_F^2 m_b^5} \cdot \frac{\mathrm{Br}(B \to Xl\nu)}{0.43|V_{cb}|^2 + 0.85|V_{ub}|^2} \tag{16}$$

As stated in the previous section, the spectator model quite adequately describes semileptonic B decays. The calculation of Γ_{sl} is analogous to the muon decay rate $\Gamma(\mu \to e\bar{\nu}_e \nu_\mu)$ except for a few minor modifications. The b quark mass replaces the muon mass. The factors 0.43 and 0.85 describe the phase space suppression and the soft gluon corrections for $b \to c$ and $b \to u$ transitions, respectively. The W decay vertex also includes the CKM matrix element V_{cb} or V_{ub}.

Heavy quarks with full mixing will have lifetimes significantly shorter than the muon lifetime (τ_μ=2.20 μs), stemming from the m_q^5 dependence. Before 1980 the CKM matrix elements V_{cb} and V_{ub} were not known experimentally. Assuming that V_{cb} was close in magnitude to the sine of the Cabibbo angle, $\sin\theta_c = V_{us} \approx 0.22$, the B lifetime would have had an immeasurably small value of 0.04 picoseconds. B hadrons from Z^0 decays would travel on average 70 microns before decaying. This distance would be extremely difficult to measure even with today's sophisticated silicon strip vertex detectors.

Prior to 1983, only upper limits had been placed on the B lifetime. The most stringent limit of τ_b< 1.4 ps (95% CL) was set by the JADE collaboration in 1982. It therefore came as quite a surprise when in the following year, the MAC and Mark II collaborations at the PEP storage ring measured the B lifetime to be 1-2 ps. Since that time, PEP and PETRA have made numerous refinements on the τ_b

measurement. Recently, the LEP groups have added new precision to the lifetime measurement. Figure 7 and Table 5 highlight the evolution of the measured B lifetime from the 1982 JADE upper limit to the current LEP results. The world average is presently $\tau_b = 1.29 \pm 0.05$ ps.†

The fact that τ_b is thirty times larger than was previously expected indicates that the second and third quark generations are more weakly coupled than the first and second generation. Inserting the values into Eqn. (16) yields a CKM element for $b \to c$ transitions of $|V_{cb}| \approx 0.04$. The CLEO [73] and ARGUS [74][75] collaborations, operating at the Υ_{4S}, have recently measured $b \to u$ transitions to be about 1% of all B decays, yielding a value of $|V_{ub}| \approx 0.004$.

1.6 Bottom Lifetime Measurement Techniques

The bottom quark has been studied extensively at lower center of mass energies. The CLEO and ARGUS experiments copiously produce the Υ_{4S} excited $b\bar{b}$ bound state, which has sufficient rest mass energy to decay into bottom mesons. Unfortunately, because this process is at the threshold of B meson production, the mesons do not travel a measurable distance before decaying. Most of our knowledge of the bottom lifetime comes from experiments at the PEP and PETRA e^+e^- storage rings at center of mass energies of 29-34 GeV. In the past two years a new window for observing bottom hadrons has opened up on the Z^0 resonance at the LEP e^+e^- storage ring and the SLC e^+e^- collider. The Z^0 resonance offers a better platform to measure the bottom hadron lifetime for a number of reasons:

- Bottom quarks are produced in greater abundance at the Z^0resonance. The Z^0 boson is copiously produced at LEP, and $b\bar{b}$ events account for 22% of all hadronic decays of the Z^0, whereas they make up only 9% of the hadronic events at PEP/PETRA energies
- The charm background is substantially lower. This is particularly important since charm decays mimic many of the properties of bottom decays. The process $Z^0 \to c\bar{c}$ occurs in 18% of hadronic decays, while charm production occurs 36% of the time at lower center of mass energies.
- The flight path of the bottom hadron before it decays is approximately 2 mm at the Z^0resonance due to the Lorentz boost of the bottom hadron. This is a factor of three longer than at PEP/PETRA energies.

---

† From the 1992 Particle Data Group.

Table 5 Chronology of bottom lifetime measurements. For each measurement, the enrichment scheme and lifetime method is listed.

Experiment (include ref.)	Year	B tag	Lifetime method	Lifetime (ps)
JADE [1]	1982	High P_T lepton	Lepton δ	< 1.4
MAC [2]	1983	High P_T lepton	Lepton d	$1.8 \pm 0.6 \pm 0.4$
Mark II [3]	1983	High P_T lepton	Lepton δ	$1.20^{+0.45}_{-0.36} \pm 0.30$
TASSO [4]	1984	Boosted sphericity product (BSP)	All chg trk δ	$1.83\ ^{+0.38}_{-0.37}\ ^{+0.37}_{-0.34}$
DELCO [6]	1984	High P_T lepton	Lepton δ	$1.16\ ^{+0.37}_{-0.34} \pm 0.23$
JADE [5]	1986	High P_T lepton	Lepton δ	$1.8\ ^{+0.5}_{-0.4} \pm 0.4$
HRS [7]	1987	High P_T lepton	Lepton δ	$1.02\ ^{+0.42}_{-0.39}$
MAC [8]	1987	High P_T lepton	All chg trk δ	$1.29 \pm 0.20 \pm 0.20$
DELCO [9]	1988	High P_T lepton	Lepton δ	$1.17\ ^{+0.27}_{-0.22}\ ^{+0.17}_{-0.16}$
Mark II [10]	1989	High P_T lepton	Lepton δ	$0.98 \pm 0.12 \pm 0.13$
TASSO [11]	1989	1. BSP 2. none 3. none	1. All chg trk δ 2. Decay vtx 3. Dipole moment	$1.35 \pm 0.10 \pm 0.24$
JADE [12]	1990	1. High P_T lepton 2. BSP	1. Lepton δ 2. Decay length	$1.36\ ^{+0.25}_{-0.23}$
DELPHI [14]	1991	High P_T lepton	Lepton δ	$1.30 \pm 0.10 \pm 0.08$
DELPHI [14]	1991	none	All chg trk δ	$1.27 \pm 0.04 \pm 0.12$
OPAL [18]	1991	High P_T lepton	Lepton δ	$1.37 \pm 0.07 \pm 0.07$
ALEPH [16]	1991	High P_T lepton	Lepton δ	$1.29 \pm 0.06 \pm 0.10$
L3 [17]	1991	High P_T lepton	Lepton δ	$1.32 \pm 0.08 \pm 0.09$

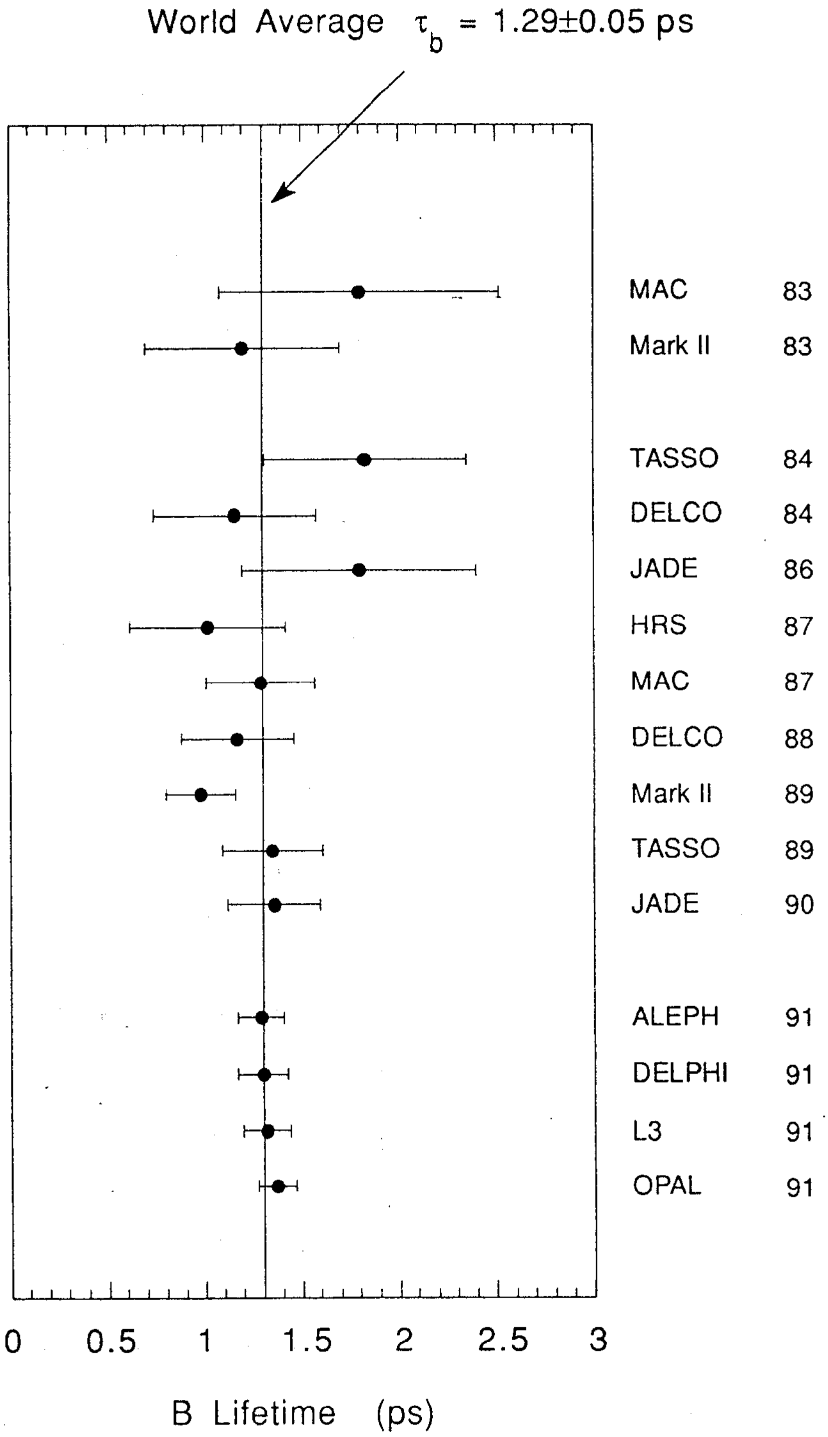

Figure 7 Chronology of bottom lifetime measurements. The current world average τ_b=1.29±0.05 ps.

- Tracks from B decays can be measured more precisely in $b\bar{b}$ production at higher center of mass energies, because the tracks undergo less multiple scattering as they traverse through the detector material.

A typical $b\bar{b}$ event is illustrated in Figure 8. The bottom hadron travels a distance $L=c\tau\beta\gamma$, where the decay time τ is exponentially distributed. Ideally, we would like to extract the bottom decay time from a measurement of both the decay length and the momentum of the B. For example, the bottom decay sequence would be fully reconstructed with the available charged tracks, and the secondary decay vertices would be isolated from the primary Z^0 vertex. Since the decay length is on average 2 mm, we might think it would be an easy task. Unfortunately, this is not the case.

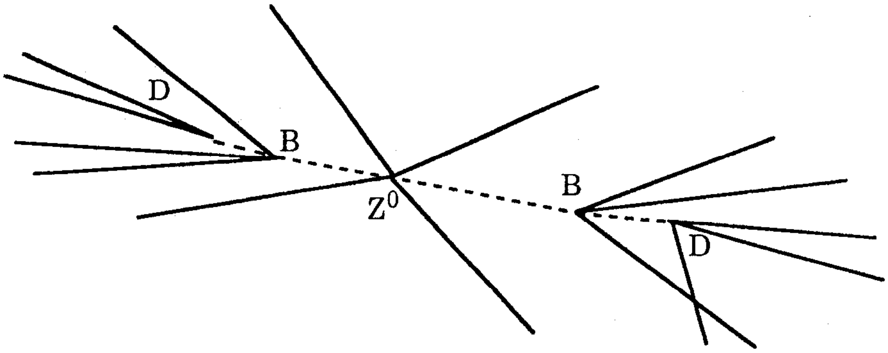

Figure 8 Topology of a $Z^0 \to b\bar{b}$ event. Tracks emanate from the primary vertex at the Z^0 decay, two secondary B decay vertices, and two tertiary charm decay vertices. The *B* and *D* decay paths are represented by the dashed lines.

The $Z^0 \to b\bar{b}$ decay kinematics and the finite resolution of a charge track detector complicates our ability to fully reconstruct the bottom hadron.

- Charged tracks can originate from any of five decay vertices. Out of roughly 20 charged tracks in a hadronic Z^0 decay, on average only five tracks will emerge from each bottom hadron. Half of these tracks will come directly from the bottom decay, while the remainder will be from the tertiary charm decay that can be about 1 mm away. Finally, 10 tracks in the event are fragmentation tracks that are produced at the Z^0 decay vertex. A few tracks can also result from strange hadrons that decay centimeters from the Z^0.

- Unlike some fixed target experiments that can take "snapshots" of the actual B decay sequence in thick emulsion plates, we start to measure the tracks long after the B has decayed. Measurement errors and multiple coulomb scattering smear the track position, and make it difficult to extrapolate the track back to its decay vertex. Decay tracks will not appear to emerge from a single point in space.
- Bottom hadrons are boosted to high energies of $\langle\beta\gamma\rangle \approx 6$, which tends to collimate the B decay tracks into a narrow cone. Reconstructing the B decay sequence becomes more complicated, since tracks will often be consistent with arising from both the primary vertex and the B decay vertex.
- Most vertex tracking chambers only measure the (r,φ) coordinates of the track in the plane perpendicular to the beam axis. Without the extra z dimension to disentangle the decay topology, any two tracks can appear to come from the same vertex. N tracks in a plane will form N(N-1)/2 intersections.

Because of the extreme difficulty in fully reconstructing the bottom decay vertex, we can instead retrieve most of the lifetime information by examining the impact parameters of charged tracks. Tracks are projected onto the plane perpendicular to the beam axis. The impact parameter (δ) is the distance of closest approach of the track to the primary vertex in the transverse plane. The sign of the impact parameter is positive if the intersection of the track and the reconstructed bottom hadron flight path corresponds to a positive decay length, otherwise it is negative (see Figure 9). Equivalently, the impact parameter sign is positive if the track trajectory $\hat{P}$ and the vector $\vec{\delta}$, which connects the primary vertex to the point of closest is approach on the track, have components that are both parallel to the reconstructed B flight direction $\hat{P}_B$, i.e. $(\hat{P} \cdot \hat{P}_B)\ (\vec{\delta} \cdot \hat{P}_B) > 0$. The sign is negative if one component is parallel and the other is anti-parallel, i.e. $(\hat{P} \cdot \hat{P}_B)\ (\vec{\delta} \cdot \hat{P}_B) < 0$. The technique for finding the primary vertex location and the reconstructed bottom direction will be postponed until Section 4.3.

$b\bar{b}$ events will have an accumulation of positively signed impact parameters. The impact parameters from B decay tracks reach an asymptotic value as the B momentum increases. We can write

$$\delta = L \sin\theta \sin\psi \tag{17}$$

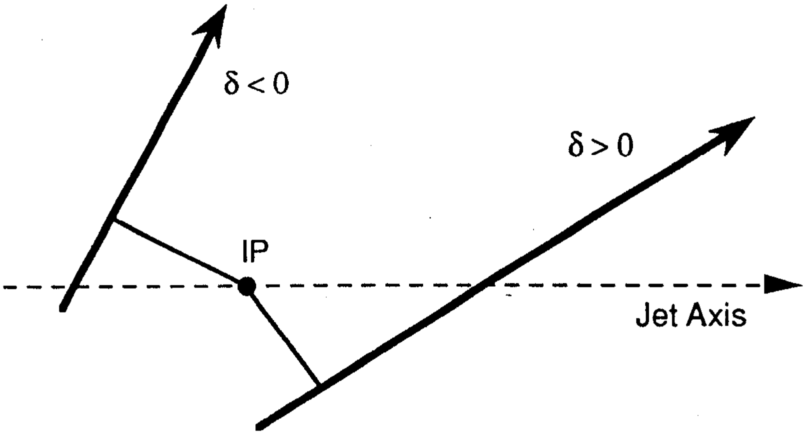

Figure 9 The track impact parameter (δ) is defined as the distance of closest approach to the interaction point (IP) in the plane perpendicular to the beam axis. The impact parameter is signed positive if the track intersects the jet axis in front of the IP; otherwise it is negatively signed.

where $L = c\tau\beta\gamma$ is the decay length, τ is the proper decay time, θ is the polar angle of the track with respect to the beam axis, and ψ is the opening angle between the track and the B direction in the transverse plane. At very large B momenta such as at LEP/SLC energies, the opening angle behaves as $\psi \propto 1/\gamma$. The γ factors cancel between the decay length and opening angle, so tracks coming from B decays will typically possess $\langle\delta\rangle \approx$ 100-300 μm. Although the impact parameter value plateaus for large B momenta, the origin of tracks with higher momentum can be discerned more accurately because the tracks scatter less through the detector.

The Mark II vertex detector can resolve impact parameter to better than 50 μm for most tracks in a hadronic Z^0 decay, hence a typical $b\bar{b}$ event will have several tracks that significantly miss the interaction point. The distribution of impact parameters displays an exponential-like decay shape (see Figure 10). Light quark events (*uds*) and fragmentation tracks from $b\bar{b}$ events will have an impact parameter distribution that is clustered about zero. Impact parameters from charm events will be intermediate between the two cases. Charm mesons have a relatively long lifetime of $\langle\tau_c\rangle \approx 0.55$ ps. They also have a non-negligible mass so that the opening angle ψ can be quite substantial.

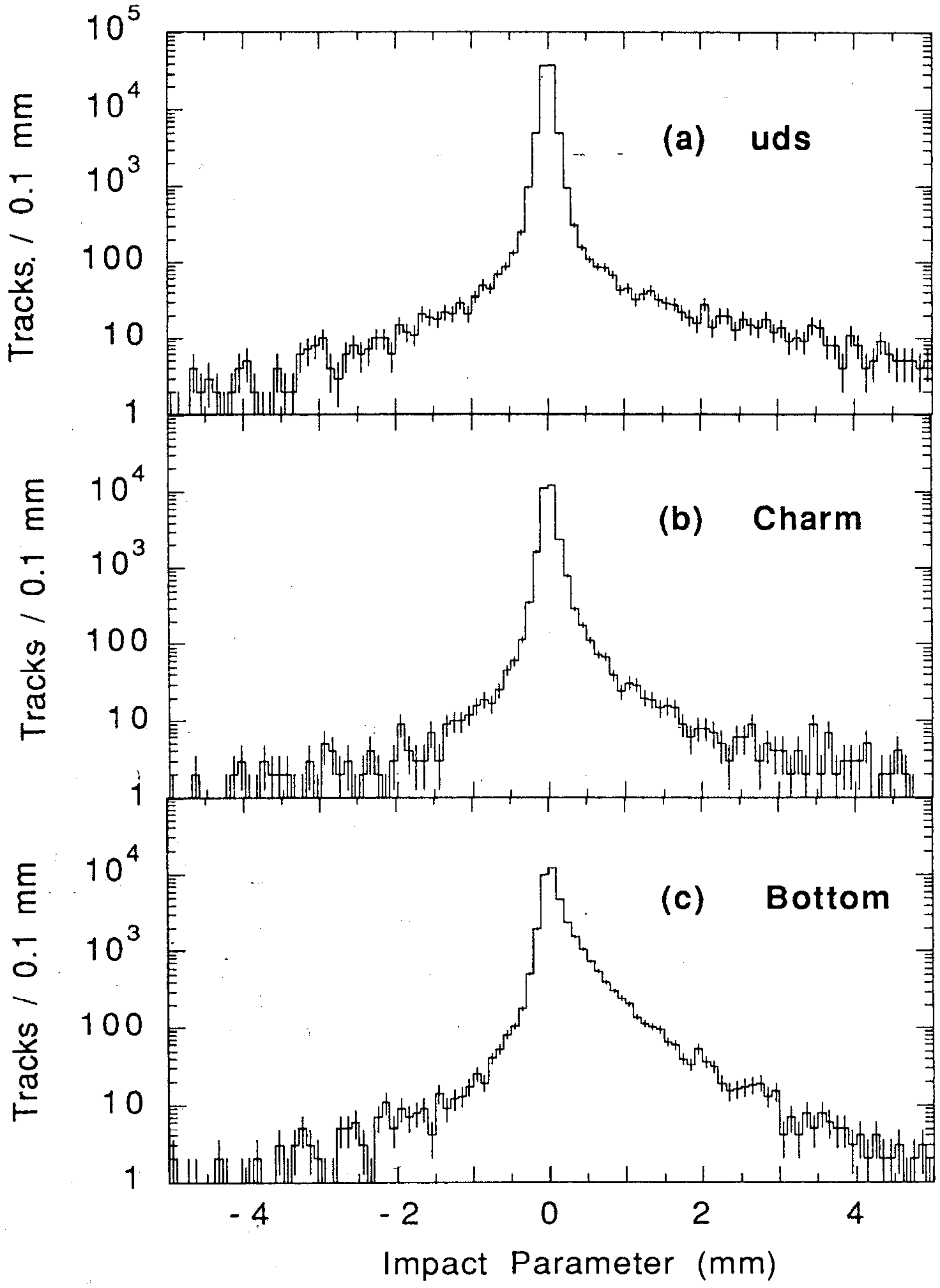

Figure 10 Impact parameter distributions for tracks from (a) *usd*, (b) charm, and (c) bottom events. The distributions include tracking resolution and beam position uncertainties.

1.7 Prior Methods Used to Measure the B Lifetime

1.7.1 High P_T Lepton Tagging

One of the most reliable techniques for measuring the bottom lifetime is to extract τ_b from the impact parameter distribution of leptons from semileptonic B decays. These leptons possess high momentum and high transverse momentum (P_T) with respect to the thrust axis. Experiments at PEP, PETRA, and LEP all have measured the lifetime using this method. Bottom hadrons decay into an electron or muon about 20% of the time. Including the efficiency for detecting a high P and high P_T lepton, roughly 2-3% of the B's are sampled at the LEP experiments. The B purity of these events is 64-88%. Leptons from semileptonic charm decays also have large momenta but are filtered out because the much smaller charm mass leads to a reduced lepton P_T.

These high P_T leptons will tend to have well measured impact parameters since they experience very little multiple coulomb scattering as they traverse through the detector elements. Furthermore, semileptonic decays of heavy quarks are well understood theoretically, and so systematic errors due to any model dependency of B decays is greatly reduced. The impact parameters for leptons have an exponential-like decay distribution in the case of perfect track resolution, but because the resolution for most vertex detectors is much greater than 100 μm, the shape more closely resembles a gaussian distribution with a slightly positive mean. The experimental results of an older version of the Mark II detector at PEP [10] is shown in Figure 11.

1.7.2 Hadronic B Decays

Other techniques have been developed to take advantage of the remaining 80% of B decays that do not yield a high P_T lepton. These methods employ general properties of the B decay topology and the long decay length to enrich the data with $b\bar{b}$ events.

One method of tagging $b\bar{b}$ events measures the "boosted sphericity product" of an event. B mesons have a substantial invariant mass and generate decay tracks with significant P_T, so if we boost the tracks in a jet to the B meson's rest frame the decay tracks will be distributed isotropically and will have high sphericity. Since we cannot determine the B momentum on an event-by-event basis, an average boost of $\langle\gamma\beta\rangle \approx 6$ is used. Lighter quarks require a substantially greater boost to be in their

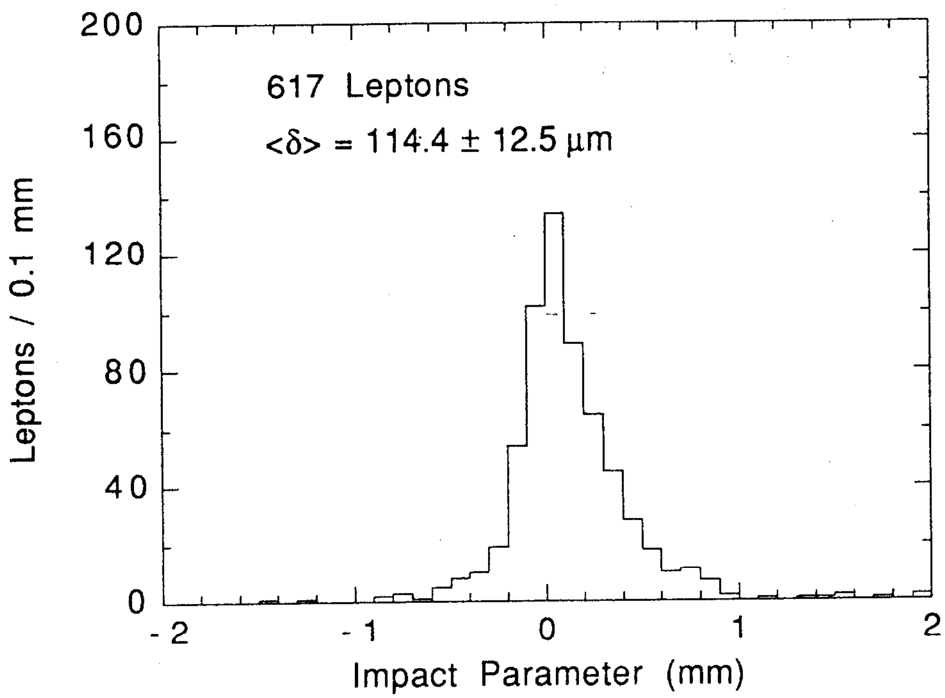

Figure 11 Impact parameter distribution for high P_T leptons from the Mark II experiment at PEP. The positive mean signifies the nonzero lifetime of the B hadron.

rest frame, hence a boost of only $\gamma\beta \approx 6$ will still preserve their jet-like appearance. This idea can be quantified by defining the sphericity

$$S = \frac{3}{2} \min \frac{\sum_i \left|\vec{p}_i \times \hat{S}\right|^2}{\sum_i \left|\vec{p}_i\right|^2}, \tag{18}$$

where $\hat{S}$ is the unit vector that minimizes S and is commonly called the sphericity axis. $S \approx 1$ for spherical events and $S \approx 0$ for tightly collimated 2-jet events. The B-tag consists of boosting track momentum vectors in each hemisphere by a fixed amount and computing the sphericity for this boosted set of tracks. The data is enriched with $b\bar{b}$ events by requiring the product of boosted sphericity for the two hemispheres to exceed a minimum value. TASSO [11] has used this tag at $E_{cm}=35$ GeV with the value $\beta=0.74$ to achieve a purity of 29% and an efficiency of 35% in selecting $b\bar{b}$ events. DELPHI [27] has also used this technique to measure the $Z^0 \rightarrow b\bar{b}$ branching fraction, but has not pursued it to extract the B lifetime. They used a boost of $\beta=0.96$ to obtain an enriched sample of $b\bar{b}$ events that is 40% pure and 15% efficient.

Another method of isolating B events is to search for separated vertices. The method finds an "average" vertex from the amalgamation of tracks in the bottom and tertiary charm decays. Tracks with significant impact parameters are used to form the seed for a separated vertex. Additional tracks consistent with the vertex are accreted onto the vertex. Events are chosen with a separated vertex that has at least four tracks and a positive decay length. The Mark II at PEP [72] used this technique to tag 5% of the B hadrons with a 55% sample purity. Since the opposite hemispheres are not used in the separated vertex search, they represent an unbiased source of B hadrons for the lifetime analysis.

Once an enriched sample of B hadrons is collected, the lifetime can be extracted from the inclusive impact parameter distribution. This process is more difficult than extracting the lifetime from a high P_T lepton impact parameter distribution. Care must be used to interpret the distribution since the hadronic B decays are less understood than the semileptonic decay. The tracks will originate from three sources: the primary vertex, the secondary B decay vertex, and tertiary charm decay vertex. The enriched events from the boosted sphericity product tag will not necessarily represent an unbiased sample of B hadrons because the tagging efficiency depends on the momentum of the two B's which in turn has some influence on the impact parameters. The MAC, Mark II, and TASSO collaborations have measured τ_b using this method with a number of different enrichment schemes. The DELPHI collaboration has recently measured τ_b without any enrichment scheme by examining the impact parameter distribution for all high P and P_T charged tracks.

An alternate method developed by TASSO and JADE measures the decay length of the pseudo decay vertex composed of all tracks in a single hemisphere. TASSO uses a boosted sphericity product tag while JADE uses no bottom enrichment scheme. The pseudo decay length only approximates the true B decay length, since again, the reconstructed vertex is composed of tracks from the primary, secondary B and tertiary charm decays.

Finally, MAC tags $b\bar{b}$ events by requiring a high P_T lepton and measures the lifetime from the inclusive impact parameter distribution from all tracks in the event. These results are all listed in Table 1.

1.7.3 Specific B Hadron Decay Modes

With the integrated luminosity increasing at LEP, we will start to see lifetime analyses for specific decay modes of bottom hadrons. The signature of a specific decay mode is more distinctive and better understood than that of generic B decays. For instance, kinematic constraints and particle identification have proved helpful in searching for ψ, $D^{*-}l^{+}$, and $\bar{D}^{0}l^{+}$ candidates. This procedure not only offers a highly pure B sample but also allows an accurate B vertex reconstruction by eliminating the fragmentation tracks. Of course the major drawback is that reconstruction efficiencies are inherently low.

OPAL[15] has measured τ_b from the inclusive ψ production: $B \rightarrow \psi X$. They gain a big handle on the decay kinematics by equating the ψ boost to the B hadron boost. Using the decay length and momentum of 45 reconstructed ψ's they measure $\tau_b=1.31^{+0.31}_{-0.25} \pm 0.15$ ps.

All the B lifetime measurements described above examine the average B lifetime. The B hadrons produced at high energy $e^{+}e^{-}$ collision are a mixture of B^0, B^+, B_s. and B baryons which are all believed to have approximately equal lifetimes of 1.3 ps. The details will be discussed in the next section. The Mark II at PEP[13] was the first to study the lifetime of an individual B meson species. They identified 15 B^0 mesons by partially reconstructing the semileptonic decay $B^{0} \rightarrow D^{*-}l^{+}\nu$. The high P_T lepton, the soft satellite pion from the D^{*-} decay, and a partially reconstructed $\bar{D}^{0}$ were all required. The lifetime extracted from the decay lengths of the B^0 mesons was $\tau(B^0)=1.20^{+0.52+0.16}_{-0.36-0.14}$ ps. ALEPH[19] has refined this technique to measure the exclusive B^0 and B^+ lifetimes by also partially reconstructing semileptonic decays. Their sample consists of 25 $D^{*-}l^{+}$ events and 50 $\bar{D}^{0}l^{+}$ events. They measured $\tau(B^0)=1.40^{+0.52+0.18}_{-0.48-0.40}$ ps and $\tau(B^+)=1.35^{+0.42+0.26}_{-0.46-0.40}$ ps.

1.8 B^0 / $B^{\pm}$ Lifetime Differences

Most of the published results on τ_b measure the average B lifetime from an ensemble of B hadrons. If the charged and neutral B meson lifetimes differ, then the average lifetime is sensitive to the mixture of B hadrons. The spectator model predicts that all B hadrons have the same lifetime, since it assumes the spectator quark does not participate in the decay of the heavy quark.

Experimental evidence suggests that the B^0 and B^+ mesons have approximately the same lifetime. CLEO and ARGUS have measured the ratio of lifetimes $\tau(B^+)/\tau(B^0)$ by comparing the semileptonic branching fractions for B^0 and B^+ mesons in Υ_{4S} decays. Assuming the semileptonic decay rates are equal, as predicted by the spectator model, the lifetimes will be proportional to the semileptonic branching fractions of the B^0 and B^+. One method examines the lepton and dilepton inclusive rates. The second method compares the exclusive semileptonic branching fraction

Table 6 Ratio of lifetimes for B^+ and B^0 mesons.

Experment	Method	$\tau(B^+)/\tau(B^0)$
CLEO [25]	dilepton rate	[0.49,2.27] 95% CL
ARGUS [21]	dilepton rate	$1.00^{+0.49}_{-0.32}$
CLEO [22]	exclusive $D^{(*)}$	0.89±0.19±0.13
ARGUS [24]	exclusive $D^{(*)}$	1.00±0.23±0.14
ALEPH [56]	decay length	$0.96^{+0.69+0.58}_{-0.44-0.25}$

Table 7 Charm hadron properties. Λ_c represents all charm baryons. The semileptonic branching fraction for D_s has not been measured experimentally.

Charm Hadron	Mass (GeV)	Lifetime (10^{-13} sec)	Semileptonic branching fraction
D^0	1.865	4.21±0.10	7.7±1.2 %
D^+	1.869	10.62±0.28	19.2±1.5 %
D_s	1.969	4.45±0.33	~8%
Λ_c	2.285	1.91±0.15	4.5±1.5 %

into vector and pseudoscalar charm mesons for the two B mesons (see Table 6). As discussed in Section 1.7.3, direct measurements of the exclusive B meson lifetime have just begun by using partially reconstructed semileptonic decays. Much higher statistics are needed to reach any firm conclusions.

The Fermilab E653 hybrid emulsion experiment is the only group that reports a difference in charged and neutral B lifetime. [20] They use an active target of 1.5 cm thick nuclear emulsion, which allows direct observation of the B production and decay vertices and also the sign of the B hadron candidate. However, since the estimated B momenta are typically greater than 100 GeV, the emulsion is inefficient in detecting the longest decay times. From 20 bottom candidates, the E653 collaboration measures $\tau(B^0) = 0.95^{+0.5}_{-0.3}$ ps and $\tau(B^+) = 2.5^{+2.0}_{-0.8}$ ps.

The situation is completely different in the charm sector. The spectator model utterly fails to explain the factor of 2.5 difference between the D^0 and the D^+ lifetimes (see Table 7). The semileptonic decay rates are the same for both D^0 and D^+ since the ratio of lifetimes equals the ratio of semileptonic branching fractions. Hence, the nonleptonic decay rate must be the culprit. There are two possible explanations: [41][42][43]

1. Γ_{nl} is enhanced for D^0
2. Γ_{nl} is diminished for D^+

or some combination of the two. In both cases nonspectator diagrams must play a substantial role in the total decay rate.

The nonleptonic decay rate for D^0 and D_s^+ can be enhanced by two additional decay paths: the W exchange and the W annihilation between the charm quark and the spectator quark (Figure 12). The D^+ meson can also decay via the W exchange diagram, although it is heavily Cabibbo suppressed. Even though the amplitude gains a large factor in phase space, these diagrams are helicity suppressed because a pseudoscalar meson cannot decay weakly into two massless fermions. The decay rate is proportional to the square of the fermion mass, which explains why pions and kaons will decay into $\mu\bar{\nu}$ but rarely into $e\bar{\nu}$. Instead of a m_c^5 dependence, the decay rate is proportional to $f_D^2 m_q^2 m_c$, where f_D is the charm pseudoscalar decay constant which relates the overlap of the quark wavefunctions for the $c\bar{q}$ system, and m_q is the mass of the final state quark. The helicity suppression might be circumvented if hard gluons in heavy meson decays carry away momentum and spin from the valence quarks so that the $c\bar{q}$ system is no longer in a spin 0 state. Charm baryons can decay through the W exchange channel without being subject to helicity suppression and do in fact have lifetimes shorter than the D^+ meson. These extra decay modes also help to explain why the semileptonic branching fraction is significantly lower than the spectator model prediction of 20%. If the W exchange and annihilation rates are large, then we should observe D_s^+ decays into strange-free final states such as 3π, $\rho\pi$, and $\omega\pi$. The E691 collaboration, however, has observed the dominant decay modes to be $s\bar{s}$ states such as $\phi\pi$ and $K^{(*)}K$. The importance of the W exchange and annihilation decay modes is far from being clear.

On the other hand, the lifetime difference could also be explained by a reduction of the nonleptonic decay rate for D^+ mesons due to destructive interference between the color-allowed and the color-suppressed spectator diagrams (Figure 13). The color singlets are $s\bar{d}$ and $u\bar{d}$ for both diagrams. Since charm mesons usually decay

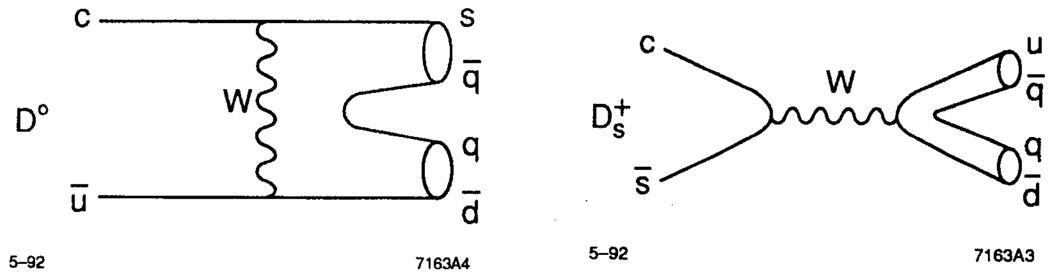

Figure 12 Non-spectator W exchange and W annihilation diagrams for the D^0 and D_s mesons can enhance their total decay rate, and hence decrease their lifetime. The corresponding W annihilation diagram for D^+ is Cabibbo-suppressed.

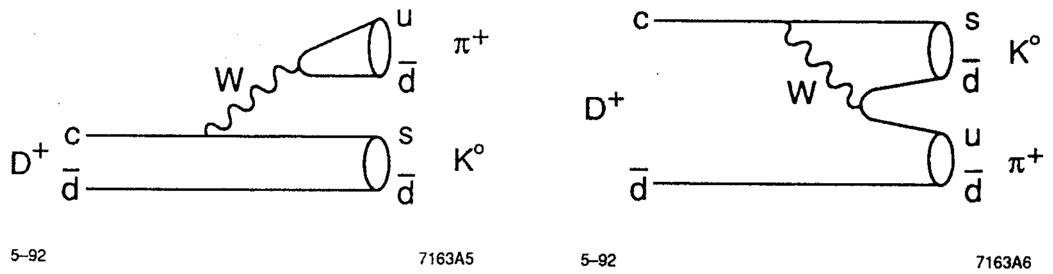

Figure 13 Both the color-favored and color-suppressed spectator diagrams for D^+ can produce the same two-body final state, $K^0\pi^+$. Destructive interference reduces the total D^+ decay rate, and hence increases its lifetime.

into two-body pseudoscalar-pseudoscalar or pseudoscalar-vector modes, the identical final states will interfere destructively. [47] No such interference exists for the D^0 decay since the two sets of color singlets are either $(s\bar{u})$ $(u\bar{d})$ or $(s\bar{d})$ $(u\bar{u})$. Instead of the m_c^5 dependence as in the spectator diagram, the decay rate for the interference diagram will be proportional to $f_D^2 m_c^3$. Unfortunately this contribution is expected to be too small to explain the lifetime difference. We should realize that these arguments are solely heuristic, since QCD processes are becoming non-perturbative at the charm mass scale.

The theoretical situation for the bottom sector is somewhat clearer. The decay constants for all pseudoscalars are expected to be roughly equal, i.e. $f_\pi \approx f_K \approx f_D \approx f_B \approx 100 - 300$ MeV. [83] Thus, since the decay rate for the non-spectator diagrams increase as a smaller power of the heavy quark mass, their contribution to the total decay rate of B mesons should be diminished by a factor of $m_b^2/m_c^2 \sim 10$ compared to that of charm mesons. Also the destructive interference effects for B^+ should be further reduced, since B hadrons decay rarely into two-body final states. Hence, current theoretical prejudice suggest that the lifetimes are indeed close.

However, if an appreciable difference exists between the B^0 and B^+ mesons lifetimes, then different lifetime analyses could measure different values for the average B lifetime. For instance, since the semileptonic branching fraction is proportional to the lifetime of the B hadron, assuming that the semileptonic decay rates are identical, a high P_T lepton tag will preferentially select the B species with the larger semileptonic branching fraction and hence the longer lifetime. If we extract τ_b from the impact parameter distribution of high P_T leptons, the measured lifetime will be biased toward the longer-lived B hadron.

A tag based on impact parameters will also favor the longer-lived B hadron. However, the two B hadrons in a $Z^0 \to b\bar{b}$ event are completely uncorrelated in either the B hadron type or the decay time. If we select jets with either an impact parameter tag or a high P_T lepton tag, but use only the jet opposite the tag in the lifetime analysis, the lifetime sample will be composed of an equal number of long-lived and short-lived B's. Hence, the high P_T lepton method using lepton impact parameters will tend to observe a larger average B lifetime.

Assuming that B^0 and B^+ mesons are produced in equal abundance at the Z^0 resonance and that the semileptonic decay rates are identical, the average lifetime measured by an impact parameter tag is $(1+\alpha)/2 \cdot \tau(B^0)$, where α is the ratio of the charged to neutral B lifetimes, $\tau(B^+)/\tau(B^0)$. The corresponding average using a high P_T lepton technique is $(1+\alpha^2)/(1+\alpha) \cdot \tau(B^0)$. Hence the ratio of the two average B lifetime measurements is

$$\frac{\langle\tau\rangle_{lepton}}{\langle\tau\rangle_{impact}} = \frac{2(1+\alpha^2)}{(1+\alpha)^2} \tag{19}$$

This ratio has a minimum of 1.0 in the case that the B^0 and B^+ lifetimes are identical (Figure 14). We would have to resolve this ratio to an accuracy of 11% (4%) to exclude a lifetime difference of a factor of two (1.5). Reducing the systematic errors to this level of precision would be a challenge.

Presently, direct measurements of the individual B^0 and B^+ lifetimes by partially reconstructing semileptonic decays are beset by low reconstruction

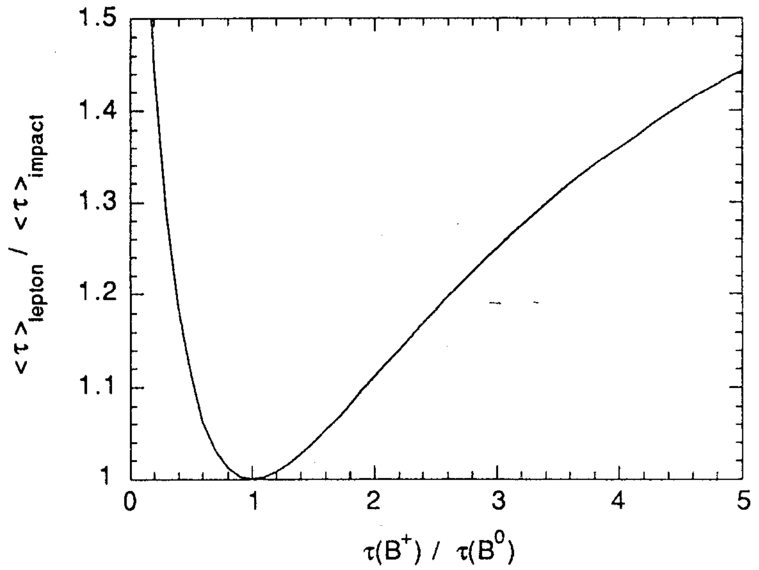

Figure 14 Ratio of the average B lifetime measurements using a high P_T lepton tag versus an impact parameter tag, as a function of the actual charged to neutral B lifetime ratio.

efficiencies. A comparison of average B lifetimes using impact parameters from hadronic B decays versus high P_T leptons could offer a complementary method to uncover differences in the B^0 and B^+ lifetimes. The CKM matrix element V_{cb} can still be extracted from the measured average B lifetime as long as the relative fractions of each B species in the enriched sample is taken into account.

1.9 Preview of Our Experimental Method

The Mark II vertex detector system at the SLC has appreciably more resolving power than the vertex detectors used in the past by the Mark II at the PEP storage ring. $b\bar{b}$ events from hadronic Z^0 decays typically have several tracks with large impact parameters. In this thesis, we will obtain a sample enriched in $b\bar{b}$ events by requiring a jet to have two or more tracks with significant impact parameter. The jet opposite the tag represents a sample of B hadrons unbiased in decay times, which can be used to extract the B lifetime. Rather than examine the inclusive impact parameter distribution of all charged tracks in the unbiased sample, we will introduce the quantity $\Sigma\delta$, which is the sum of impact parameters from all charged tracks in the unbiased jet. The $\Sigma\delta$ distribution for the bottom enriched sample has a roughly exponential decay shape and possesses a number of properties that are advantageous over the inclusive δ distribution. Our measurement of the B lifetime will be extracted from the $\Sigma\delta$ distribution for jets opposite the tagged jets.

In Chapter 2, we will discuss the elements of the Mark II detector salient to the lifetime measurement. In Chapter 3, we will describe the Monte Carlo used to generate hadronic events and simulate the response of the Mark II detector. Next, we will characterize the tracking resolution in Chapter 4. In Chapter 5, we will introduce the impact parameter tag, which enriches our data with bottom hadrons. The purity and efficiency of the tag is compared with other methods. In Chapter 6, we will describe the properties of the $\Sigma\delta$ distribution, from which our measurement of the B lifetime is extracted. Consistency checks and systematic errors of the measurement are investigated. Finally, in Chapter 7 we will summarize the results of this thesis and suggest the prospects for future B lifetime measurements.

Knowledge is a sacred cow, and my problem will be
how we can milk her while keeping clear of her horns.
– Albert Szent-Gyorgyi

2 Tracking

The measurement of the bottom hadron lifetime in this thesis was accomplished using the Mark II detector at the Stanford Linear Collider (SLC). [88] The SLC is a pioneer accelerator built to produce Z^0 bosons from e^+e^- collisions at a center of mass energy of 91 GeV. To avoid the large synchrotron energy losses in the beams, the SLC collides particle beams once and then discards them. All other contemporary accelerators in the world that collide electron and positron beams head-on use the more conventional storage rings, which can recirculate particle beams for hours, but must restore energy losses in the beams every revolution.

The layout of the SLC is shown in Figure 15. Electrons and positrons are first stored in the damping rings, which reduce the emittance of the particle bunches. Subsequently, the electron and positron bunches are simultaneously accelerated down the two-mile linear accelerator (LINAC) to energies of ~50 GeV. At the end of the LINAC, the beams are transported through two arcs, focused to a few microns in diameter, and collided head-on at the interaction point.

The Mark II detector was positioned at the collision point and observed the production and decay of Z^0 bosons. The Mark II detector at the SLC is an upgraded version from its days at the SPEAR and PEP storage rings. An upgraded Central Drift Chamber was installed in the Mark II detector in 1985 and tested at the PEP storage ring, prior to the move to the SLC collision site.

The SLC underwent a lengthy and arduous commissioning process, and struggled with high beam backgrounds and low instantaneous luminosities. It was

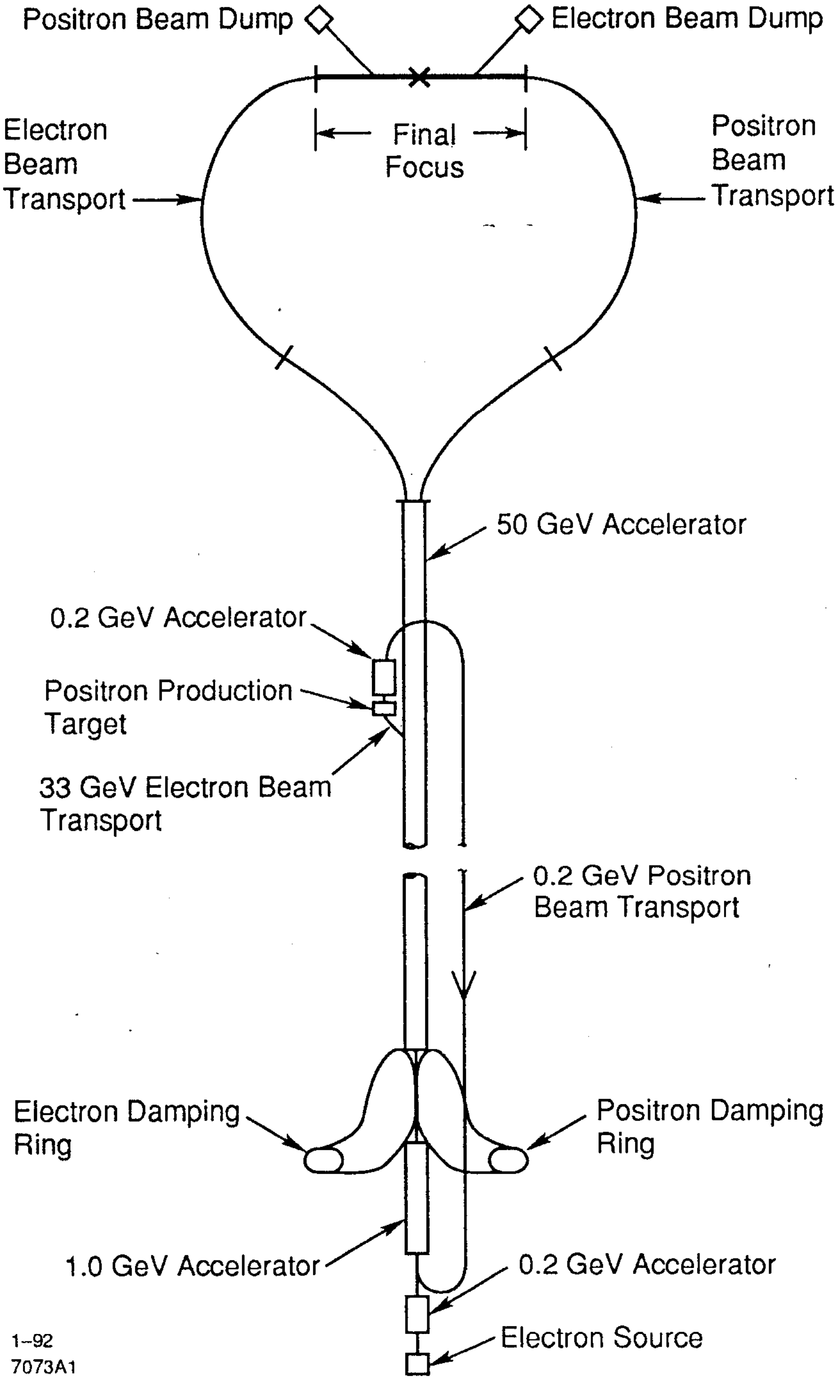

Figure 15 Layout of the Stanford Linear Collider (SLC).

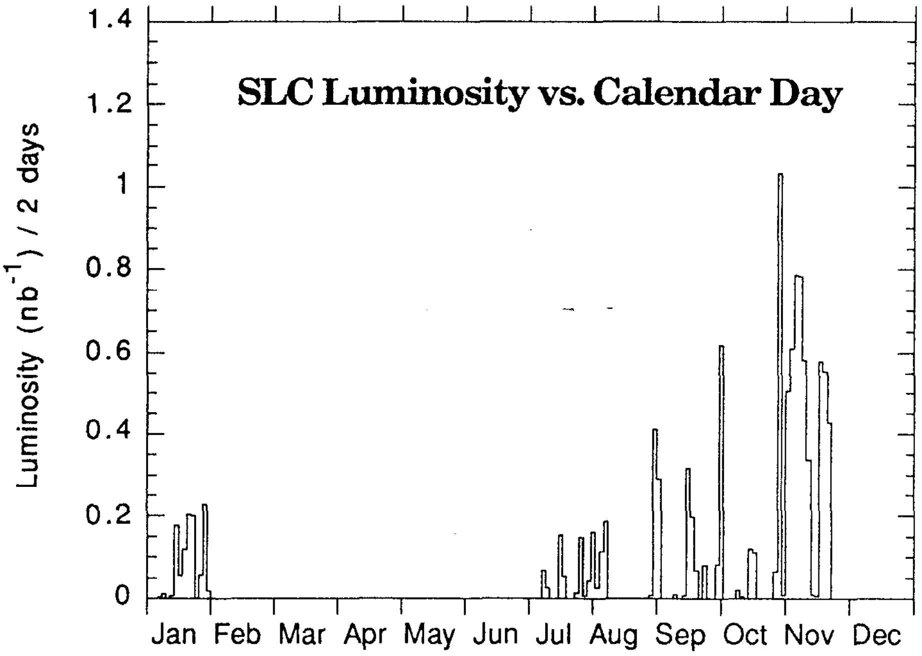

Figure 16 Luminosity collected by the Mark II detector in 1990 at the SLC. The total integrated luminosity was 10.1±0.7 nb^{-1}.

not until April 11, 1989 that SLAC observed its first hadronic Z^0 decay. The Mark II collected a total of 528 Z^0 decays from April to October of 1989. With this sample, the Mark II Collaboration measured the mass and width of the Z^0 resonance, and showed that the number of light neutrino families was less than four. [89][90] The Loma Prieta earthquake struck the San Francisco bay area that October with a magnitude of 7.1 on the Richter scale, caused minor damage to the SLC, and delayed operations for the remainder of the year.

The Drift Chamber Vertex Detector and the Silicon Strip Vertex Detector were installed into the Mark II detector at the end of 1989, and during a short engineering run in January 1990 to test the vertex detector system, 37 Z^0 events were collected. After a lengthy shutdown, colliding e^+e^- beams were resumed from June through November. Luminosity delivered to the Mark II was sporadic, because the bulk of the effort was devoted to SLC LINAC studies and improvements (Figure 16). A total of 294 Z^0 events were recorded by the Mark II in 1990, of which 208 passed our hadronic event selection requirements.

The rest of the chapter details the description and performance of the Mark II detector. In particular, we will focus on the tracking system for charged particles, which is achieved with a central tracking detector and two high precision vertex detectors.

2.1 Overview of the MARK II Detector

The Mark II detector [60] illustrated in Figure 17 is a general purpose detector designed to provide precision tracking, electromagnetic calorimetry, and lepton identification. Charged tracks in the angular range of $|\cos\theta| \leq 0.8$ are measured by three tracking devices: an outer 72 layer Central Drift Chamber, an intermediate 38 layer Drift Chamber Vertex Detector, and an inner 3 layer Silicon Strip Vertex Detector. The B lifetime analysis hinges on the ability to measure charged tracks with great precision, which includes not only measuring track impact parameters to high accuracy, but also understanding the tracking resolution errors. Also, the efficiency for finding tracks in the fiducial volume of the detectors must be known with great certainty.

The coordinate system of the Mark II detector is defined as follows: $\hat{x}$ points horizontally in the direction perpendicular to the beam axis away from the Linear Accelerator, $\hat{y}$ points upwards, and $\hat{z}$ points horizontally along the beam axis in the direction of the electron beam. Due to the cylindrical symmetry of the Mark II detector, positions are often defined in terms of r, φ, and θ coordinates, where the polar axis coincides with the beam direction at the collision point.

The Mark II does not have any hadron calorimetry, nor is it effective in separating *π/K/p* particles. Expanding radially from the collision point, the major detector components include:

Beampipe

> The Mark II beampipe is an aluminum cylinder 25 mm in radius and 480 microns thick. It has a 25 micron coating of copper along the inside surface to reduce backgrounds from synchrotron radiation. At normal incidence the beampipe is 0.71% of a radiation length. Located inside the beampipe are two "wire flippers" used to determine the beam profile. Each wire flipper holds a carbon fiber at the end of an aluminum fork. The forks are perpendicular to each other and measure the beam by pivoting the carbon fiber into the beam. The flippers subtend 11% in azimuth and are 0.90% of a radiation length thick.

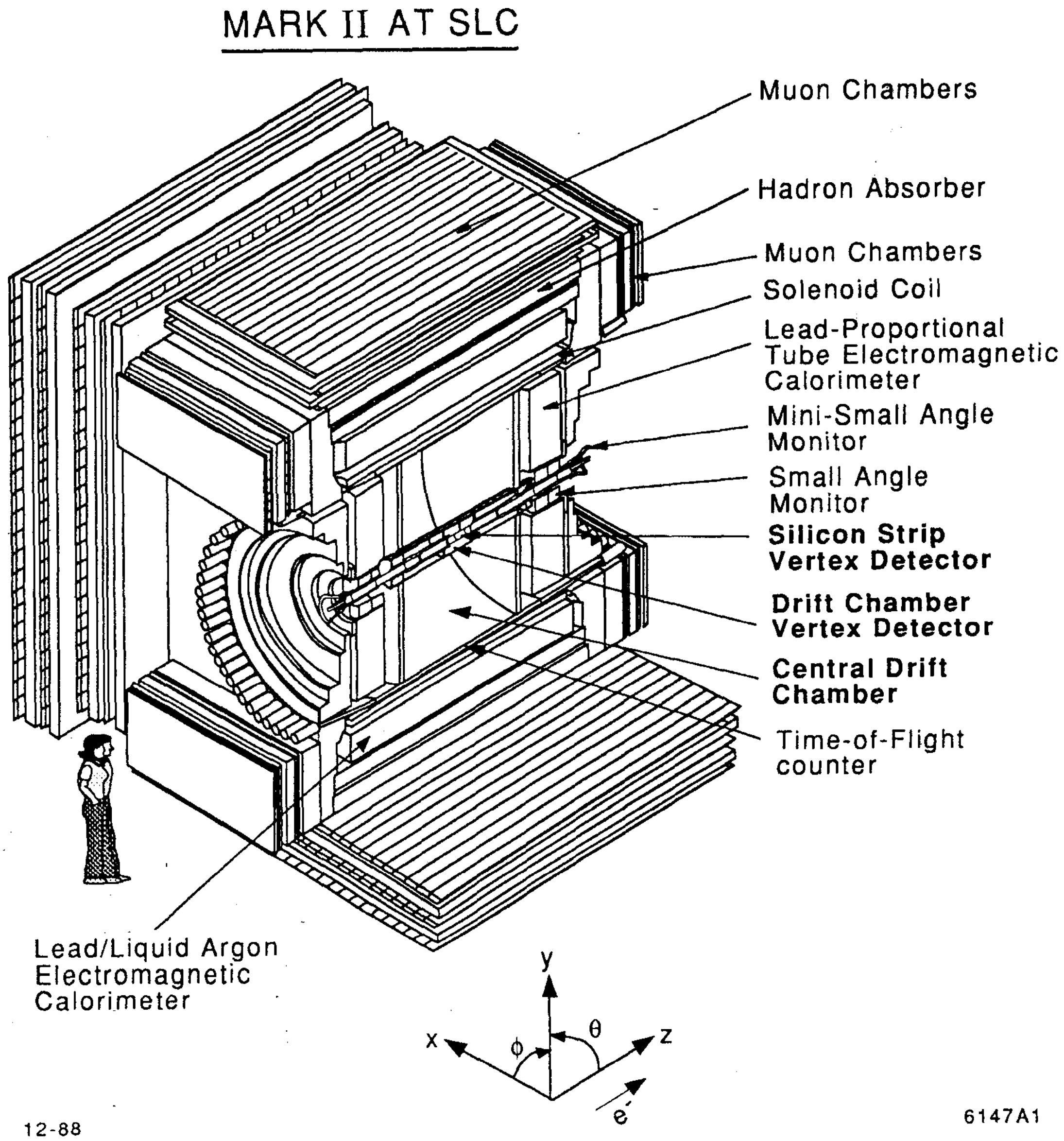

Figure 17 Overview of the Mark II detector. The tracking system is labeled in bold.

Silicon Strip Vertex Detector (SSVD)

High precision tracking is provided by the Silicon Strip Vertex Detector using three layers of silicon modules, with strips aligned with the beam axis. The modules span the region in radius between 29 mm and 38 mm from the interaction point. The SSVD has a spatial resolutions of 7.1 microns per measurement and a two-track separation of 100 microns (~0.3 mrad in azimuthal angle).

Drift Chamber Vertex Detector (DCVD)

The intermediate tracking is performed by a 38 layer vertex drift chamber. The wires are all axial and extend in radius from 5 cm to 17 cm. Its role is to link the main drift chamber tracks to the silicon detector and to provide better angular resolution. The DCVD has an average spatial resolution of 60 microns per measurement and a double-hit resolution of 500 microns in hadronic events.

Central Drift Chamber (CDC)

Composed of 72 axial and stereo wire layers, the Central Drift Chamber performs the pattern recognition for charged tracks, determines the track parameters, and helps separate electrons from pions with the track dE/dx information. The momentum resolution is $\sigma/p^2 = 0.31\%\ \mathrm{GeV}^{-1}$, and the spatial resolution in hadronic events is 200 microns. The CDC is the only track detector of the three that provides $\cos\theta$ and z information.

Time-of-Flight

The time-of-flight system provides a trigger for cosmic events and limited charged particle identification. It consists of 48 scintillator slabs arranged in a barrel of radius 152 cm and covers 70% of the 4π solid angle. The signals are read out by photomultiplier tubes at both ends, yielding a timing resolution of 220 ps.

Magnet

The magnet is a conventional aluminum solenoid with an inner radius of 156 cm and a thickness of 1.3 radiation lengths. It was operated at 4.75 kG and maintained a solenoidal field uniform to 3%. The field nonuniformities were mapped out and known locally to 0.1%. Hall probes at both ends of the CDC determined the absolute strength of the field to better than 0.1% accuracy.

Electromagnetic Calorimetry

Electromagnetic energy is measured by both a barrel and an endcap calorimeter. The barrel calorimeter is composed of eight azimuthal modules of interleaved layers of lead and liquid argon for a total depth of 14.1 radiation lengths. 3° gaps existed between modules, and the total angular coverage was 64% of 4π. The energy resolution is $\Delta E/E = 13.3\%/\sqrt{E} \oplus 3.3\%$. Studied at PEP energies, the identification efficiency for an electron of energy 1 GeV is 78% with a misidentification probability of 3% in the core of jets. These values improve for more energetic electrons.

The endcap calorimeter is an assembly of lead and proportional tubes with a thickness of 18 radiation lengths. It spans 22% of 4π, giving the combined electromagnetic calorimetry system a coverage of 86% of the total solid angle. The energy resolution of the endcap is $\Delta E/E = 22\%/\sqrt{E}$.

Muon Chambers

Muons with momenta greater than 1.8 GeV are identified with high efficiency. The muon system is composed of four layers of proportional tubes and steel absorber. The total thickness of 1.8 meters is equivalent to 7.3 interaction lengths. The muon system covers 45% of the 4π solid angle.

Luminosity Monitors

The integrated luminosity is monitored by two devices that measured the small angle Bhabha scattering rate. The Small Angle Monitor is located 1.4 m from the collision point and has an angular acceptance of 50–160 mrad. Bhabhas are identified using a nine layer drift tube tracking system and a six layer lead and proportional tube sampling calorimeter. The Bhabha cross section in the small angle monitor is 20% higher than the visible Z^0 cross section.

The Mini-Small Angle Monitor surrounds the beampipe at 2.1 m from the collision site and measures bhabhas at even lower polar angles over a range of 15-25 mrad. It is composed of six alternating layers of tungsten and plastic scintillator and has a thickness of 15 radiation lengths. The Bhabha rate is approximately seven times greater than the visible Z^0 rate.

2.2 Central Drift Chamber (CDC)

2.2.1 Chamber Description

The Central Drift Chamber [60][62] functions as the primary tracking device in the Mark II detector, with track parameters provided by measurements from 72 axial and stereo wire layers. The CDC is arranged in 12 concentric cylinders of cells called "superlayers", with each cell composed of six anode wires 2.3 meters in length. The 72 measurements span from 19 cm to 152 cm in radius. Staggering the sense wires by ±380 μm resolves the left-right ambiguity in a cell. Figure 18 and Figure 19 illustrates the CDC wire layout. The odd numbered superlayers are axial; the other superlayers are tilted off-axis by ±3.8° in order to provide stereo information. The CDC is the only tracking device that provides the z and $\cos\theta$ parameters of the track. The drift chamber gas is a mixture of Argon/CO_2/CH_4 in the ratio 89/10/1 (HRS gas) and flows through the chamber at a pressure just above one atmosphere. The gas is operated in a saturated regime, which makes the drift velocity relatively insensitive to perturbations in temperature, pressure, and high voltage. The drift velocity is roughly 52 μm/ns.

The ionization signal from each sense wire is amplified and split to two readout devices: a Lecroy 1879 TDC system which record hits above threshold and a 100 MHz Flash-ADC system which digitize the pulse waveform. TDC offers better spatial resolution but provides poorer double-hit resolution in dense hadronic jets. Second hits on a wire can be detected at 80% efficiency with the FADC for hits separated by 3.8 mm compared to 6.4 mm with the TDC alone. The double-hit capabilities of the two electronic systems are shown in Figure 20. When both TDC and FADC hit information exist, the TDC value is used. Time-slewing corrections from the integrated FADC charged could have been used to improve the TDC hit times but were never implemented. Another important feature of the FADC, particle identification through the track's dE/dx energy loss, was not used in this analysis.

2.2.2 Hit Efficiency

Drift chamber hit efficiencies were studied in cosmic and hadronic events and incorporated into the Monte Carlo to properly model hadronic events. The hit efficiency is defined as the probability that a CDC layer will detect a hit for a found track, excluding inefficiencies due to geometric acceptance. (Tracks from the chamber origin with $|\cos\theta| \geq 0.65$ will fail to pass through all 72 CDC layers.) The hit efficiency was nearly perfect for cosmic ray tracks (98%) but was significantly

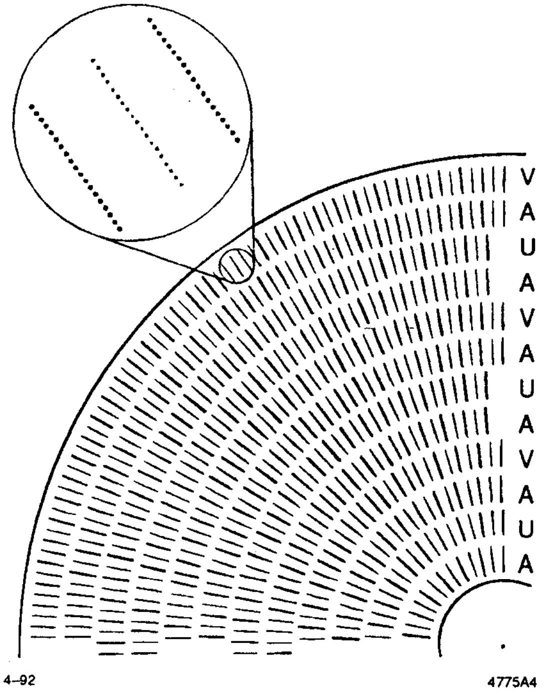

Figure 18 Superlayer design for the Central Drift Chamber, showing the axial (A) and stereo (U,V) arrangement.

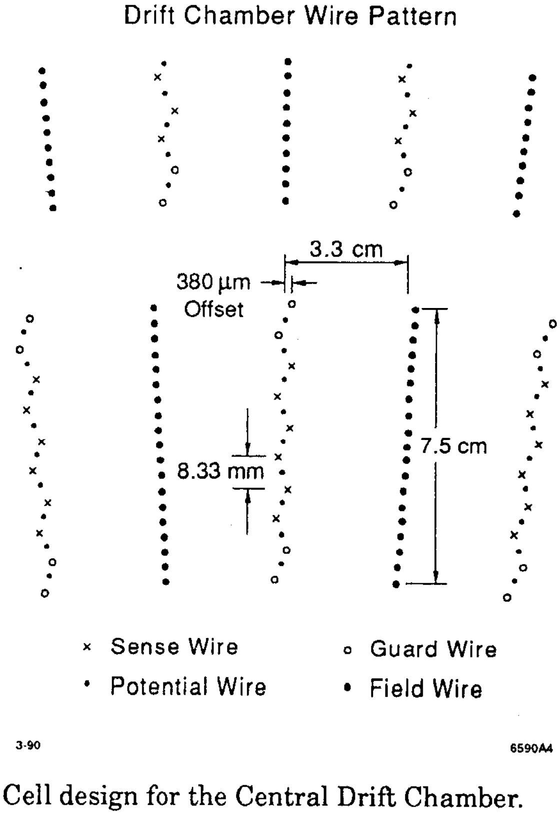

Figure 19 Cell design for the Central Drift Chamber.

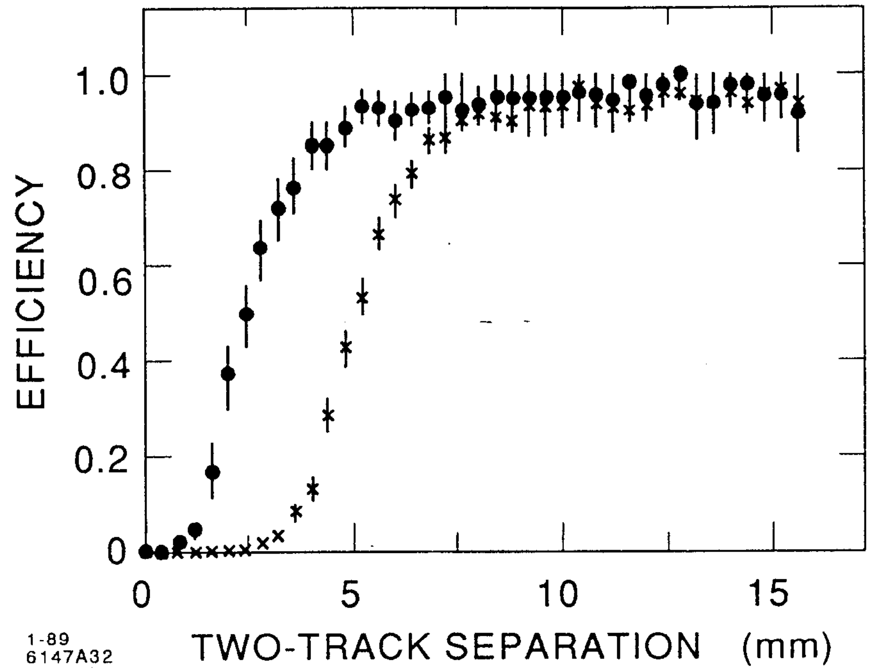

Figure 20 Efficiency for separating two tracks as a function of their distance apart in the Central Drift Chamber. The X's use only TDC hits, while the closed circles also use FADC pulse information.

worse for hadronic tracks. The individual wire efficiency for the 72 layers is shown for hadronic events in Figure 21. The histogram displays the most degradation in efficiency for the inner layers, dropping to 74% due to the limited multi-hit resolution as tracks in dense jets converge toward the interaction point. Beam-related backgrounds, most severe for the inner layers, also contributed to the loss of efficiency. In addition, some the of losses were correlated within a cell, resulting in zero out of an expected six hits in the cell. Figure 22 shows which of the 12 superlayers were especially problematic. High voltage problems plagued superlayer 12 throughout much of the run causing a total loss of hits in cells 20% of the time. Correlated cell inefficiencies also needed to be introduced into the Monte Carlo for superlayers eight and ten. Averaged over all tracks, the hit efficiency was 84%.

2.2.3 Spatial Resolution

The position of the track in the chamber was unfolded from TDC and FADC drift time information using a time-distance relation computed empirically from cosmic ray data. The left and right drift regions for each of the 72 wire layers were

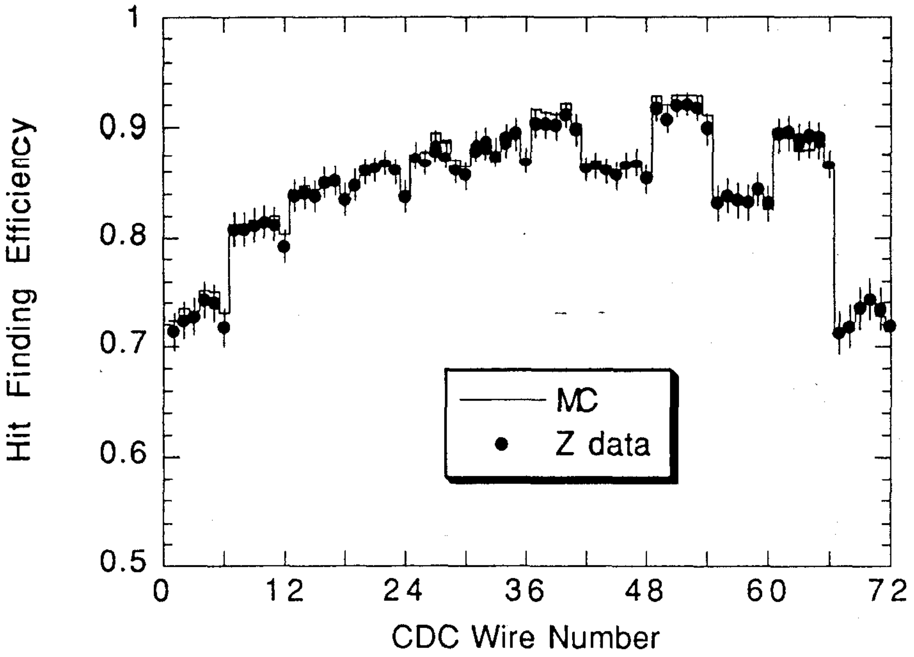

Figure 21 Hit finding efficiency in the Central Drift Chamber versus wire number. Loss of efficiency in the inner layers results from beam backgrounds and track convergence in jets.

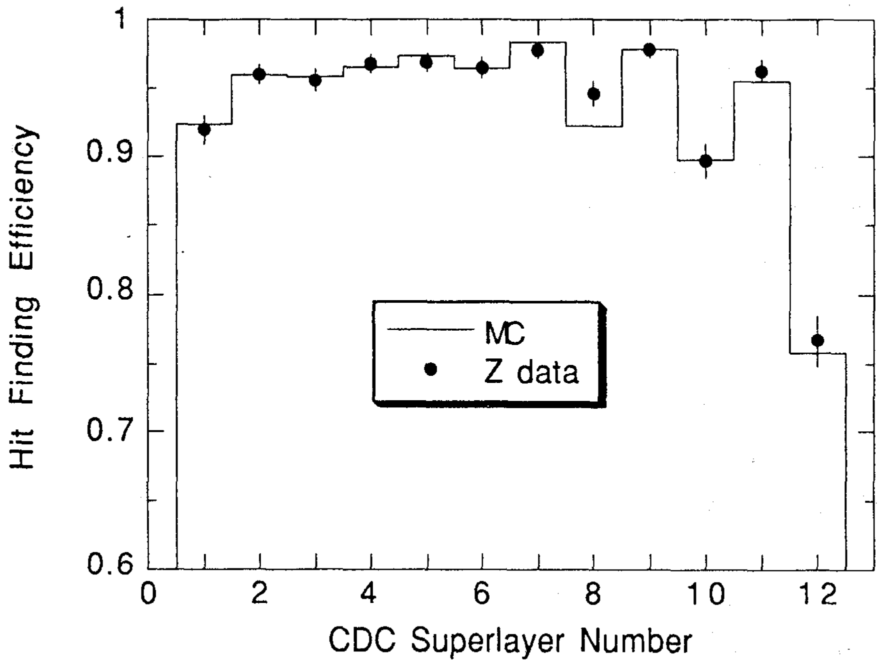

Figure 22 Hit finding efficiency in the Drift Chamber versus superlayer number, defined when at least one hit is found in the cell for that superlayer.

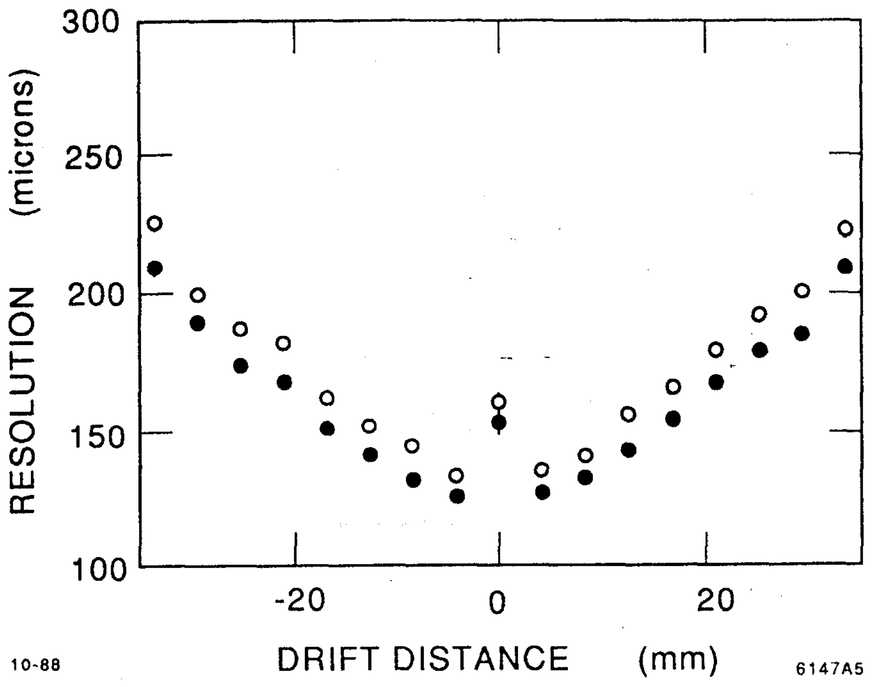

Figure 23 Spatial resolution of the Central Drift Chamber as a function of drift distance, with (closed circles) and without (open circles) time-slewing corrections.

subdivided into three drift regions, each with a constant drift velocity. This compensated for non-uniformities in the drift fields that were the most severe in the upper right corner and the lower left corner of the CDC cell, due to the drift of ionization charge at a Lorentz angle of ~20° in the 4.75 Kgauss field. Every two months, a new reservoir of HRS gas was installed, and the 432 drift velocity constants (72x2x3) were recalculated from a current block of cosmic events.

The accuracy of the track parameters depends on the accuracy of the individual hits on the track at the 72 radial positions. The spatial resolution of the individual hits was determined from the rms distribution of the track residuals. This quantity ranged from 130 μm to 250 μm and increased with drift distance due to charge diffusion (Figure 23). At maximum drift distances of 5 cm, diffusion contributes ~150 μm to the spatial resolution. Other errors included 35 μm from uncertainties in wire placement and 50 μm from time jitters in the electronics. Averaged over the entire cell, the position resolution is about 200 μm in hadronic events.

Second hits on a wire suffer from worse spatial resolution because late-arriving ionization from the first hit often distorts the leading edge of the second pulse. These effects were modeled in the Monte Carlo by smearing these pulses an additional 100 μm. Orphan FADC hits, i.e. those without TDC information, occur when the hit comes within 5 mm of a prior hit and experience an extra spatial degradation of 250 μm. The resolution also worsens near the anode plane, because the drift velocity is no longer uniform in the higher drift field and is not modeled well by the time-distance relation. Also the leading edge of pulses near the anode is subject to greater fluctuations due to poorer ion statistics, since the paths of the primary electrons are no longer as isochronous; a significantly smaller fraction of the total signal will arrive with the leading edge.

2.2.4 Track Finding

Charged particles travel along a helix in a 4.75 kG solenoidal magnetic field. The trajectory is parametrized by five quantities: the azimuthal angle of the track at the point of closest approach to the origin in the xy plane (φ_0), the track curvature ($1/P_{xy}$), where P_{xy} is the track momentum perpendicular to the beam axis, the impact parameter in the xy plane (δ), the position along the beam axis in z at the point of closest approach in the xy plane (z_0), and the polar direction with respect to the beam axis ($\cos\theta$). The errors associated with the track parameters (φ_0, $1/P_{xy}$, δ, z_0, $\cos\theta$) are extracted from the 5x5 covariance matrix computed by minimizing the track residuals normalized by their errors in a least squares fit.

The main drift chamber pattern recognition programs have been tested extensively from data collected during the PEP and the SLC pre-vertex runs. [65] In essence, colinear hits in a CDC cell are combined into straight track segments. These segments are the building blocks used to construct the helical tracks. Segments with identical curvature and φ_0 from the six axial superlayers are grouped first. Cosθ and z information are next determined by adding stereo segments to the track. The algorithm allows for dE/dx energy losses and multiple scattering contributions. The multiple scattering is not computed at every layer since this would demand the inversion of a 72x72 matrix. Instead it is approximated by augmenting the track error matrix via the Glückstern prescription. [66]

2.2.5 Tracking Performance

A typical two-jet hadronic event displaying the found tracks in the Central Drift Chamber is shown in Figure 24. The track finding efficiencies have been studied extensively using Bhabha events at PEP and Monte Carlo simulations at SLC energies. For isolated tracks that go through all layers, the efficiency was measured to be 99%, where a track is required to have at least 20 position measurements out of a possible 72. MC studies suggest that the efficiency decreases to 96% for tracks with $|\cos\theta| \leq 0.8$ in hadronic events at the SLC. Figure 25 shows the efficiency as a function of cosθ for bhabhas and hadronic tracks. The Monte Carlo models hadronic tracks less accurately where the efficiency falls at large cosθ or small P_{xy} (Figure 25 and Figure 28). In order to avoid regions where the efficiency is less well understood, we will use tracks with $|\cos\theta| \leq 0.8$ and $P_{xy} \geq 0.15$ GeV. The hit distribution for fiducial tracks is displayed in Figure 26.

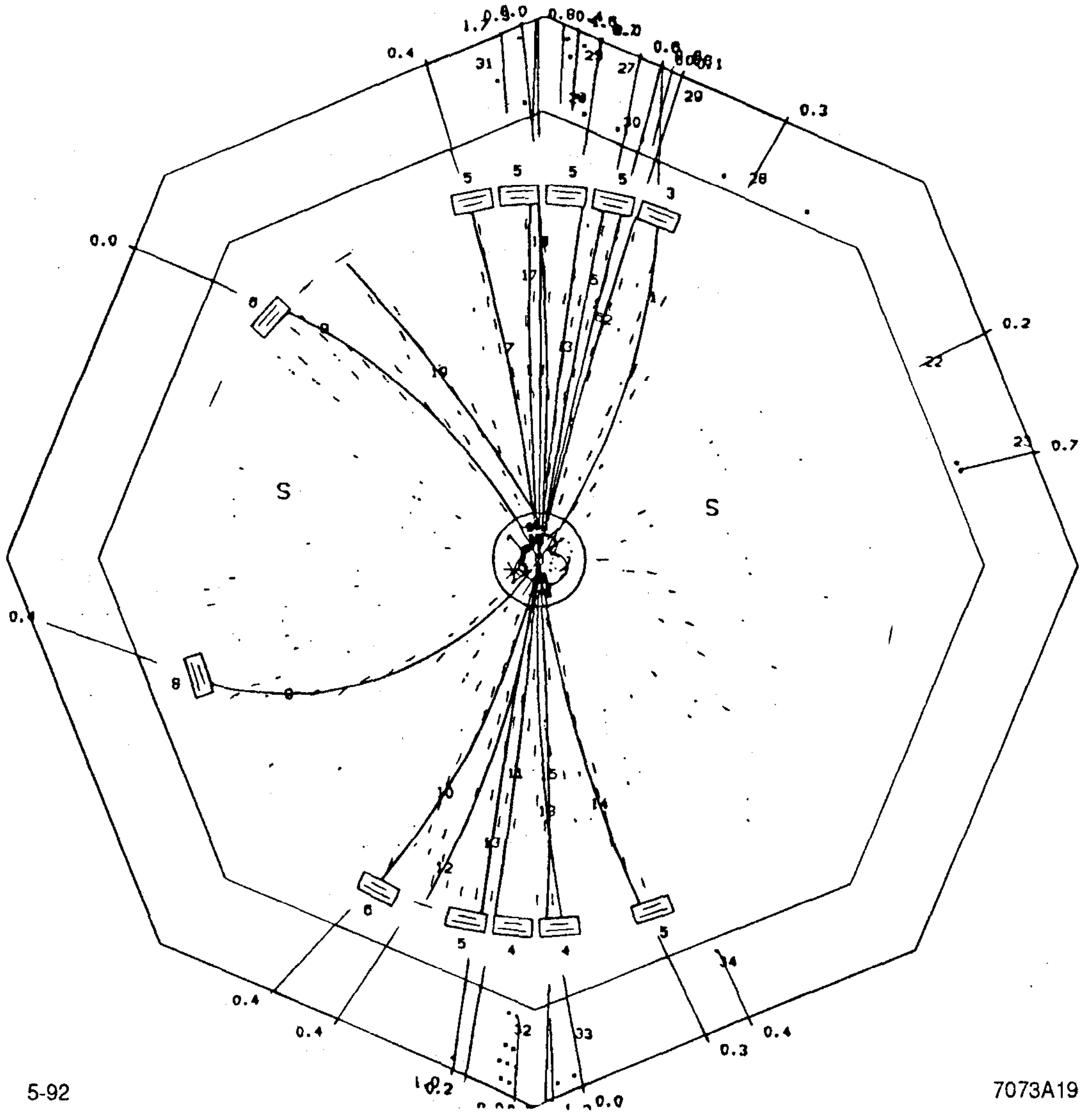

5-92

7073A19

Figure 24 A typical two-jet hadronic event in the Central Drift Chamber displayed in the plane perpendicular to the beam axis.

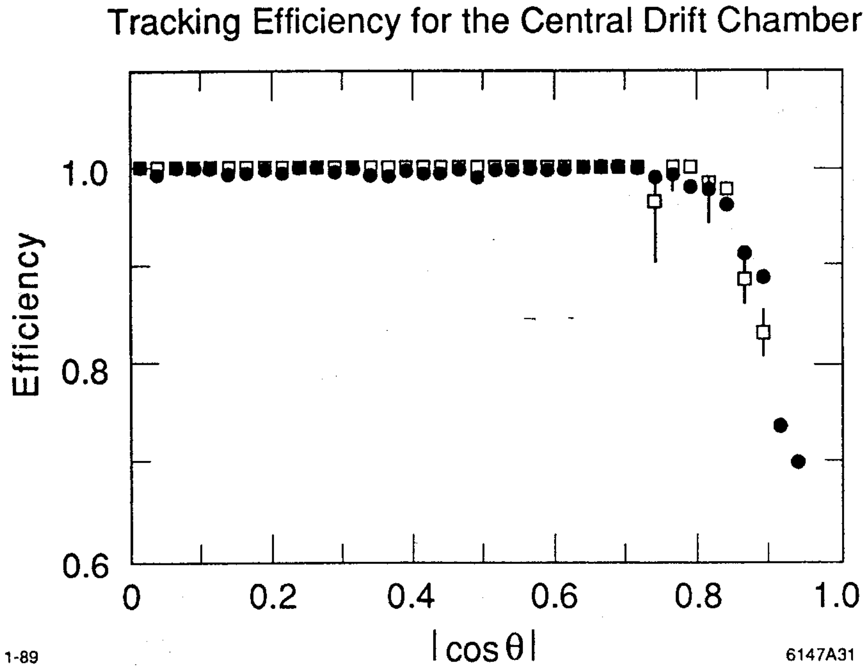

Figure 25 Track finding efficiency as a function of cosθ. The points are from wide angle bhabhas at PEP, and the boxes are from a hadronic Monte Carlo study at SLC energies.

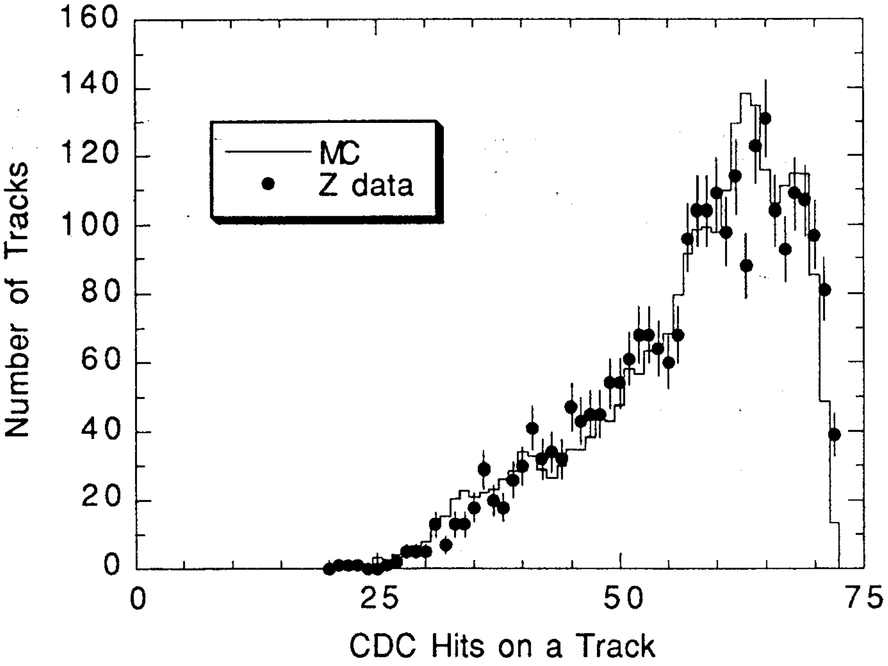

Figure 26 The number of CDC hits on a track. A maximum of 72 measurements are possible.

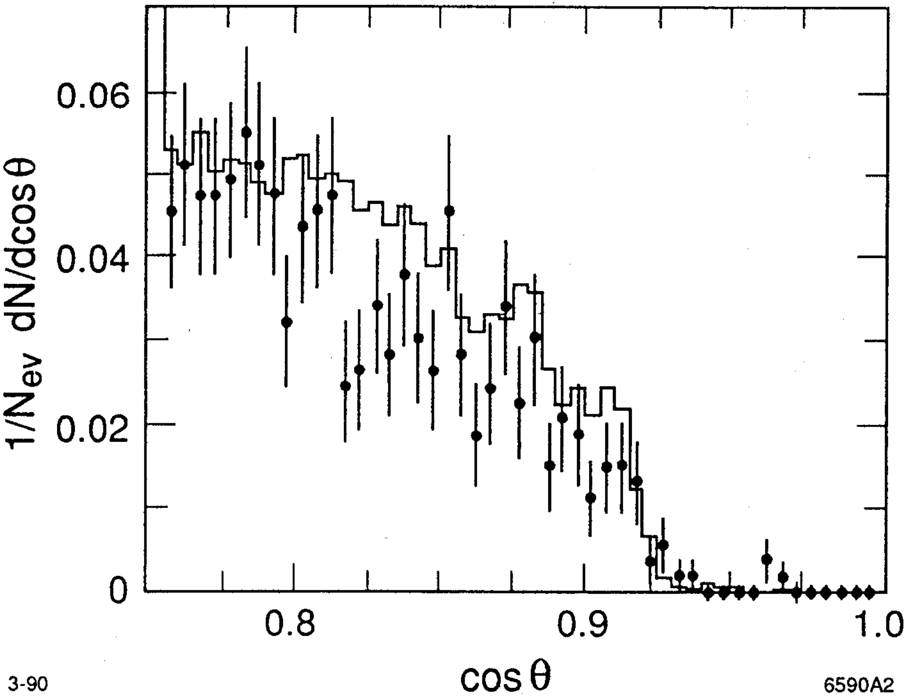

Figure 27 Track multiplicity in the Central Drift Chamber for large cosθ. The data from the 1989 run (points) and the Monte Carlo simulation (histogram) are normalized to the number of events.

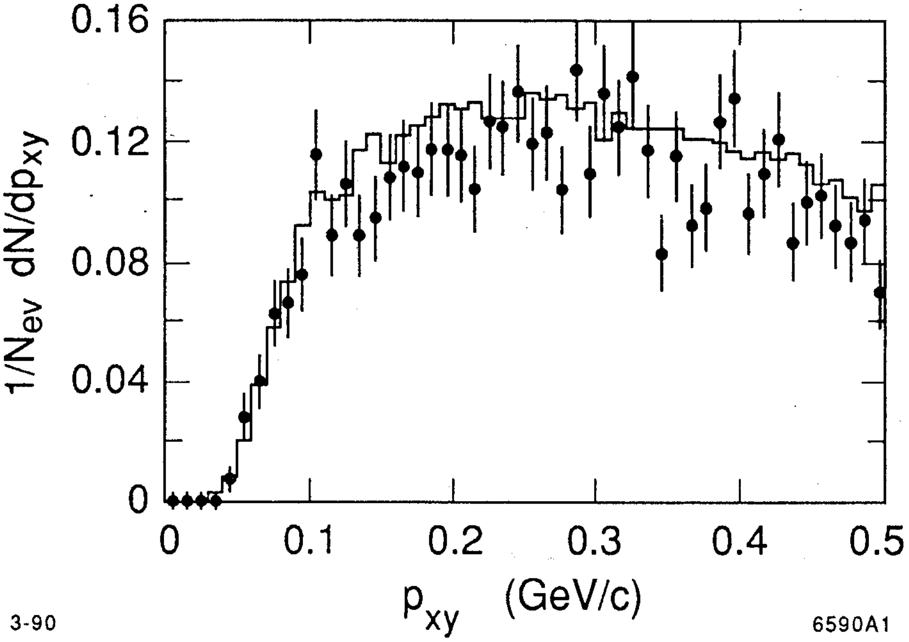

Figure 28 Track multiplicity in the CDC for small transverse momentum. The data from the 1989 run (points) and the Monte Carlo simulation (histogram) are normalized to the number of events.

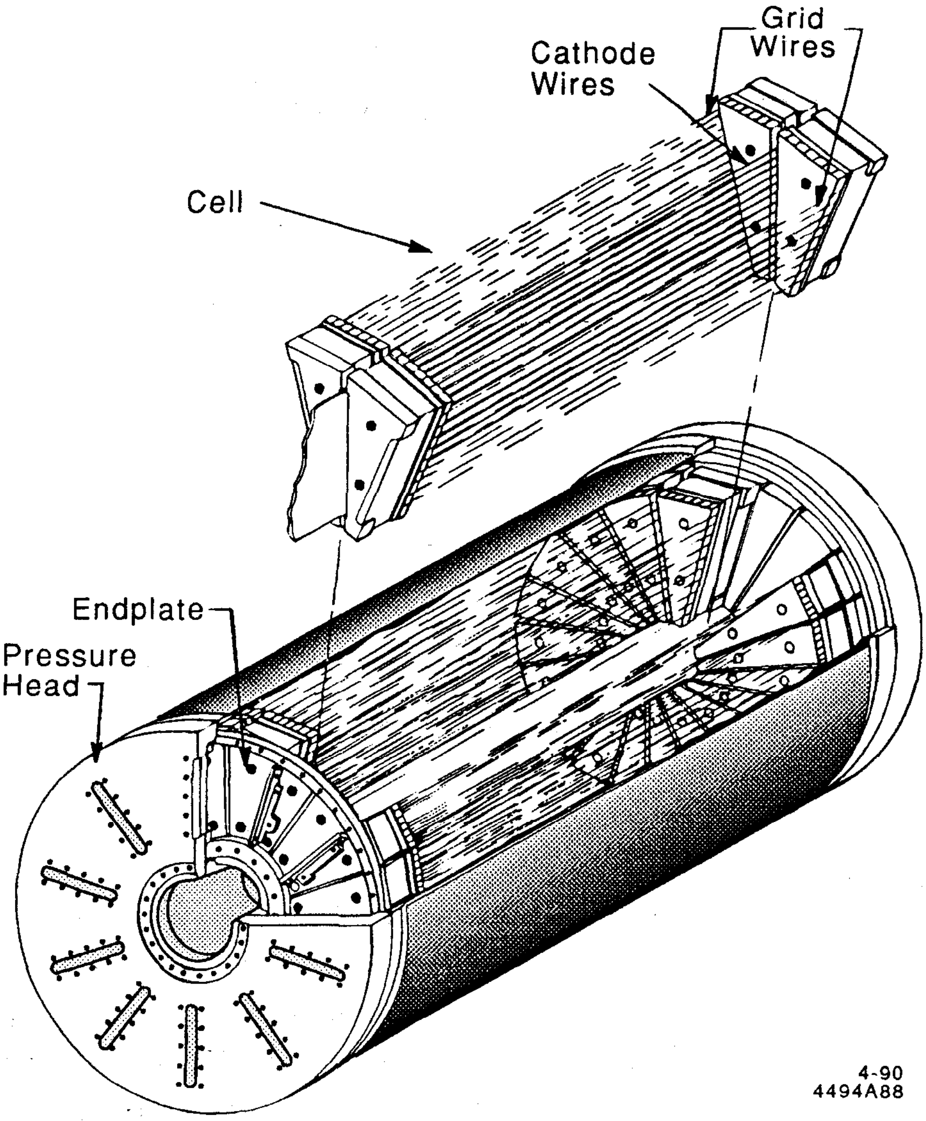

Figure 29 Isometric view of the Drift Chamber Vertex Detector.

2.3 Drift Chamber Vertex Detector (DCVD)

2.3.1 Chamber Description

Directly inside the Central Drift Chamber is the Drift Chamber Vertex Detector (DCVD). [59][61] As shown in Figure 29, the DCVD is partitioned into ten jet cells, each with 38 anode wires aligned in a plane. The anode wires extend from 5 cm to 17 cm in radius and have an active length of 47 cm (Figure 30). The active length was determined prior to the chamber assembly by measuring the anode wire gains as a collimated ^{55}Fe source traveled along the face of the jet cell in $\hat{z}$. Planes of grid wires sandwich the anode plane in order to focus the charge onto the sense wires

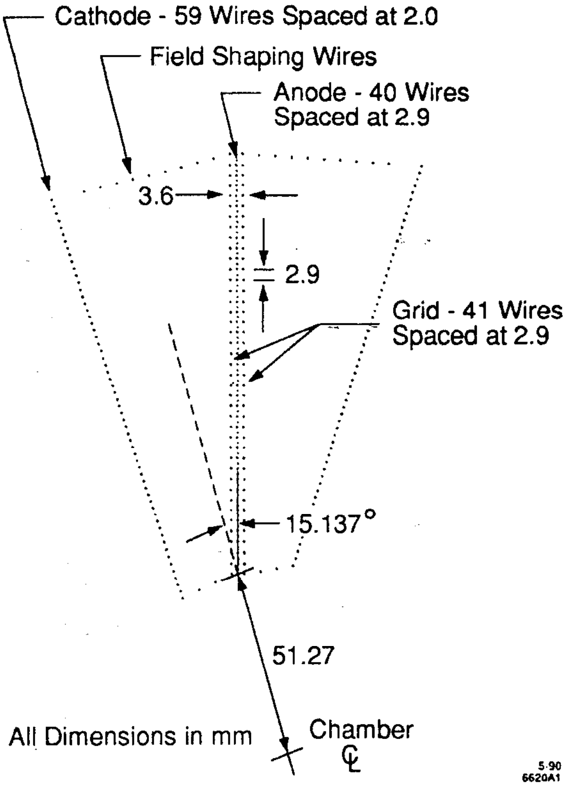

Figure 30 Cell design for the Drift Chamber Vertex Detector.

and to create a uniform drift field throughout the jet cell. Since the wires are all axial, cosθ and z information for the track must come from the main chamber. Unlike the CDC, the wires are not staggered, and so both the true hit positions and their mirror images will reproduce viable tracks. To aid in pattern recognition, the anode planes are tilted by 15°. First, the left-right ambiguity is resolved since the mirror image of a track emanating from the origin will have a large miss distance. Second, tracks cannot pass entirely along the anode or cathode wire planes, which are the regions of worst hit efficiency and spatial resolution. Third, tracks that cross cell boundaries are useful in characterizing the time-distance relation.

The DCVD was designed to achieve spatial resolutions of better than 25 μm. The dense jets of tracks and noisy beam-related backgrounds require that the vertex chamber not only have excellent spatial resolution but also excellent multi-hit resolution. To meet these goals the chamber was precision crafted: wires are located within ~3 μm of the anode plane, and the plane itself is positioned with an accuracy of 20 μm. In addition, a "cool" gas which is a mixture of $C0_2$/ethane (92/8) at two atmospheres pressure was used in the chamber to achieve superior spatial resolutions. Unlike the HRS gas in the Central Drift Chamber, cool gases minimize the electron diffusion of the ionization signal as it migrates to the anode wire, and thereby offer a better spatial resolution. For cosmic ray tracks (see Figure 31), the rms of the track residuals is diffusion dominated and has the characteristic square root dependence on the drift distance, D.

$$\sigma^2(\mu m^2) = (20\mu m)^2 + (38\mu m)^2 D(cm) \qquad (20)$$

The maximum drift distance is 5 cm. The intrinsic term of 20 μm is limited by the primary ionization statistics and the non-isochrony of the track's ionization trail. As is true for the main chamber, the DCVD spatial resolution diverges near the anode due to ion statistics and non-uniformities in the drift velocity (see Figure 32).

At a reduced drift field of $\vec{E}/P$=0.75 kV/cm/atm the drift velocity is 5.7 μm/ns, approximately ten times slower than the CDC drift velocity. The slower velocity makes it easier for the electronics to discern multiple hits on a wire since the hits are separated by a larger interval in time. The track signals are amplified and subsequently digitized by a 6 bit, 100 MHz FADC modified to be active over a 10 μs range.

2.3.2 Environmental Control

The major drawback of using a cool gas is that the drift velocity is highly sensitive to external factors such as temperature, pressure, drift field, and gas composition. Variations in the drift velocity will contribute to the spatial resolution and, if unchecked, can easily overwhelm any benefits achieved in carefully assembling the chamber or choosing a gas that minimizes electron diffusion. To ensure that the drift distance is known to within 5-10 μm over the entire jet cell, these environmental factors have to be monitored to within a few parts in 10^4. [59]

A resistor-divider chain provided voltages to the cathode wires to within ~0.05% of the design voltage. Guard wires, field shaping electrodes, and conducting surfaces attached to the inner and outer pressure cylinders also helped provide a uniform drift field near the inner and outer radius of the chamber. The drift field was uniform to better than 0.1% over two-thirds of the active volume. The oxygen level was kept below 2 ppm to maintain an electron lifetime in excess of 30 μs. Over a drift distance of 5 cm, the loss in pulse height was under 25%. The pressure was controlled to within ±0.7 mbar of its nominal value of two atmospheres absolute.

The temperature of the gas was controlled by modulating the chamber temperature with water circulating through tubes that spiraled around the outer hull of the chamber. The temperature control system had to dissipate 20 watts of

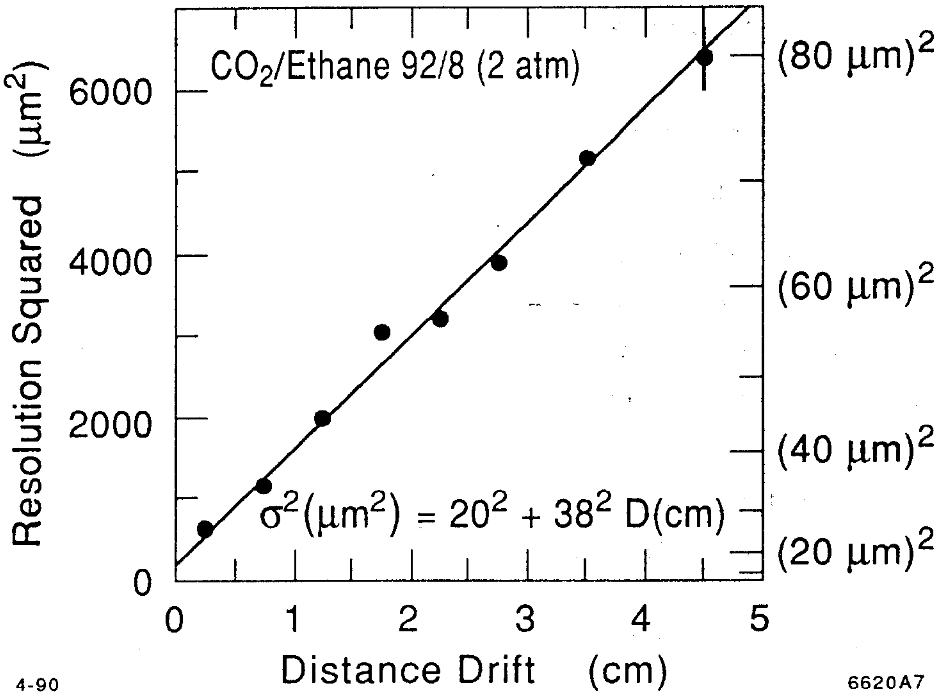

Figure 31 Spatial resolution of the DCVD as a function of drift distance for cosmic ray events.

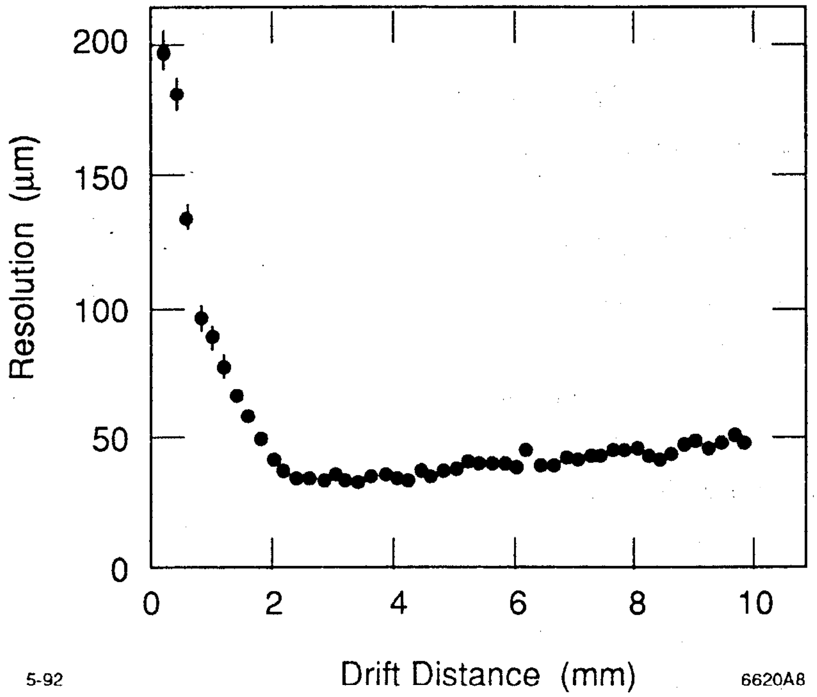

Figure 32 Spatial resolution near the anode wire.

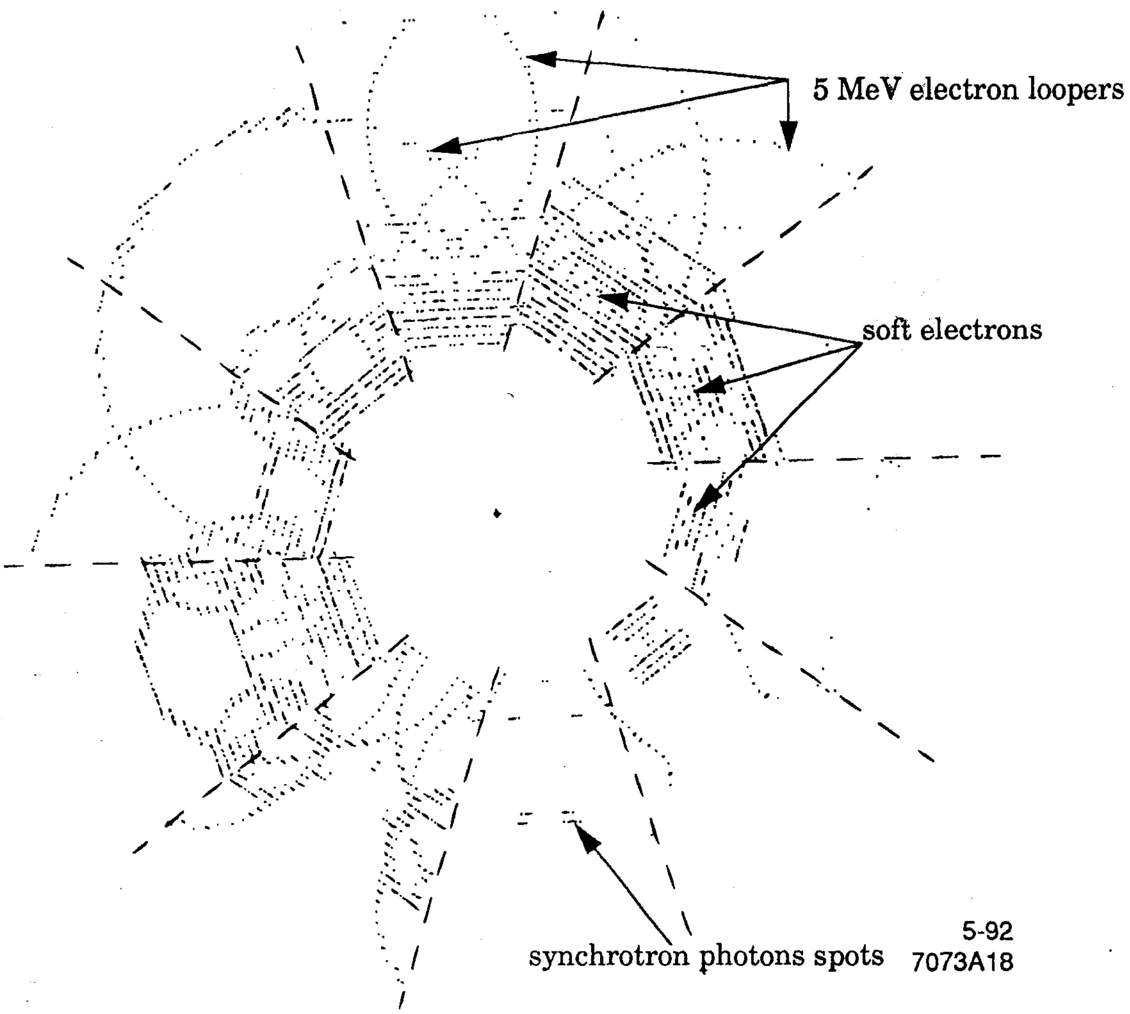

Figure 33 Typical noise hits in the Drift Chamber Vertex Detector due to beam-related backgrounds.

heat generated by the preamps and compensate for the 2-3°C diurnal variations outside the Mark II detector. A feedback system, provided by 48 thermistors located in the gas volume, pressure heads, inner and outer shells, and the electronics cages, stabilized the gas temperature to within ±0.1°C. The largest temperature gradient existed along the z axis due to the preamp cards and was $\Delta T=0.15°C$.

2.3.3 Beam Backgrounds

During data collection, the DCVD was most sensitive to beam-related backgrounds, which were heavily biased towards inner radii. The silicon strips, although much closer to the interaction point, have a much smaller active volume. Hence, significantly less energy got deposited in the SSVD. Figure 33 illustrates the typical background ionization that plagued the vertex drift chamber. The small loops are generated by 5-10 MeV electrons circling in the magnetic field. The fuzzy patches near the inner DCVD wall are thought to be electrons from soft photon conversions that spiral inward as they lose all their energy. Synchrotron radiation also peppers the entire chamber with small spots. The backgrounds prevent track hits from being identified in these regions since the noise patches saturate large portions of the FADC pulse heights.

The SLC was often tuned for hours before beam backgrounds were reduced to acceptable levels. Yet the chamber occupancy averaged about 13% for random beam-crossing triggers taken at the time of the Z^0 events. The chamber occupancy is defined as the percentage of FADC buckets with signals above threshold, and is normalized to the number of FADC buckets that correspond to active regions of the chamber. By contrast, hadronic events in the absence of beam backgrounds are expected to contribute 10% to the chamber occupancy. The distribution of DCVD occupancy for hadronic events is presented in Figure 34. The backgrounds have a strong radial dependence as seen in Figure 35, with the number of hits diminishing in the outer layers. Clean events, on the other hand, would display a flat distribution equal to the hadronic charged track multiplicity of about 20. The total number of hits in the vertex chamber averaged 1975±65 in hadronic events. The MC displays a chamber occupancy and total hit count roughly 90% of the data. This deficiency is present for all wire layers, as seen in Figure 35. Although not fully understood, the discrepancy could be related to limitations in the way that beam background events are overlaid onto clean MC events in the process of fully simulating the Mark II detector environment. (Discussed further in Section 3.4).

The beam-related backgrounds were believed to be caused by the far non-gaussian tails of the 45 GeV electron and positron beams striking material upstream of the interaction region. [63] Collimators along the linear accelerator and arcs of the collider clip off the far tails of the beams, and tungsten and lead masks shield the Mark II detector from showers that develop from particles striking the edge of the collimators or the walls of the beampipe. Nevertheless, EGS simulations indicated that of order one 50 GeV particle hitting the mask inside the detector, 50 particles hitting the beampipe inside the final focus triplet magnets, or 1000 particles hitting the inner edge of the mask at the entrance of the triplet magnets could reproduce the background noise seen in the DCVD. Since 5-10% of the random beam-triggered events exhibited no DCVD backgrounds except for small synchrotron spots, Poisson statistics suggests that the number of primary particles that initiate the showers is small. The shape of the lead mask at the entrance of the

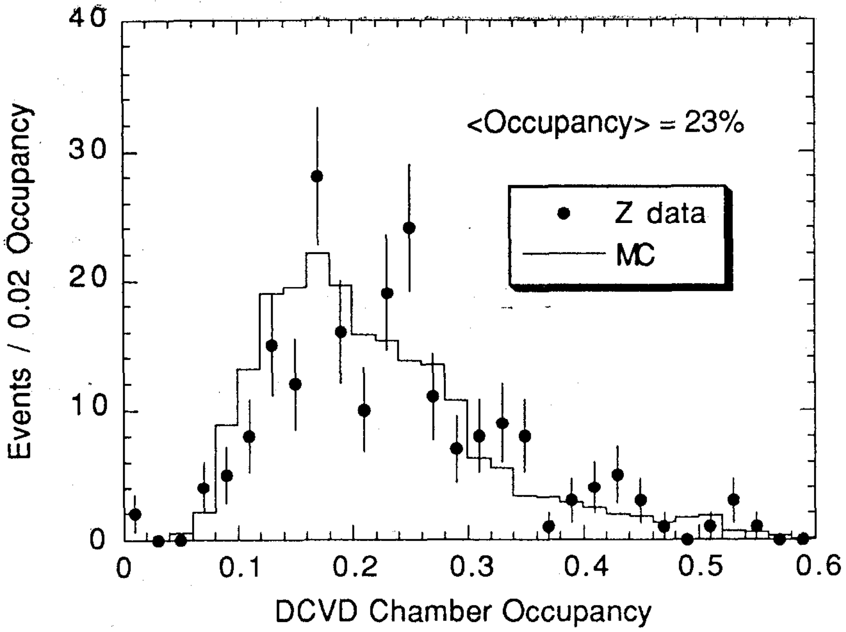

Figure 34 Chamber occupancy in the DCVD for hadronic Z^0 events. Roughly 10% of the pulses are generated by charged tracks in Z^0 decays and 13% from beam backgrounds.

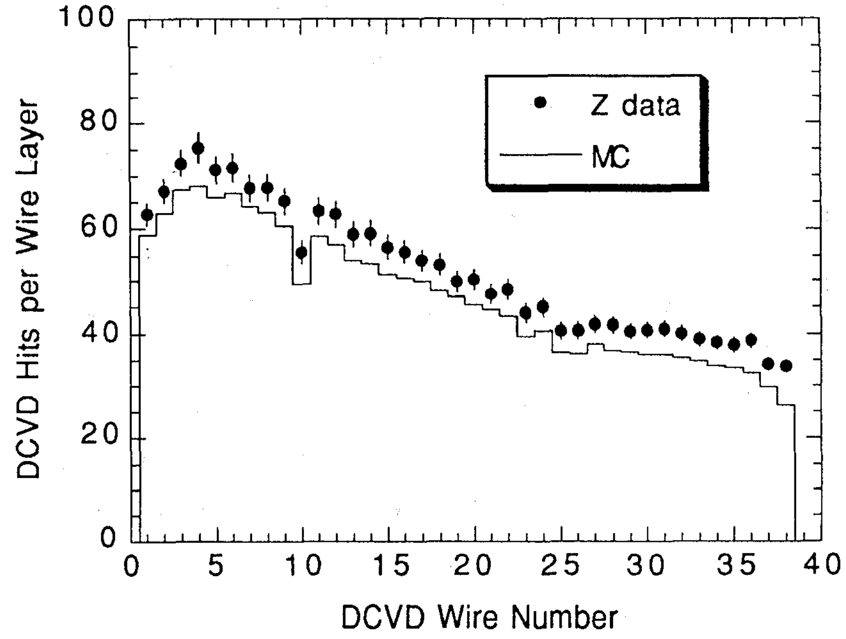

Figure 35 Number of hits in the DCVD versus wire number for hadronic events. Beam backgrounds are most severe at smaller radii. The data has ~10% more DCVD hits than the MC.

final focus magnets was discovered to be flawed, since it did not properly shield the downstream elements from off-momentum tails of the beam. After redesigning and installing a new mask, the beam-backgrounds diminished significantly in the DCVD.

Under normal operating conditions, each jet cell drew 10-50 nA, depending on the severity of the beam backgrounds. However, the beam backgrounds were sometimes so severe that one or more DCVD cells would spontaneously begin to draw a steady-state current in excess of 1 μA. Usually, the large current draws were confined to a couple of anode wires in the cell, which would collect huge ionization pulses. Treatment demanded that the high voltage for these troubled cells be lowered to 1000 V for several hours, during which the track hit efficiency was zero in the cell. On average 4% of the chamber cells were inoperative, although a given event could lose half its DCVD track information if a jet happened to pass through one of these inoperative cells.

After the Mark II completed its 1990 data collection, the DCVD was radiated by an X-ray tube source to simulate the conditions of the beam backgrounds and recreate the large current draws. We speculated that electric charge build-up on the Macor face induced the steady-state currents. The Macor blocks are the ceramic endplates that position the grid, guard, and cathode wires to high accuracy. Adding 0.5% water to the chamber gas seemed to alleviate the electrostatic breakdowns, but this solution was never used while the Mark II was collecting data.

In addition to the high voltage problems, the DCVD pressure or temperature strayed out of tolerance for roughly 5% of the events. No DCVD hit information was used in these events. On other occasions, data acquisitions problems such as memory overflows caused loss of pulse height information for one or more cells, which affected ~1% of the cells on average.

In total, an average of 10% of the cells were inoperative. These conditions were modeled in the Monte Carlo events by turning off hits associated with bad DCVD cells. In addition, seven of the 380 chamber wires were dead throughout the entire data collection.

2.3.4 Hit Efficiency and Two Track Separation

Studies from cosmic tracks show that the hit efficiency is about 95%. The hit efficiency is defined as the probability that a DCVD layer will detect a hit for tracks found in the central drift chamber. The inefficiency arises from setting the pulse finding threshold high enough to eliminate spurious pulses. Just like the main drift chamber, the DCVD has poorer efficiencies in hadronic events, especially for the inner layers where the hit efficiency drops to 70% (see Figure 36). In this figure, we are not counting the losses from bad cells or known dead wires which would amount to an additional 10% hit loss, hence the wire efficiencies reported in Figure 36 are limited only by the multi-hit resolution in the presence of beam backgrounds and track densities in jets. The efficiency improves for the outer layers but is still below the performance for cosmic tracks.

Track hits are generated in unmixed MC events, i.e. background-free events, with a 95% efficiency independently of wire number. Hit inefficiencies due to beam backgrounds and close track pairs in hadronic jets are modeled to reflect the data (see Section 3.4). The MC hit efficiency in fully simulated hadronic events displays a similar dependence on wire number, and agrees with the data when averaged over the entire working chamber. Excluding bad cells and known dead wires, the hit efficiency was 80.5% for the data and 80.2% for the MC.

In addition, a portion of the track measurements are spurious hits from background noise. The probability for selecting the correct hit generated by the track as a function of wire number, as predicted by the MC, is shown in Figure 37. As expected, the performance is poorest for the inner wires, where the generated hits get properly associated with the track only 55% of the time. The rest of the time the hits are either spurious or not found at all. The probability for finding the correct hit improves to 75% for the outer layers, and is 69.4% averaged over the entire chamber. These accidentals are extremely problematic since they can cause the measured impact parameter to stray from its actual value. However, as long as a majority of the DCVD track measurements are the correct hits, the track will link up properly to the silicon strip detector. Moreover, tracks that fail to gather any of the correct DCVD hits will usually fail to pick up any silicon information. The track cuts listed in Section 4.2 will eliminate these badly mismeasured tracks.

In an environment of dense jets, it is crucial to be able to resolve two closely spaced tracks. The FADC pulse height profile allows us to discriminate between tracks that are as close as 250 μm from each other, corresponding to a peak-to-peak pulse separation of as few as five FADC bins. Smaller separation distances cannot be resolved since the two pulses will merge into a single hit. The pulse-finding algorithm searches for a differential pulse height signal to exceed threshold. This method discriminates double-hits better than requiring the pulse height to cross an absolute threshold since the tail of the first hit does not have to fall to zero in order

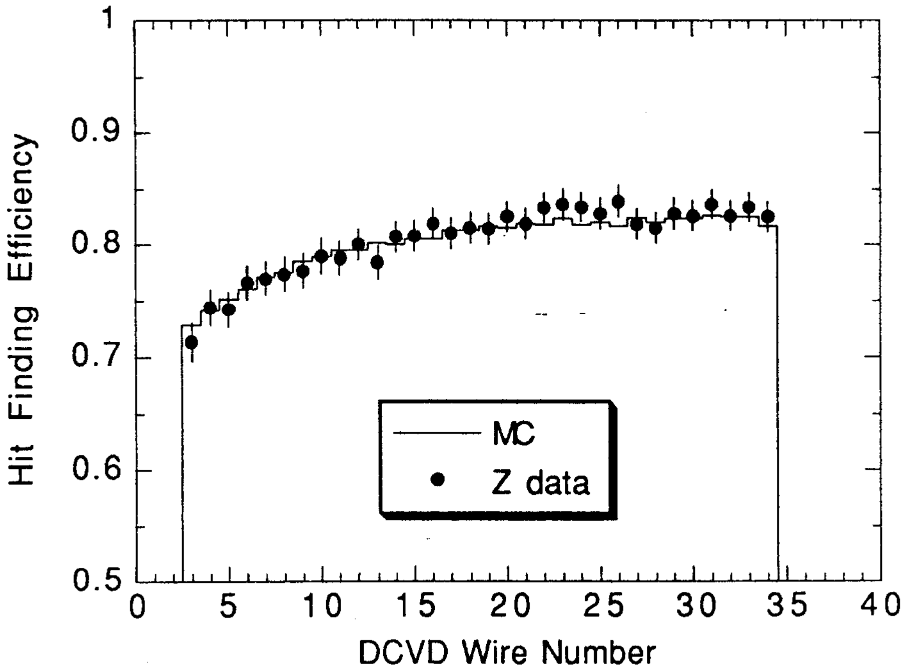

Figure 36 Hit finding efficiency versus wire number for hadronic tracks in the Drift Chamber Vertex Detector. Inefficiencies due to dead cells or wires are not included.

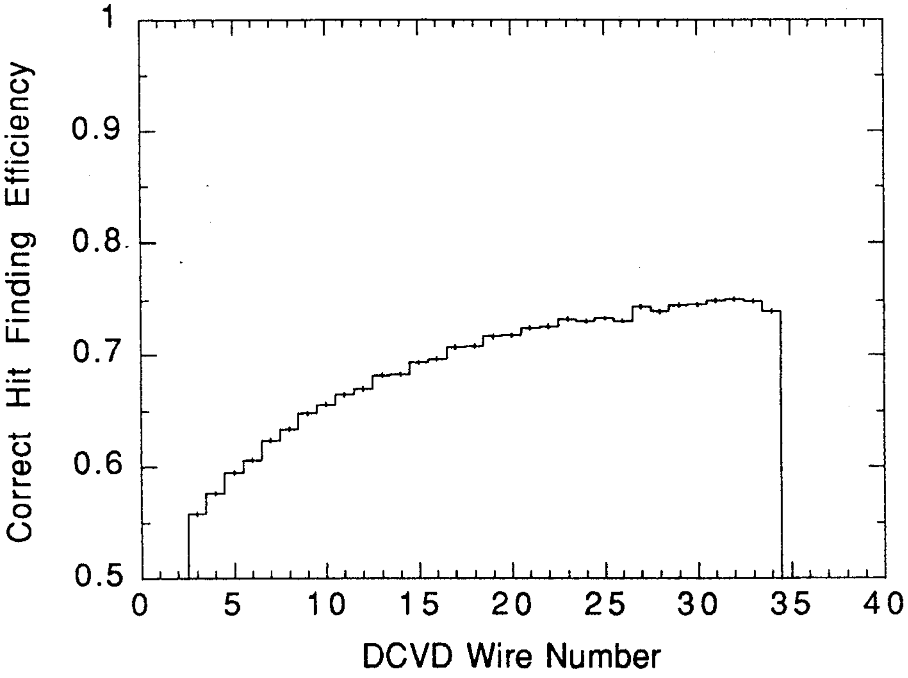

Figure 37 Efficiency for finding the correct DCVD hit, i.e. the one generated by the track, as a function of wire number. The difference in efficiencies from those in Figure 36 signifies the frequency of spurious hits associated with the track.

for the second pulse to be detected. The differential threshold is decreased linearly by 40% over the 5 cm drift distance to accommodate diffusion and pulse height attenuation.[61]

The double track resolution was studied by separating the pulse height profiles from pairs of independent cosmic hits by increasing distances, summing the two pulse profiles linearly, and processing them by the hit finding algorithm. The efficiency for resolving the second hit turned on when the separation distance exceeded 400 µm (Figure 38). This test is somewhat more ideal than can be expected in hadronic events since heavy beam backgrounds will tend to require a larger separation distance between track pairs before they can be fully resolved. Also, a large fraction of the background pulse hits saturate the FADC over dozens of bins. Synchrotron spots and 5 MeV electron loopers deposit large amounts of ionization because of their low momentum.

Spurious hits can be triggered by late-arriving ionization clusters from the original signal. The "fake" hit rate can be limited by raising the threshold, but must be tempered to maintain a high hit efficiency and double track resolution. The fake hit rate falls rapidly with the double-hit separation distance and drops below 15% beyond a distance of 0.5 mm (Figure 39).

2.3.5 Spatial Resolution

Just as the hit efficiency and two-track separation deteriorate for hadronic events as compared to cosmic ray events, so does the spatial resolution deteriorate for hits in the DCVD. The resolution worsens for inner wire layers and can be characterized by the expression

$$\sigma^2 = \sigma_0^2 + \sigma_1^2 D + \sigma_2^2 (19 - W) \tag{21}$$

where D is the drift distance in cm and W is the wire layer number. σ_0, σ_1, and σ_2 are the intrinsic-, diffusion-, and wire-dependent contributions to the resolution, respectively. The expression is identical to Eqn. (20) except for the added dependence on the wire number. The parameters σ_0, σ_1, and σ_2 differ for tracks that come from hadronic events, MC simulated hadronic events with and without beam background mixing, and cosmic ray events. The values, listed in Table 8, are derived from gaussian fits to the track residuals for tracks that have at least 15 measurements in the DCVD.

The behavior of the spatial resolution is best illustrated in Figure 40. The hit resolution for cosmic tracks as a function of drift distance is plotted as the thick

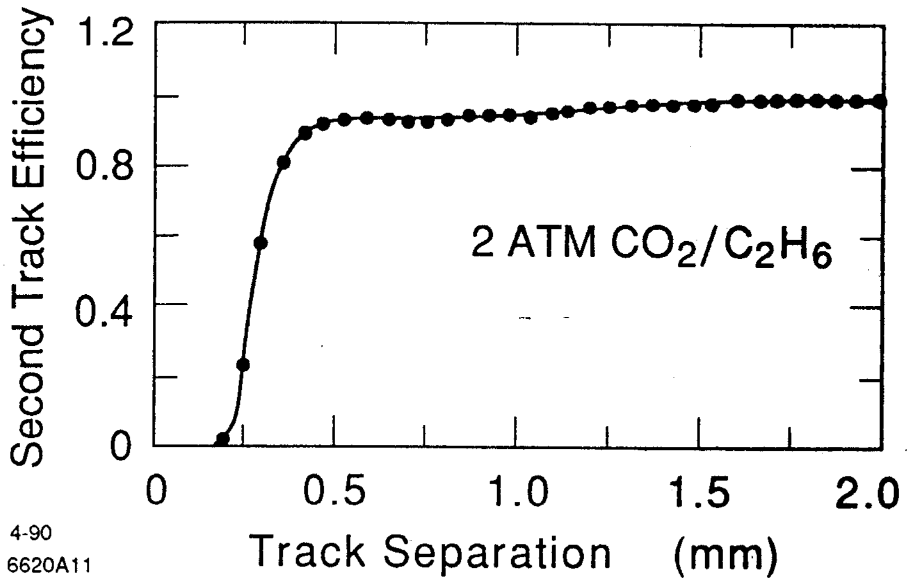

Figure 38 Efficiency to detect a second track as a function of the track separation.

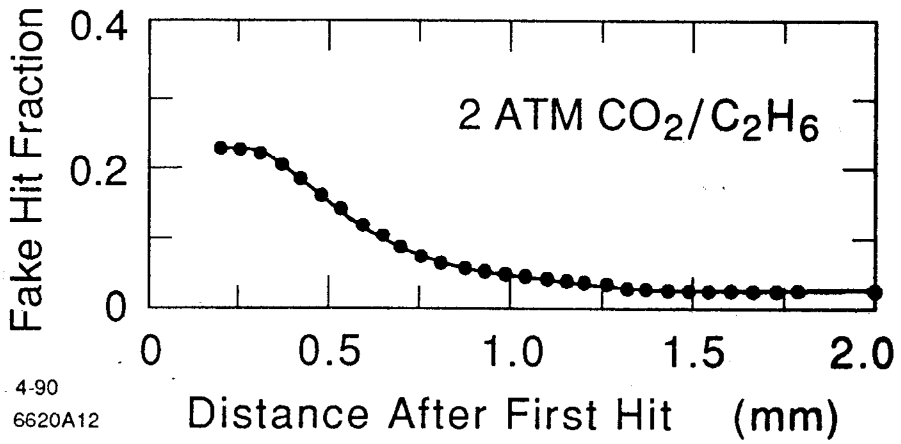

Figure 39 Fraction of "fake" hits as a function of the distance after the first hit.

contour. The spatial resolution for hadronic tracks is plotted as thin contours for a subset of the DCVD layers. Layer 34 has a resolution that is nearly identical to that of cosmics; however, the inner layers are 15-20 μm worse.

The Monte Carlo generated hits in the DCVD are smeared by a drift distance-dependent resolution function that optimizes the agreement between the hadronic data and the MC events mixed with beam backgrounds. No wire-dependent term is used to degrade the generated hits, hence the σ_2 term in the mixed MC arises solely from the radial dependence of beam background hits and the density of hits in jets.

Table 8 Parameters in Eqn. (21) which describe the spatial resolution for track hits in the Drift Chamber Vertex Detector. σ_0, σ_1, and σ_2 correspond to the intrinsic-, diffusion-, and wire-dependent coefficients, respectively.

Event type	σ_0 (μm)	σ_1 (μm)	σ_2 (μm)
Hadronic Z^0's	28.5	43.0	7.6
Mixed MC	27.9	42.9	6.8
Unmixed MC	22.9	41.2	3.0
Cosmics	20.4	37.6	0

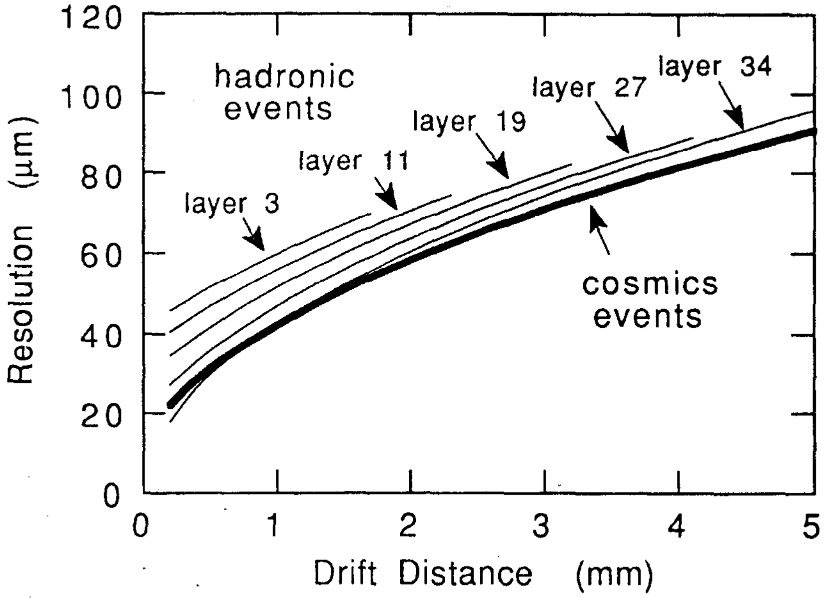

Figure 40 The DCVD spatial resolution for hadronic and cosmic tracks as a function of drift distance. The resolution for hadronic tracks degrades for the inner layers of the vertex chamber.

The resolution function used to smear the generated hits differs slightly from the cosmic performance due to an artifact in the way that drift velocities are modeled in the MC near the anode wire.

The unmixed Monte Carlo events have a wire-dependent term σ_2 that is intermediate to the value for hadronic and cosmic tracks. The value suggests that the bulk of the layer dependency is due to the degradation from beam backgrounds and not from dense jets. Both hadronic and cosmic tracks have nearly identical diffusion terms. Note that although the resolution for wire 34 at a drift distance of zero is undefined, there is no problem since Eqn. (21) applies only for drift distances greater than 2 mm from the anode wire. Inside of 2 mm, the spatial resolution degrades rapidly due to ion statistics (Figure 32 on page 52), and the MC generated hits are smeared accordingly.

2.3.6 Track Finding

Two different strategies were used to find charged tracks in the DCVD. In the first method, the pattern recognition consisted of software "curvature modules" that looked for an accumulation of hits along predefined paths with a given azimuthal angle φ_0, impact parameter δ, and curvature κ. Track segments in the DCVD are found independent of any track information from the central drift chamber. This technique is analogous to the hardware curvature modules used in the Mark II event trigger, which were programmed to find charged tracks in the Central Drift Chamber by identifying patterns of CDC cells hit along predefined curved roads through the twelve superlayers. [64]

The abundance of layers in the vertex drift chamber allows most tracks to be clearly visible in a one-event display of the DCVD raw hits, as shown in Figure 41 on page 66. Each hit appear on both the left and right side of the anode plane since the directional ambiguity of the drifting charge cannot be resolved prior to track finding. Very little confusion exists between the track and its mirror image reflected across the anode plane, since the mirror image almost always misses the origin by a substantial distance.

For tracks with a small impact parameter ($\delta \ll R$) and small curvature ($\kappa \ll 1/R$), the path in the xy plane can be parametrized as

$$\varphi(R) = \varphi_0 + \frac{\delta}{R} + \frac{\kappa R}{2} \tag{22}$$

where R is the radial coordinate of the hit (5 to 17 cm in the DCVD). The predefined paths searched by the software curvature modules are optimized to the double-hit resolution of the DCVD, which turns on for a separation of 250 μm and becomes fully efficient beyond 400 μm. The azimuthal angle is divided into 4000 discrete values of φ_0, so that the distance between two successive φ_0's in the outer layer of the chamber is ~250 μm. This allows the maximum resolving power for close track pairs. For each φ_0, we construct 45 paths over a range of curvatures and impact parameters. The curvature is selected to be 0, ±0.2, or ±0.4 m^{-1}, which corresponds to a momentum of ∞, 0.71, or 0.32 GeV, respectively. The curvature values are chosen so that the sagitta of the track segment inside the DCVD changes by ~250 μm for each successive κ. The impact parameter of the curvature modules range from –4 mm to +4 mm in increments of 0.5 mm for $\kappa = 0$, and from –3 mm to +3 mm in increments of 1.0 mm for $\kappa = \pm 0.2$ and $\pm 0.4\ \mathrm{m}^{-1}$. Altogether, there are 45 x 4000 software curvature modules.

Hits are associated with a specific curvature module if they are within 150–200 μm of the path. The allowed separation between the hit and the curvature module path increases with layer to accommodate the graininess between adjacent paths. The algorithm is optimized to hunt for tracks with $P_{xy} \geq 0.25$ GeV and impact parameter $|\delta| \leq 4$ mm. More modules could have been devised to search for tracks outside these ranges, but the present set of modules are sensitive to the vast majority of tracks from hadronic events. Also, the computational speed of tracking decreases with the number of curvature modules. Tracks with both high momentum and small impact parameter are reconstructed first, while low momentum tracks and large impact parameter tracks are assembled with any remaining DCVD hits. The track segment is further refined by adding and dropping hits in an attempt to minimize the residuals from a fit of the segment to a circular arc in the xy plane. Track segments are required to have a minimum of ten DCVD hits.

The DCVD track segments are next linked to known CDC tracks by minimizing the χ^2 formed from the differences in φ_0, δ, and κ of the two segments and the full 3x3 covariant error matrix for these parameters. The χ^2 also allows a kink $\Delta\varphi_{kink}$ between the two track segments, weighted by the calculated angular resolution $\sigma_{\varphi,ms}$ for multiple scattering between the two chambers. The full χ^2 is

$$\chi^2 = \begin{bmatrix} \Delta\varphi_0 \\ \Delta\delta \\ \Delta\kappa \end{bmatrix}^T \begin{bmatrix} \text{3x3} \\ \text{error} \\ \text{matrix} \end{bmatrix}^{-1} \begin{bmatrix} \Delta\varphi_0 \\ \Delta\delta \\ \Delta\kappa \end{bmatrix} + \left(\frac{\Delta\varphi_{kink}}{\sigma_{\varphi,ms}}\right)^2 \qquad (23)$$

If more than one CDC track matches the same vertex segment or if a close pair of DCVD segments is aligned with a pair of CDC tracks, then arbitration is conducted to minimize the total χ^2 of the linkage. Approximately one-third of the DCVD track segments are not linked to CDC tracks. These unused segments are predominantly spurious tracks formed from the glut of background hits in the vertex chamber and usually have only 10-20 associated hits. Some are real tracks that don't extend into the main chamber due to the greater $\cos\theta$ coverage of the DCVD.

The second track finding algorithm is complementary to the curvature module approach.† CDC tracks are extrapolated layer-by-layer into the DCVD, and nearby hits are accreted onto the track. After a hit is added, the track parameters are reevaluated, and the search proceeds to the next wire layer. Unlike the curvature module method, the extrapolation method can find tracks with $P_{xy} \leq 0.25$ GeV or $|\delta| \geq 4$ mm. However, this algorithm has a lower track finding efficiency in the presence of high backgrounds and dense jets. The extrapolated path often diverges from the true track direction by picking up accidental hits, which are then used to update the track parameters. The algorithm is also not very successful at traversing across a dense patch of background hits in the DCVD, since it looks for the next track hit in a very localized region.

Because the curvature modules perform a global search for the entire track segment, large regions of noise can be effectively bypass. Also, the CDC and DCVD segments for close track pairs can be correctly linked more frequently, since the azimuthal angle, impact parameter, and curvature information for the DCVD track segments are all used to arbitrate between the possible linkage choices. On the other hand, the extrapolated CDC track will tend to lock onto the DCVD segment which is closest to the extrapolation at the outer layers, irrespective of the other parameters of the DCVD segment since it cannot know their values a priori.

Because of the limitations of the extrapolation method, hadronic events are first tracked using the curvature module technique, which finds approximately 90% of the tracks. Next, the extrapolation method finds hits for the remaining CDC tracks, predominately those with low momentum or large impact parameters. Also, because the extrapolation method is computationally much faster, it is used to track cosmic ray events.

The five track parameters: φ_0, $1/P_{xy}$, δ, z_0, and $\cos\theta$, are then extracted from a combined fit to the CDC and DCVD track hits using a program called SARCS6. [85] Hits near the perimeter of the jet cell are eliminated from the fit since the drift fields are less uniform and modeled poorly in this region. Only track hits from wire layers 3 through 34 are used. In addition, hits within 2 mm of the anode plane or 3 mm of the cathode plane are used in the pattern recognition but are deweighted in the fit. Thus track finding efficiency is enhanced without jeopardizing the track parameter resolutions with these poorly measured hits.

---

† Algorithm tailored to the DCVD by Bill Ford.

2.3.7 CDC/DCVD Tracking Performance

A typical two-jet hadronic event in the Drift Chamber Vertex Detector is shown in Figure 41, including noise hits from beam backgrounds. Both the hits and their mirror image across the anode plane are plotted, since the DCVD cannot resolve the left/right ambiguity in the direction of the drifting charge until after tracking. Hence, half the apparent tracks are just the mirror image of the true tracks and miss the origin by a substantial distance. The same event is presented in Figure 42 with only the hits associated with the tracks displayed.

The DCVD hit distribution for tracks well measured in the central drift chamber and passing through an active DCVD cell is presented in Figure 43. (Recall that roughly 10% of the tracks enter malfunctioning cells). In addition, the track must have at least 20 CDC measurements, $P_{xy} \geq 0.15$ GeV, $|\cos\theta| \leq 0.80$, $|\delta| \leq 5\text{mm}$, and $|z| \leq 30\text{mm}$. Only wires 3 through 34 are used in the vertex chamber track fit, so the maximum number of DCVD measurements is 32. The DCVD track hit distribution is peaked near the maximum allowed, with 91±1% of the tracks picking up 15 or more hits in the vertex chamber. For the 9% of CDC tracks that do not link with a DCVD track segment, Monte Carlo studies suggest that half the failures are due to photon conversions, K_s^0 and Λ decays, or kinks in tracks from $\pi^{\pm}$ decays, all which have occurred outside the DCVD. The remaining tracks were most likely not found because of the finite double-track resolution, where typically the nearest track was under 10 mrad away.

Monte Carlo studies indicate that in addition to the track finding inefficiency of 9%, and additional 8% of the tracks get linked to the wrong DCVD segment. In other words, the hits that the track finds are not the ones generated by the track in the MC. The mechanism is not well understood, although sometimes the arbitration performed on close track pairs crisscross the assignment, which results in two incorrect matchups. The true DCVD segment can also have accidental noise hits that have not yet been removed by the SARCS6 fitter in the final polishing, and fails to link up correctly due to the poor χ^2 match in Eqn. (23) between the CDC and DCVD track parameters. In about a quarter of the mismatches, the correct DCVD segment was either attached to another track or was found by the software curvature modules but not used.

These mismatched tracks are particularly troublesome. They reduce the efficiency of linking the CDC/DCVD track with the silicon strip detector and increase the probability that incorrect silicon hits will be selected. Moreover, the

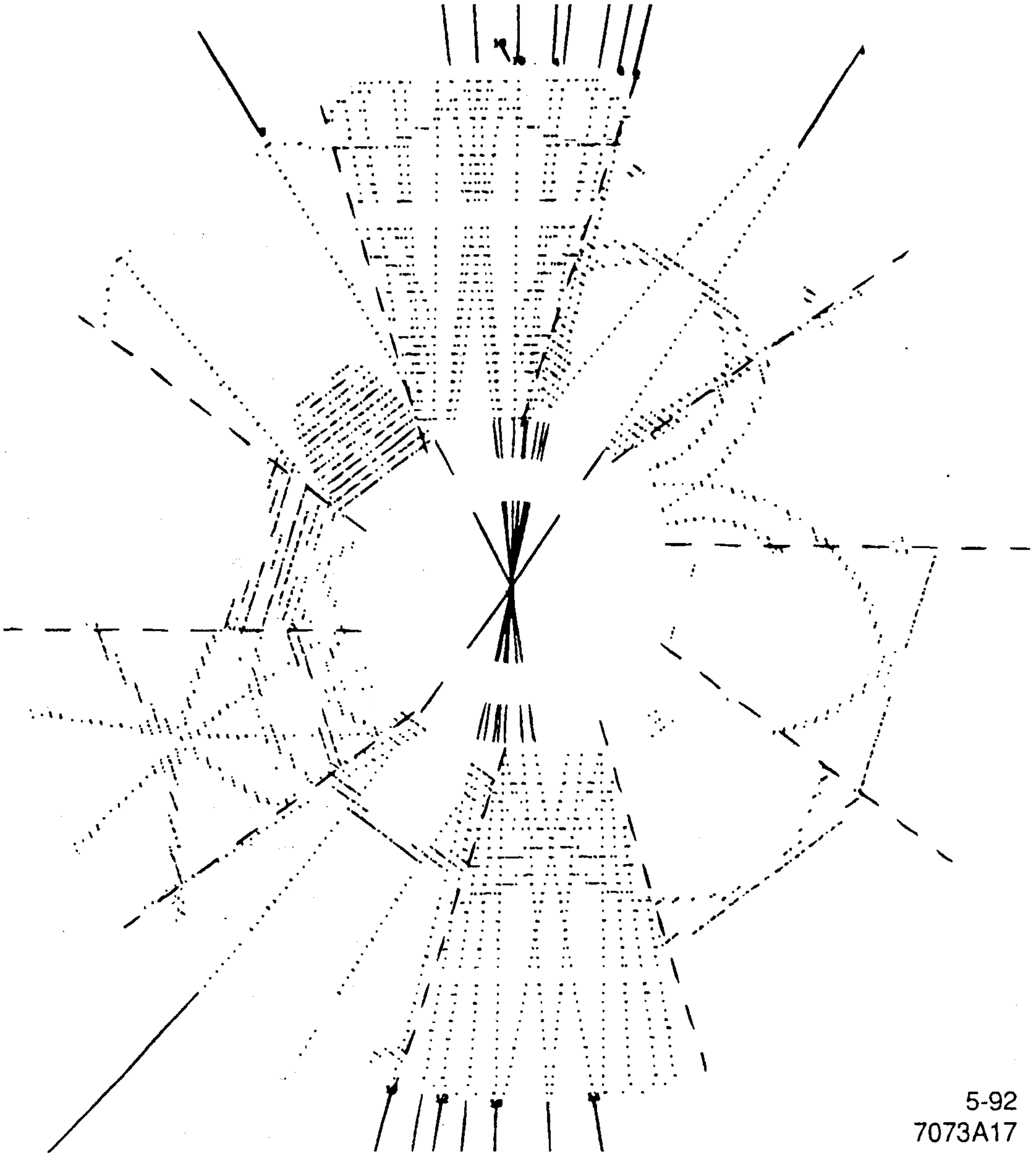

Figure 41 Typical two-jet hadronic event in the Drift Chamber Vertex Detector. All hits in the chamber are displayed, including the beam background noise and the mirror image of the track hits reflected across the anode planes.

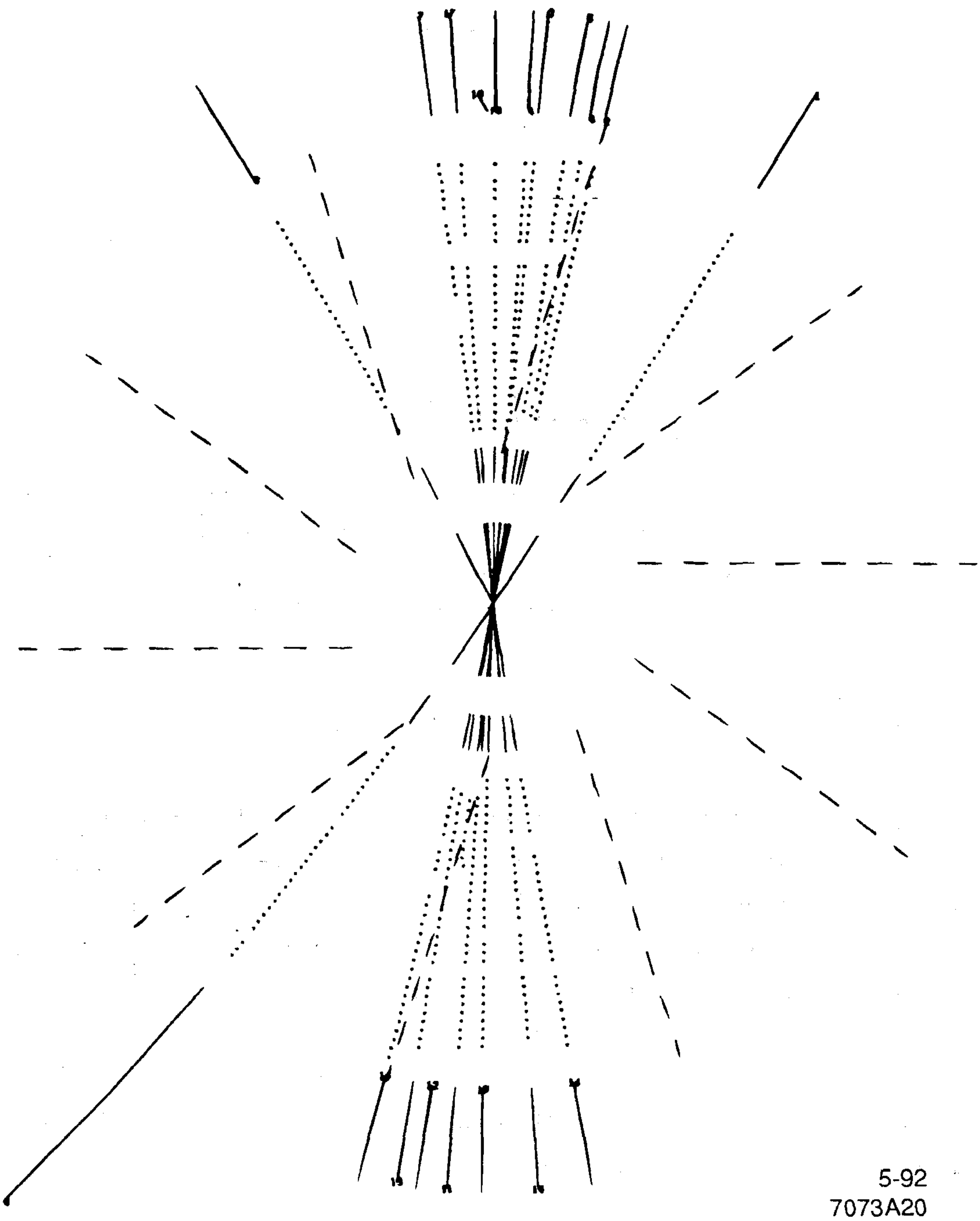

Figure 42 The same two-jet event. Only hits associated with the found tracks are displayed.

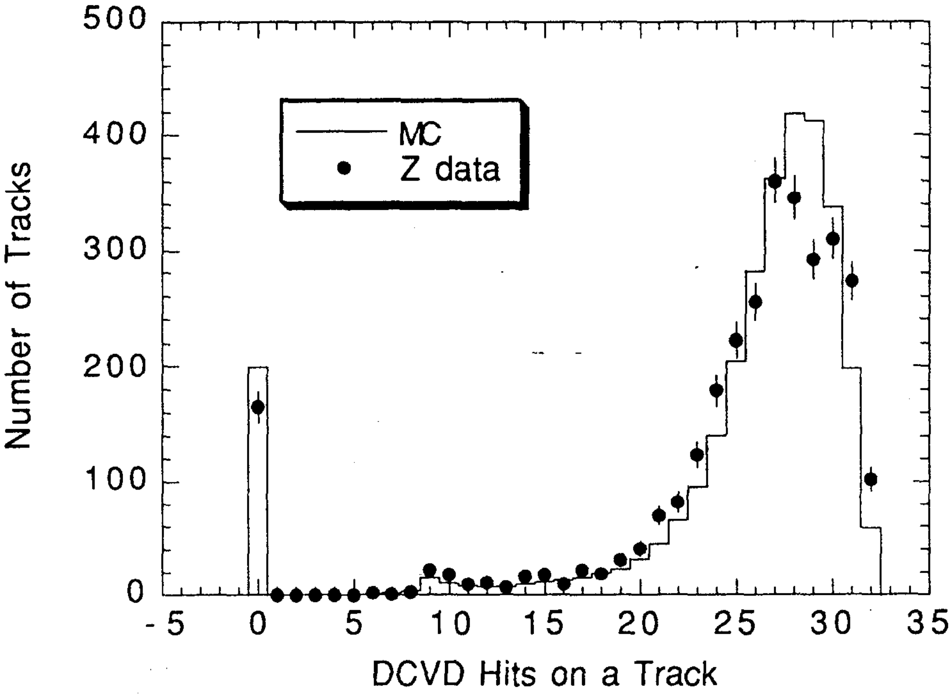

Figure 43 The number of DCVD hits on a track. Tracks are required to pass through a live DCVD cell, and must have at least 20 CDC hits, $P_{xy} \geq 0.15$ GeV, $|\cos\theta| \leq 0.8$, and $|\delta| \leq 5$ mm. 91% of the tracks pick up at least 15 DCVD hits.

reconstructed impact parameter will often differ significantly from its true value, effectively introducing non-gaussian tails into the resolution function. Using an impact parameter tag, the fraction of B hadrons in the enriched sample will decline since tracking errors in *udsc* events will fake a bottom signal. Fortunately, we can eliminate many of the tracks with DCVD tracking errors by requiring tracks to pick up at least one silicon measurement (discussed further in Section 2.4). Only 5.5% of these tracks have the wrong DCVD track segment, down from 8%. Moreover, nearly half of these tracks manage to find at least one correct SSVD cluster generated by the track, which will dominate the impact parameter measurement and steer the track back on course. Hence, only 3% of the tracks with at least 15 DCVD hits and at least 1 SSVD hit fail to pick up even one correct measurement in either vertex detector.

We have ignored the effects of cosθ on the spatial resolution. Tracks with small polar angles deposit more ionization in each wire layer, hence the resolution improves by a factor of $1.057\sqrt{\sin\theta}$ due to ion statistics, which varies by 20% over the fiducial range of $|\cos\theta| \leq 0.8$. The normalization factor 1.057 keeps the average

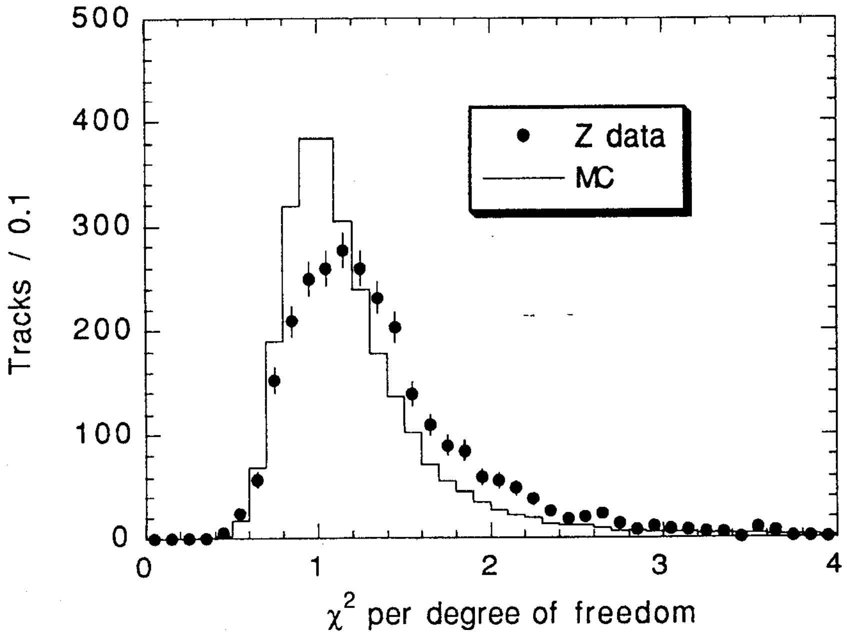

Figure 44 χ^2 per degree of freedom for the CDC/DCVD hits on the track. Tracks have at least 15 DCVD hits and $P_{xy} \geq 0.15$ GeV. The distribution means are 1.42 (1.30) for the data (MC).

resolution unchanged when averaged over all tracks. This correction is used for both the CDC and the DCVD track fitting. Figure 44 illustrates the χ^2 per degree of freedom for hadronic tracks after all these improvements are in place.

The miss distance for cosmic events is defined as the separation between the two halves of a cosmic track when extrapolated to the center of the chamber. This distribution has a width that is a factor of $\sqrt{2}$ wider than the impact parameter resolution. We used cosmic tracks with $P \geq 15$ GeV to determine the tracking performance for isolated high momentum tracks in the chamber. The impact parameter resolution was 37 μm (Figure 45) and the angular resolution was 0.5 mrad. These values are about 30% worse than what could be expected with perfect wire geometry and detector alignment.

The drift chambers displayed a few minor blemishes that could be contributing to the additional track smearing experienced by high momentum cosmics. The miss distance and acoplanarity distributions for high momentum cosmic tracks ($P \geq 5$ GeV) were not centered exactly at zero. For instance, the mean geometric miss distance for cosmics using CDC tracking alone was 70±15 μm, which is still small compared to the standard deviation of 360 μm. The offset was independent of the charge of the cosmic track. With DCVD information, the miss distance distribution

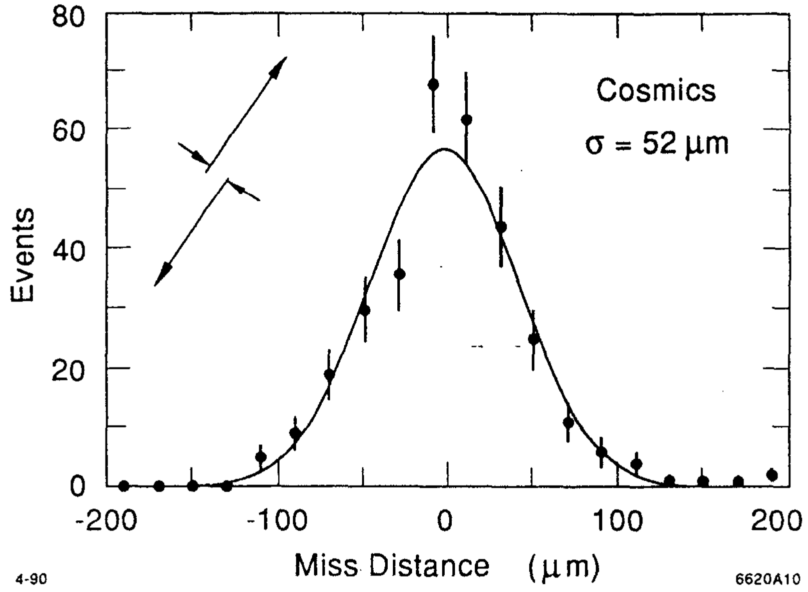

Figure 45 Miss distance for cosmics with momentum $P \geq 15$ GeV. The impact parameter resolution is a factor $\sqrt{2}$ smaller than the miss distance resolution.

became centered about the origin, but the acoplanarity between the two cosmic segments now acquires a small nonzero mean of 0.15±0.05 mrad, independent of the charge of the cosmic particle. If we track the cosmic using only DCVD hits, the kink doubles in magnitude. These symptoms suggest a subtle interplay possibly between remaining errors in the time-distance relation, uncertainties in the CDC lorentz angle, uncertainties in the alignment between drift chambers, and small distortions of the drift chambers. The time-distance relation for the DCVD is sensitive to the angle ξ between the track and the DCVD anode plane. [61] Although modeled by electrostatics simulations, the mean miss distance still displayed a residual linear dependence on the sum of $\tan\xi$ for the two tracks in a cosmic event. This effect was small (≤ 15 μm).

2.4 Silicon Strip Vertex Detector (SSVD)

2.4.1 Detector Description

The highest precision in tracking is achieved with the Silicon Strip Vertex Detector (SSVD). [58] Its layout is shown in Figure 46 and Figure 47. Located between the drift chamber vertex detector and the vacuum beampipe, this device has three layers of silicon strip modules at radii of 29.4 mm, 33.7 mm, and 38.0 mm (see Table 9). The modules can be placed this close to the beam axis because the

Table 9 Physical characteristics of the modules in the Silicon Strip Vertex Detector.

Detector Property	Layer 1	Layer 2	Layer 3	units
layer radius	29.4	33.7	38.0	mm
strip pitch	25	29	33	μm
detector size	13.8x74.8	15.8x85.1	17.9x93.5	mm^2
thickness	314	314	314	μm
Number of strips	512	512	512	—

beampipe is only 25 mm in radius. In each layer there are twelve non-overlapping modules which have an azimuthal coverage of 85% of 2π. The polar coverage is $|\cos\theta| \leq 0.77$ for tracks that come from the interaction site.

Composed of aluminum endplates and connected by an inner and outer beryllium shell, two half-cylinder support structures house the silicon modules. The mechanical support is mounted directly onto the vacuum beampipe. Capacitive monitors are used to detect any relative motion between the SSVD and the outer drift chambers, and are discussed in further detail in Section 4.4.4.

Each module consists of 512 axial strips with a pitch between 25 and 33 microns depending on the layer. Since the strips are axial, only r and φ information is available. The signal on every channel is readout by Microplex chips which are custom designed VLSI circuits located at the ends of the silicon modules. The Microplex performs a double-correlated sample-and-hold and sends the signals to the input of a microprocessor controlled ADC called a BADC. The BADCs digitize the pulse heights, subtract pedestals, perform gain corrections, and sparcify the data. Since only 2.5% of the 18432 channels have pulse heights above threshold in a typical hadronic Z^0 event, the sparsification provided by the BADCs is needed to streamline the data acquisition.

2.4.2 Cluster Finding

During the Z^0 running period approximately 8% of the SSVD channels were not operational. One cable was damaged during installation, another was severed partway through the 1990 run when the Mark II endcap doors were closed. Thus two silicon modules were deactivated. The five strips nearest each module edge experienced higher leakage currents and lower signal/noise ratios and were not

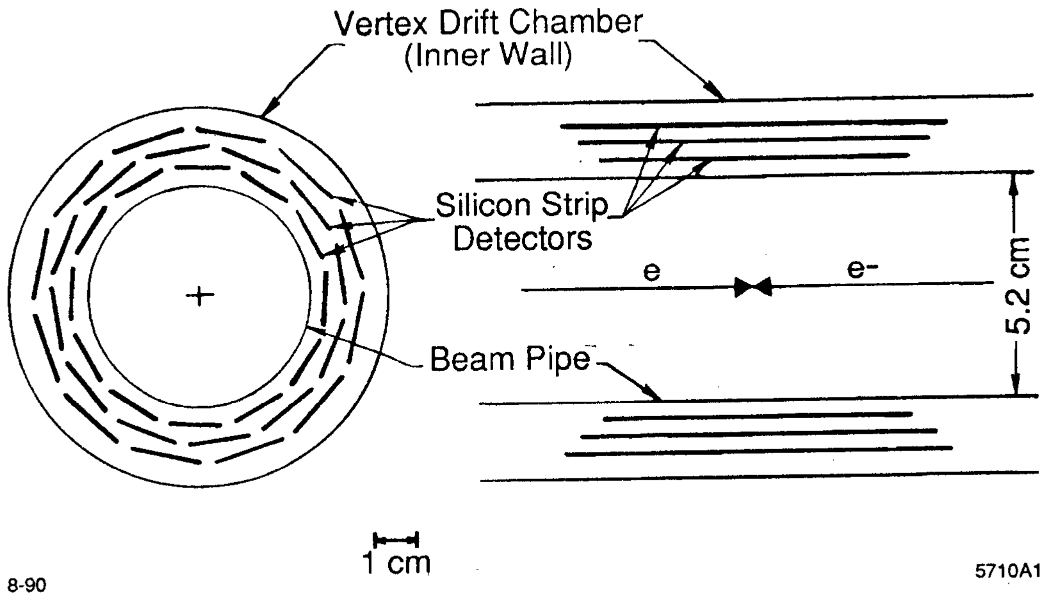

Figure 46 Layout of the modules in the Silicon Strip Vertex Detector.

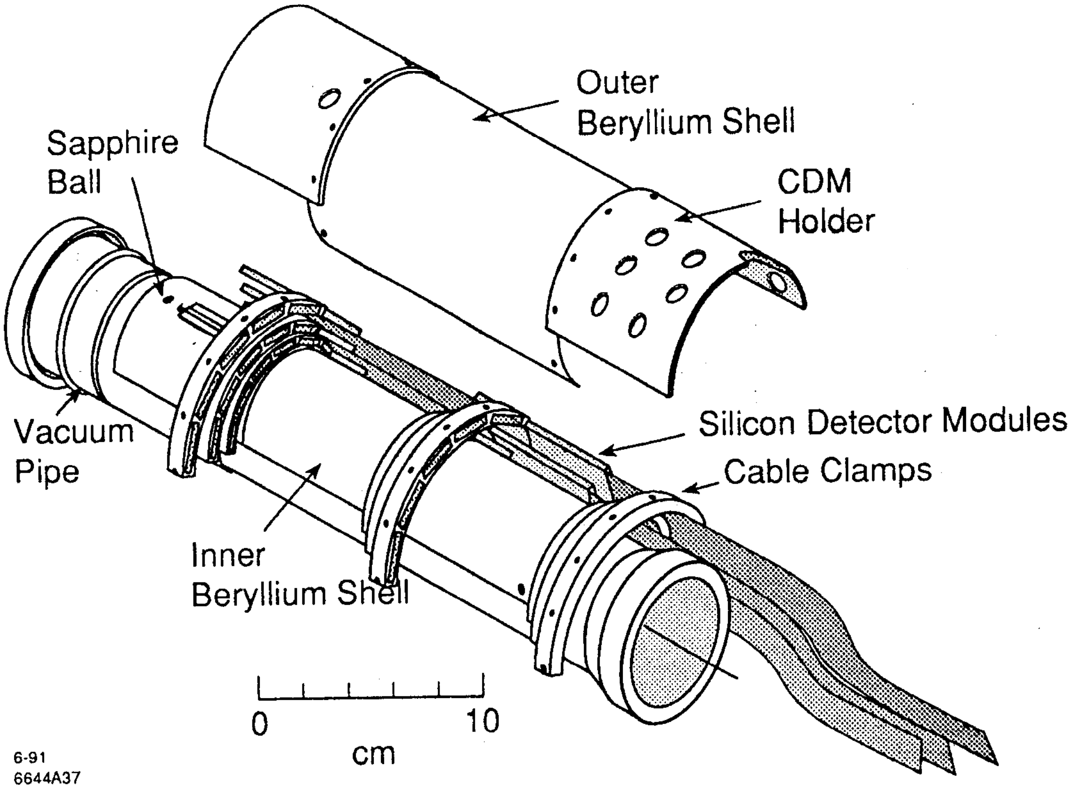

Figure 47 Isometric view of the Silicon Strip Vertex Detector.

used. Isolated channels that had poor signal/noise ratios were identified with a pre-installation gain study using a ^{241}Am source and were removed from the data acquisition. On occasion the pedestals for an entire module would shift off-scale due to heavy beam backgrounds, and the data would be lost for several hours until the next calibration obtained new pedestal values.

The ionization deposited by a track in the silicon module typically spread over 2-4 strips. Resolutions significantly better than the strip pitch of ~30 μm were achieved by taking the centroid of the cluster. The SSVD was highly efficient at detecting charged tracks with a measured signal-to-noise ratio of approximately 18:1. Although the silicon strips are much closer to the beams than the DCVD, the SSVD was considerably less sensitive to beam backgrounds because the active volume per strip is so small. Most of the backgrounds were from synchrotron photons and low momentum charged tracks from photon conversions at the beampipe. Altogether only 1.7% of the channels had pulse heights above threshold for random beam triggers and 2.5% for typical hadronic events.

Hit clusters separated by two or more strips were efficiently distinguished by looking for a dip in the cluster height greater than $1.5\sigma_i$, where σ_i is the rms noise of the individual channel. Both clusters were required to have a signal greater than $5\sigma_i$. The two-track separation in hadronic events was better than 100 μm, which corresponds to an angular separation of 0.3 mrad.

2.4.3 Tracking Performance

SSVD tracking is performed by calculating an 8x8 covariance matrix composed of the 5x5 track error matrix from the CDC/DCVD track fit and the 3x3 error matrix from the silicon strip hits.† A least squares fit minimizes the residuals at every silicon layer and optimizes the track parameters for the combined three detector fit. Multiple scattering errors from the silicon layers induce correlations among the silicon measurements and between the silicon hits and CDC/DCVD track parameters, which generate nonzero off-diagonal elements in the covariance matrix. Hence, the errors are computed exactly in the 8x8 covariance matrix. This procedure contrasts with the treatment of multiple scattering from drift chamber wires and gas; after the track was fit in the CDC or DCVD, multiple scattering contributions were approximated by augmenting the 5x5 track error matrix via the Glückstern prescription. Figure 48 demonstrates the tracking performance of the Silicon Strip Vertex Detector.

---

† SSVD tracking algorithm was developed by Chris Adolfsen and Bob Jacobsen.

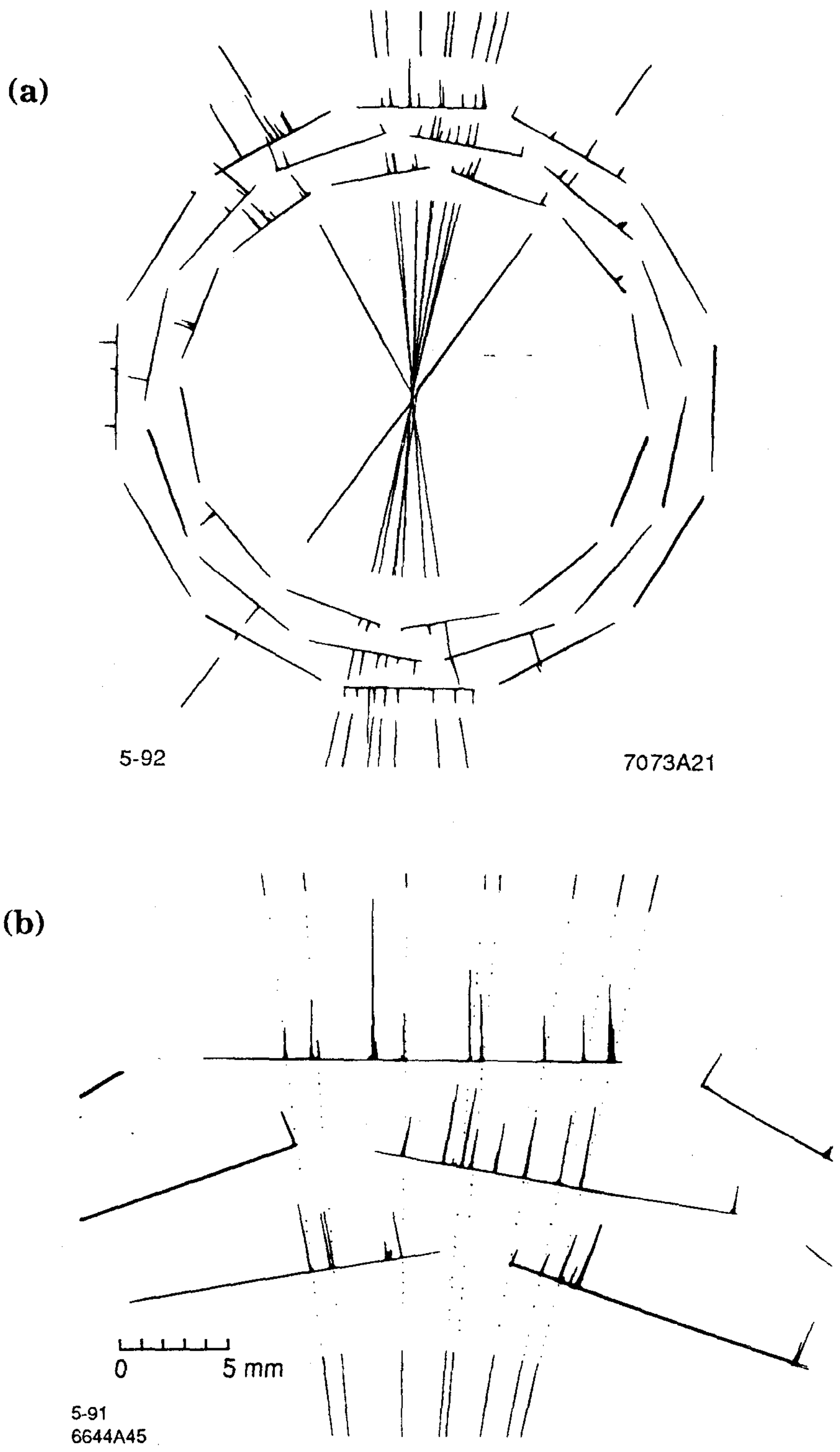

Figure 48 (a) Same event as in Figure 41 zoomed in to show the tracking performance of the Silicon Strip Vertex Detector. (b) Blowup of the upper region of the SSVD. The energy deposition per strip is histogrammed along the silicon modules.

The number of silicon hits picked up by a track is presented in Table 10 for tracks with at least 0.15 GeV of transverse momentum, $|\cos\theta| \leq 0.80$, and minimum CDC and DCVD hit requirements. Tracks collected on average 1.86 hits, and 90% of the tracks picked up at least one silicon cluster, agreeing well with the Monte Carlo. Background noise and track densities in jets caused minor hit loss, down from an expected 2.14 generated hits per track after accounting for dead silicon channels. From MC studies, we concluded that most of these silicon hits are correctly assigned to the track, i.e. very few silicon hits are accidentals. On average 1.76 out of the 1.86 found hits are the ones generated by the track in the MC, and only 5% of the tracks with silicon information fail to have at least one correctly assigned cluster (Table 10). Half of the 5% of tracks that pick up nothing but spurious silicon hits occur because the track also has a completely spurious track segment in the DCVD. Furthermore, if we require a track to have at least one silicon measurement, half the poorly measured CDC/DCVD tracks are weeded out. The distribution of silicon hits by layer number is also in good agreement between data and MC, as shown in Table 11.

The intrinsic resolution of the silicon strip vertex detector can be determined from tracks that pick up all three hits. Define Δ to be the distance between the cluster in layer 2 and the line segment formed by hits in layers 1 and 3. With the silicon strip detector aligned (see Section 4.4.4), the distribution of Δ for all tracks with momentum greater than 1 GeV is shown in Figure 49. The width of the distribution corresponds to an intrinsic spatial resolution of 7.1 μm.

Tracks pass through a dead DCVD cell roughly 10% of the time. These tracks find 1.63 silicon hits of which only 1.38 are generated by the track. Substantially more hits are spurious clusters either from the beam backgrounds or confusion from close track pairs. The success rate is lower because without the DCVD, the central drift chamber extrapolates the track into the SSVD with greater difficulty. Tracking errors can be reduced by only using tracks with two or three silicon measurements, which has a selection efficiency of 60%. Exceedingly few spurious silicon hits get associated with the track; 96% of these tracks find at least one hit generated by the track.

If the CDC/DCVD track goes through an active section of the DCVD but fails to find the DCVD hits, then the silicon tracking performance is truly terrible. Only 0.78 silicon hits are found of which half are spurious. Most likely the DCVD failed to pick up any hits because the CDC mismeasured the track. These tracks comprise ~8% of all tracks and are discarded in the lifetime analysis.

Figure 50 plots the χ^2 per degree of freedom in the SSVD track fit. Only tracks with at least 15 DCVD measurements and at least one SSVD measurement are included in the plot. The number of degrees of freedom is equal to the number of silicon hits on the track

Table 10 Distribution of silicon hit for tracks that are well measured by the CDC and DCVD. Tracks must have $P_{xy} \geq 0.15$ GeV, $|\cos\theta| \leq 0.8$, $|\delta| \leq 5$ mm, at least 20 CDC hits, and at least 15 DCVD hits.

	% of tracks with N SSVD hits		**% of tracks with N correct SSVD hits**
N	**Z data**	**MC**	**MC**
0	10.3±0.6	10.1	14.1
1	16.0±0.7	14.6	15.8
2	51.7±1.0	52.3	49.8
3	22.1±0.8	23.0	20.4

Table 11 Location of silicon hits on the tracks.

	% of Tracks	
Location of SSVD hits on the track	**Z data**	**MC**
No hits	10.3±0.6	10.1
Layer 1 only	6.0±0.5	5.3
Layer 2 only	6.9±0.5	6.1
Layer 3 only	3.2±0.3	3.2
Layers 1 & 2	22.5±0.8	22.2
Layers 1 & 3	14.4±0.7	14.7
Layers 2 & 3	14.8±0.7	15.4
Layers 1,2, & 3	22.1±0.8	23.0

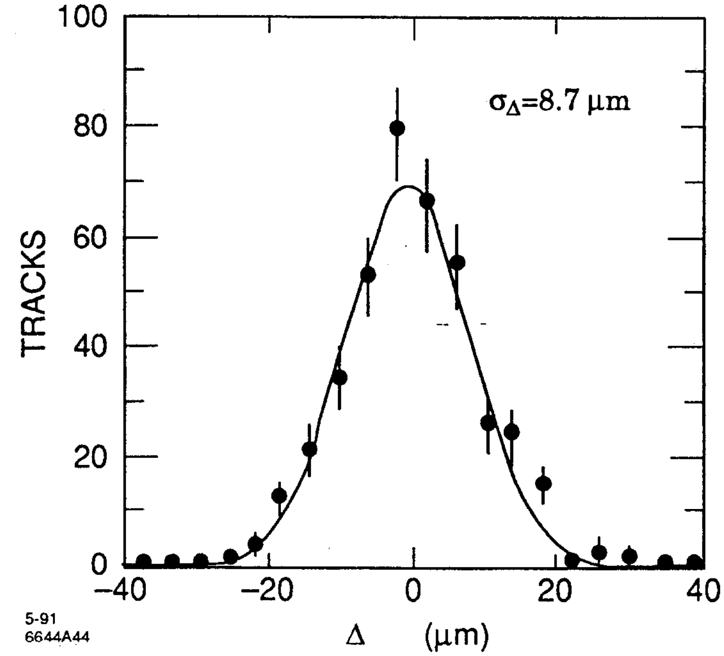

Figure 49 Distribution of the variable Δ for tracks with momenta greater than 1 GeV. Δ is defined as the distance between the cluster in layer 2 and the line segment formed by the hits in layers 1 and 3. It has a resolution that is $\sqrt{3/2}$ times larger than the impact parameter resolution.

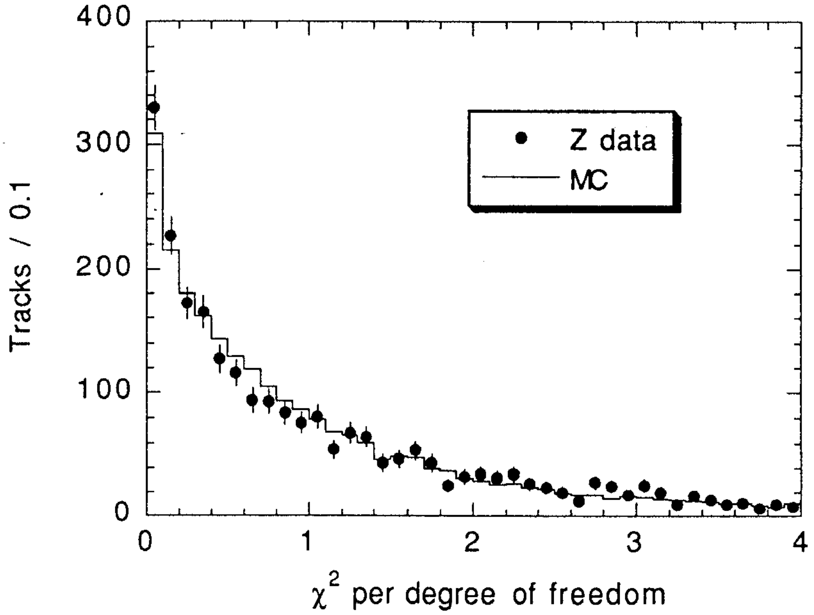

Figure 50 χ^2 per degree of freedom for the SSVD hits on tracks with at least $P_{xy} \geq 0.15$ GeV. The distribution means are 1.10 (1.04) for the data (MC).

In summary, the silicon strip detector not only provides precision measurements on the track, but also discriminates against poorly measured tracks coming from the outer drift chambers due to the stringent spatial tolerance that the track fitting algorithm imposes on the silicon clusters.

He uses statistics as a drunken man uses lamp-posts –
for support rather than illumination.

– Andrew Lang

3 The Monte Carlo Simulation

The Monte Carlo simulation programs are a vital tool used to simulate high energy physics processes that subsequently can be compared with experimental results observed by the Mark II detector. Detailed Monte Carlo simulations use probability distributions dictated by the Standard Model theory and phenomenological models. They are necessary because most distributions such as the impact parameter distribution cannot be predicted from first principles.

The collection of Monte Carlo programs can be divided into two categories: the Monte Carlo event generator and the Mark II detector simulation. The event generator transforms a Z^0 boson into a collection of final state charged and neutral particles along with their momentum and production location. This transformation evolves through a process of quark production, hard gluon radiation, fragmentation, hadronization, and finally weak decay of heavy hadrons. The generated tracks are next sent through a detector simulation to reproduce the physical response of the Mark II detector to an actual Z^0 event. The Monte Carlo events can then be processed with the identical software package used for the Z^0 data recorded by the Mark II.

In this chapter we first discuss the B hadron production and decay issues that were not covered in the introductory chapter. We will conclude with a description of the Mark II detector simulation.

3.1 Monte Carlo Event Generator

The Monte Carlo generates the fraction of $b\bar{b}$ events in hadronic Z^0 decays, $\Gamma(Z^0 \to b\bar{b})/\Gamma(Z^0 \to hadrons)$, equal to the Standard Model prediction of 0.217. The corresponding fraction for $c\bar{c}$ events is 0.179. The four LEP experiments have measured the $b\bar{b}$ fraction using high P and high P_T leptons from semileptonic B decays (Table 12). The $b\bar{b}$ fraction has also been measured by DELPHI using the boosted sphericity product and by the Mark II using an impact parameter tag. The average from all these experiments is Γ_b/Γ_{hadron}=0.213±0.010, in good agreement with the Standard Model.

The charm branching fraction has been extracted from fits to the entire lepton P and P_T spectrum. Leptons from charm will populate the low P_T region. Another technique relies on fully reconstructing the D^{*+} mesons. Searching for the satellite pion of the D^{*+} decay without reconstructing the D^0 is accomplished by looking for an excess of pions with small P_T with respect to the jet axis. This method has met with some success but concedes much larger systematic errors. The results are listed in Table 13 and yield an average branching fraction of Γ_c/Γ_{hadron}=0.176±0.027, agreeing with the Standard Model prediction.

The event generator used to simulate Z^0 boson decays is the JETSET 6.3 code with parton shower fragmentation, often called the LUND shower Monte Carlo. [67] This method uses the leading log approximation (LLA) to generate a cascade of quark and gluon partons. The shower stops when the parton energies in the cascade falls below a minimum cutoff Q_0. The collection of partons form color singlets and hadronize using a string fragmentation model. The parameters in the Lund symmetric fragmentation function for light quarks and the Peterson fragmentation function for heavy quarks are listed in Table 14

The LUND shower parameters were tuned at 29 GeV from the PEP data and are expected to predict the distributions at the 91 GeV Z^0 resonance. [70] The Peterson parameters of ε_c=0.15 and ε_b=0.007 correspond to an average energy of $\langle x_E \rangle_c$=0.41for charm hadrons and $\langle x_E \rangle_b$=0.68 for bottom hadrons. The mean fragmentation $\langle x_E \rangle$ has been measured accurately by the four LEP experiments using the lepton momentum spectra from heavy quark semileptonic decays (see Table 15 and Table 16). Leptons from B decays populate the high P_T region, whereas leptons from charm decays populate the low P_T region. The LEP results yield a mean fragmentation of $\langle x_{b \to l} \rangle = 0.705 \pm 0.013$ for bottom and $\langle x_{c \to l} \rangle = 0.519 \pm 0.030$ for charm. A second method of checking the charm

Table 12 Measurements of the $Z^0 \to b\bar{b}$ branching fraction. The high P_T lepton results use a semileptonic branching fraction of 11.7±0.6% from the PEP, PETRA, and L3 measurements. The Standard Model predicts Γ_b/Γ_{hadron}=0.217.

Experiment	**Method**	$\Gamma_b / \Gamma_{hadron}$
ALEPH [28]	high P_T lepton	0.191±0.014±0.013
DELPHI [40]	high P_T lepton	0.209±0.011(stat only)
L3 [31]	high P_T lepton	0.221±0.004±0.013
OPAL [30]	high P_T lepton	0.193±0.006±0.015
DELPHI [38]	boosted sph product	0.222±0.015±0.013
MARK II [32]	impact parameter	0.251±0.049±0.030
Average	—	0.213±0.010

Table 13 Measurements of the $Z^0 \to c\bar{c}$ branching fraction. The semileptonic methods use Br($c \to l$)=9.0±1.3%, averaged over all charm hadrons. OPAL also reconstructs the D^*, and DELPHI searches for the low P_T satellite pion from D^* decays. The Standard Model predicts Γ_c/Γ_{hadron}=0.179.

Experiment	**Method**	$\Gamma_c / \Gamma_{hadron}$
OPAL [30]	$c \to \mu$	0.196±0.028±0.055
ALEPH [28]	$c \to e/\mu$	0.148±0.044±0.041
OPAL [34]	$c \to D^*$	0.186±0.035±0.020
DELPHI [38]	$c \to D^*$	0.162±0.030±0.050
Average	—	0.176±0.027

fragmentation has been developed by ALEPH and OPAL by measuring the momentum spectrum of reconstructed D^{*+} mesons and suggests that $\langle x_{D^*} \rangle$ = 0.507±0.016. The two methods need not give the same results for the mean charm fragmentation since the lepton momentum spectrum from non-D^{*+} production may be slightly different. Since the MC generated charm hadrons with a lower $\langle x_E \rangle_c$ than the results of either method, a correction is performed that will be discussed in the section on systematics.

Table 14 LUND shower fragmentation parameters.

LUND Shower Parameters	Value
Λ_{LLA}: QCD scale	0.4 GeV
Q_0: cutoff for parton evolution	1.0 GeV
A: *uds* fragmentation	0.45
B: *uds* fragmentation	0.9
σ_q: width of hadron P_T	0.23
ε_c: Peterson parameter (charm)	0.15
ε_b: Peterson parameter (bottom)	0.007
Strange quark suppression factor	0.3
Diquark suppression factor	0.1
Probability of spin 1 meson (b & c quarks)	0.75

Charm from direct $Z^0 \to c\bar{c}$ production will hadronize into a vector meson three times more frequently than a pseudoscalar meson since the D^* has three spin states. These excited charm mesons will decay both electromagnetically and strongly, which will result in a D^0:D^+:D_s:Λ_c fraction of 0.53 : 0.25 : 0.13 : 0.09 in the LUND Monte Carlo, where Λ_c represents all charm baryons. The relatively low production of D_s and Λ_c results from the suppression of strange quarks and diquarks created out of the vacuum. The charge versus neutral meson asymmetry occurs not because of an inherent asymmetry between the $u\bar{u}$ and $d\bar{d}$ pair creation in the vacuum, but because of a decay asymmetry of the vector meson into a pseudoscalar meson. The charged vector meson can decay into both D^0 and D^+ in the amounts of $Br(D^{*+} \to D^0\pi^+)=0.50$ and $Br(D^{*+} \to D^+ \pi^0/\gamma)=0.50$. On the other hand, the D^{*0} vector meson decays into a D^0 pseudoscalar plus a π^0 or photon 100% of the time. The $D^{*0} \to D^+\pi^-$ transition is kinematically just barely forbidden by 2 MeV. Taking into account the relative charm hadron production rates and their respective lifetimes, the lifetime averaged over all charm hadrons from $Z^0 \to c\bar{c}$ events is $\langle\tau_c\rangle$ = 0.56 ps.

Unlike the charm sector, there is no enhanced production expected for the neutral B meson. The direct vector-pseudoscalar B meson production is again in the ratio of 3:1. Since the vector-pseudoscalar mass difference is only 50 MeV, vector B^* mesons can only decay electromagnetically. The $B^* \to B\pi^\pm$ sign-changing transition

Table 15 Measurements of the bottom fragmentation parameter.

Experiment	Method	$\langle x_E \rangle_b$
L3[31]	b→e/μ	0.686 ± 0.006 ± 0.016
ALEPH[35]	b→e/μ	0.714 ± 0.021
OPAL[30]	b→μ	0.726 ± 0.007 ± 0.022
DELPHI[35]	b→μ	0.709 ± 0.018
Average	b→lepton	0.705 ± 0.013

Table 16 Measurements of the charm fragmentation parameter. The D^* and the leptonic methods need not yield the same results since they sample different selections of charm hadrons.

Experiment	Method	$\langle x_E \rangle_c$
ALEPH[33]	$c \to D^*$	0.504 ± 0.015 ± 0.008
OPAL[34]	$c \to D^*$	0.52 ± 0.03 ± 0.01
ALEPH[35]	c→e	0.465 ± 0.04
OPAL[30]	c→μ	0.56 ± 0.02 ± 0.03
Average	D^*	0.507 ± 0.016
Average	leptons	0.519 ± 0.030

is strictly forbidden. The bottom quark will hadronize into B^0:B^+:B_s:Λ_b particles in the fraction 0.395 : 0.395 : 0.12 : 0.09 in the LUND Monte Carlo. As with charm, Λ_b represents all B baryons, and the relatively low production of B_s and Λ_b is due to the difficulty of creating strange quarks and diquarks out of the vacuum.

3.2 Properties of Hadronic Z^0 Decays

Properties of hadronic Z^0 decays have been studied in great detail both at the SLC and at LEP. Using the 1989 SLC sample of 538 hadronic Z^0 decays, Figure 51 through Figure 55 display the charged track multiplicity, jet multiplicity, and event shape parameter distributions. [69] For all distributions, the hadronic data and Monte Carlo agree quite well.

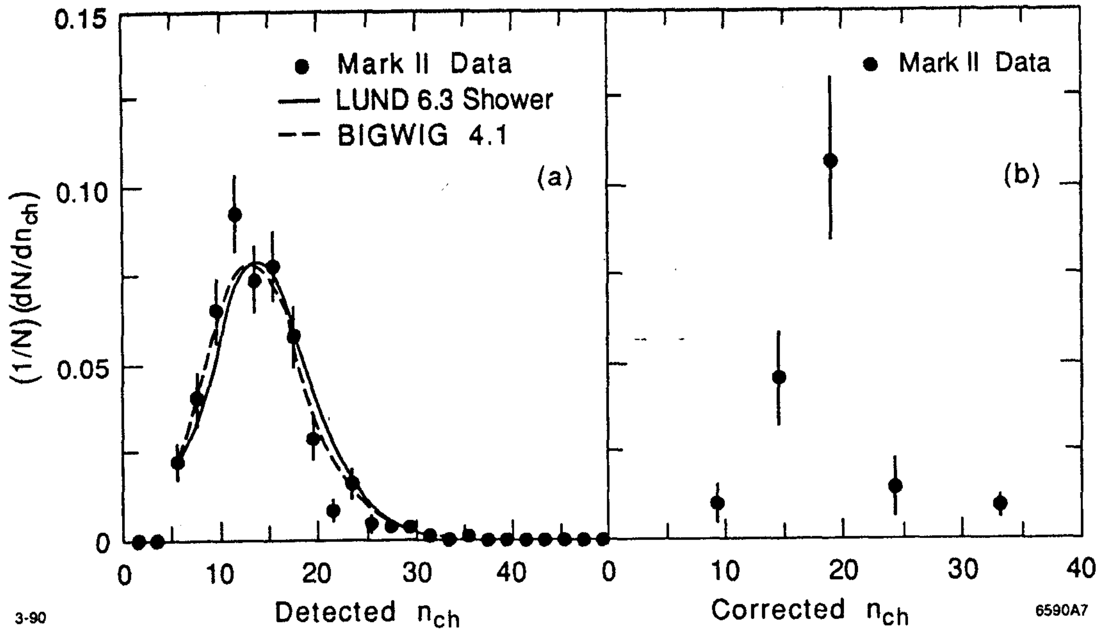

Figure 51 Charged track multiplicity (a) observed in the Mark II detector and (b) after acceptance corrections.

The charged track multiplicity when corrected for track efficiency and acceptance was $\langle n_{ch} \rangle_{cor} = 20.03 \pm 0.36\,(stat)$, where tracks from weak decays of K_s^0 and Λ's are included. Charged tracks from decays of longer lived particles, photon conversion, or nuclear inelastic scattering are excluded from the corrected multiplicity. Roughly 70% of the tracks are detected by the central drift chamber.

The jet multiplicity is a measure of the number of partons that are initially produced in the e^+e^- annihilation. Usually an event has only two colinear jets, each jet generated from the initial quark parton. Occasionally the quarks will radiate hard gluons at a rate proportional to the strong coupling constant α_s which will manifest themselves as additional jets. We can quantify the number of jets observed in an event by using a track clustering algorithm such as YCLUS, [68] developed by the JADE experiment, to group tracks into well defined jets. Define the normalized invariant mass of two clusters as

$$y = \frac{2E_iE_j(1 - \cos\theta_{ij})}{E_{vis}^2} \tag{24}$$

where E_i is the jet energy, θ_{ij} is the angle between the two jets, and E_{vis} is the visible energy in the event. Tracks pairs are combined into clusters, and pairs of clusters are merged together as long as the y for the pair does not exceed some

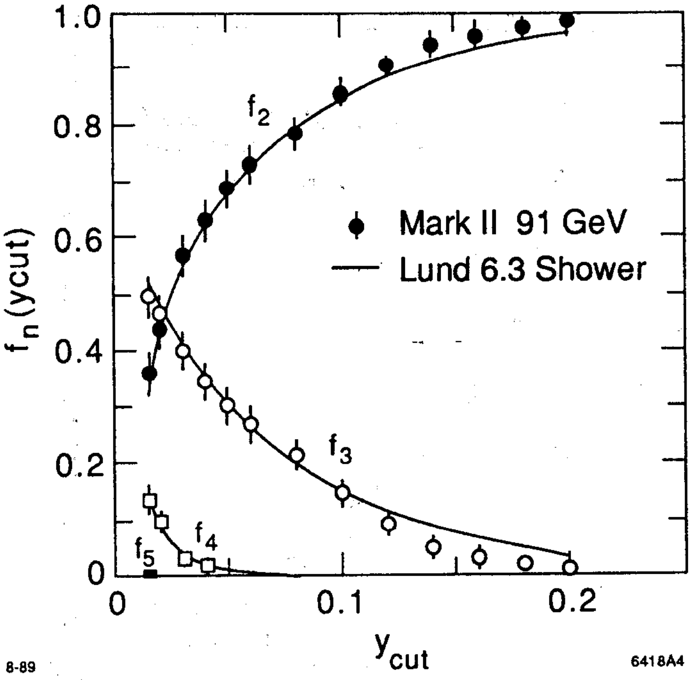

Figure 52 Jet multiplicity distribution as a function of the separation parameter y_{cut}. A typical y_{cut} value of 0.04 leads to 60% two-jet events, 37% three-jet events, and 3% four-jet events.

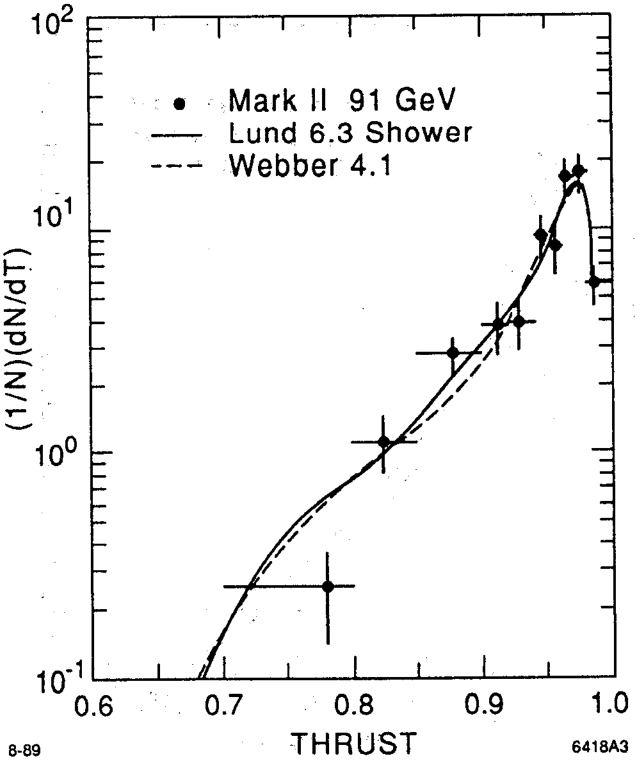

Figure 53 Thrust distribution for hadronic events.

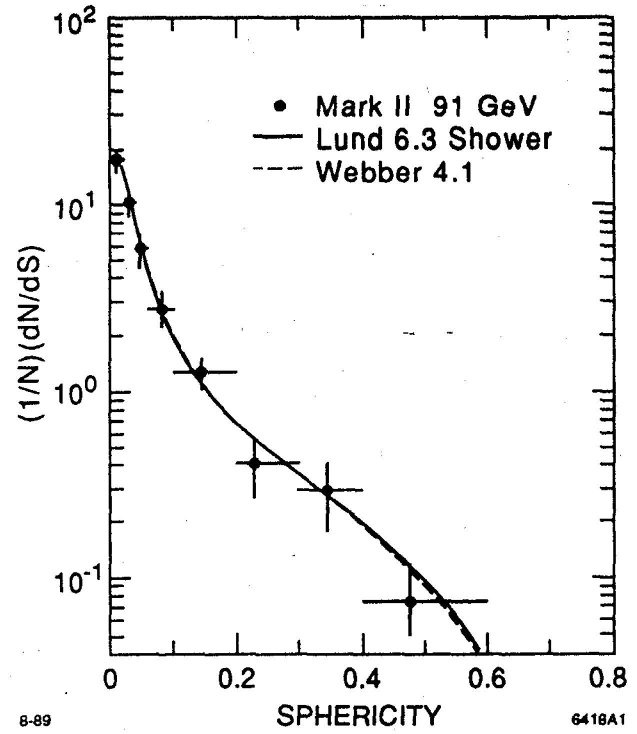

Figure 54 Sphericity distribution for hadronic events.

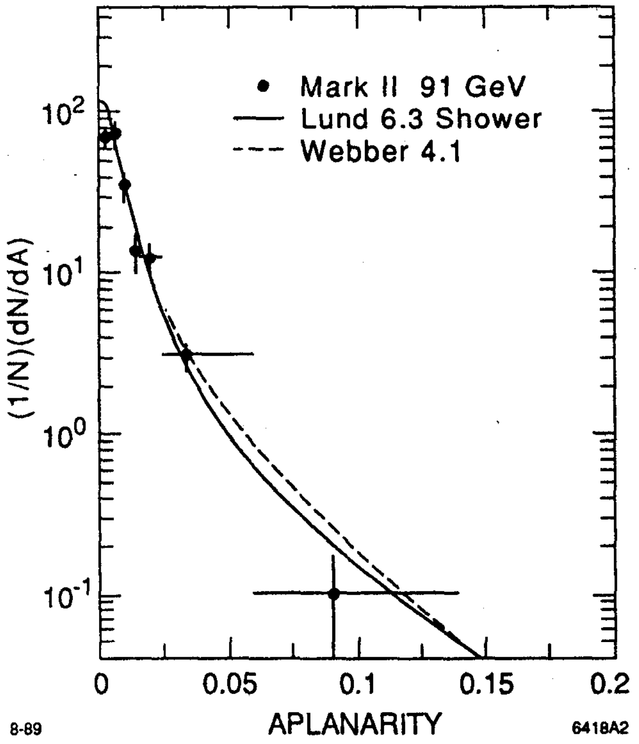

Figure 55 Aplanarity distribution for hadronic events.

cutoff value y_{cut}. The parameter y_{cut} defines the minimum separation between clusters before they can be considered as an independent jet. A typical value of y_{cut}=0.04 separates hadronic events into 60% two-jet, 37% three-jet, and 3% four-jet events.

The thrust (T) and sphericity (S) of an event are shape parameters that also describe how "jetty" an event is. Defined as

$$T = \max \frac{\sum_i |\vec{p}_i \cdot \hat{T}|}{\sum_i |\vec{p}_i|}, \tag{25}$$

$$S = \frac{3}{2} \min \frac{\sum_i |\vec{p}_i \times \hat{S}|^2}{\sum_i |\vec{p}_i|^2}, \tag{26}$$

where $\hat{T}$ is the unit vector that maximizes T, and $\hat{S}$ is the unit vector that minimizes S. $\hat{T}$ and $\hat{S}$ are commonly called the thrust and sphericity axis, respectively. For narrow two-jet events, the thrust and sphericity will be T≈1 and S≈0. Events with a perfectly isotropic track distribution have a thrust of T=0.5 and sphericity of S=1. Since the thrust is derived from the linear sum of particle momenta, it has the rather nice property of being "colinear safe". Thus if a particle in an event splits into two colinear tracks, the thrust value will remain invariant. The sphericity does not possess this property since it depends on the square of the particle momentum. In two-jet events, the thrust axis faithfully reproduces the direction of the initial $q\bar{q}$ pair.

The aplanarity measures the energy flow perpendicular to the event plane. Two and three-jet events will typically have small aplanarity since the jets tend to lie in a plane. Hence only relatively rare four-jet events will have a substantial aplanarity.

3.3 Heavy Quark Decay Properties

Through the efforts of the Mark III and E691 experiments, we now know roughly 90% of the exclusive D^0 and D^+ decay modes. The LUND Monte Carlo uses these exclusive branching fractions and distributes the momentum of the decay products according to the available phase space. Semileptonic decays are handled with a weak decay matrix where the $s\bar{q}$ color singlet collapses into a K or K^*. These two states are expected to dominate over nonresonant Kπ and Kππ states and the Cabibbo suppressed modes. [42]

Table 17 LUND Monte Carlo branching fractions for B hadron decays. The parentheses enclosing the quark pairs denote the color singlets. LUND includes the color-suppressed decay modes.

B Meson Decay	Branching Fraction (%)
$B \to (c\bar{q})e\bar{\nu}$	11
$B \to (c\bar{q})\mu\bar{\nu}$	11
$B \to (c\bar{q})\tau\bar{\nu}$	3
$B \to (c\bar{q})\ (\bar{u}d)$	50
$B \to (c\bar{q})\ (\bar{c}s)$	18
$B \to (d\bar{q})\ (\bar{u}c)$	5
$B \to (s\bar{q})\ (\bar{c}c)$	2

Unlike the charm sector, very little is actually known about exclusive B meson decays except for the semileptonic modes and a handful of two-body final states that comprise 15-20% of the hadronic decay rate. Our knowledge comes primarily from the efforts of the CLEO and ARGUS collaborations, and is basically limited to inclusive decays of B^0 and B^+ mesons into an assortment of charm hadrons. The LUND Monte Carlo assigns all B pseudoscalar mesons and B baryons with the same lifetime. The MC decays the b quarks through inclusive modes ($b \to c f_1 f_2$) and hadronizes the color singlets. The relative branching fractions used by the Monte Carlo are listed in Table 17.

In the LUND Monte Carlo, the resultant charm quark and spectator quark in semileptonic B decays collapse into a D^* or D meson in the ratio 3:1, and the momenta are assigned according to the weak decay matrix. The picture is not completely accurate because a sizeable fraction of the semileptonic decays are known to include either a D^{**} or a nonresonant $(D\pi)_{nr}$ or $(D\pi\pi)_{nr}$ state. [53] CLEO and ARGUS have studied this by measuring the inclusive and exclusive semileptonic rates. The ISGW model predicts that D and D^* saturate roughly 87% of the inclusive semileptonic mode. However, when the fraction of D^{**} and nonresonant $(Dn\pi)_{nr}$ is allowed to float, the D and D^* states account for only 64±10% of the total semileptonic width. [22] The MC inclusive semileptonic branching fraction for B's produced at the Z^0 is chosen to agree with the PEP/PETRA and L3 results (Table 18), since CLEO and ARGUS examine only B^0

Table 18 Inclusive semileptonic branching fraction for *B* hadrons. The result at the Υ_{4S} resonance depends heavily on models and describes only B^+ and B^0 meson decays. The average of the PEP/PETRA/L3 measurements is 11.7±0.6%.

Experiment	Model	B_{sl}(%)
Υ(4S) [53]	ACM	10.4±0.3
	ISGW	9.9±0.3
	WSB	8.4±0.7
	KS	8.4±0.5
	ISGW*	11.2±0.5
PEP/PETRA [39]	—	11.9±0.7
L3 (dileptons) [31]	—	11.3±1.2

and B^+ mesons. Also the values at the Υ_{4S} are heavily model dependent since the inclusive semileptonic branching fraction is calculated by integrating the lepton momentum spectrum, which requires theoretical estimates to extrapolate to low momenta. All models except for the ISGW* version expect a lower semileptonic branching fraction compared with higher energies.

The hadronic modes also decay via the weak decay matrix. The spectator system condenses into one particle, while the color singlet system from the weak current generates particles according to the available phase space. Since the *W* propagator also couples to $\bar{c}s$, B hadrons produce on average 1.20 charm hadrons, and the D_s meson occurs more frequently than in $Z^0 \to c\bar{c}$ events. In addition to the dominant Cabibbo-allowed $B \to (c\bar{q})\,(\bar{u}d)$ and $B \to (c\bar{q})\,(\bar{c}s)$ modes, the color-suppressed decays are also included and make up 7% of the B decays in the MC. The relative charm production ratios for D^0:D^+:D_s:Λ_c:ψ equal 0.59 : 0.28 : 0.23 : 0.12 : 0.02 (see Table 19). The inclusive D_s and Λ_c production rate is significantly higher in the MC than at the Υ_{4S} since the B_s meson and Λ_b baryon decay predominantly via the $B_s \to D_s$ and $\Lambda_b \to \Lambda_c$ weak transitions. However, if we consider only B^0 and B^+ mesons, there is still a discrepancy between the LUND MC and the CLEO/ARGUS results. The MC produces the correct amount of D_s but fails to generate any Λ_c from B^0 and B^+ decays.

Taking into account the relative charm hadron production rates and their respective lifetimes, the average lifetime for charm hadrons from B decays is

Table 19 Inclusive branching fraction of B mesons into charm hadrons. The $B \to D^{*+}X$ mode is not included in the total. [36][37]

Decay Mode	CLEO	ARGUS	LUND MC
$B \to D^{*+}X$	32±6±6 %	30±5±5 %	31.7 %
$B \to D^0X$	53±7±7	46±7±6	59.2
$B \to D^+X$	22±5±4	23±5±3	28.1
$B \to D_sX$	9.9±1.5	8±2±2	22.9
$B \to \Lambda_cX$	6.1±0.8±1.0	7.6±1.4	12.1
$B \to \psi X$	1.12±0.10±0.23	1.07±0.16±0.19	1.7
$B \to \psi' X$	0.33±0.08±0.12	0.46±0.17±0.11	<1
Total	(97±15) %	(89±13) %	120 %
Predicted	115 %	115 %	120 %

$\langle \tau_c \rangle = 0.53$ ps. The $b \to u$ transitions are ignored in the Monte Carlo, since they are expected to contribute to only 1% of the decays.

The LUND Monte Carlo possesses several deficiencies in simulating the production and decay of B hadrons as outlined in this chapter. For example, the inclusive decay rates into leptons or specific charm states carry some discrepancies. Also, exclusive semileptonic decays do not include the D^{**} or nonresonant $(Dn\pi)_{nr}$ modes. However, most of these shortcomings can be ignored since we are not investigating a specific decay mode. Rather, we are concerned with general properties of $b\bar{b}$ events — the substantial decay length, the B mass, and the decay multiplicity of B hadrons — all contribute to the abundance of high impact parameter tracks. In order to characterize a B-tag using impact parameters and to perform the B lifetime analysis, we must properly model the impact parameter distribution for tracks from B decays. The δ distribution is highly sensitive to the B decay multiplicity and momentum spectrum. For instance, a higher multiplicity and a harder momentum spectrum will increase the impact parameter tag efficiency not only because there are more high impact parameter tracks but also because the resolution errors improve since stiffer tracks undergo less deflection from multiple scattering. Thus by tuning the MC to these distributions, which have been measured accurately by the CLEO and ARGUS collaborations at the Υ_{4S}, we can compensate for our ignorance on the exclusive decay modes and faithfully reproduce the impact parameter distribution for $b\bar{b}$ events.

3.4 Mark II Detector Simulation

After the LUND Monte Carlo creates a hadronic Z^0 decay, the charged and neutral particles generated by the MC must enter the Mark II detector simulation so that the Monte Carlo events can be compared with the hadronic data. The detector simulation needs to faithfully reproduce both the track signals and the beam background noise read out by the data acquisition electronics. A total of 20,000 Monte Carlo events with full detector simulation were used throughout this analysis whenever comparisons were made with the hadronic data.

First, the LUND MC simulates the trajectory of generated tracks through the Mark II detector. Charged tracks arc through the detector in helical orbits inside the 4.75 kilogauss solenoidal magnet. Tracks leave ionization signals in the silicon strips and drift chamber gas, lose energy like a minimum ionizing particle, and undergo angular deflections from multiple coulomb scattering and elastic nuclear scattering in the detector. The full Molière theory, [76] which includes non-gaussian tails from single hard scatters at large angles, was integrated into the MC. Inelastic nuclear scattering was also allowed in the detector simulation, but because interaction is extremely complex, the particle is removed from the MC track list at the scattering site without generating a spray of low momentum debris.

Hits in the three tracking devices are generated for each charged track, taking into account the geometric detector acceptance, layer inefficiencies, spatial resolution, double-hit resolution, and known dead silicon strips and drift chamber wires. The drift times for DCVD and CDC hits are calculated from the inverse of the time-distance relation and smeared by the spatial resolution of the detectors. The centroids of the silicon clusters are smeared by ~7 μm. The CDC track information consisted only of the drift times and integrated charges, whereas the DCVD and SSVD systems record a simulated pulse height profile for the hits in the detector. The Monte Carlo simulated the data by using a library of prerecorded pulses. The lookup table for DCVD hits was created from cosmic ray tracks and accommodated variations in the pulse shape due to drift distance effects.

The intense beam backgrounds, which had especially plagued the vertex drift chamber performance, were also simulated in the Monte Carlo. Random beam-crossing events were logged near the time of each Z^0 event and overlaid onto clean MC events. Since beam backgrounds were relatively stable over a period of minutes to hours, the level of backgrounds in these “mixed” MC events was representative of the backgrounds in the Z^0 data. An average of 10 beam background events were collected for each logged Z^0 event, making a total of ~2600 background events. These events were recycled many times during the process of constructing the 20,000 fully simulated Monte Carlo events. Hits in the mixed MC events were eliminated in all DCVD cells that were inoperative for the corresponding Z^0 event. Hits from known dead silicon strips and chamber wires were discarded. Hit inefficiencies in wires, cells, and strips were also modeled.

SSVD and DCVD pulse height information from track hits and beam backgrounds were summed linearly up to saturation. The double-hit resolution of the two detectors due to background noise and track densities in jets were naturally incorporated because the same hit finding algorithms were used on both data and MC events. Since the central drift chamber stored only drift times and charges, the double-hit performance shown in Figure 20 on page 42 was used to merge closely spaced CDC hits.

As can be seen from the numerous plots in Section 2.3, our method of incorporating the beam-related backgrounds adequately simulated the degradation in spatial resolution and the loss of hit and track finding efficiencies associated with the intense beam backgrounds in the DCVD. Perhaps, the only discrepancy between data and MC is that both the DCVD chamber occupancy and the total number of chamber hits was roughly 10% higher in the data. Although not fully understood, the explanation could result from the way that the DCVD records pulse height information. To limit the amount of data logged to tape, the tail of the signal pulse is truncated, and typically only 30 FADC bins of information are stored. The pulse library used by the MC also consists of truncated signals. (Of course, noise hits that saturate dozens of FADC bins are all recorded.) Late-arriving ionization from tracks can produce a long sub-threshold tail, which ordinarily is truncated. However, if this tail is coincident with another sub-threshold signal from other tracks or beam backgrounds, the sum may yield a valid DCVD hit. Note that the second sub-threshold noise can drift from either half of the anode plane. The mixed MC will not register such hits since the sub-threshold tails have already been truncated before mixing was performed.

One must learn by doing the thing; though you think you know it, you have no certainty until you try.

– Sophocles

4 Track Impact Parameter Resolution

Track impact parameters are measured extremely accurately by the vertex detectors and provide the cornerstone to the B lifetime measurement. In this chapter, we characterize the impact parameter resolution which includes both a central gaussian core and non-gaussian tails.

The chapter first introduces the criterion used to select hadronic Z^0 events from the Mark II data. We desire only charged particles that are well measured by the Mark II tracking system, and we achieve this goal by requiring tracks to satisfy a series of quality cuts. These track cuts are applied in the studies on impact parameter resolution, but they are also applied to the impact parameter tag and the B lifetime measurement.

We next define the track impact parameter and its sign convention. We characterize the calculated impact parameter resolution and demonstrate that it describes the central core of the δ distribution. Finally, we model the non-gaussian tails of the resolution function by examining the negative half of the inclusive impact parameter distribution.

4.1 Hadronic Event Selection Cuts

Hadronic Z decays are selected on the basis of charged track information from the Central Drift Chamber and neutral energy from the electromagnetic calorimetry. Charged tracks must have a transverse momentum of at least 0.150 GeV and a polar angle of $|\cos\theta| \leq 0.82$ with respect to the beam axis ($\hat{z}$) to be considered well measured by the CDC. We desire only tracks from the Z^0 production point, which is achieved by requiring the distance of closest approach to the collision point in the transverse (xy) plane to be less than 10 mm, i.e. $|\delta| \leq 10\text{mm}$, and the track position at this point to be less than 30 mm in z. Vertex chambers cuts are excluded at this stage to ensure the highest track efficiency.

Photons are accepted if they have a minimum energy of 0.5 GeV and travel through the fiducial region of the Liquid Argon Barrel Calorimeter ($|\cos\theta| \leq 0.68$) or the End Cap Calorimeter ($0.74 \leq |\cos\theta| \leq 0.95$).

Events are considered to be hadronic decays if:

1. The event has at least 7 charged tracks that pass the above cuts.
2. The visible energy, composed of both charged and neutral energy, exceeds 45 GeV.
3. The polar angle of the thrust axis θ_T satisfies $|\cos\theta_T| \leq 0.8$.
4. The thrust of the event is greater than 0.7.

The minimum charged track requirement eliminates Bhabha, $\mu^+\mu^-$, and $\tau^+\tau^-$ events. The visible energy cut removes two-photon and beam gas events. Hadronic events that are poorly contained in the fiducial volume of the Mark II detector are also eliminated. The last two cuts remove a small fraction of hadronic events that do not allow the jet axis to adequately represent the true B hadron direction. Errors in the reconstructed B direction cause errors in the sign of the impact parameter for $b\bar{b}$ events, as will be discussed further in Section 4.3. Multi-jet events and two-jet events with the thrust axis at low polar angles are especially susceptible to mistakes in determining the B direction.

The Mark II collected a total integrated luminosity of 10.1±0.7 nb^{-1} at the Z^0 resonance. 208 hadronic events passed the event selection cuts, and Table 20 lists the number of events that satisfied each cut. The MC predicts that 73.9% of the hadronic events are selected. The event cuts increase the fraction of $b\bar{b}$ events in the hadronic Z^0 sample by 3%, from the Standard Model prediction of f_b=0.217 to f_b=0.224, because $b\bar{b}$ events have a slightly higher selection efficiency than do lighter quark events: ε_{uds}=73.2%, ε_c=74.4%, and ε_b=75.7%.

4.2 Track Quality Cuts

The charged tracks used in the B hadron tag and the B lifetime analysis need to be extremely well measured by the vertex detector system. They undergo a more stringent set of cuts than those imposed on charged tracks by the event selection

Table 20 Hadronic event selection cuts.

Event Cuts	Selection Efficiency from the MC	Number of Z events in Mark II data
$N_{chg} \geq 7$	0.876	232
$E_{vis} > 45$ GeV	0.800	220
$\lvert\cos\theta_T\rvert > 0.8$	0.745	210
Thrust > 0.7	0.739	208

criteria listed in the previous section. The first five cuts ensure that the track is well measured by the central drift chamber, eliminate spurious tracks not associated with the Z decay, and remove low momentum tracks that are dominated by multiple scattering and contribute very little knowledge about the B lifetime. The track cuts are:

1. There are at least 20 out of 72 possible measurements in the CDC.
2. The track must be within the angular coverage of the three tracking systems, i.e. $|\cos\theta| \leq 0.80$
3. The impact parameter is less than 5mm, i.e. $|\delta| \leq 5$ mm.
4. The distance along the z axis from the origin to the point of closest approach in the xy plane is less than 30mm, i.e. $|z| \leq 30$ mm.
5. The transverse momentum must be at least $P_{xy}\sqrt{\sin\theta} \geq 0.5$ GeV.

These tracks are referred as CDC tracks. The last cut eliminates 20% of the tracks from *udsc* events, 30% of the fragmentation tracks from $b\bar{b}$ events, but only 9% of the tracks from B decays. We examine $P_{xy}\sqrt{\sin\theta}$ rather than just P_{xy} in the fifth track cut, since the former term is the key parameter in multiple Coulomb scattering.

The next two cuts require the track to have a minimum number of hits in the vertex drift chamber and the silicon strip detector:

6. There are at least 15 out of 38 possible measurements in the DCVD.

There are at least 1 out of 3 possible measurements in the SSVD.

The Monte Carlo indicates that almost 95% of these tracks link up with the correct DCVD track segment, that is the DCVD segment finds at least 15 hits that were generated by the track, and 95% pick up at least one silicon hit generated by the track. Only 3% of the tracks that satisfy all seven cuts fail to find either the correct DCVD or SSVD hits. (Refer back to Section 2.3.7 for more details).

As an alternative to requirements 6 and 7, the track will also be used if they satisfy the cut:

6b. If the track passes through an inoperative DCVD cell, there are at least 2 out of 3 possible measurements in the SSVD.

Option 6b increases the number of available tracks because an average of one DCVD cells out of ten were inoperative, and so the hit information was either lost or unusable. At times, excessive beam backgrounds forced us to lower the anode voltage of cells drawing high currents. Occasionally, excessive backgrounds also caused loss of hit information due to memory overflows in the data acquisition system. All DCVD hits were discarded whenever the temperature or pressure of the chamber strayed out of tolerance.

Since the CDC must extrapolate the track to the silicon strip detector without the aid of the DCVD, a minimum requirement of two SSVD hits will reduce the probability of picking up spurious SSVD hits. 96% of these tracks find at least one silicon hit generated by the track. (Refer back to Section 2.4.3 for more details).

Table 21 lists the charged track multiplicity after satisfying the track requirements. Out of an average charged multiplicity of ~20 in hadronic events, 12.4 tracks per event satisfy the first five cuts. An average of 9.9 tracks per event pass all seven cuts (or cuts 1-5 and 6b). The charged multiplicity in the Monte Carlo is slightly higher because the MC generates about one track more than the multiplicity results from the LEP groups. This difference is unimportant in the B lifetime analysis since the B decay multiplicity is fine-tuned to the CLEO and ARGUS results, and any uncertainty in the number of fragmentation tracks does not affect the lifetime determination. However, the efficiency for a CDC track to pick up the minimum number of vertex hits must be in good agreement between data and Monte Carlo: 80% of the CDC tracks have the requisite number of DCVD and SSVD hits. When tracks are subdivided according to whether or not they

Table 21 Charged track multiplicity and tracking efficiency. Track are categorized according to whether they enter a good DCVD cell. An average of one jet cell per event was inoperative. The efficiency for a CDC track to find the minimum number of vertex hits is 81% (68%) for tracks that go through live (dead) DCVD cells.

	All tracks		Tracks in good DCVD cells		Tracks in bad DCVD cells	
Track Cuts	**Z data**	**MC**	**Z data**	**MC**	**Z data**	**MC**
CDC: cuts 1-5	12.4	13.2	11.2	12.1	1.27	1.02
Vertex: cuts 1-7	9.9	10.6	9.0	9.9	0.86	0.69
Efficiency of finding vtx hits	79%	81%	81%	82%	68%	68%

entered a functioning DCVD cell, the data and MC efficiencies are also in agreement. The efficiency for CDC tracks to satisfy requirement 6b is slightly lower at 68% because at least two silicon hits are needed.

4.3 The Impact Parameter (Definition)

To a good approximation, the jet axis can be used to represent the B hadron direction. The impact parameter is defined as the distance of closest approach to the primary Z^0 vertex in the xy plane. As seen in Figure 56, the sign of the impact parameter is positive if the track intersects the nearest jet axis with a positive decay length, otherwise it is negative. Equivalently, the impact parameter sign is positive if the track trajectory $\hat{P}$ and the vector $\vec{\delta}$, which connects the primary vertex to the point of closest is approach on the track, have components that are both parallel to the jet axis $\hat{P}_{jet}$, i.e. $(\hat{P} \cdot \hat{P}_{jet})\,(\vec{\delta} \cdot \hat{P}_{jet}) > 0$. The sign is negative if one component is parallel and the other is anti-parallel, i.e. $(\hat{P} \cdot \hat{P}_{jet})\,(\vec{\delta} \cdot \hat{P}_{jet}) < 0$. We use the average beam position as the primary Z^0 vertex for calculating δ, and defer its determination until Section 4.4.3.

Tracks from B decays typically have positively signed impact parameters, which are distributed roughly exponentially. A portion will have negative impact parameters due to the finite tracking resolution. Tracks from uds events and fragmentation tracks from $b\bar{b}$ events will have impact parameters distributed about the origin.

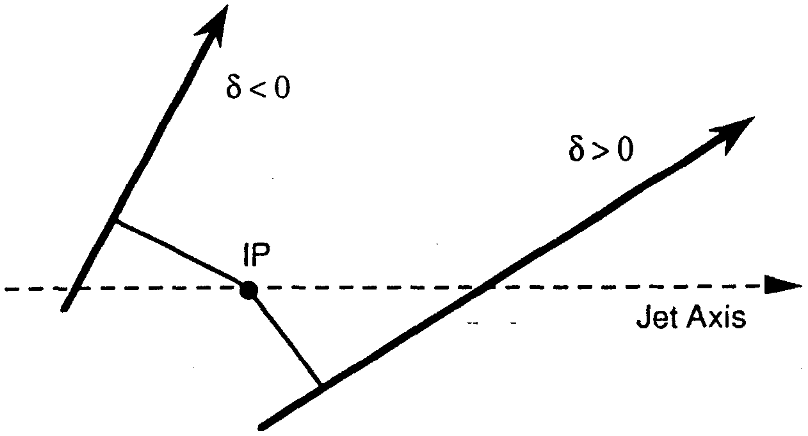

Figure 56 The track impact parameter (δ) is defined as the distance of closest approach to the interaction point (IP) in the plane perpendicular to the beam axis. The impact parameter is signed positive if the track intersects the jet axis in front of the IP; otherwise it is negatively signed.

However, even in the absence of track smearing, tracking errors, or beam motion, tracks from $b\bar{b}$ events can have negative impact parameters if they come from a decay vertex that does not lie along the jet axis. This occurs for two reasons:

- The jet axis differs from the true B hadron direction.
- K_s^0 or tertiary charm decay vertices usually do not lie along the *B* direction.

A narrow range in angle for the outgoing track will yield a negative impact parameter. Shown in Figure 57 is a decay vertex with positive decay length that is off-axis. Decay tracks in regions I and III have positive impact parameters, whereas tracks in region II have negative impact parameters. Moreover, the impact parameter jumps discontinuously from negative to positive at the boundary between regions II and III. Note that δ is zero at the interface of regions I and II.

On the whole, the jet axis does a fine job at reproducing the *B* direction, with an average deviation of only 5 degrees in the *xy* plane (Figure 58). However, large tails exist in the distribution, mainly from events with low thrust. In these events, the gluon jet overlaps with the nearest *B* jet making it difficult to reconstruct the *B* hadron direction. Viewed from the primary vertex, tertiary charm decays are on average only 2.5° off-axis from the *B* direction. These two effects cause very few tracks to be signed negative.

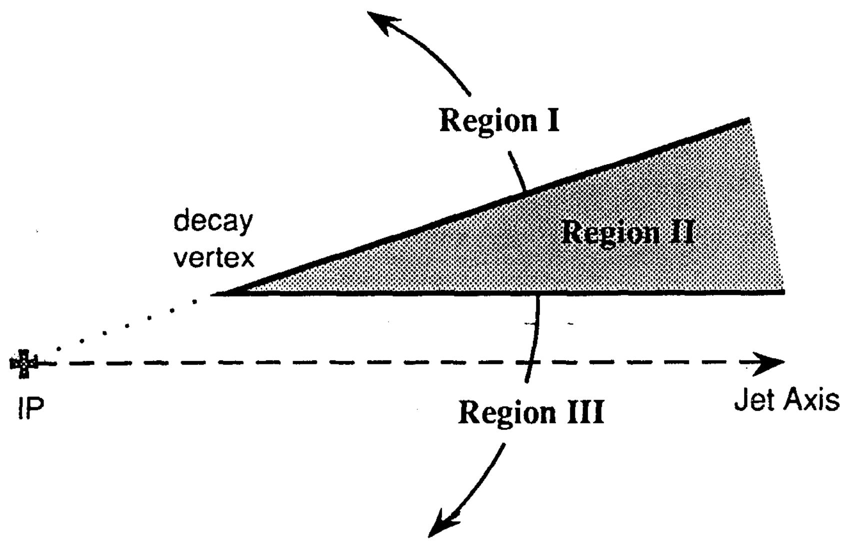

Figure 57 Tracks coming from a decay vertex that is off-axis from the jet axis can have negative impact parameters if they possess an outgoing angle in Region II (shaded). Tracks with outgoing angles in Regions I or III have positive impact parameters. Note that jet axis originates from the interaction point (IP).

The story is quite different for strange decays. K_s^0 and Λ particles differ from the B direction on average by 35 degrees, which forces approximately one-third of the decay tracks to have a negative impact parameter (Figure 59). The δ distribution is roughly exponential on both sides with decay lengths of ~1.6 mm. The bias toward positive impact parameters yields $\langle\delta\rangle = 0.43\text{mm}$. Since only tracks that pass the cuts listed in Section 4.2 are included in the distribution, the distribution width is moderated by the fact that the K_s^0 and Λ particles must decay within 3.8 cm of the collision point in order to pick up SSVD hits.

We can isolate these effects in a series of plots shown below. Figure 60 (a) is the δ distribution for tracks in $b\bar{b}$ events in the absence of track smearing, tracking errors, beam motion, and photon conversions. The true B direction is used to sign the impact parameters, and so negative values are entirely from K_s^0 decays and tertiary charm decays. Plot (b) shows what happens when we use the jet axis to approximate the B direction. Slightly more tracks now have negative impact parameters. Finally, the impact parameter distribution for the full Monte Carlo simulation is presented in plot (c) of Figure 60. The number of tracks with negative impact parameters increases steadily as the MC simulation becomes more realistic.

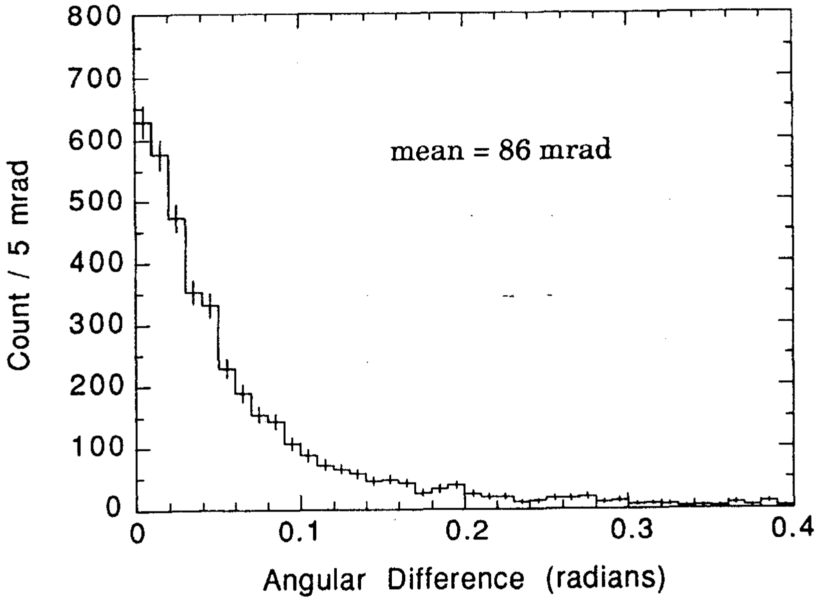

Figure 58 Angle between the nearest jet axis and the B hadron direction in the plane perpendicular to the beam axis.

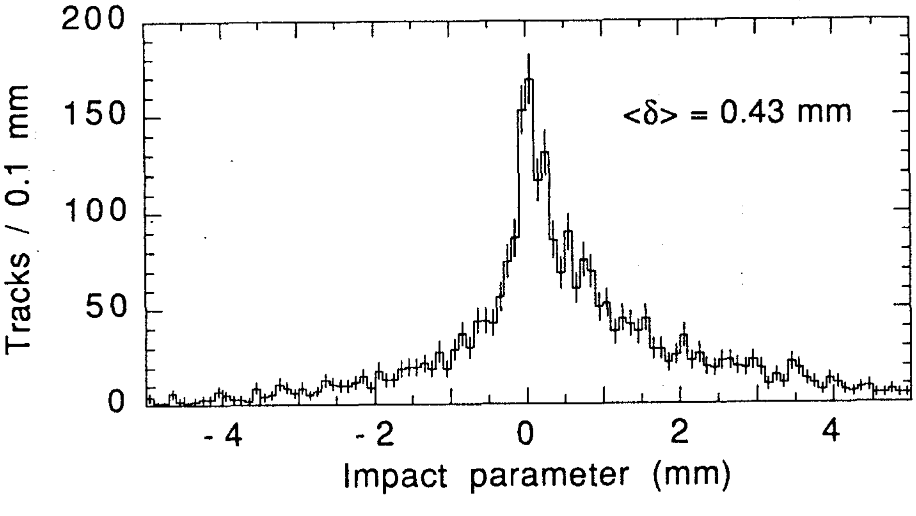

Figure 59 Impact parameter distribution for tracks that come from K_s^0, Λ, and other strange hadron decays. The tails are moderated somewhat because the tracks must pick up at least one silicon hit.

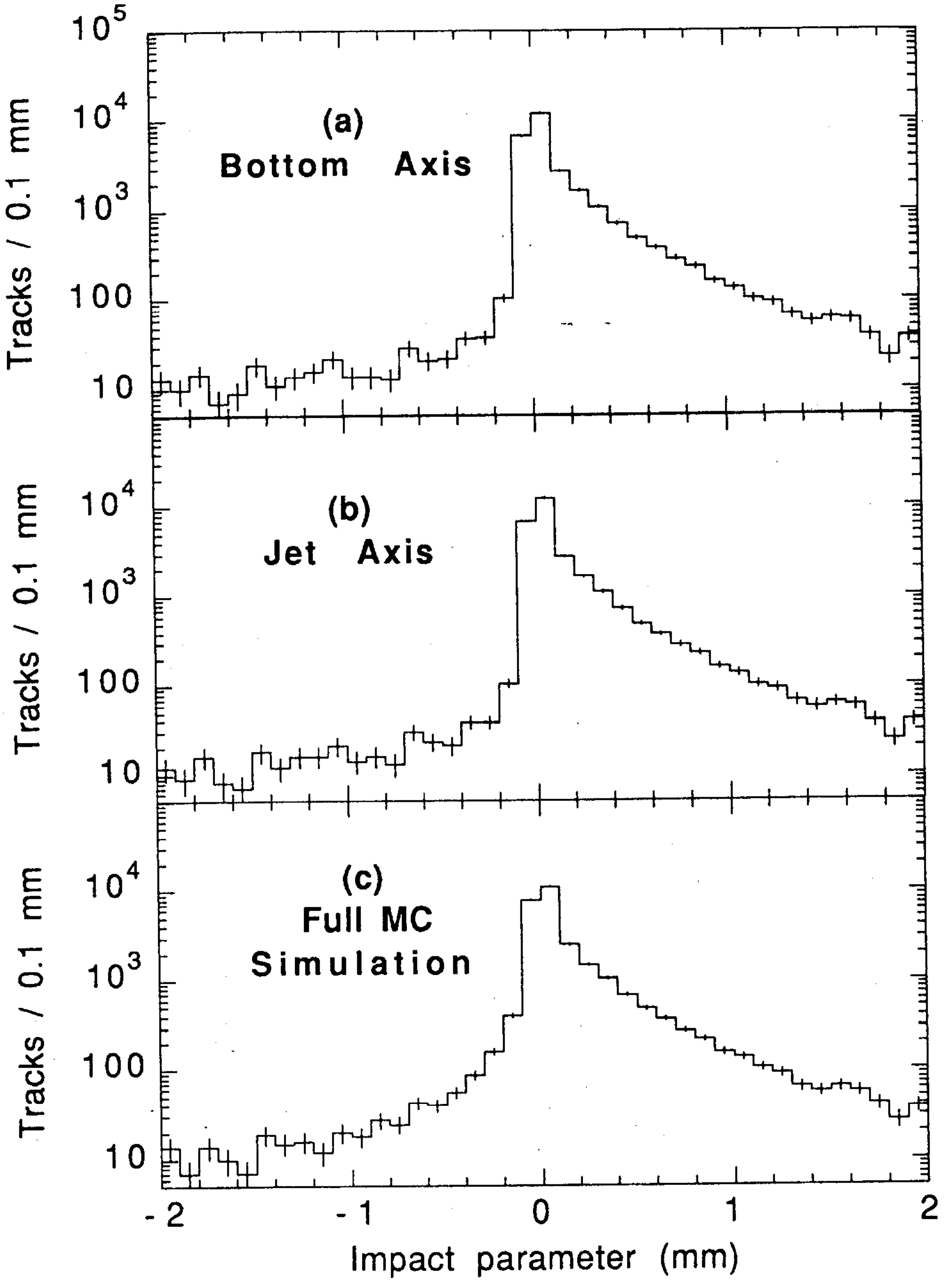

Figure 60 Impact parameter distribution for tracks from $b\bar{b}$ events in the absence of track smearing and beam motion. Tracks must have $P_{xy} \geq 0.5$ GeV and $|\cos\theta| \leq 0.8$, and must emanate from a decay vertex within 3.8 mm of the interaction region, which ensures that it traverses through at least one silicon layer. The impact parameters are signed using (a) the true B direction and (b) the reconstructed jet axis. Finally, plot (c) shows the δ distribution for the full Monte Carlo simulation, including track smearing and beam motion.

For instance, the percentage of tracks with $\delta \leq -100\mu\text{m}$ is 2.2%, 4.3%, and 8.5% in plots (a), (b), and (c), respectively.

4.4 Calculating the Impact Parameter Resolution

Unlike certain fixed target experiments such as Fermilab E653 [20] which use a 1.5 cm thick emulsion to visually observe both the B hadron production and decay vertex, collider facilities cannot instrument devices directly at the Z^0 production site. Instead, the Mark II detector must calculate the track impact parameter by extrapolating the track roughly 3 cm from the silicon strip layers to the beam axis. The error on the distance of closest approach to the Z^0 production point arises from the combination of four effects:

- Intrinsic accuracy of the track hits.
- Multiple coulomb scattering from the beampipe and detector elements.
- Uncertainty in the primary vertex location due to beam motion.
- Errors in the detector alignment.

4.4.1 Intrinsic Detector Resolution

The first effect is the contribution from the intrinsic measuring power of the three charged tracking devices. It depends on the position resolution at each of the individual layers and the overall arrangement of hits in providing a lever-arm to extrapolate the track back to the origin. The track error matrix incorporates all the hit information and included correlations between impact parameter, angular, and momentum uncertainties. Because the silicon detector has far superior spatial resolution, the component of the impact parameter resolution related to the detector performance is given approximately as

$$\sigma_0^2 = \sigma_{ss}^2 + R^2\sigma_\varphi^2 \qquad (27)$$

where σ_{ss} is the intrinsic resolution of the silicon strips (~7 μm), R is the radius of the inner-most silicon layer that measures the track, and σ_φ is the angular resolution measured primarily by the outer tracking chambers (~0.5 mrad for stiff tracks). Thus for isolated, high momentum tracks, the intrinsic tracking resolution at the chamber center is approximately 15 μm.

4.4.2 Multiple Coulomb Scattering

A charged particle emerging from within the beampipe undergoes many small-angle scatters in the material of the beampipe due to Coulomb scattering. These multiple Coulomb scatterings introduce errors in the impact parameter as the track is extrapolated from its first measurement in the SSVD back to the center of the chamber.

The amount of angular scattering is governed by a random walk in which multiple small-angle scatters displays a roughly gaussian distribution for the total angular deflection. The Molière scattering theory [76] characterizes the angular distribution as gaussian for the central 98% of the distribution, along with long non-gaussian tails due to hard elastic scatters. The width of the central gaussian depends on the particle momentum and can be expressed empirically as

$$\varphi_{ms} = \frac{0.0136\sqrt{L}}{\beta P} f(L) \tag{28}$$

where L is the material thickness in radiation lengths, P is the particle momentum, β is the particle velocity, and the function *f(L)* is defined as

$$f(L) = 1 + 0.088 \log_{10}(L) \tag{29}$$

The formula for φ_{ms} is accurate to about 11% over a range of material thicknesses of 10^{-4} to 10^3 radiation lengths.

The amount of material in the vertex tracking system is listed in Table 22. In the cylindrical coordinate system of the Mark II detector, the total material traversed by a particle is $L/\sin\theta$ where L is the thickness at normal incidence. A lever-arm of $R/\sin\theta$ is used to extrapolate the track from the scattering radius back to the origin. The effect of a single layer of material on the impact parameter resolution is thus

$$\sigma \approx \frac{R}{\sin\theta}\varphi_{ms} \approx \frac{R}{\sin\theta} \cdot \frac{0.0136\sqrt{L/\sin\theta}}{\beta P} f(L/\sin\theta) \equiv \frac{\sigma_{ms}}{P_{scat}} \tag{30}$$

where

$$P_{scat} = P_{xy}\sqrt{\sin\theta} \tag{31}$$

In this equation, if we ignore the small dependence on log(sinθ), σ_{ms} is a constant for relativistic tracks ($\beta \approx 1$).

Table 22 Location and thickness of materials inside the Central Drift Chamber. The wire monitor frames are mounted inside the vacuum beampipe and cover about 11% in azimuth.

Item	Material	Radius (mm)	Thickness (mm)	Thickness $L=X/X_0$ (%)
Wire Monitor Frame	Al	23.7	0.8	0.90
Beam pipe	Cu, Al	25.0	0.51	0.71
SSVD Inner Shell	Be	27.6	0.38	0.11
SSVD Layer 1	Si, Cu, Kapton	29.4	0.55	0.50
SSVD Layer 2		33.7	0.55	0.50
SSVD Layer 3		38.0	0.55	0.50
SSVD Outer Shell	Be	41.0	0.38	0.11
DCVD Inner Wall	—	44.0	1.76	0.85
DCVD Active Region	Cu, gas	—	—	0.72
DCVD Outer Wall	—	180.0	—	5.32

Tracks generated by the MC are scattered at every layer of material by the Mark II detector simulation. The scattering is performed according to the full Molière theory, which includes the long non-gaussian tails. The wire monitors inside the vacuum beampipe are modeled to subtend 11% of 2π in azimuth.

The track fitting programs calculate the track parameter errors exactly due to multiple scattering off the beampipe, wire monitors, silicon layers, and the inner and outer walls of all three chambers, basically by allowing kinks in the track trajectory at each of the scattering sites. The kink angle is assumed to follow a gaussian distribution of width φ_{ms} given by Eqn. (28), i.e. no non-gaussian tails are assumed in calculating the multiple scattering errors. Only the multiple scattering by the gas and wires in the two drift chamber is approximated using the Glückstern formalism. [66] Track fitting in each of the chambers is first performed assuming no scattering within the chamber volume, and the error matrix is subsequently inflated. The Glückstern method accommodates most of the correlations between measurements in a chamber due to scattering.

Multiple scattering dominates the impact parameter resolution for low momentum charged particles. Figure 61 is a plot of the inclusive δ/σ_δ distribution for all tracks with a transverse momentum $0.15\ \mathrm{GeV} \le P_{xy} \le 1.0\ \mathrm{GeV}$, at least 15 DCVD hits, and at least one SSVD hit. σ_δ is the computed impact parameter resolution from the track fit, which includes both intrinsic measurement errors and multiple scattering errors. In the absence of any hard scattering and if the Mark II detector simulation models the multiple Coulomb scattering properly, the distribution should be a unit gaussian. A gaussian fit over the range $|\delta/\sigma_\delta| \le 2$ reveals a width of 1.11±0.04 for the data and 1.10 for the MC.

We can disentangle the effects of multiple scattering from strange particle decays, heavy flavor decays, and photon conversions, by examining the distribution $\Delta\delta/\sigma_\delta$, where $\Delta\delta$ is the difference between the Monte Carlo generated impact parameter and the track reconstructed impact parameter, and σ_δ is the computed impact parameter resolution. This distribution is plotted in Figure 62 for tracks with transverse momentum $0.15\ \mathrm{GeV} \le P_{xy} \le 1.0\ \mathrm{GeV}$ that have at least 15 DCVD hits and at least one SSVD hit. The distribution has a gaussian core with a width of 1.13 when fit over the range $|\Delta\delta/\sigma_\delta| \le 3$. The tails beyond $\pm 3\sigma$ are clearly non-gaussian and contain 5.6% of the tracks. Roughly half the tracks in the tails are due to the hard scattering as described by the Molière theory and the other half are from track finding errors in which not even one silicon hit on the found track was generated by the track.

4.4.3 Beam Motion

The e^+e^- beams at the SLC were focused to a spot size of under 5 μm in both x and y, which is significantly smaller than the elliptical beams of 400 μm x 70 μm at PEP or 200 μm x 25 μm at LEP. Unfortunately the exact location of the colliding beams at the SLC with respect to the chamber axis was known to a much lesser degree of approximately 25 μm.

Information from the beam position monitors and beam steering magnets allowed any relative beam motion to be monitored and corrected. However, to determine the absolute position of the beam in relation to the Mark II detector, we had to reconstruct the primary vertex position in a hadronic Z^0 decay from the available charged tracks and average the reconstructed vertex positions over all events. Care was taken to reduce the influence of tracks from secondary B decays that could potentially pull the computed vertex away from its true location.

Only "vertex quality" tracks were used in the primary reconstruction. These tracks satisfied the same requirements listed in Section 4.2, except the transverse momentum cut was loosened to $P_{xy} \ge 0.15$ GeV. A crude estimate of the average

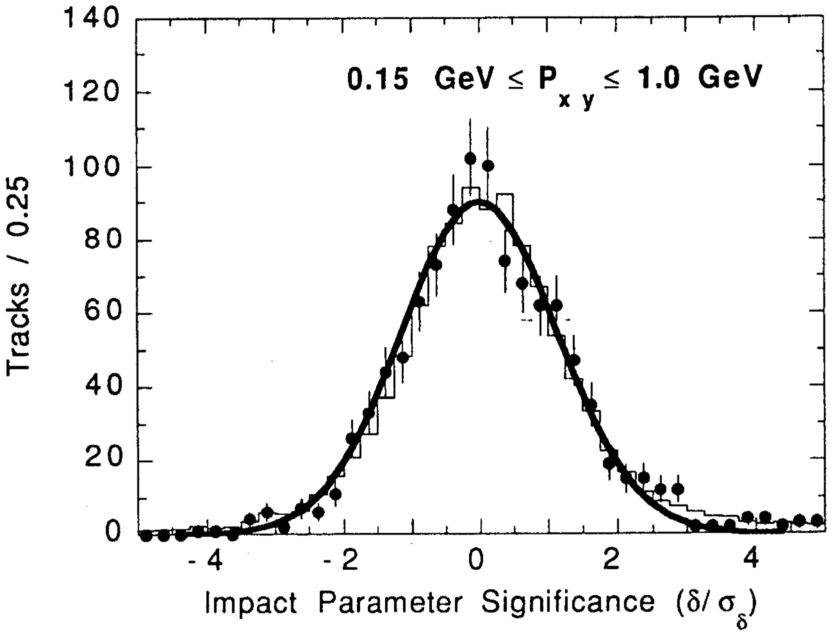

Figure 61 Distribution of δ/σ_δ for tracks with transverse momentum 0.15 GeV $\le P_{xy} \le$ 1 GeV. The data is compared with the Monte Carlo simulation (histogram). A gaussian fit to the central core of the data (thick curve) yields a width of 1.11±0.04.

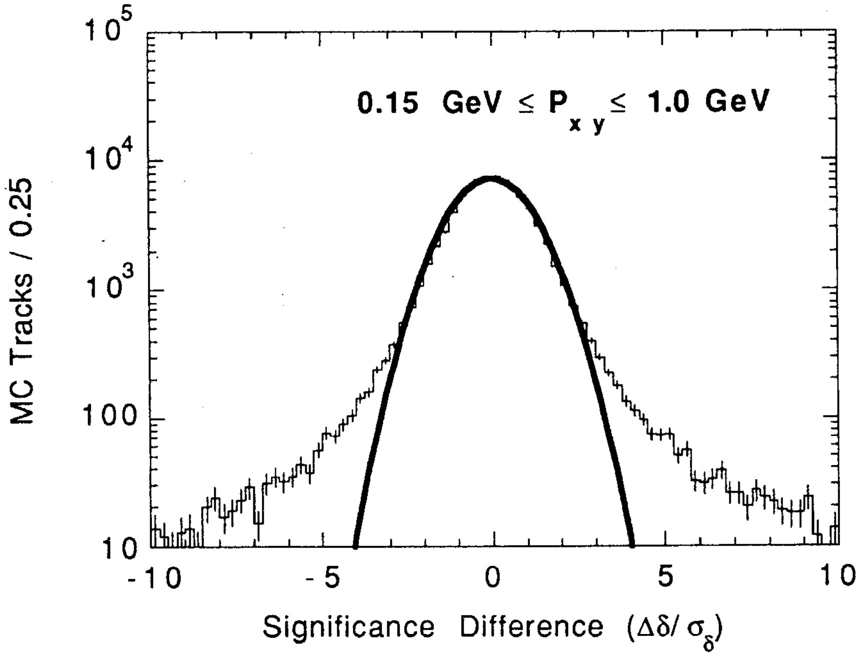

Figure 62 Distribution of $\Delta\delta/\sigma_\delta$, where $\Delta\delta$ is the difference between the MC generated impact parameter and its reconstructed value, for tracks with transverse momentum 0.15 GeV $\le P_{xy} \le$ 1 GeV. The distribution shows non-gaussian tails for $|\Delta\delta/\sigma_\delta| \ge 3$.

beam position, good to about 0.2 mm, can be determined by minimizing the impact parameter significance with respect to this average beam position, summed over all tracks in all hadronic events.

The algorithm[†] first selects the three tracks in the event closest to the average beam position and forms a vertex in the xy plane, which serves as an initial estimate of the primary vertex. Additional tracks are added to the vertex as long as the χ^2 probability for a good fit exceeds 1%. Tracks are accreted onto the vertex in a sequence that maximizes the fit probability at every stage. The vertex reconstruction is completed when no more tracks are available or if no other track can be added that will allow the fit probability to exceed 1%. Most fit vertices in the data will have an elliptical error ellipse with an aspect ratio of 5:1 which is fairly aligned with the thrust axis. The error on the major axis is typically from 30 μm to 70 μm, whereas the error on the minor axis is in the range of 5 μm to 15 μm. Thus the separation between the reconstructed primary vertex and the average beam position along the direction of the minor axis will have a distribution (Y_T) whose width will be sensitive to any apparent beam motion. The separation along the major axis will have a distribution whose shape is dominated by the major axis error.

An event has an acceptable reconstructed primary vertex if in addition to passing the hadronic selection cuts outlined in Section 4.1:

1. At least 7 vertex quality tracks are used in the primary vertex fit.
2. At least 70% of all vertex quality tracks are used in the vertex fit.
3. The minor axis of the fit vertex error ellipse be $\sigma_{YT} < 20$ μm.

The last two requirements are designed to reject $b\bar{b}$ events and events with a poorly measured vertex. $b\bar{b}$ events will typically have a high percentage of tracks that are inconsistent with the reconstructed primary vertex. Vertices with large errors in the minor axis are undesirable since the Y_T distribution will be excessively smeared by the poor fits. About 60% of hadronic events have an acceptably reconstructed primary vertex, of which only 10% are $b\bar{b}$ events. The average beam position is computed from the average position of these vertices. This procedure is repeated using the new value for the average beam position, and the position converges after a couple of iterations.

[†] The primary vertex finding algorithm was developed by Steve Wagner.

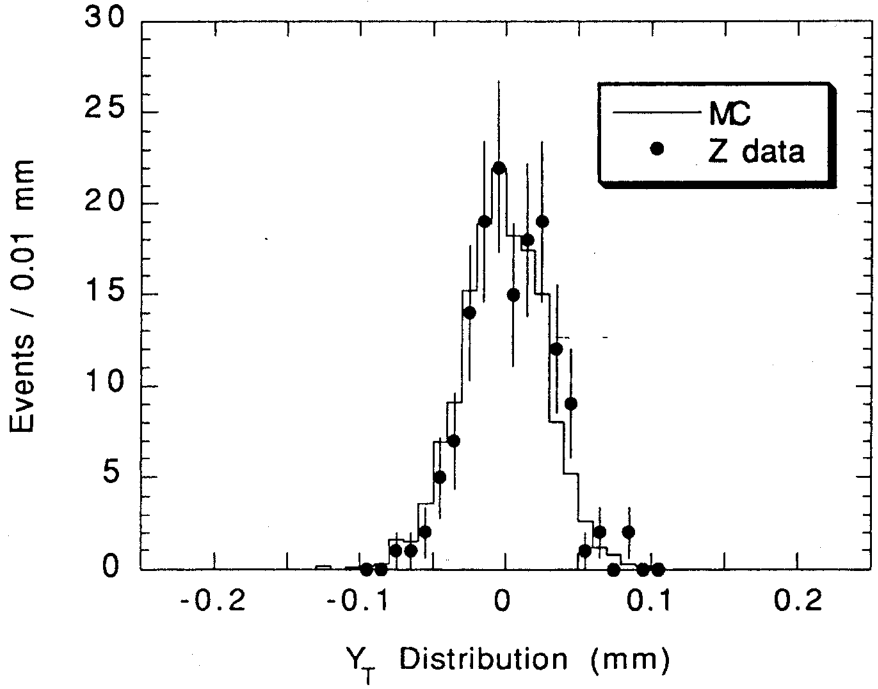

Figure 63 Distribution of the variable Y_T for 149 hadronic events. Y_T is defined as the distance between the reconstructed primary vertex and the average beam position along the direction of the minor axis of the primary. The distribution width is consistent with a beam motion of 25 μm.

A total of 149 hadronic events had reconstructed primary vertices that were acceptable. The hadronic data was divided into six blocks due to occasional gross changes in the beam optics. An average beam position was computed for each block, and this value was used to compute track impact parameters for all events in the block. The Y_T distribution for the 149 reconstructed primary vertices is shown in Figure 63. The scatter of reconstructed vertices about the mean beam position represents contributions from beam motion, uncertainties in the steering magnet corrections, and uncertainties in the fit vertex position. The Y_T distribution in the data has a standard deviation of 29 μm and is without non-gaussian tails. The MC shows that in the absence of beam motion, the Y_T distribution has a width of 18 μm. Hence, the hadronic data is consistent with a beam motion of roughly 25±5 μm in both x and y. This motion is a combination of actual beam motion and errors in the beam position monitors and steering magnet corrections. However, the exact breakdown is not important.

4.4.4 Silicon Alignment

The silicon strip vertex detector achieves a local spatial resolution of 7.1 μm, allowing a precise measurement of the impact parameter only if the location of each silicon module in their support structure is known to high precision. The SSVD is anchored to the beam pipe and can therefore experience relative motion with respect to the DCVD. Hence, any motion of the silicon detector relative to the rest of the tracking system must be monitored accurately. Much care was taken to align the 36 silicon modules in the SSVD. These include[58]

- Optical alignment of the silicon modules during assembly into their cylindrical support structure.
- X-ray alignment of the SSVD system before installation into the Mark II detector. The X-ray surveying was reproducible but had small discrepancies with the optical alignment, possibly due to shifts or distortions of the detector during assembly.
- A capacitive displacement measurement (CDM) system to monitor displacements of the SSVD with respect to the outer tracking chambers. Capacitive sensors placed outside the silicon detector observed a 20 μm diurnal motion of the beam pipe, but saw no evidence for rotational or longitudinal motion.
- Global and local alignment of the SSVD after installation into the Mark II detector using tracks from hadronic Z events.

We had originally hoped that the information from the X-ray alignment along with a global alignment of the SSVD mechanical support structure would be sufficient to describe the orientation of the 36 individual silicon modules. However, it soon became clear that after installation into the Mark II detector, the silicon modules had shifted around in their mechanical support and needed to be locally realigned.

The global alignment for each half-cylinder of the SSVD support structure is defined by three rotation angles and two translation offsets, x and y. Since the strips are parallel to the beam axis, the SSVD is fairly insensitive to uncertainties in z. The orientation of each silicon module relative to its nominal setting can be described by seven parameters: two linear offsets, Δx and Δy, three angles, α_x, α_y, and α_z, and two shape parameters, twist and bow (see Figure 64). Of the seven parameters, track measurements are most sensitive to a transverse displacement, Δx, a radial displacement, Δy, and a yaw angle, α_y.

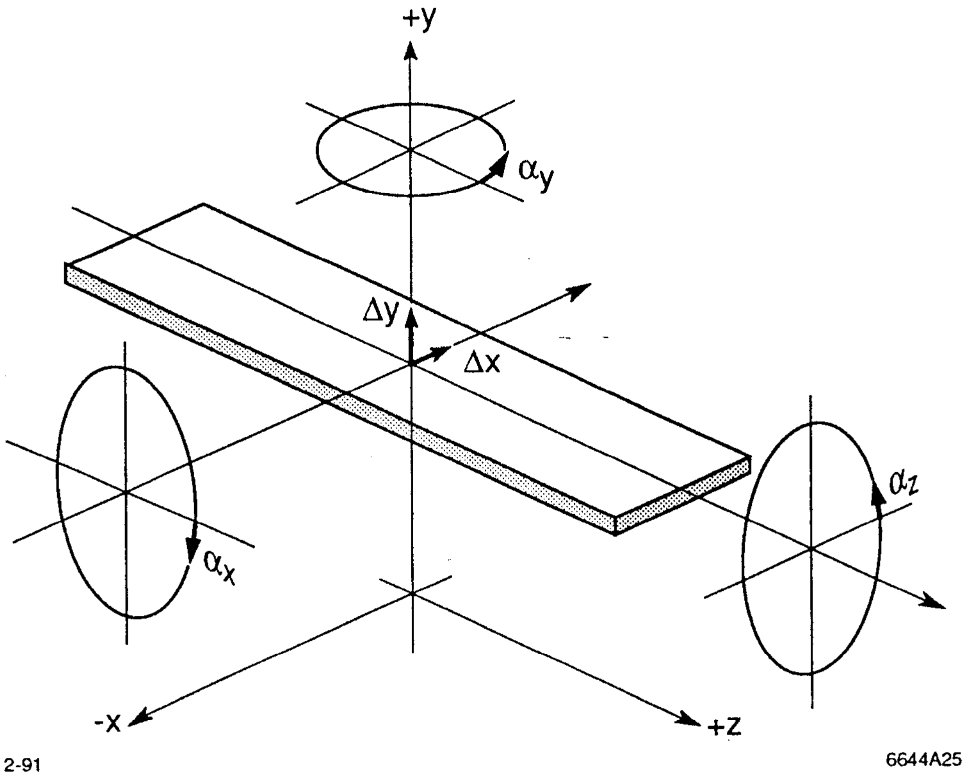

Figure 64 Coordinate system for a silicon strip module and the displacement parameters (Δx, Δy, Δz, α_x, α_y, and α_z) relative to its nominal position.

Ordinarily we would like to use muon pairs and wide angle Bhabhas to align the silicon strip detector since these tracks originate from a single vertex, are colinear, and undergo a negligible amount of multiple scattering. However, only 20 such events were collected by the Mark II. The DCVD used high momentum cosmic ray tracks to verify the alignment of the anode plane in each of the ten jet cells and to determine the orientation of the vertex drift chamber with respect to the main drift chamber. Unfortunately, this technique was also not available for the silicon strip detector because the SSVD electronics were unable collect cosmics. The microplex electronics were only able to be live at the 120 hz rate necessary to take colliding beam data. Global and local SSVD alignments were achieved using tracks from hadronic events. Approximately 2100 tracks were used which had at least two hits in the SSVD and a transverse momentum greater than 0.5 GeV.

Global and local alignment constants are derived from a χ^2 fit that minimizes the differences between the positions and angles of tracks extrapolated to the SSVD from the outer drift chambers and the values as measured by the SSVD. We can define position and angular differences for tracks with two silicon hits in layers j and k as

$$\Delta b_{jk} \equiv (\xi_j + \xi_k)/2 \quad \text{and} \quad \Delta\phi_{jk} \equiv (\xi_j - \xi_k)/\Delta r_{jk}, \tag{32}$$

where ξ is the distance between the silicon hit and the extrapolation of the track at that layer, and Δr_{jk} is the radial separation between the two layers. Tracks with hits in all three silicon layers have three independent measures of the alignment:

$$\Delta b_{123} \equiv (\xi_1 + \xi_2 + \xi_3)/3, \quad \Delta\phi_{123} \equiv (\xi_1 - \xi_3)/\Delta r_{13}, \quad \text{and} \quad \Delta\delta \equiv (\xi_1 - 2\xi_2 + \xi_3)/2, \tag{33}$$

where $\Delta\delta$ describes the intrinsic spatial resolution.

The χ^2 is the sum of squares of all the Δb, $\Delta\phi$, and $\Delta\delta$, weighted by their errors. It is equivalent to $\chi^2 = \sum \xi^2/\sigma^2$, but is rewritten in terms of Δb, $\Delta\phi$, and $\Delta\delta$ in order to be more illustrative. Global and local alignment constants are fit separately. The procedure is iterated several times before the alignment constants converge. The alignment uncertainties for the local parameters are $\Delta x \approx 5\,\mu\text{m}$, $\Delta y \approx 25\,\mu\text{m}$, and $\alpha_y \approx 0.1$ mrad. There were significant changes in the orientation of the modules since the previous X-ray alignments, with rms deviations of 13 μm, 78 μm, and 0.12 mrad, respectively. Figure 65 shows the local alignment shifts for all 36 silicon modules. The global and local alignments were used to correct the orientation of the silicon modules, while the optical and X-ray measurements were used only as checks.

Due to space constraints, the SSVD was constructed without any overlap between adjacent modules in the same layer. Overlaps would have allowed a small fraction of tracks to pass through adjacent silicon modules, thereby defining their orientation in that layer. Neighboring modules in the SSVD, on the other hand, are only weakly linked together through the module above or below, which makes the SSVD more susceptible to certain "breathing" distortions of the detector that the local alignments are relatively insensitive to. Antipodal misalignments are best discerned using back-to-back e^+e^- or $\mu^+\mu^-$ events.

Even though tracks from B decays are used in the silicon alignment, the impact parameter distribution will remain unbiased for both B and non-B tracks since the alignments are performed without constraining the tracks to come from a single vertex. However, residual uncertainties in the silicon alignment from limited track statistics will introduce errors in the impact parameter resolution at the level of 15 μm. The Monte Carlo assumes perfect alignment of the SSVD, and so realigning the detector with a track sample equal in size with the data will introduce residual misalignments into the MC that are comparable to the data.

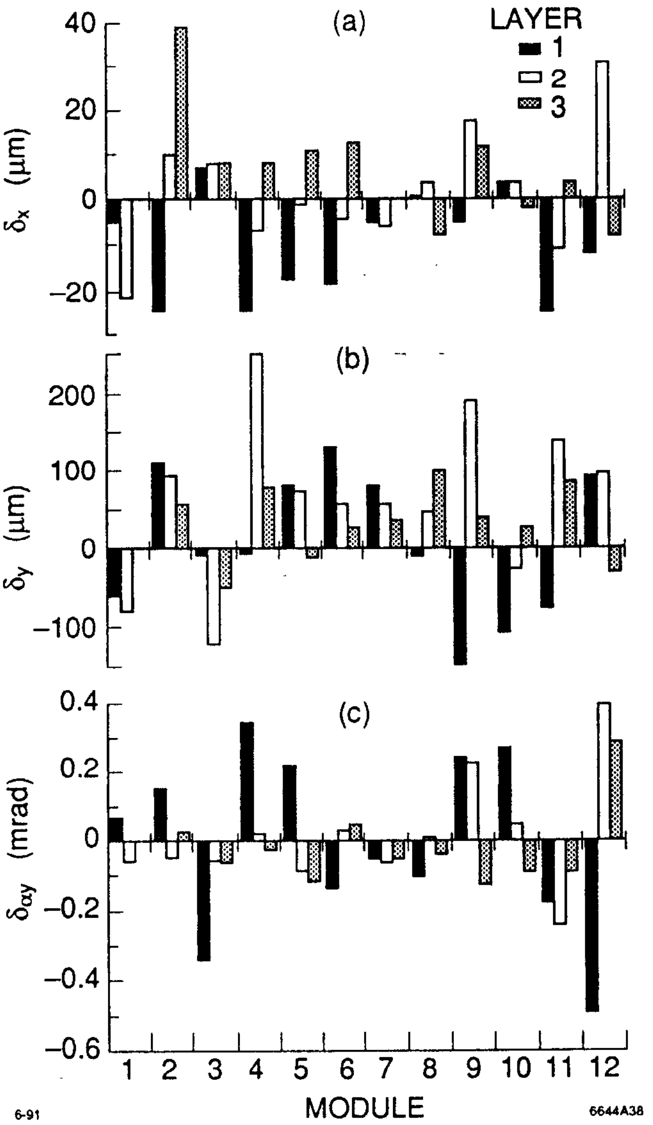

Figure 65 Shifts in the local alignments of the individual silicon modules measured with hadronic tracks relative to those obtained from the X-ray survey. The dominant sensitivities are in (a) the transverse offset, δx, (b) the radial offset, δy, and (c) the angular offset, $\delta\alpha_y$.

4.4.5 Total Impact Parameter Resolution.

The impact parameter has an error that is the sum in quadrature of contributions due to the intrinsic detector resolution, multiple Coulomb scattering, beam motion, and residual uncertainties in the silicon alignment. The total calculated resolution is

$$\sigma_\delta^2 = \sigma_{trk}^2 + \sigma_{beam}^2 + \sigma_{align}^2 \tag{34}$$

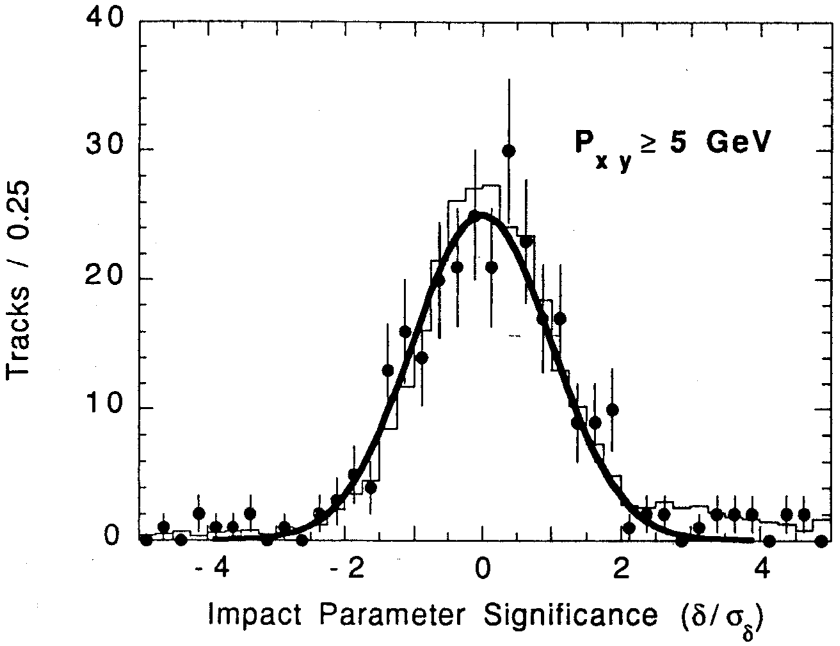

Figure 66 Distribution of δ/σ_δ for tracks with transverse momentum $P_{xy} \geq 5$ GeV. The data is compared with the Monte Carlo simulation (histogram). A gaussian fit to the central core of the data (thick curve) yields a width of 1.07±0.06.

where σ_{trk} is the calculated uncertainty from the error matrix in the track fit that includes both detector measurement errors and multiple scattering, $\sigma_{beam} \equiv 25\ \mu m$ is due to beam motion, and $\sigma_{align} \equiv 15\ \mu m$ is the extra smearing needed to ensure that the core of the δ/σ distribution is a unit gaussian for high momentum tracks.

Figure 66 shows the δ/σ distribution for charged tracks with transverse momentum greater than 5 GeV. The impact parameter resolution for these tracks is dominated by uncertainties in both the intrinsic spatial measurements and the detector alignments. A fit to the central core of the distribution in the data, $|\delta/\sigma| \leq 2$, reveals a gaussian width of 1.07±0.06 with $\sigma_{align} \equiv 15\ \mu m$ and 1.46±0.18 without the extra smearing. For comparison, the same gaussian fits to MC events are 0.94 and 1.21, respectively.

To a good approximation, σ_δ can be written as

$$\sigma_\delta^2 \approx \sigma_0^2 + \frac{\sigma_{ms}^2}{P_{scat}^2} \tag{35}$$

where σ_0 includes the contributions from intrinsic measurement errors, σ_{beam}, and σ_{align}; σ_{ms} describes the multiple scattering error; and $P_{scat} \equiv P_{xy}\sqrt{\sin\theta}$. The

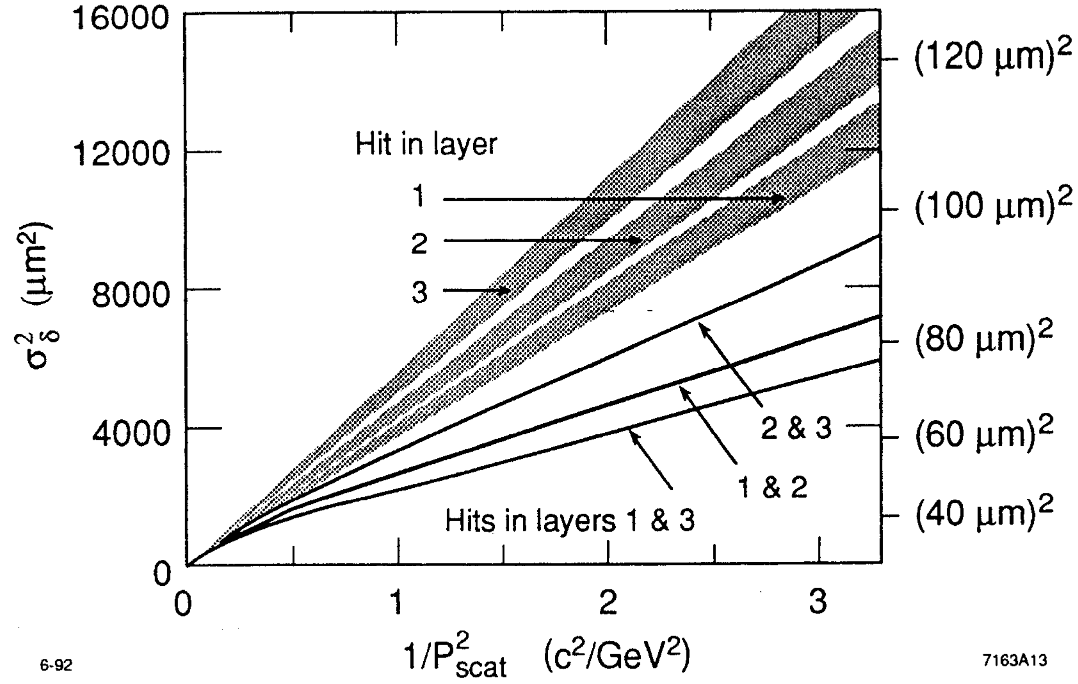

Figure 67 Calculated impact parameter resolution of the combined tracking system as a function of P_{scat}. The labels indicate the SSVD layers that contributed to the track fit.

parameters σ_0 and σ_{ms} depend strongly on the precise arrangement of measured hits on the track.

The calculated impact parameter error is most sensitive to which layers in the SSVD have measured hits on the track. For tracks with only one SSVD measurement, σ_δ^2 is linearly proportional to P_{scat}^{-2}, where the proportionality constant relates the amount of multiple scattering that occurs before the first silicon measurement (see Figure 67). The slope is greater if the single SSVD hit occurs in layer 3 as opposed to layer 1 because the track is extrapolated a greater distance and goes through more material from the measured hit to the origin. The calculated resolutions form broad swaths at low momentum due to the range in the calculated azimuthal error σ_φ, which can vary significantly depending on the number of measurements in the outer tracking chambers.

Tracks with two or three silicon hits have a calculated impact parameter resolution that behaves quite differently. The most striking feature is the kink in plot of σ_δ^2 at a momentum $P_{scat}{\approx}2$ GeV. At high momenta, the resolution depends mainly on the innermost measured silicon layer and is only marginally different from tracks that have a single SSVD hit. The track angle is measured quite adequately by the outer chambers. But at low momenta, the track experiences so much multiple scattering in the outer SSVD wall and inner DCVD wall that the angular information from the outer drift chambers becomes effectively decoupled from the impact parameter calculation. With a maximum lever-arm of 9 mm, the SSVD can provide at best a 1 mrad angular resolution which is in quadrature with the angular uncertainty from multiple scattering in the beampipe. Yet, this amount is better than the angular information from the long lever-arm of the CDC/DCVD track segment for tracks with $P_{scat} \leq 2$ GeV. Obviously, no φ information is provided by the SSVD if the track has only one silicon hit. Hence, tracks with $P_{scat} \leq 2$ GeV that have more than one silicon hit possess a much smaller resolution σ_δ. Finally, tracks with hits in layers 1 and 3 have the best resolution since they possess a better lever-arm and/or pass through less material than tracks with SSVD measurements in layers 1 and 2 or in layers 2 and 3. The track momentum is still measured most effectively by the outer drift chambers.

Averaged over all quality tracks, the impact parameter resolution presented in Figure 68 is roughly

$$\sigma_\delta^2 \approx (29 \pm 3\mu\mathrm{m})^2 + \frac{(70 \pm 4\mu\mathrm{m})^2}{P_{scat}^2} \tag{36}$$

Thus tracks with high momentum have a resolution approaching 29μm. Tracks under 2 GeV in momentum are dominated by multiple scattering, with for example a 75μm resolution for a 1 GeV particle. Approximately half the tracks in hadronic events are multiple scattering dominated, and so multiple silicon measurements are crucial in reducing the impact parameter errors.

The data points in the plot are the rms of the impact parameter distribution for $\delta<0$ tracks taken about an assumed mean of zero. These tracks should be a good indicator of the tracking resolution since there is little contribution from charm and bottom hadrons, which populate the $\delta>0$ region.

Without SSVD information the impact parameter resolution would degrade to roughly $\sigma_\delta \approx 45\mu\mathrm{m} \oplus 110\mu\mathrm{m}/P_{scat}$. The multiple scattering term is large because the track still gets scattered in the silicon modules.

4.5 Verifying the Impact Parameter Resolution

In the last section, we defined the calculated impact parameter resolution σ_δ in Eqn. (34), decomposed σ_δ into its main components, demonstrated that the central core of the δ/σ_δ distribution is roughly a unit gaussian, and showed that the Monte

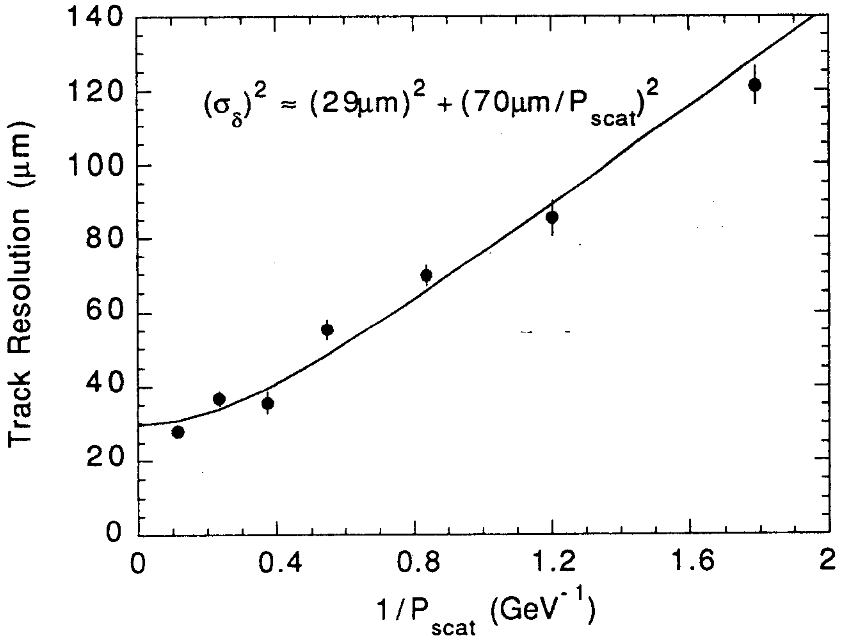

Figure 68 Impact parameter resolution as a function of P_{scat}, averaged over all quality tracks.

Carlo modeled the core of the resolution function quite well. However, this is only half the battle. We must still understand the tails of the tracking resolution function and prove that the Monte Carlo adequately models the Mark II data. Aside from lifetime tracks from bottom and charm decays, tails in the inclusive impact parameter distribution can arise from pattern recognition errors in track finding. Non-gaussian tails can also originate from physical causes such as K_s^0 and other strange decays, hard scatters at large angles, photon conversions, and decays of $\pi^\pm$ and $K^\pm$ particles. In the remainder of the chapter, we will focus on these issues.

An understanding of the tails in the resolution function will allow us to predict the purity of $b\bar{b}$ events in an enriched sample after applying an impact parameter tag. Tails in the resolution function and tracks from charm decays are the principle contributors to a fake B signal. Accurately predicting the purity is particularly important with our small data size since we do not have the statistics to independently fit for purity. Also the shape of the MC impact parameter distribution, which we rely on to extract the B lifetime, will not be correct if the resolution function is wrong.

Ordinarily we would test Eqn. (34) by using tracks from wide angle Bhabha, $\mu^+\mu^-$, two-photon, and cosmics ray events. These events provide pairs of isolated tracks that are colinear in the xy plane. In addition, all these tracks except for cosmics come from the primary vertex.

A supply of e^+e^- and $\mu^+\mu^-$ events will provide us with the impact parameter resolution for isolated high momentum tracks. These events offer an alternate method of finding the interaction point that is free from both multiple scattering errors and biases from tracks that come from secondary vertices in bottom and charm events. Beam motion can be isolated by comparing the miss distance resolution with the impact parameter resolution. Also since these tracks undergo almost no multiple scattering, they are useful in aligning the silicon vertex detector.

Two-photon and cosmic rays events are dominated by low momentum tracks and can yield information on the multiple scattering term of the resolution. The resolution for hadronic tracks will be slightly worse due to the density of tracks in hadronic jets.

Unfortunately, with a total integrated luminosity of 10.1 nb^{-1}, the Mark II detector collected only 18 e^+e^- and $\mu^+\mu^-$ events and a comparable number of two-photon events. Furthermore, the SSVD could not measure cosmics due to the limitations of its electronics. Thus the prescription for verifying the tracking resolution that worked so well at LEP, PEP, and PETRA can only provide an indication that we understand our tracking system. Also none of these studies shed any light on the tails of the resolution function due to tracking difficulties in the core of hadronic jets.

4.5.1 e^+e^- and $\mu^+\mu^-$ Events

From the sample of 18 e^+e^- and $\mu^+\mu^-$ events, 27 tracks passed all the track quality cuts. The impact parameter distribution with respect to the average beam position has a width of $\sigma_{rms}=24\pm5$ μm (see Figure 69), which is consistent with expectations. In twelve events both tracks had SSVD hits. The miss distance between the two tracks is insensitive to beam motion and its distribution suggests that the impact parameter resolution in the absence of beam motion is $\sigma_{rms}=15\pm4$ μm. The acoplanarity of these twelve events yields an angular resolution of $\sigma_\varphi=0.33\pm0.10$ mrad for isolated high momentum tracks.

4.5.2 Negative Impact Parameter Distribution

In spite of the limited Z^0 sample, we can effectively use the inclusive impact parameter distribution from all hadronic events to understand the tracking resolution function. Shown in Figure 70, the inclusive δ distribution includes all

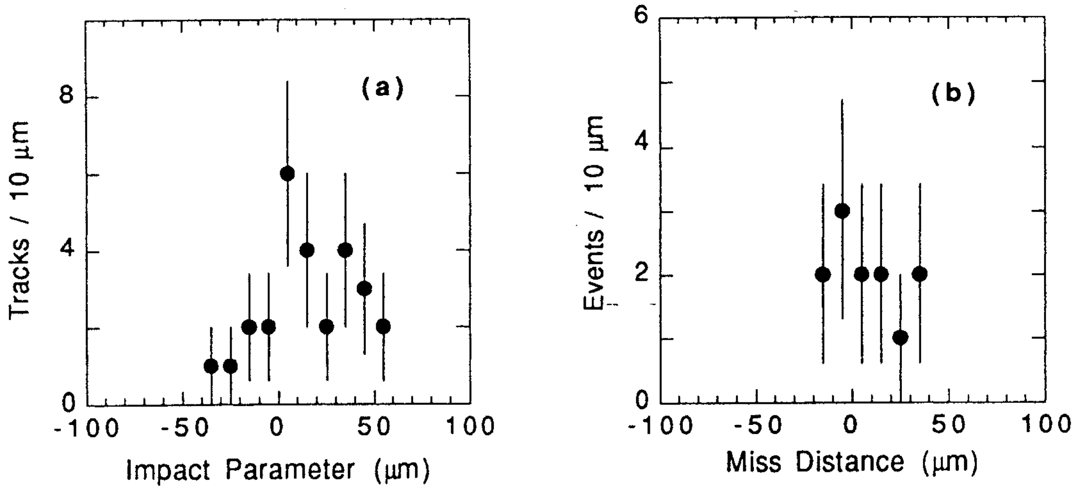

Figure 69 (a) The impact parameter distribution for tracks from wide angle Bhabhas and $\mu^+\mu^-$ events yields a standard deviation of 24±5 μm. (b) The miss distance has a standard deviation of 21±6 μm.

tracks that pass the standard cuts listed in Section 4.2. The distribution is highly asymmetric about the origin with a positive mean of $\langle\delta\rangle = 53 \pm 8\mu\text{m}$. The abundance of tracks that populate the $\delta>0$ region provide information on the bottom quark lifetime. Roughly 15% of the tracks from B decays have an impact parameter greater than 0.5 mm. As Table 23 illustrates, these B decay tracks constitute over half the tracks with $\delta\geq0.5$ mm. In decreasing order of importance, the rest of the large impact parameter tracks come from strange decays, tracking errors in which all the silicon measurements are accidental background hits, tails in the multiple scattering, and charm hadrons.

On the other hand, the negative tail of the δ distribution contains very few tracks from bottom or charm hadrons and provides vital information on the tracking resolution function. The central core of the inclusive δ distribution is composed primarily of tracks from the primary vertex. The shape of the core for $\delta<0$ is roughly a superposition of gaussians, since the calculated track resolutions span in range from 30 μm to 150 μm. Beyond −250 μm, the δ distribution loses its gaussian shape and assumes an exponential decay profile. Roughly 1.02±0.22% of the tracks in the hadronic data fall in the range $\delta \leq -0.5\text{mm}$. The Monte Carlo expects 0.8%, and Table 24 lists the major sources.

Over 50% of negative exponential tail is from strange decays: K_s^0, Λ, Σ, and Ξ particles, of which the majority are K_s^0. The MC generates K^0 mesons at a rate consistent with the OPAL measurement of 2.10±0.02±0.14 K^0 per hadronic

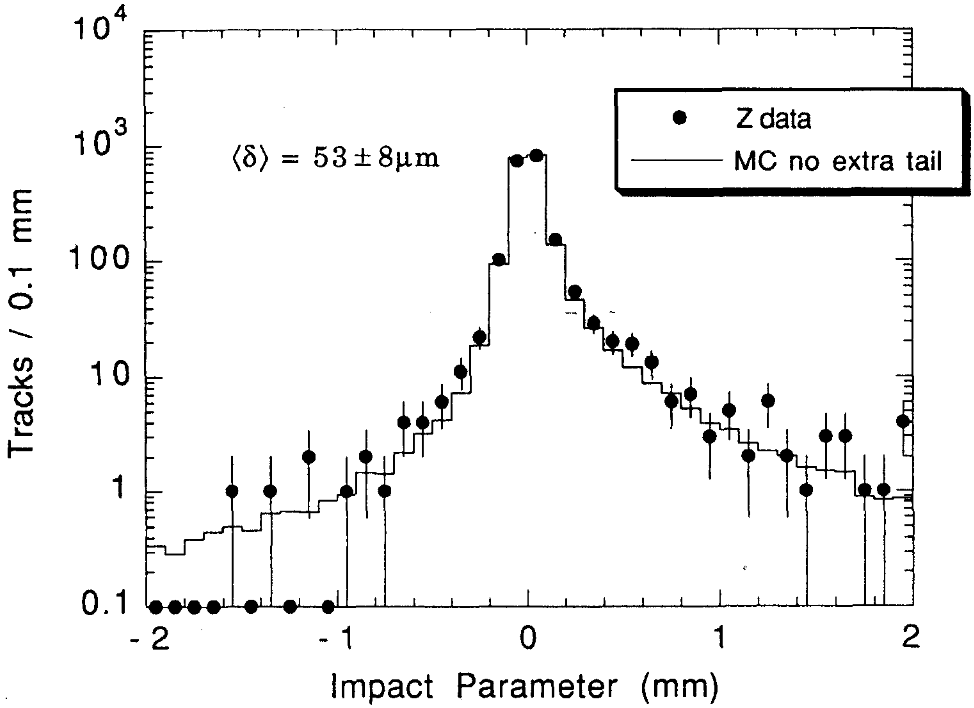

Figure 70 The impact parameter distribution for all hadronic tracks that pass the standard cuts listed in Section 4.2.

event. [55] These tracks come from decays vertices that must occur within the first three cm of the interaction point since the Monte Carlo indicates that the daughter tracks pick up the correct SSVD information, i.e. no spurious SSVD hits. We have not tried to reconstruct K_s^0 particles from the available tracks; however, the tracks with $\delta \leq -0.5\text{mm}$ possess a softer momentum spectrum as can be expected from K_s^0 decays: $\langle P_{xy} \rangle$=1.3±0.1 GeV for tracks with $\delta \leq -0.5\text{mm}$ in the data, as compared to $\langle P_{xy} \rangle$=3.0±0.1 GeV overall. The Monte Carlo expects 1.6 GeV and 3.0 GeV, respectively. The impact parameter distribution from strange decays is highly asymmetric. Referring back to Figure 59 on page 100, approximately two-thirds of the strange decay tracks have positive impact parameters. Both sides fall off somewhat exponentially, with a net distribution mean of $\langle \delta \rangle = 0.43\text{mm}$.

Tracks coming from the primary vertex can also have impact parameters that are computed to be grossly negative. Both tracking errors in which all the silicon hits are fake hits and non-gaussian tails in the multiple Coulomb scattering à la Molière will generate substantial errors in the measured impact parameters. These two sources make up 33% of the tracks with $\delta \leq -0.5\text{mm}$. Multiple scattering and mistakes in the track finding algorithms both generate symmetric errors in the

Table 23 Origin of the tracks with $\delta \geq 0.50$ mm, which comprise 4.24±0.14% of all tracks in the data and 3.23% in the MC. The total fraction with very positive δ is highly sensitive to the B lifetime.

Origin of Track	%
Trks from B hadrons	55
K_s^0, Λ, Σ, Ξ particles	24
Mistracking	8.1
Multiple scattering	6.2
Trks from charm hadrons	4.4
γ conversions, K/π decays, bremsstrahlung	2.1

Table 24 Origin of the tracks with $\delta \leq -0.5$ mm, which comprise 1.02±0.22% of all tracks in the data and 0.79% in the MC. The fraction of tracks with very negative δ is relatively insensitive to B hadrons.

Origin of Track	%
K_s^0, Λ, Σ, Ξ particles	51
Mistracking	20
Multiple scattering	13
Trks from B hadrons	9
Conversions: $\gamma \to ee$	3.3
Decays: $K^{\pm},\pi^{\pm} \to \mu$	1.7
Trks from charm hadrons	1.7
Bremsstrahlung	>1

computed impact parameter. If we consider only the MC tracks generated at the primary vertex that pass all the track cuts, 5% of these tracks have $|\delta| \geq 0.2\text{mm}$, whereas 44% of the tracks which fail to pick up even one correct silicon hit have $|\delta| \geq 0.2\text{mm}$. In both cases, the means of the distributions are zero, and the size of the positive and the negative tails are roughly equal.

B hadron decays account for only 9% of the tracks with $\delta \leq -0.5\text{mm}$. These tracks would still miss the primary vertex by more than 0.5 mm even in the absence of detector smearing, but they have a negative impact parameter because they come from a decay vertex that is off-axis from the nearest jet axis. Either the jet direction differs from the true B direction or the track comes from a tertiary charm decay. Since the decay vertices are only slightly off-axis compared with K_s^0 decay vertices (see page 98), only a small fraction of B decay tracks have very negative impact parameters.

Finally, photon conversions, decays of charged kaons and pions, decays of charm hadrons, and bremsstrahlung contribute to the remaining few percent of the far negative tails of the impact parameter distribution.

4.5.3 Extra Tail Smearing

Earlier in the chapter, we showed that the central core of the impact parameter distribution is described well by the Monte Carlo. The core of the inclusive δ/σ_δ distribution, where σ_δ is the calculated impact parameter resolution defined in Eqn. (34) on page 112, has a gaussian width of nearly unity for all track momenta. More importantly, the data and Monte Carlo concur.

The tails of the resolution function are more difficult to model because they come from so many sources. Some are detector related such as hard scatters at large angles, pattern recognition errors in track finding, and photon conversions at the beampipe. Others are actually physics related that nevertheless generate tails in the inclusive δ distribution, such as from strange decays. Of course, the lifetime tracks from B's populate the positive tail of the inclusive δ distribution. Occasional sign errors when the decay vertex is off-axis from the jet direction generate a small negative tail.

By measuring the negative δ tail, we can place limits on the extent of the positive δ tail not caused by the B lifetime. In general, unless we model every uncertainty and defect in the tracking system, the Monte Carlo will tend to underestimate the actual track resolution. We will assume that any discrepancy in the negative δ tail between data and MC is due to additional degradation of the impact parameters for a small fraction of tracks by a symmetric function. Although certainly true if the disparity is due to uncertainties in the level of mistracking or multiple scattering, the assumption is false if the difference is actually due to the frequency of K_s^0 decays. We cannot predict the source and hence cannot predict the degree of asymmetry from any additionally required track smearing. Instead, we will address this problem in the discussion of systematics in Section 6.9.1.

The inclusive impact parameter distribution is simulated fairly well by the Monte Carlo in the region $\delta<0$ (see Figure 70). The data shows a slight excess of tracks with extremely negative impact parameters, $\delta \le -0.50\mathrm{mm}$: 1.02±0.22% for hadronic tracks and 0.79% for MC tracks. The excess is a little worse when we expand the region to $\delta \le -0.25\mathrm{mm}$: 2.24±0.33% for data tracks and 1.71% for MC tracks. The tracks in the non-gaussian tails are divided roughly equally among charge. If we subdivide the distribution into five bins bounded by –5.0 mm, –0.5 mm, –0.3 mm, –0.2 mm, –0.1 mm, and 0 mm, the χ^2 fit between data and Monte Carlo is decent: 7.8 for 5 degrees of freedom.

The amount of extra symmetric smearing that best reproduced the inclusive δ distribution in the range $-5<\delta<0$ mm was determined by a binned maximum log likelihood fit with 0.1 mm bins. The binned log likelihood is defined as

$$L = -\sum_i n_i \log M_i \qquad (37)$$

where n_i is the number of data tracks and M_i is the number of MC tracks in the ith bin. The bins in the far tails of the distribution were combined to reduce fluctuations in the MC.

Added symmetric impact parameter smearing was achieved by degrading a fraction of the track impact parameters by a gaussian and an even smaller fraction by a symmetric, double-sided exponential decay function.† The extra gaussian degradation was allowed a width of 25 μm to 300 μm and affected between 0% and 40% of the tracks. The decay length of the symmetric exponential smearing was fixed at λ=1 mm and allowed to affect 0–2% of the tracks. The optimal amount of additional track smearing corresponds to

5% of tracks by a gaussian of width σ=175 μm, and
1% of tracks by a symmetric exponential of decay length λ=1 mm

The Monte Carlo impact parameter distribution with the additional smearing is shown in Figure 71. With limited statistics the MC with and without the extra resolution degradation both appear to fit the data adequately. The optimized version

---

† The extra symmetric exponential tail smearing is of the form $R(\delta) = \frac{1}{2\lambda}\exp(-|\delta|/\lambda)$ where λ=1mm.

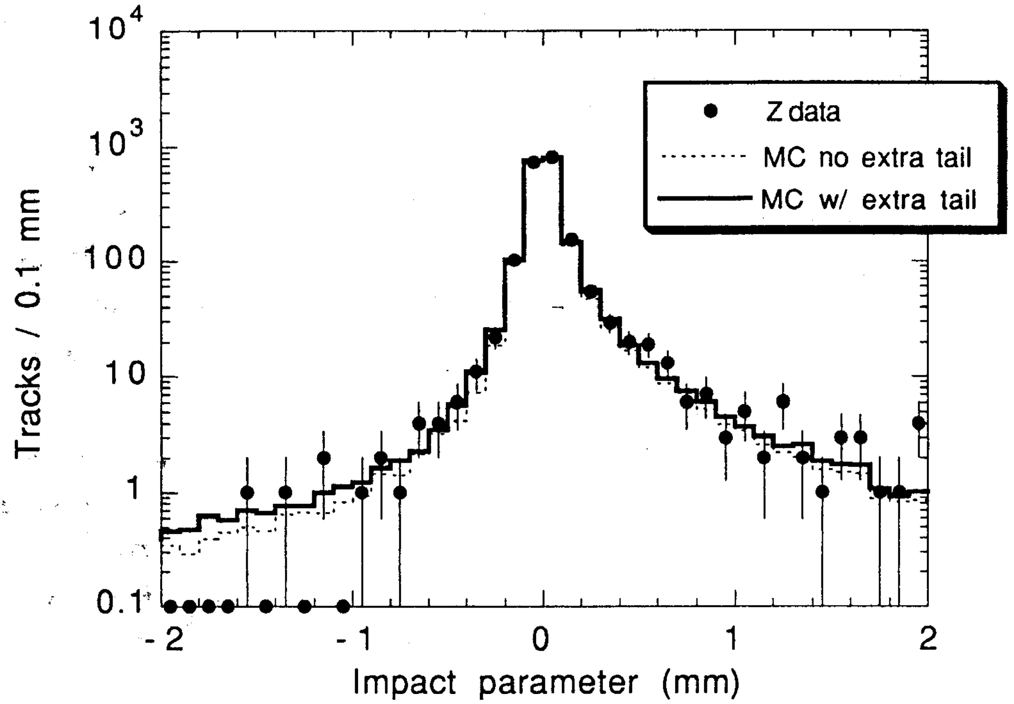

Figure 71 Impact parameter distribution with and without the additional track smearing.

has a better χ^2 fit of 2.2 for 5 degrees of freedom. Also the fraction of MC tracks with $\delta \leq -0.50$mm now agrees exactly with the data.

The phase space of allowed resolution degradation is delineated by the 1σ uncertainty in the number of tracks with $\delta \leq -0.50$mm and the 2σ contour in log likelihood space. The requirement that 1.02±0.22% of the hadronic tracks have $\delta \leq -0.50$mm limits the percentage of tracks that receive an additional symmetric exponential smearing to under 2%. Table 25 and Table 26 show the log likelihood values for 0%, 1%, 1.5%, and 2% exponential smearing and a complete range of gaussian smearing. The log likelihood value of 0 corresponds to our optimum amount of 5% of the tracks with a gaussian (σ=175μm) and 1% with an exponential (λ=1mm) smearing. The 2σ (1σ) contour occurs at a drop of 2.0 (0.5) units in log likelihood, and the interior is highlighted to show the range of possible symmetric tail smearing that is allowed by the data.

The hypothesis of no additional smearing is ruled out by the log likelihood fit by nearly three standard deviations. However, in Chapter 6 we will discover that this additional impact parameter degradation results in a small shift in τ_b compared to the statistical power of our measurement. Also, we will explore how this range of additional track smearing, allowed by the likelihood fit and the integrated track count beyond -0.5 mm, affects the measured B lifetime.

Table 25 Maximum Log Likelihood values for fits to the negative impact parameter distribution. The MC has additional gaussian smearing for a small fraction of the tracks as shown in the tables. Furthermore, in the top (bottom) table, 0% (1%) of the tracks are broadened with an additional exponential tail of decay length 1 mm. The thin (thick) contour shows the 1σ (2σ) limits.

Gaussian width	Percentage of tracks with additional Gaussian smearing								
	0%	5%	10%	15%	20%	25%	30%	35%	40%
25 μm	**-4.10**		**-3.79**	**-3.60**	**-3.53**	**-3.47**	**-3.36**		
50 μm	-4.10	-3.51	-3.05	-2.68	-2.61	-2.64	-2.78		
75 μm	-4.10	-2.87	-2.28	-2.21	-2.98	-4.29	-5.96		
100 μm	-4.10	-2.23	-1.85	-2.66	-4.89				
125 μm	-4.10	-1.56	-1.62	-3.75					
150 μm	-4.10	-1.05	-1.86	-5.44					
175 μm	-4.10	-0.56	-2.15						
200 μm	-4.10	-0.36							
250 μm	-4.10	-0.02							
300 μm	-4.10	-0.11							

Gaussian width	Percentage of tracks with additional Gaussian smearing								
	0%	5%	10%	15%	20%	25%	30%	35%	40%
25 μm	-2.66	-2.36	-2.22	-2.06	-1.97	-1.92	-1.79	-1.76	-1.63
50 μm	-2.66	-1.94	-1.62	-1.33	-1.08	-1.09	-1.45	-1.77	-2.04
75 μm	-2.66	-1.38	-0.96	-1.10	-1.61	-2.88	-5.00		
100 μm	-2.66	-0.88	-0.76	-1.91	-3.89	-7.08			
125 μm	-2.66	-0.44	-1.00	-3.46	-7.36				
150 μm	-2.66	-0.19	-1.54	-5.50					
175 μm	-2.66	0.00	-2.27						
200 μm	-2.66	-0.08							
250 μm	-2.66	-0.33							
300 μm	-2.66	-0.94							

Table 26 Maximum Log Likelihood values for fits to the negative impact parameter distribution. The MC has additional gaussian smearing for a small fraction of the tracks as shown in the tables. Furthermore, in the top (bottom) table, 1.5% (2%) of the tracks are broadened with an additional exponential tail of decay length 1 mm. The thick contour shows the 2σ limit.

	Percentage of tracks with additional Gaussian smearing								
Gaussian width	**0%**	**5%**	**10%**	**15%**	**20%**	**25%**	**30%**	**35%**	**40%**
25 µm	-2.64	-2.53	-2.37	-2.32	-2.21	-2.12	-2.01	-1.91	-1.89
50 µm	-2.64	-2.06	-1.72	-1.53	-1.34	-1.36	-1.50	-1.71	-2.11
75 µm	-2.64	-1.53	-1.17	-1.41	-1.87	-3.04	-4.80	-6.82	
100 µm	-2.64	-1.10	-1.17	-2.41	-4.41	-7.50			
125 µm	-2.64	-0.81	-1.52	-4.02	-7.81				
150 µm	-2.64	-0.69	-2.31	-6.46					
175 µm	-2.64	-0.72	-3.47						
200 µm	-2.64	-0.85							
250 µm	-2.64	-1.21							
300 µm	-2.64	-2.03							

	Percentage of tracks with additional Gaussian smearing								
Gaussian width	**0%**	**5%**	**10%**	**15%**	**20%**	**25%**	**30%**	**35%**	**40%**
25 µm	-2.90		-2.68	-2.52	-2.46	-2.39	-2.26		
50 µm	-2.90	-2.42	-2.06	-1.83	-1.88	-1.96	-2.12		
75 µm	-2.90	-1.95	-1.60	-1.86	-2.86	-4.25	-6.02		
100 µm	-2.90	-1.58	-1.62	-2.96	-5.50	-8.89			
125 µm	-2.90	-1.32	-2.08	-4.90					
150 µm	-2.90	-1.28	-3.08	-7.44					
175 µm	-2.90	-1.33	-4.15						
200 µm	-2.90	-1.64							
250 µm	-2.90	-1.87							
300 µm	-2.90	-2.32							

The great tragedy of Science –
the slaying of a beautiful hypothesis by an ugly fact.
– Thomas Henry Huxley

5 Impact Parameter Tag

An impact parameter tag takes advantage of the rather long lifetime and large mass of the bottom quark in order to isolate a subset of hadronic events that is rich in *B* hadrons. Since the *b* quark is substantially heavier than other quarks, charged tracks from the *B* decay will generally possess a substantial transverse momentum with respect to the B direction, and hence these tracks will depart from the decay vertex with a considerable angle with respect to the B direction. Many of the tracks from the B decay will significantly miss the Z^0 production point. Although charm hadrons have comparable lifetimes, the charm imparts less transverse momentum to its daughter tracks due to the lighter charm mass. Thus these tracks will have smaller impact parameters.

The basic premise for an impact parameter tag is to look for jet hemispheres with some minimum number of charged tracks with significant impact parameter, say $\delta/\sigma_\delta \geq +3.0$. The two jet hemispheres in an event are separated by the plane perpendicular to the thrust axis. For tracking systems with good impact parameter resolution, this method is expected to efficiently tag *B*'s produced in e^+e^- and $p\bar{p}$ collisions. It can also be generalized to detect the presence of any long-lived, massive particle, which includes any long-lived heavy 4th generation fermion or the top quark through its cascade into *B* hadrons.

The previous chapter characterized the tracking performance in hadronic events. In this chapter, we take advantage of the high resolution vertex detectors to define a tag using track impact parameters that is both extremely pure and efficient at selecting B hadrons. We next examine variations of the tagging requirements in order to map out the full spectrum of efficiencies and purities. Finally, we perform checks on the impact parameter tag to establish confidence in its performance.

5.1 The Impact Parameter Tag

With only 208 hadronic Z^0 events selected by the Mark II detector, we cannot measure the B lifetime using the canonical high P_T lepton tag. Roughly 90 B hadrons exist in our data, but only about 18 B's will decay semileptonically. After imposing lepton identification and kinematic cuts on the candidates, we would be left with a negligible sample.

Instead, we need to introduce a tag that is efficient at tagging all B hadrons, i.e. for both semileptonic and nonleptonic decays. We can accomplish this goal by taking advantage of the rather long decay length of bottom hadrons (~2 mm), the frequency of large impact parameter tracks that emerge from B decays, and the precision impact parameter resolution afforded by the Mark II vertex detector system.

Only tracks that pass the series of cuts listed in Section 4.2 are used in order to guarantee that they are well measured by all three charged particle detectors. In addition, tracks that have an impact parameter greater than 2 mm are discarded; that is, we require $|\delta| \leq 2\mathrm{mm}$. This cut diminishes the contributions from K_s^0 and Λ decays, gross tracking errors, and hard scatters, that would otherwise reduce the purity of the B tag by allowing *udsc* events to filter into the tagged sample. It has a small effect on the tagging efficiency for bottom jets. The impact parameter cut is relaxed to 5 mm for the lifetime analysis in the next chapter.

As described in Section 4.3, the impact parameters are measured with respect to an average beam position. The impact parameters are signed using the axis of the nearest jet. Since the jet axis models the B direction more accurately than the thrust axis, especially for three-jet events, fewer impact parameter signing errors will occur for tracks that originate from B decays.

In the previous chapter, we attempted to characterize the impact parameter resolution and tune the Monte Carlo so that it accurately reflected the data. We asserted that the negative half of the impact parameter distribution provides a strong indicator of the tracking resolution function. Aside from the small fraction of lifetime tracks generated with wrong signed impact parameters, the core ($\delta \approx 0$) is composed of tracks that come from the primary vertex, and the non-gaussian tail

($\delta << 0$) are from strange decays, large angle scatters, and tracking errors. Assuming that tracks are smeared by a symmetric function, the MC tracking resolution was optimized with the inclusion of a small amount of additional track degradation: 5% of the MC impact parameters are smeared by a gaussian of width 175 μm and 1% are smeared by a symmetric exponential function of decay length 1mm (refer to Figure 71). Asymmetric track smearing is considered in the section on systematics in Chapter 6.

The impact parameter significance distribution (δ/σ_δ) provides another handle in understanding the resolution function (Figure 72). If the calculated resolution σ_δ from Eqn. (34) on page 112 is accurately determined, then the core of the δ/σ_δ distribution should be a unit gaussian. For the hadronic data the distribution in the range $|\delta/\sigma_\delta| \leq 2$ can be fit to a gaussian of width 1.09±0.03. The Monte Carlo has a slightly narrower width of 1.02. This difference has a negligible effect on the B lifetime measurement and is discussed in the next chapter. Also in good agreement between the data and Monte Carlo is the fraction of tracks in the tails of the impact parameter significance distribution. The fraction of tracks in the negative tail ($\delta \leq -3\sigma$) is 3.3±0.4% for the data and 3.3% for the MC. The fraction in the positive tail ($\delta \geq +3\sigma$) is 9.8±0.7% for the data and 9.5% for the MC. The distribution is asymmetric because the positive tail includes the lifetime tracks from bottom and charm decays.

Figure 73 is an integral distribution which shows the fraction of quality tracks with significance δ/σ_δ greater than some minimum value S_{min}. The distribution for each quark flavor is plotted separately to illustrate the stark differences between bottom and *udsc* events. $b\bar{b}$ events have by far the largest percentage of high impact parameter tracks. For instance, the fraction of bottom, charm, and *uds* tracks that have a significance greater than $S_{min}=+3$ is 25.7%, 8.1%, and 3.1%, respectively. We can construct an efficient and pure tag for B hadrons by requiring the coincidence of several tracks in an event with large impact parameters.

This technique was successfully applied in the Mark II measurement of the B branching fraction f_b given by $\Gamma(Z^0 \to b\bar{b})/\Gamma(Z^0 \to \mathrm{hadrons})$. [32] Events were tagged as $b\bar{b}$ events by requiring the coincidence of three or more tracks in the event with impact parameter significance $\delta/\sigma \geq +3$. The event tag was 50% efficient and yielded a sample purity of 85%. A slightly different event selection criterion was used than what is listed in Section 4.1, and from a collection of 220 hadronic events 32 were tagged. The fraction of $b\bar{b}$ events in hadronic Z^0 decays was measured to be

$f_b = 0.251 \pm 0.049 \pm 0.030$ which is in good agreement with the Standard Model prediction of $f_b = 0.217$.

For a B lifetime measurement, a hemisphere tag is prefered over an event tag. The event tag, used by the Mark II to measure f_b, tagged a sample of $b\bar{b}$ events which was heavily biased towards long decay times. Extracting τ_b from this tagged sample demands a strong reliance on the Monte Carlo to remove the bias. Instead of using the properties of the entire event, a hemisphere tag attempts to isolate B hadrons by examining the tracks in a single jet hemisphere, defined by the plane perpendicular to the thrust axis. The hemisphere tag requires some number of tracks with large δ/σ in the same hemisphere to enrich the sample with B hadrons. Since the two B hadrons in a $b\bar{b}$ event decay independently, the collection of hemispheres opposite the tag constitutes a collection of B hadrons which is unbiased in decay time. The two *B* hadrons communicate only through their common thrust axis. $b\bar{b}$ events with smaller $|\cos\theta_{thrust}|$ have larger impact parameters. Also, events with smaller $|\cos\theta_{thrust}|$ are better contained in the fiducial volume of the Mark II detector, hence the number of detected tracks from

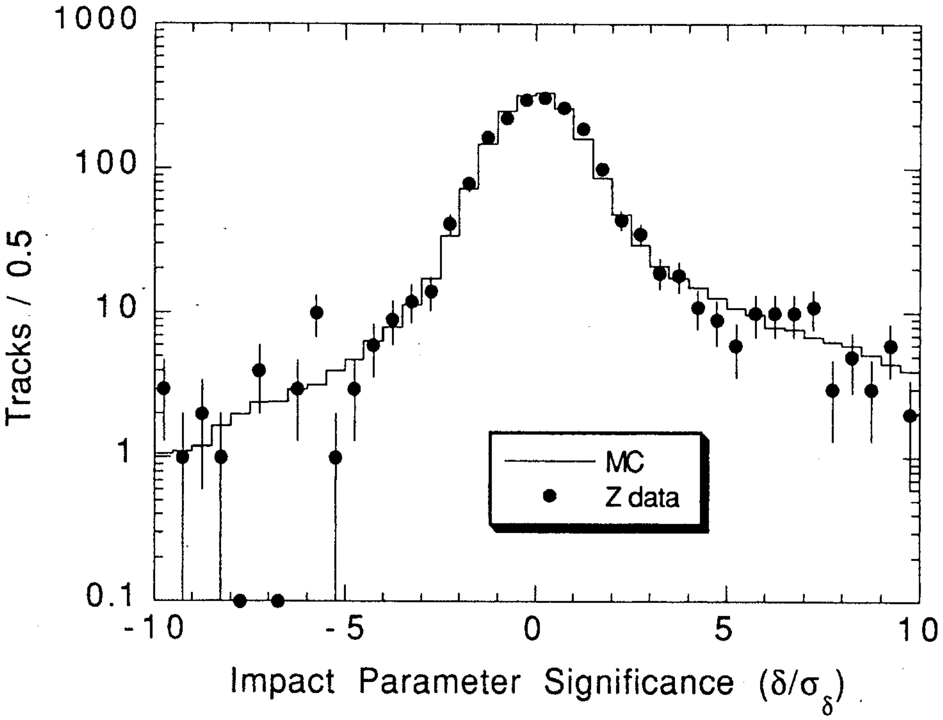

Figure 72 Distribution of impact parameter significance for all quality tracks with $|\delta| \leq 2$ mm. The central core is roughly a unit gaussian, and the tails are well described by the MC simulation.

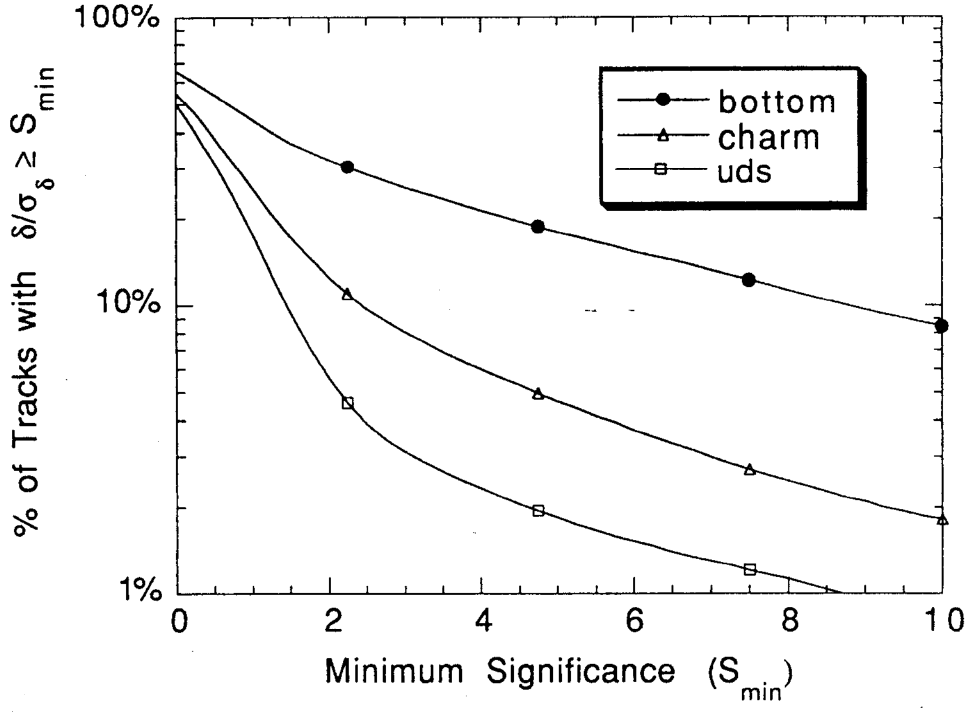

Figure 73 Percentage of tracks with $\delta/\sigma_\delta \geq S_{min}$. The fractions for *uds*, charm, and bottom events are plotted separately.

the B decay increases. Both effects enhance the tag efficiency. However, this bias is significantly weaker than the bias from an event tag.

Charged tracks are divided into the two thrust hemispheres. Only tracks that pass all the track quality cuts listed in Section 4.2 and additionally satisfy the requirement $|\delta| \leq 2\mathrm{mm}$ are used, which leaves about 4.9 tracks per hemisphere. The hemisphere is tagged if it has two or more tracks with impact parameter significance $\delta/\sigma_\delta \geq +3$. Monte Carlo studies have shown this tag is remarkably efficient at selecting 40% of the *B* hemispheres with an sample purity of 81%.

Table 27 compares our B hemisphere tag with some of the recent results from LEP. The high P_T lepton tag has a comparable level of purity, but because it is sensitive only to semileptonic B decays, requires a positive lepton identification, and discards all low P_T leptons, the tag efficiency is only 2-3%. The DELPHI efficiency is even lower because it examined only the $B \rightarrow e$ decay channel. Finally, the boosted sphericity product tag by DELPHI works on events not hemispheres, and so this method of enrichment carries all the associated lifetime biases. It also has a much lower purity and efficiency than the impact parameter tag.

Table 27 Bottom hadron tagging efficiency and sample purity. A comparison of our method with recent methods used at LEP.

Experiment	Method	Efficiency	Purity	Comments
Mark II (our results)	Impact Parameter	40%	81%	Two or more tracks with $\delta/\sigma \geq +3.0$
ALEPH	High P_T lepton	2.9%	73%	$P \geq 5$ GeV, $P_T \geq 2$ GeV
DELPHI	High P_T lepton	1.0%	64%	$P \geq 3$ GeV, $P_T \geq 1$ GeV, $B \rightarrow e$ channel only
L3	High P_T lepton	2.4%	88%	$P \geq 4$ GeV, $P_T(e) \geq 1$ GeV, $P_T(\mu) \geq 1.5$ GeV
OPAL	High P_T lepton	3.0%	85%	$P \geq 4.5$ GeV, $P_T \geq 1.5$ GeV
DELPHI	Boosted sphericity product	15%	40%	Not a hemisphere tag

Table 28 Number of tagged hemispheres and double tagged events in our data of 208 hadronic Z^0 decays. For comparison, the Monte Carlo expectations for varying B lifetimes are also presented.

	Z data	MC (τ_b=1ps)	MC (τ_b=1.5ps)	MC (τ_b=2ps)
Tagged hemispheres	53	44.9	49.7	53.0
Double tagged events	11	7.2	9.7	11.5

Shown in Figure 74, the purity and efficiency of our canonical impact parameter tag display a mild dependence on the B lifetime. At purities of ~80%, any increase in the efficiency will contribute to a correspondingly smaller increase in the purity, and so the purity of the tag is nearly decoupled from the B lifetime. For instance, if the B lifetime in the MC increases from 1 ps to 2 ps, the tag efficiency increases by 26%, whereas the sample purity rises by only 4%.

The impact parameter tag efficiency depends quite strongly on the decay times of the B hadrons (Figure 75). For decay times near zero, a B hemisphere has vanishingly small but finite probability of being tagged. Even for B's that decay at

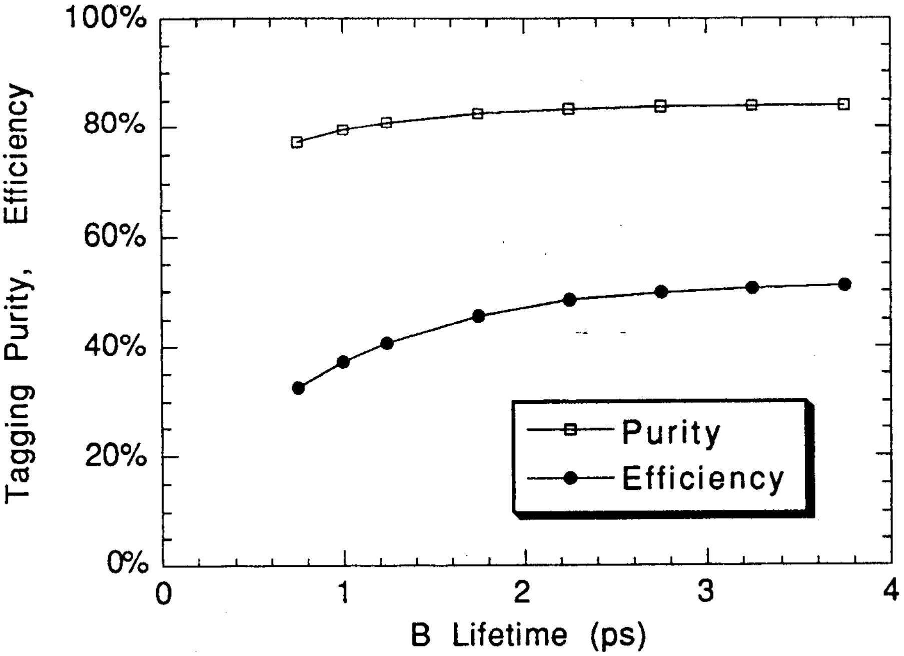

Figure 74 The tagging efficiency and the sample purity as a function of the B lifetime. A hemisphere is tagged if it has two or more tracks with impact parameter significance δ/σ_δ exceeding 3.0.

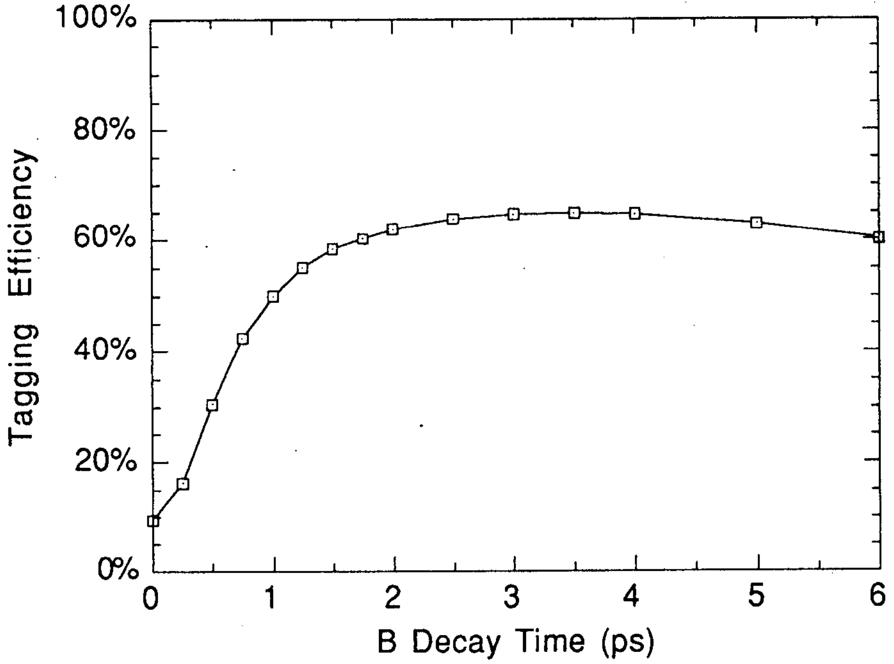

Figure 75 Tag efficiency as a function of the decay time of B hadron. The efficiency decreases slightly for large decay times due to the impact parameter cutoff of $|\delta| \leq 2$ mm.

the origin, tracks from tertiary charm decays and tails in the resolution function allow ~10% of these B hemispheres to be tagged. The tag efficiency climbs rapidly until it plateaus at 60-65% for decay times greater than 1.5 ps. The tag efficiency saturates below 100% due to low multiplicity B decays and tracking inefficiencies. For instance, in 15% of the B decays not a single track from the B hadron passes the track quality cuts. For very long decay times, the efficiency actually begins to drop due to the loss of high impact parameter tracks from B decays, which are removed by the track cut $|\delta| \le 2\,\mathrm{mm}$.

Applying the impact parameter tag to our 208 hadronic events results in 53 tagged hemispheres, of which 22 hemispheres come from 11 double tagged events. Table 28 lists the outcome along with Monte Carlo expectations for B hadrons with generated lifetimes of 1.0, 1.5, and 2.0 ps. The number of tagged and double tagged events agrees roughly with the MC expectations for B hadrons that decay with the world average B lifetime of 1.3 ps.

For a choice of y_{cut}=0.1 in the track clustering algorithm YCLUS, roughly one-sixth of the hadronic events are three-jet events from the process $Z^0 \rightarrow q\bar{q}g$. Two of the jets evolve from the parent quark partons, while the third jet arises from hard gluon radiation. Since mass suppression prevents gluons from splitting into $c\bar{c}$ or $b\bar{b}$ pairs, we do not expect large impact parameter tracks to exist in the gluon jets. Hence, a three-jet event with significant impact parameters in all three jets could signal new physics. Analogous to the hemisphere tag, a jet is tagged if it has two or more tracks with impact parameter significance (δ/σ) greater than three. The cut on minimum P_{xy} was lowered to 0.15 GeV to utilize a greater portion of the detected tracks. Out of 34 three-jet events in the data, nine were single-tagged, one was double-tagged, and none were triple-tagged. The MC prediction is similar.

5.2 Variations of the Impact Parameter Tag

The impact parameter tag that we have described selects bottom hemispheres both efficiently and cleanly; however, it is by no means unique. By altering the definition of the tag, we can increase the efficiency even further, but at the cost of compromising the purity. The converse is also true — attempts to improve the purity of the tag will decrease the efficiency. Figure 76 illustrates the trade-off between efficiency and purity as we vary the minimum track significance S_{min} from two to four and vary the minimum number of required tracks with $\delta/\sigma_\delta \ge S_{min}$ from one to three tracks. Increasing the minimum significance S_{min} or increasing the minimum number of significant tracks N_{min} will increase the B purity but

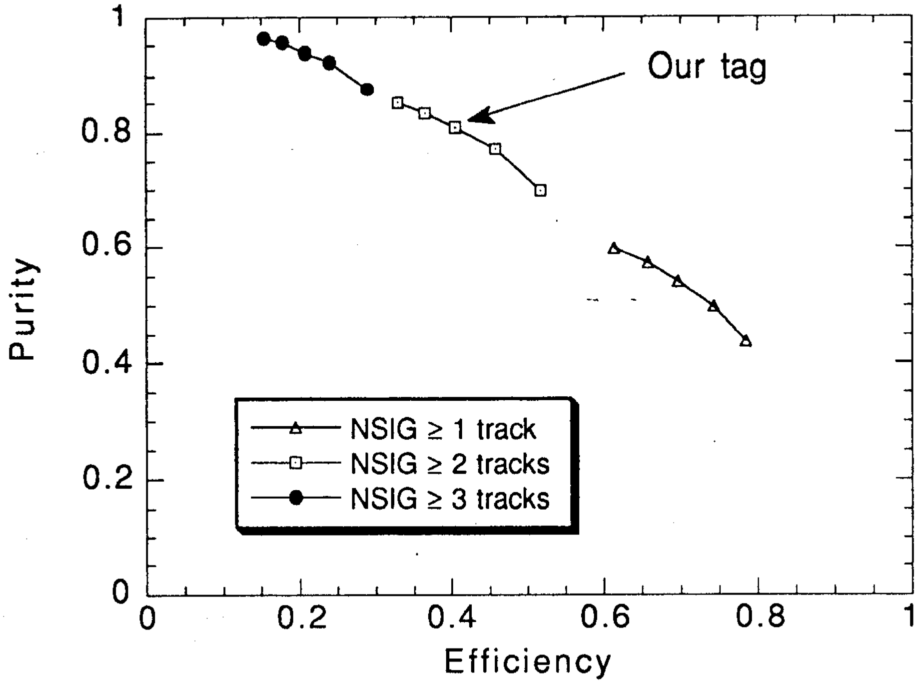

Figure 76 Trade-off between tagging efficiency and sample purity. The tagging requirement varies from a minimum of one to three significant tracks in a hemisphere (NSIG), and for each choice of NSIG, a minimum track significance from $\delta/\sigma \geq 2$ to $\delta/\sigma \geq 4$ in increments of 0.5.

reduce the tag efficiency. The two extremes are the hemisphere tag (N_{min}=1, S_{min}=2) with 79% efficiency and 44% purity, and the hemisphere tag (N_{min}=3, S_{min}=4) with 15% efficiency and 96% purity.

Charm jets have a much higher tagging efficiency than *uds* jets. In fact, as the tag requirements become more severe, not only does the impurity fall rapidly but the fraction of charm hemispheres in the *udsc* background climbs dramatically from 38% to 74%, indicating that the lifetime tracks from charm decays dominate in generating background tags as compared to the non-lifetime effects such as K_s^0 and Λ decay particles, mistracking, and hard coulomb scattering. The increased dependency on charm decay kinematics is fortunate because it is more easily modeled by the Monte Carlo.

Table 29 lists the different choices of impact parameter tag, and the purity and efficiency derived from the MC. Also presented are the number of hemispheres tagged in the hadronic data by each variation of the impact parameter tag.

Table 29 Purity and efficiency of the impact parameter tag as a function of the tagging requirement: the minimum track significance, S_{min}, and the minimum number of significant tracks in a hemisphere, N_{min}. The corresponding number of tagged hemispheres in the data and the characteristics of the *udsc* background is also presented.

N_{min}	S_{min}	Tagged hemispheres (Z data)	Purity (%)	ε_b	ε_{udsc}	f_c/f_{udsc}
1	2.0	157	43.8	0.786	0.293	0.38
	2.5	126	49.7	0.742	0.219	0.41
	3.0	104	54.0	0.697	0.172	0.42
	3.5	96	57.2	0.658	0.142	0.42
	4.0	90	59.8	0.615	0.120	0.42
2	2.0	66	69.8	0.518	0.065	0.55
	2.5	59	77.1	0.458	0.039	0.61
	3.0	53	80.8	0.405	0.029	0.62
	3.5	45	83.4	0.365	0.021	0.63
	4.0	39	85.1	0.330	0.017	0.63
3	2.0	32	87.6	0.289	0.012	0.69
	2.5	29	92.2	0.240	0.006	0.71
	3.0	25	93.7	0.208	0.004	0.71
	3.5	22	95.4	0.178	0.003	0.71
	4.0	20	96.2	0.154	0.002	0.74

Our choice of hemisphere tag from the options listed in Table 29 was guided by several considerations:

- The *B* tag should be as efficient as possible, due to limited statistics. The tags in Table 29 collect anywhere from about 14 to 72 *B*'s in the Mark II hadronic data.
- The purity should be as high as possible. The range of purities listed in Table 29 extends from 44% to 96%. High levels of purity reduce the systematic error in a B lifetime measurement due to uncertainties in both the *udsc* tag efficiency and the precise shape of the *udsc* impact parameter distribution.

- The tag should require the coincidence of at least two high impact parameter tracks. The coincidence dramatically heightens the purity and desensitizes the tag to the non-gaussian tails in the resolution function. Furthermore, the tails are more difficult to parameterize than the core of the resolution function.
- S_{min} should be greater than two. In the *uds* impact parameter significance distribution, the gaussian core and the exponential tail meet at $\delta/\sigma \approx 2$ (see Figure 73). Beyond this point, the distribution falls more slowly, and so larger values of S_{min} will have diminishing gains in purity at a growing cost to the efficiency of the tag. In addition, uncertainties in the width of the core are not as consequential for a choice of $S_{min} \geq 2$.

Some of the criterions are in direct conflict with each other: the highest efficiency and the highest purity cannot both be simultaneously achieved. At first glance, rather than the previously stated tag of two or more tracks in a hemisphere with impact parameter significance $\delta/\sigma_{\delta} \geq +3$, i.e. ($N_{min}=2$, $S_{min}=3$), we might prefer to choose the most efficient tag because of our small hadronic data set, since the statistical error should dominate over the systematic error. However, as will be discussed in the next chapter, the gains in statistical power from higher tagging efficiencies coupled with significantly lower purities are small. Thus, our tag is a good choice in that it minimizes the background and has a statistical power that is nearly equal to those of the more efficient tags.

5.3 Checks on the Purity and Efficiency

The number of tagged hemispheres in the data is given by

$$N_{tag} = [\varepsilon_b f_b + \varepsilon_{udsc}(1 - f_b)] N_{hemi} \tag{38}$$

where N_{hemi} is the number of hemispheres in the hadronic sample (N_{hemi}=416), ε_b is the efficiency for tagging a B hemisphere, ε_{udsc} is the efficiency for tagging a *udsc* hemisphere, and f_b is the fraction of $b\bar{b}$ events in the hadronic sample. f_b is 3% higher than $R_{b\bar{b}}$, given by $\Gamma(Z^0 \to b\bar{b})/\Gamma(Z^0 \to \text{hadrons})$, due to the slight preference toward $b\bar{b}$ events in the event selection cuts.

By rearranging Eqn. (38), we can determine the fraction of $b\bar{b}$ events in hadronic Z^0 decays for each of the different impact parameter tags. The efficiencies are computed by the Monte Carlo, and N_{tag} is the number of tagged hemispheres observed in the data. The branching fraction $R_{b\bar{b}}$ as a function of tag efficiency is plotted in Figure 77. For all cases including the canonical tag, $R_{b\bar{b}}$ is slightly high but within errors of the Standard Model value of 0.217, bolstering confidence in the robustness of the purity and the efficiency of the impact parameter tag.

Finally, there is no evidence that tracks with significantly positive or negative impact parameters are distributed unevenly in φ, which could indicate a distortion or residual misalignment in the tracking chambers and silicon strip detector. The distribution of large impact parameter tracks as a function of cosθ and P_{xy} are also modeled well by the Monte Carlo.

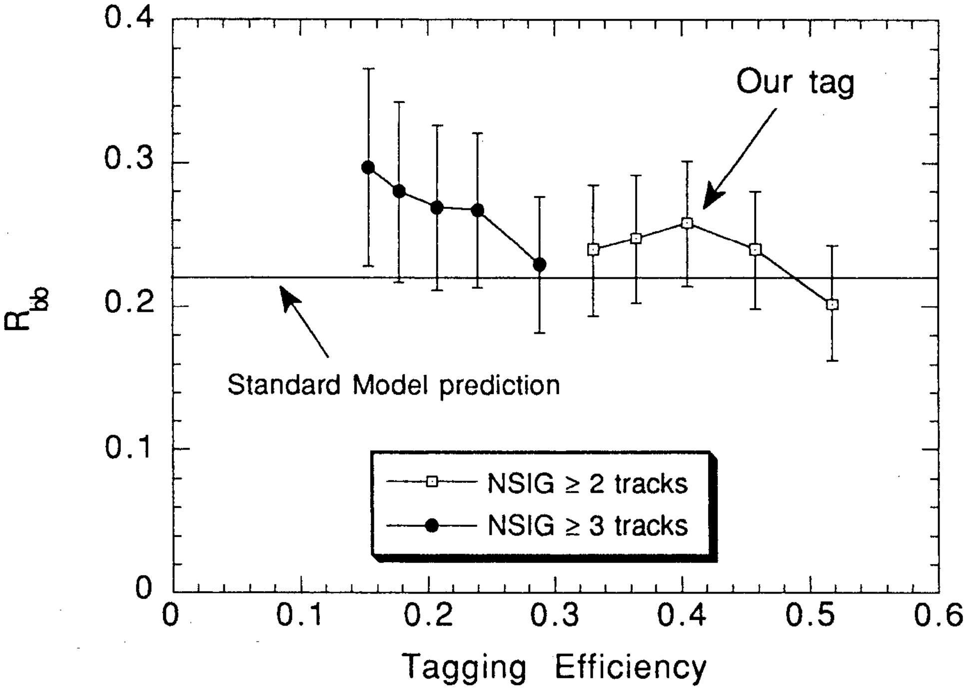

Figure 77 $Z^0 \rightarrow b\bar{b}$ branching fraction versus the tagging efficiency, where the errors are statistical only. All values of $R_{b\bar{b}}$ agree with the Standard Model prediction of 0.217. Smaller tagged hemisphere samples are encompassed by those from more efficient tags, so the error bars on the points are not independent.

Get you facts in first, then you can distort them as much as you please.

– Mark Twain

6 The Lifetime Measurement

In the last chapter we described an impact parameter tag that has a 40% efficiency and 81% purity in selecting bottom jets. We tagged 53 hemispheres out of a total of 208 hadronic events in the Mark II 1990 data. B jets with longer decay lengths clearly have a higher probability of being tagged, and so the tagged hemispheres represent a collection of B hadrons that are heavily biased toward long decay times. In fact, the average decay time is roughly twice the B lifetime τ_b. However, the hemispheres opposite the tag represent a distribution of bottom jets unbiased in decay times and are referred to as the untagged sample. We can use this sample to extract the B lifetime with a minimal reliance on the Monte Carlo to remove any lifetime bias. Note that in the case of double tagged events, each hemisphere is both a "tagged" and an "untagged" hemisphere.

In this chapter, we will measure the B lifetime by examining the quantity $\Sigma\delta$, defined as the sum of impact parameters from all tracks in the hemisphere. Our measurement uses the untagged hemisphere sample, because it contains a relatively pure and unbiased sample of B hadrons. However, we also probe the $\Sigma\delta$ distribution for the tagged sample and for all hemispheres in the hadronic events.

Next, we apply a number of checks on the lifetime measurement to show that it is relatively insensitive to variations in the impact parameter tag, track quality cuts, and tails in the resolution function. Finally, we enumerate the systematic errors in the measurement. These errors fall under two main categories:

uncertainties in the physics parameters and uncertainties in the detector performance.

6.1 Properties of the $\sum\delta$ distribution

There are many ways to measure the B lifetime from the untagged hemisphere sample. For instance, we can examine the inclusive impact parameter distribution from this sample. The δ distributions were presented separately for *uds*, charm, and bottom events back in Figure 10 on page 22. Events were required to pass the hadronic selection cuts in Section 4.1, and tracks had to pass the track quality requirements in Section 4.2. This method not only requires that we know the fraction of *uds*, charm, and bottom hemispheres in the tag (Table 29 on page 136), but also the charged multiplicity for each quark flavor. In addition, we need to distinguish between the tracks that come from B decays and the fragmentation tracks, which come from the Z^0 production point in $b\bar{b}$ events. Since B hadrons carry away about 70% of the beam energy, a substantial amount of energy is still available to generate fragmentation tracks. Only half of the charged multiplicity in $b\bar{b}$ events originates from the two B hadrons. Since the non-B decay tracks will have impact parameters near zero, any uncertainty in the fraction of tracks from non-B decay sources will cause an error in the mean of the inclusive δ distribution and hence a corresponding error in the B lifetime measurement.

Recently, the Mark II has measured the charged multiplicity in $b\bar{b}$ events to be 23.1±1.9 using an impact parameter event tag. [32] CLEO and ARGUS have measured the B meson decay multiplicity with high accuracy, and including a correction for B_s and Λ_b, the average multiplicity for B hadrons produced at the Z^0 resonance is 5.56±0.11. [80] Measured by the four LEP experiments, the charged multiplicity averaged over all quark flavors in hadronic Z^0 decays is 20.94±0.20. [79] By far, the largest uncertainty is associated with the $b\bar{b}$ event multiplicity. This 8% error will translate into an even larger systematic error for a B lifetime measurement.

We can remove the sensitivity to uncertainties in the number of fragmentation tracks in $b\bar{b}$ events by examining the sum of impact parameters from all quality tracks in the hemisphere ($\Sigma\delta$). The tracks must pass the set of cuts listed in Section 4.2. The sum is independent of the multiplicity of fragmentation tracks since these tracks generally have an impact parameter of zero. The $\Sigma\delta$ also incorporates the lifetime information from all tracks in a B decay. This is important because the impact parameter of a single track conveys only a fragment of the original B hadron's decay time. Contrarily, the high P_T lepton method discards the impact parameter information from the remaining non-leptonic particles in the B decay. Of course, many of these tracks emanate from tertiary charm decays and hence will have impact parameters enhanced by the charm lifetime. But the additional contribution is small and can be properly accounted for in the Monte Carlo. Turning off the charm lifetime in the Monte Carlo reduces the $\Sigma\delta$ in $b\bar{b}$ events by only 25%.

A second advantage is that resolution effects are less significant in the $\Sigma\delta$ distribution than in the inclusive δ distribution. Impact parameters of tracks from bottom hadrons get summed coherently, and track errors are uncorrelated. Hence the average significance of the $\Sigma\delta$ for bottom hemispheres

$$\frac{\Sigma\delta}{\text{Error }(\Sigma\delta)} \approx \sqrt{n} \cdot \frac{\bar{\delta}}{\sigma_\delta} \tag{39}$$

tends to be substantially larger than the typical impact parameter significance $\bar{\delta}/\sigma_\delta$ of a track from a $b\bar{b}$ event. Here, n is the number of tracks included in the sum (~5), and $\bar{\delta}$ is the average impact parameter.

Thirdly, the signal-to-noise ratio, defined as the average $\Sigma\delta$ for B hemispheres divided by the width of the $\Sigma\delta$ distribution for *uds* hemispheres, is larger in the $\Sigma\delta$ distribution than in the inclusive δ distribution for the same reason: impact parameters of tracks from B's get summed coherently. The core of the *uds* $\Sigma\delta$ distribution is dominated by the error on $\Sigma\delta$. The shape approximates a gaussian distribution of width $\approx \sqrt{n}\sigma_\delta$.

Figure 78 illustrates the $\Sigma\delta$ distribution for B jet hemispheres generated with a lifetime of τ_b=1 ps and τ_b=2 ps. The events are required to pass the event selection cuts, and the tracks in the $\Sigma\delta$ must satisfy the track quality cuts. The shape of the $\Sigma\delta$ distribution for bottom jets resembles an exponential decay function convoluted with the resolution function. The distribution means are $\langle\Sigma\delta\rangle = 620\mu\text{m}$ and $\langle\Sigma\delta\rangle = 1040\mu\text{m}$, respectively. The mean for the 2 ps distribution is less than double that of the 1 ps distribution since a portion of the $\Sigma\delta$ arises from the nonzero charm lifetime. This amount is independent of the generated B lifetime and contributes ~200 μm to the sum. Non-gaussian tails in the resolution function generate tails in the $\Sigma\delta$ distribution. This contribution is more visible in the negative tail of the $\Sigma\delta$ distribution since the positive tail is dominated by hemispheres with long B decay times.

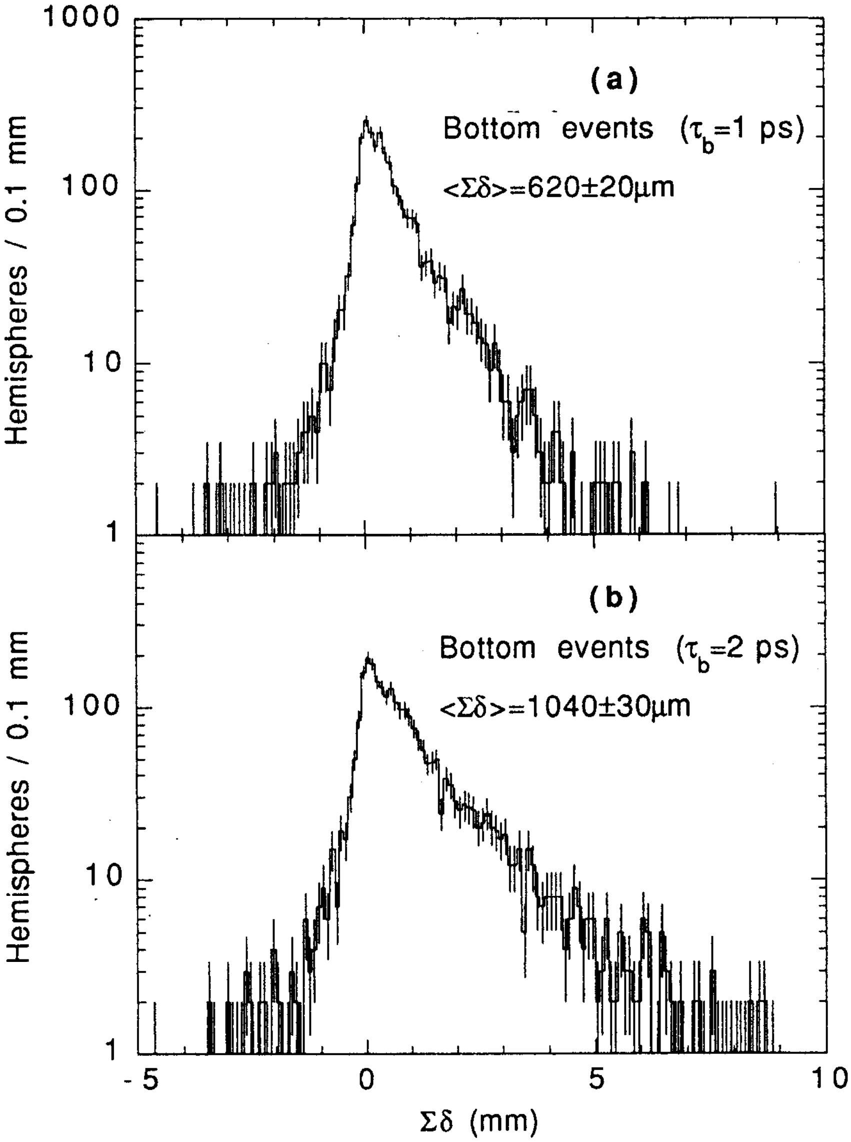

Figure 78 $\Sigma\delta$ distribution for B hemispheres generated with a lifetime of (a) 1 ps and (b) 2 ps. The shape is roughly an exponential decay, with a decay length approximately proportional to the B lifetime.

Table 30 Mean and standard deviation of the $\Sigma\delta$ distribution for bottom hemispheres generated with either a fixed B lifetime $<\tau>$ or a fixed B decay time τ.

B lifetime or decay time	$\mu_{\langle\tau\rangle}$ **in µm**	$\sigma_{\langle\tau\rangle}$ **in µm**	μ_τ **in µm**	σ_τ **in µm**	$\sqrt{\mu_\tau^2+\sigma_\tau^2}$ **in µm**
1 ps	621±20	1047±14	636±17	873±12	1080±32
2 ps	1038±30	1539±21	1097±23	1166±16	1601±40

The underlying exponential-like shape of the $\Sigma\delta$ distribution for B's comes from the exponential distribution of decay times. However, since the $\Sigma\delta$ is not an exact representation of the decay time, the $\Sigma\delta$ distribution for B hadrons generated with a constant decay time is not a delta function, but rather a broad distribution. Figure 79 presents the $\Sigma\delta$ distribution for B hadrons which decay with discrete decay times of 1 ps and 2 ps. Note that in the previous figure, the decay times of the B hadrons are exponentially distributed with lifetimes of 1 ps and 2 ps. As seen in Table 30, the means of the two types of distributions, discrete lifetime versus discrete decay time, are nearly the same. The standard deviation of the $\Sigma\delta$ distribution at a given lifetime is approximately the sum in quadrature of the mean of the distribution and the standard deviation for the distribution with constant decay time. The shape of the $\Sigma\delta$ distribution for a fixed decay time of 2 ps is not quite a scaled up version of the 1 ps decay time distribution since the standard deviation divided by the mean, σ_τ/μ_τ, diminishes as the decay time increases.

The width of the $\Sigma\delta$ distributions in Figure 79 occurs because of fluctuations in the B decay multiplicity and B fragmentation. The multiplicity of daughter tracks of the B hadron which pass all track quality cuts is on average 3.0, with a standard deviation of 1.7. The mean $\Sigma\delta$ scales roughly with the number of charged tracks in the sum from the B hadron decay (Figure 80).

The $\langle\Sigma\delta\rangle$ is also linearly proportional to x_E of the B hadron. A number of factors contribute to the rise in $\langle\Sigma\delta\rangle$ as the B momentum increases. The multiplicity of tracks in the sum from B decays increases because more satisfy the track cut in P_{xy} Correspondingly, the number of fragmentation tracks falls rapidly with x_E due to the decrease in the remaining energy not associated with the B hadrons, although the fragmentation multiplicity has little effect on $\Sigma\delta$. The event thrust increases and the jet axis approximates the B flight direction more accurately as the B

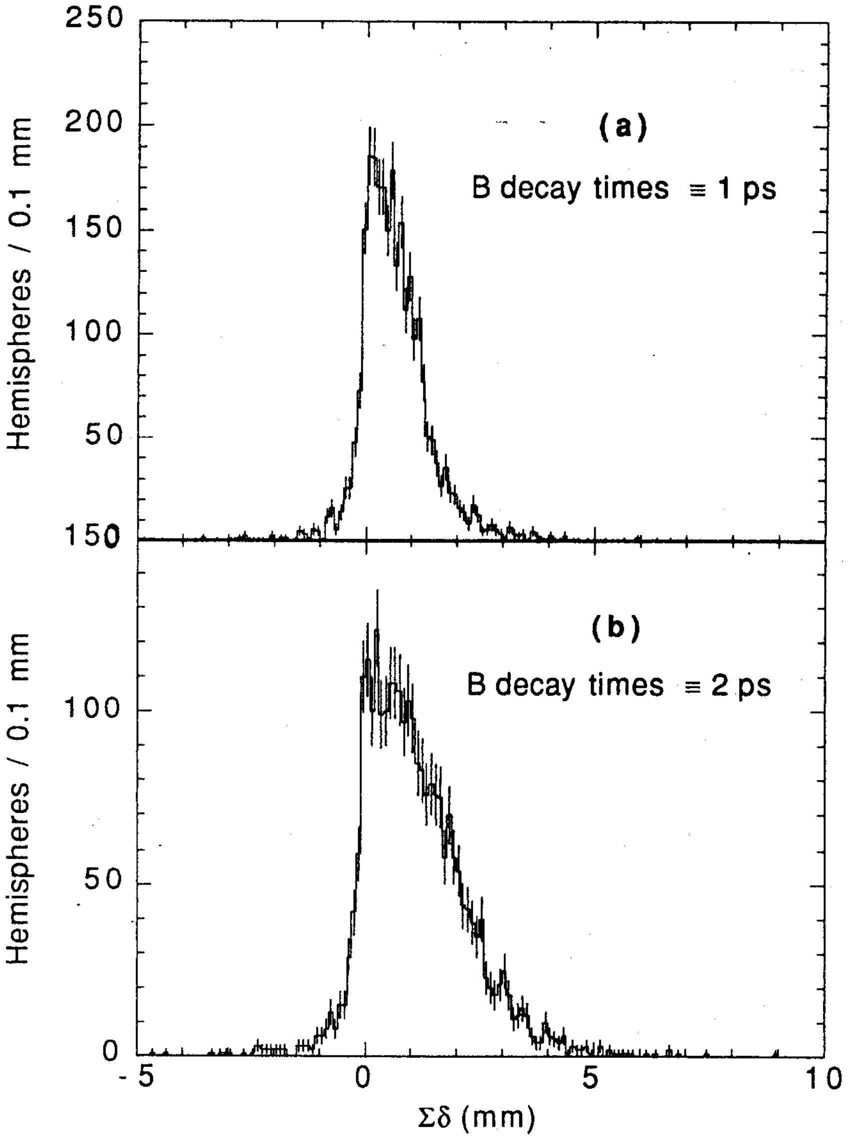

Figure 79 Σδ distribution for B hadrons generated with a fixed decay time of (a) 1 ps and (b) 2 ps. The width of the distribution is primarily due to variations in the B momentum and B decay multiplicity.

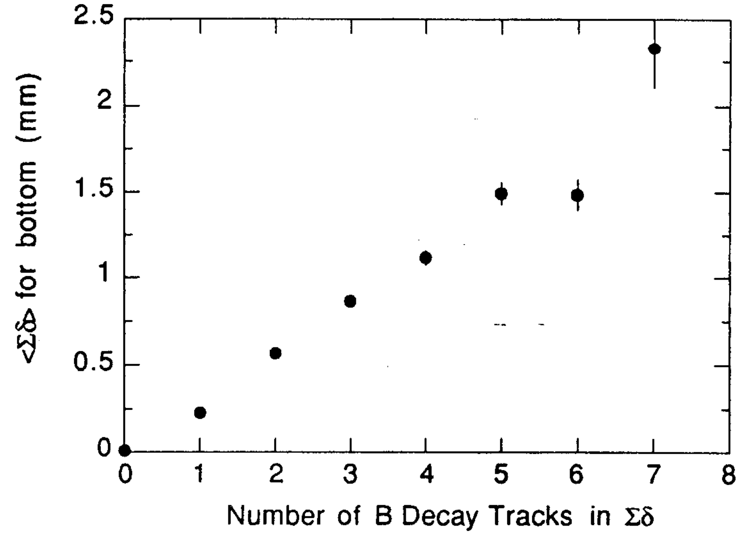

Figure 80 Linear relationship between the mean Σδ for bottom hemispheres and the number of B decay tracks in the sum.

momentum stiffens. This reduces the number of wrong-signed impact parameters due to uncertainty in the B direction. Finally, the magnitude of the impact parameter of tracks from B decays grows slightly with relativistic boost of the B's. These effects are plotted in Figure 81.

The tagging efficiency also shows a marked rise as a function of the B momentum. Although impact parameters from B decay tracks in fact grow slightly with larger B momentum, the dominant factor is the reduction in the calculated impact parameter resolution due to multiple scattering. The B decay tracks will have momenta that scale roughly with the B hadron momentum.

For comparison, the Σδ distributions for charm and *uds* hemispheres are presented in Figure 82. The charm distribution has only a trace of the exponential lifetime shape with a mean of $\langle\Sigma\delta\rangle = 157\mu\mathrm{m}$. The *uds* distribution is composed of a gaussian core of width 150 μm along with positive and negative exponential tails. The Σδ will lie in the exponential tails if it contains a track that is from K_s^0 and Λ decays, mistracked, or scattered by large angles. The impact parameter distribution for tracks from K_s^0 and Λ decays is skewed positive (see Figure 59 on page 100), which accounts for the asymmetric tail in the Σδ distribution and the positive mean of $\langle\Sigma\delta\rangle = 53\mu\mathrm{m}$.

A final advantage of the Σδ distribution over the inclusive δ distribution is its diminished sensitivity to beam motion due to a rather fortuitous cancellation effect (Figure 83). To understand this effect, consider a *uds* event in which all the tracks

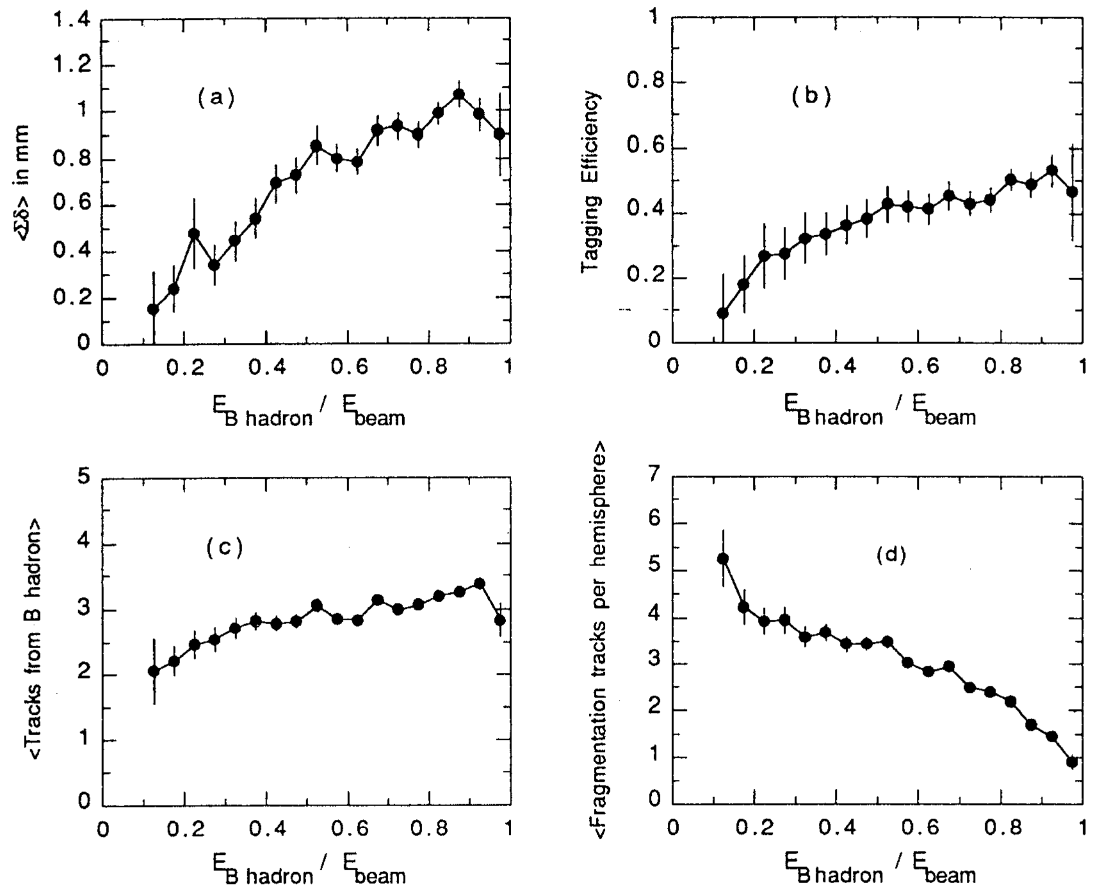

Figure 81 Effects of the B hadron energy on (a) the mean $\Sigma\delta$ for bottom hemispheres, (b) the tagging efficiency, (c) the average number of tracks from B hadrons in the sum, and (d) the average number of fragmentation tracks in the sum.

come from the origin. With perfect track resolution and perfect primary vertex determination, the $\Sigma\delta$ for both hemispheres would be exactly zero. However, uncertainties in the beam position or the width of the beam ellipse will generate nonzero impact parameters. If an error of magnitude Δl is along the jet axis, the shift in impact parameter will be small since most tracks are tightly collimated along the jet axis. The shift is $\Delta\delta = \Delta l \sin\psi$, where ψ is the angle between the track and the jet axis. Hence, only errors in the beam position perpendicular to the jet axis are detrimental. In this case the shift in impact parameter is $\Delta\delta = \Delta l$, and the inclusive δ distribution is broadened accordingly. The $\Sigma\delta$ distribution is less susceptible to this smearing because on average half the tracks will receive an impact parameter shift of $+\Delta l$ while the other half will experience shifts of $-\Delta l$, resulting in a partial cancellation in $\Sigma(\Delta\delta)$. Figure 83 illustrates this point for *uds*

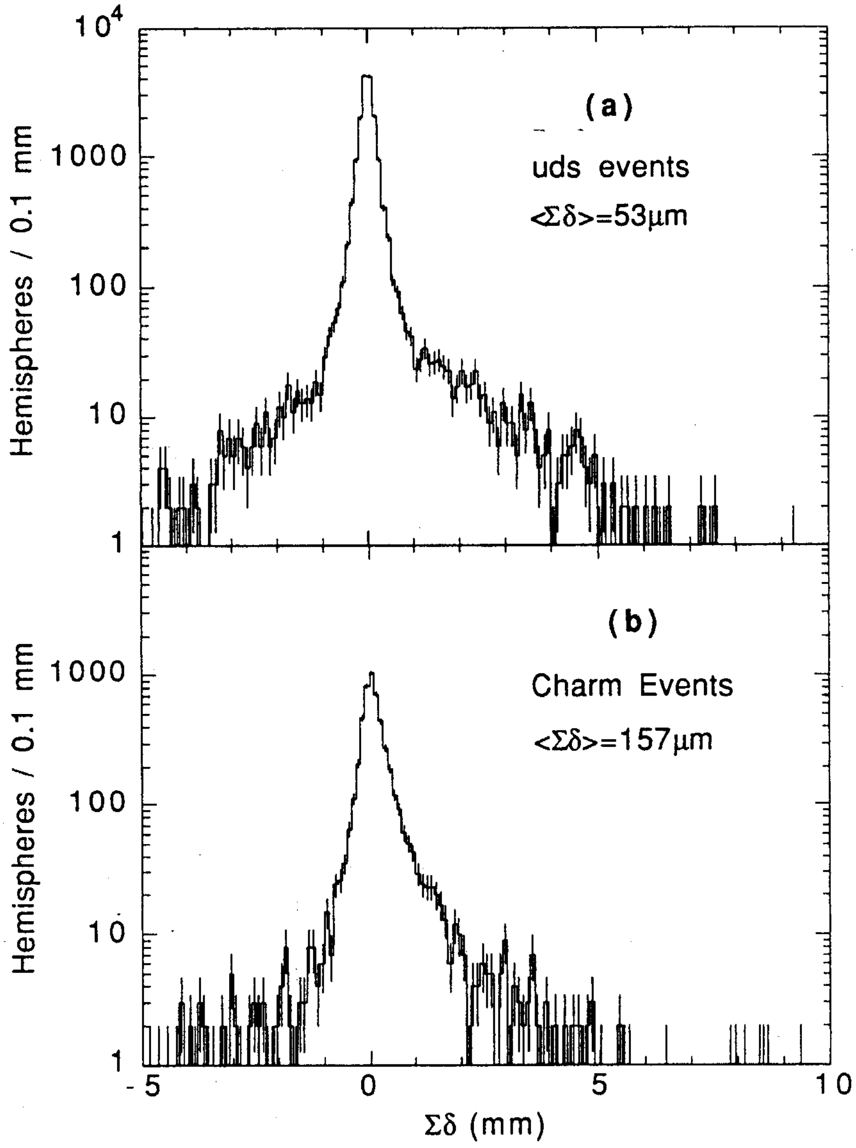

Figure 82 Σδ distribution for (a) *uds* hemispheres and (b) charm hemispheres. The non-gaussian tails in both distributions occur primarily when tracks from strange decays or tracks that experience hard scattering or mistakes in pattern recognition are included in the sum.

events. The core width of the $\Sigma\delta$ distribution and the inclusive δ distribution are plotted as a function of beam motion. The gaussian core of the inclusive δ distribution has a width of $\sigma_\delta^2 = \sigma_{int}^2 + \sigma_{beam}^2$, where σ_{beam} is the amount of beam motion, and σ_{int} is the intrinsic core width without beam motion. If beam motion introduces uncorrelated errors in the sum, then with an average of 5 tracks in the sum, the core width of the $\Sigma\delta$ distribution should be $\sigma_{\Sigma\delta}^2 = 5\sigma_{int}^2 + 5\sigma_{beam}^2$. In reality, cancellation occurs in the $\Sigma\delta$, and the actual $\sigma_{\Sigma\delta}$ is much smaller especially for large beam motion. The phase space of $\sigma_{\Sigma\delta}$ is represented by a swath in the figure because for large beam motion the core of the $\Sigma\delta$ distribution is not very gaussian, and so the width of the central core is not well determined.

Fortunately, the beam spot size at the collision point is only ~5 μm, and beam motion is not a big factor in our data. The beam position uncertainty described in Section 4.4.3 is only 25 μm which is small compared to impact parameters of 100-300 μm from B decays. On the other hand, the four LEP experiments typically have elliptical beam envelopes of $\sigma_{x,\,beam} \approx 150 - 200\mu\mathrm{m}$ and $\sigma_{y,\,beam} \approx 10 - 20\mu\mathrm{m}$. Hence, unless the LEP experiments fit for the primary vertex on an event-by-event basis, tracks in the vertical direction will have impact parameters with respect to the beam centroid that are considerably broadened. In this instance, the $\Sigma\delta$ distribution will offer a substantial cancellation of uncertainties due to the beam ellipse.

In Section 4.2 which lists the track quality cuts, we limited the magnitude of the impact parameter to be less than 5 mm. The rationale for this cut becomes apparent when we examine the mean of the $\Sigma\delta$ distribution for B hemispheres as a function of the generated B lifetime (Figure 84). We expect $\langle\Sigma\delta\rangle$ to increase linearly with τ_b. However, as the generated lifetime increases, a growing fraction of the tail of the impact parameter distribution in $b\bar{b}$ events gets truncated, causing $\langle\Sigma\delta\rangle$ to bow downward for large τ_b. The saturation of $\langle\Sigma\delta\rangle$ becomes even more severe if we impose a more restrictive cut on δ. In Figure 84 the five curves drawn correspond to a maximum allowed impact parameter of 1 to 10 mm. A 1 mm cutoff makes $\langle\Sigma\delta\rangle$ extremely insensitive to larger values of the generated B lifetime. With our low statistics, we need to reside on a curve which offers the most linear response over the widest range of generated lifetimes. The number of tracks that are truncated in $b\bar{b}$ events is actually very small: 3.7%, 1.0%, and 0.1% of the tracks have a $|\delta|$ greater than 1 mm, 2 mm, and 5 mm, respectively, using a MC generated lifetime of τ_b=1.24 ps. But unfortunately these tracks have the greatest affect on the total sum.

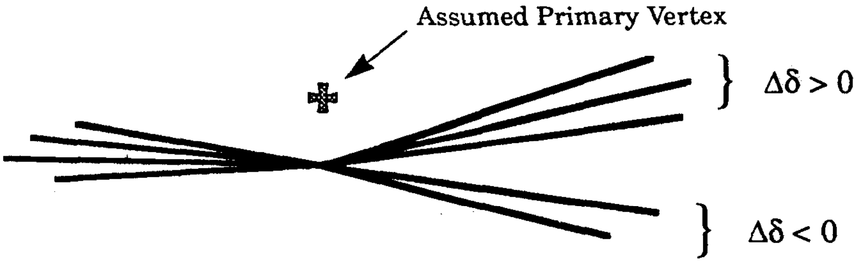

Figure 83 In this *uds* event where the assumed primary vertex is above its actual location, three tracks are mistakenly given a positive δ and two track a negative δ. Hence, the $\Delta\delta$'s nearly cancel out each other in the $\Sigma\delta$.

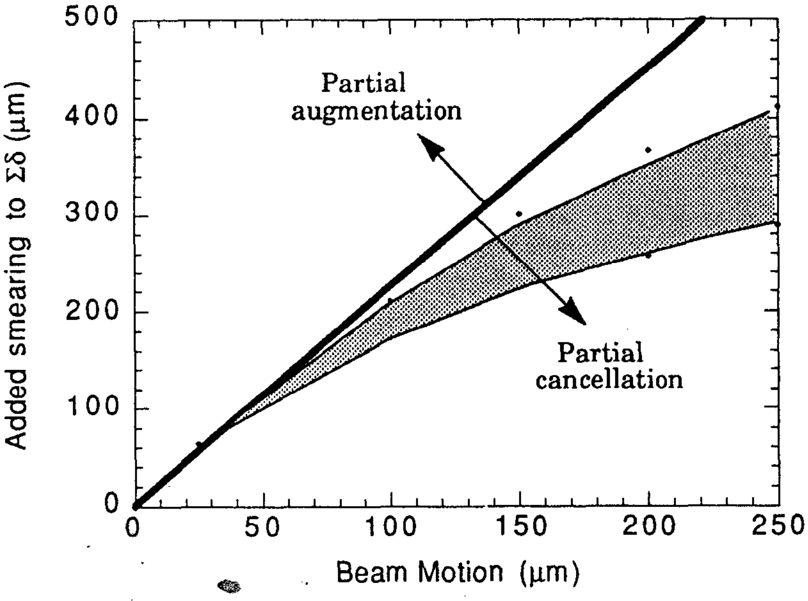

Figure 83 Additional smearing to $\Sigma\delta$ (shaded region) as a function of the beam motion. If the beam motion was uncorrelated among the tracks in the sum, the extra degradation would follow the diagonal line.

Even when the B lifetime is set to zero, the plots in Figure 84 still have a nonzero $\langle\Sigma\delta\rangle$ equal to ~200 μm due to tracks from the tertiary charm decay. This positive offset causes $\Sigma\delta$ to be less sensitive to the B lifetime. For instance, with a cut $|\delta| \leq 5\text{mm}$, suppose our measurement of $\langle\Sigma\delta\rangle$ corresponds to a generated B lifetime of 1.5 ps. Then according to Figure 84, a 10% error in $\langle\Sigma\delta\rangle$ will lead to a 13% error in τ_b. If it was possible to turn off the charm lifetime and remove the

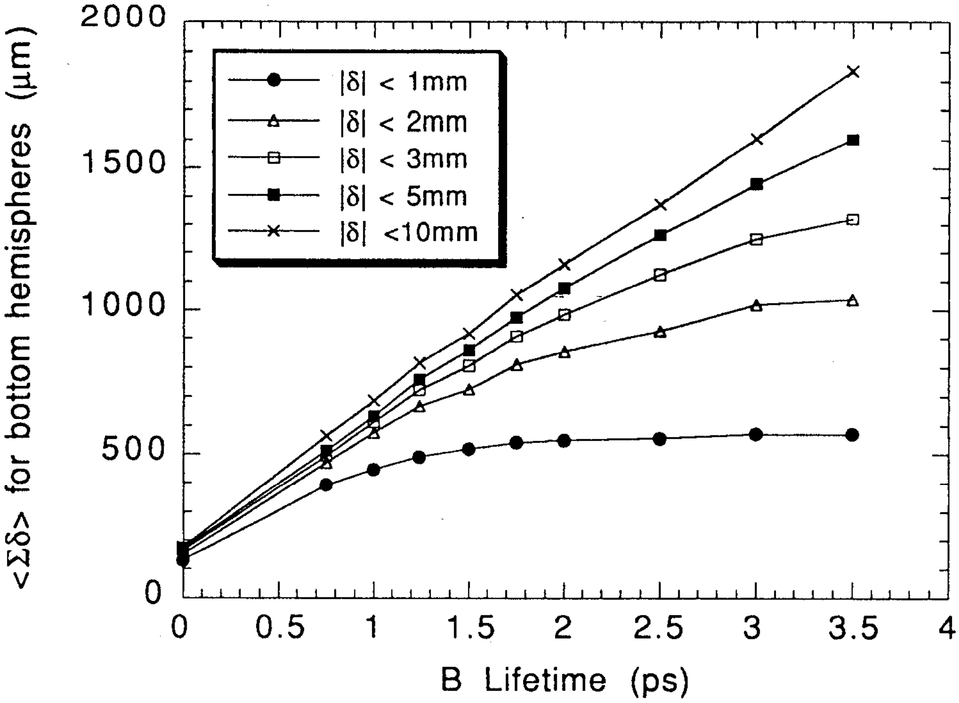

Figure 84 The saturation of <Σδ> for bottom hemispheres as a function of the B lifetime. The maximum allowed impact parameter ranges from 1–10 mm. Our choice of cutoff is 5 mm.

200 μm offset, the error in τ_b would only be 10%. To obtain the most statistical power, we must choose a cutoff that minimizes the quantity

$$\frac{\Delta\tau_b}{\tau_b} = \frac{\partial\tau_b}{\partial\Sigma\delta} \cdot \frac{\Delta(\Sigma\delta)}{\tau_b}$$

Given that the percentage error in Σδ is independent of the impact parameter cutoff value, one of the best statistical results of the contours in Figure 84 occurs for the 5 mm cutoff.

On the other hand, we cannot allow the maximum impact parameter cutoff to be arbitrarily large because fluctuations will be introduced into the Σδ due to the inclusion of tracks from K_s^0 and Λ decays, mistracking, and large angle scatters, that carry no information about the B lifetime. Later in the chapter, as a systematic check we will examine the variation of the lifetime measurement on our choice of the impact parameter cutoff. But for now, the choice of 5 mm is a reasonable one.

6.2 The Mark II Results

We present the $\Sigma\delta$ distribution for the 53 hemispheres opposite the tag in Figure 85. This collection has roughly 80% B jets and 20% *udsc* jets. Further, the sample is unbiased in B decay times. The exponential decay shape is clearly visible and can be accredited to the high resolving power of the two vertex detectors. There is virtually no negative tail in the distribution. The mean of the untagged $\Sigma\delta$ distribution is 855±155 μm, which is large compared to the average error on the $\Sigma\delta$ measurements of ~150 μm. Thus the gaussian core of the impact parameter resolution has a relatively minor effect on the shape of the $\Sigma\delta$ distribution; the dominant feature is the exponential decay profile. This contrasts sharply with the impact parameter distribution of high P_T leptons in the old PEP data and the early LEP results, where poorer impact parameter resolutions completely overwhelms the underlying exponential decay shape, creating a distribution that more closely resembles a gaussian distribution with a slightly positive mean (refer back to Figure 11 on page 24). None of the LEP experiments have yet incorporated their silicon strip detector into their lifetime analysis.

The tagged sample by virtue of being tagged represents a collection of B jets with decay times roughly twice the B lifetime τ_b. Figure 86 shows the $\Sigma\delta$ distribution for the 53 tagged hemispheres. The mean of the distribution is 1500±170 μm, nearly double the mean of the untagged sample.

Aside from a common thrust axis, the value of the tagged $\Sigma\delta$ and the untagged $\Sigma\delta$ within an event are completely uncorrelated in the Mark II data. Also, when we divide the untagged hemispheres into two groups according to the magnitude of their associated tagged $\Sigma\delta$, the means of the untagged $\Sigma\delta$ in the two groups are statistically equivalent: 900±190 μm and 820±230 μm for the low and high valued group of tagged $\Sigma\delta$'s, respectively. Thus, there is no indication that a long-lived B in one hemisphere will promote the opposite B hadron to also have a long decay time.

Finally, in Figure 87 we present the $\Sigma\delta$ distribution for all 416 hemispheres in the 1990 Mark II hadronic data. Only 22% of the hemispheres contain a bottom hadron, and these populate the positive tail of the distribution. The vast majority of hemispheres collect in the peak centered at zero and are almost entirely *udsc* jets. There are a few outliers in the negative tail, presumably due to hemispheres that contain a track with very negative impact parameter caused by strange decay, mistakes in the track pattern recognition, or large angle scatter in the material. The mean of the distribution is 271±46 μm.

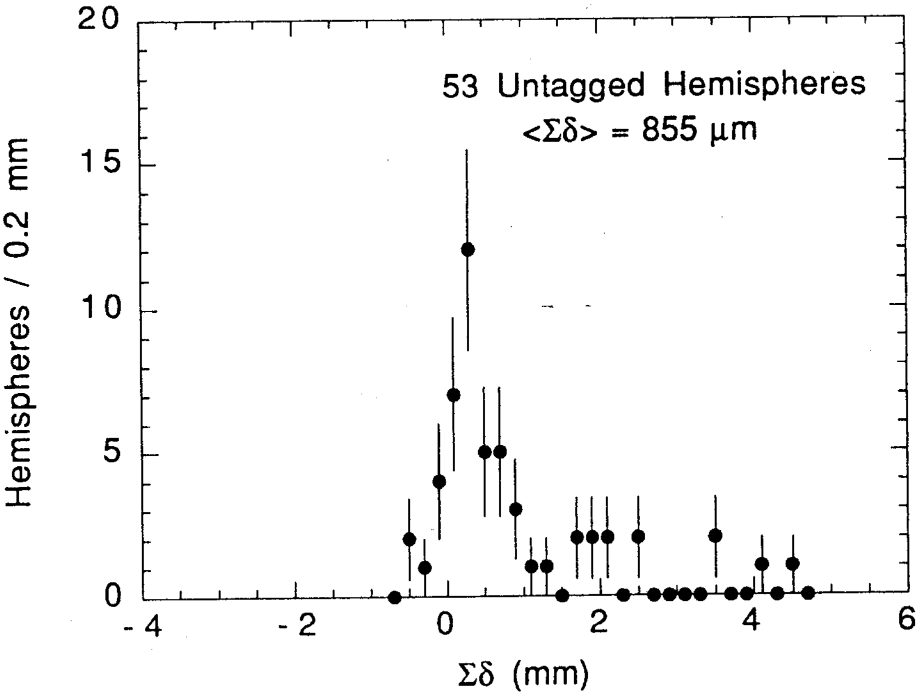

Figure 85 Σδ distribution for the 53 untagged hemispheres opposite the impact parameter tag in the Mark II data.

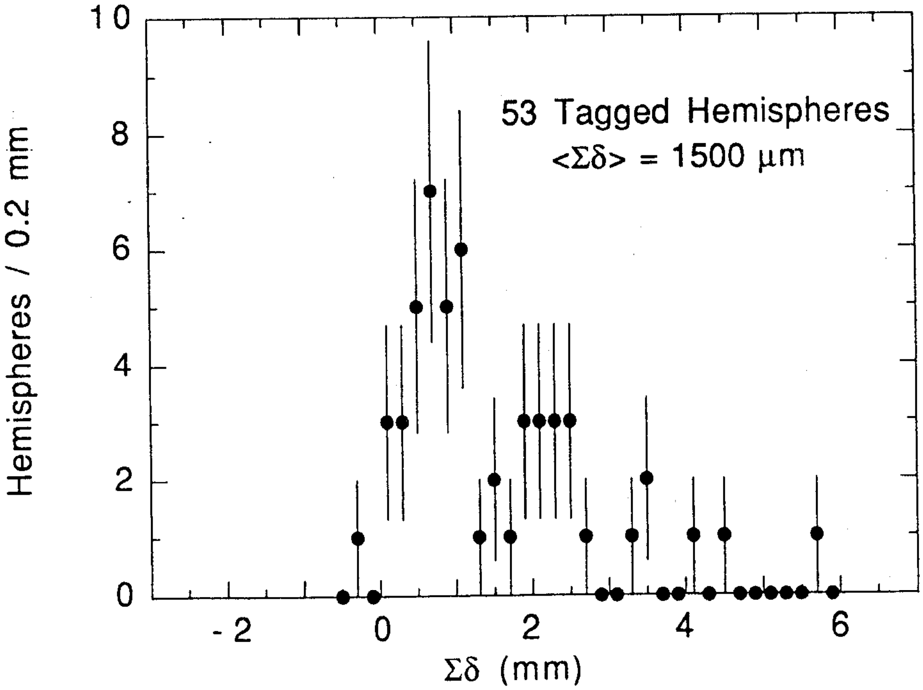

Figure 86 Σδ distribution for the 53 tagged hemispheres.

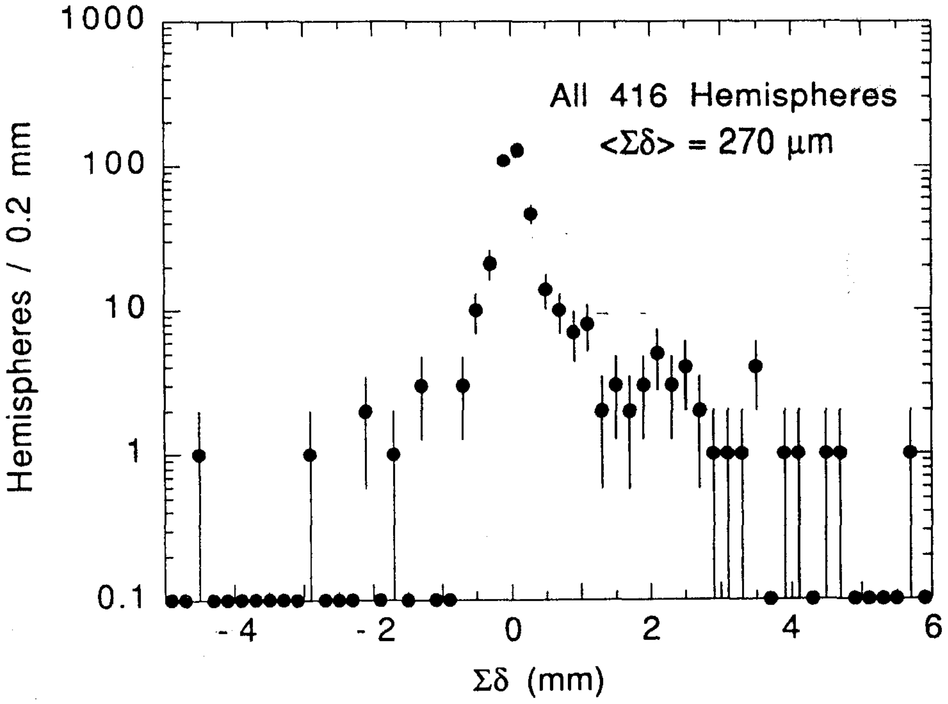

Figure 87 Σδ distribution for the 416 hemispheres from the entire Mark II hadronic data.

6.3 Two Spectacular Bottom Events

The two most spectacular $b\bar{b}$ events are displayed in Figure 88. These two events contributed to the two largest Σδ entries in the tagged sample. The first is a two-jet event in which both hemispheres were tagged. The upper jet has a decay vertex 12 mm from the interaction point in the *xy* plane, which is significantly longer than the average decay length of 2 mm. Four tracks emanate from the decay vertex with the total electric charge equal to zero. Their invariant mass is 3.1 GeV, consistent with coming from a B hadron. The $\gamma\beta$ of the four tracks probably overestimates the $\gamma\beta$ of the B hadron, but if we use this value the decay time of the candidate B is 4.1 ps. If instead we use the average $\gamma\beta$ for bottom hadrons of 6.0, then we arrive at a reasonable upper bound for the decay time of 6.5 ps. A bottom hadron with a decay time in excess of $5\tau_b$ has a 0.7% chance of occurring, so such a decay although spectacular is not completely unexpected from ~90 B hadron decays. The relevant properties of the B candidate are listed in Table 31.

The opposite jet in the event also has four tracks which miss the primary vertex by more than three standard deviations. As many as eight tracks make up the

Table 31 Properties of our two most spectacular $b\bar{b}$ event candidates.

Property	Run 21185 Rec 651		Run 21213 Rec 313	
	1st hemi	2nd hemi	1st hemi	2nd hemi
# trks with $\delta/\sigma \geq 3$	4	4	3	1
$\Sigma\delta$ (mm)	4.43	1.33	5.80	0.48
# trks consistent with decay vtx	4	8	5	—
Decay length in xy plane (mm)	11.7	3.8	12.5	—
ΣE_{chg} (GeV)	29.7	24.7	23.3	—
Invariant mass (GeV)	3.1	4.0	2.3	—
Σ(charge)	0	0	−1	—
Estimated lifetime τ_b (ps)	4.1 – 6.5	2.1	4.2 – 6.9	—

decay vertex which is separated by 4 mm from the Z^0 production site. It is difficult to tell exactly which tracks come from the secondary vertex because some of the tracks are consistent with both the primary vertex and the secondary B decay vertex. The reconstructed decay time is 2.1 ps.

The second spectacular event also has a separated vertex with a decay length of 12 mm. The jet hemisphere has three tracks with $\delta/\sigma \geq +3$, one track with $\delta/\sigma \leq -3$, and a fifth track that is consistent with both the B candidate and the primary vertex. Using the $\gamma\beta$ from the partial reconstruction of the B hadron with the 5 charged tracks, the proper decay time is estimated at 4.2 ps. However, the value of $\gamma\beta$ for this jet corresponds to an unphysical B momentum of 53 GeV. Using $\langle\gamma\beta\rangle = 6.0$ instead, we reach an upper bound of 6.9 ps for the decay time. The opposite hemisphere was not tagged and has no discernible decay vertex.

6.4 The Untagged $\Sigma\delta$ Distribution

We now will describe a procedure for extracting the B lifetime from the untagged $\Sigma\delta$ distribution. The $\Sigma\delta$ distribution for the 53 hemispheres opposite the tag show a clear exponential behavior and has a mean of $\langle\Sigma\delta\rangle = 855 \pm 153\mu\text{m}$. The simplest method to measure the lifetime is to determine what value of τ_b in the Monte Carlo will reproduce the mean of the distribution. Two factors prompt the mean of the untagged $\Sigma\delta$ distribution to increase with τ_b. First, the $\langle\Sigma\delta\rangle$ for B jets rises steadily with τ_b as seen in Figure 84. Second, the purity of the sample will also

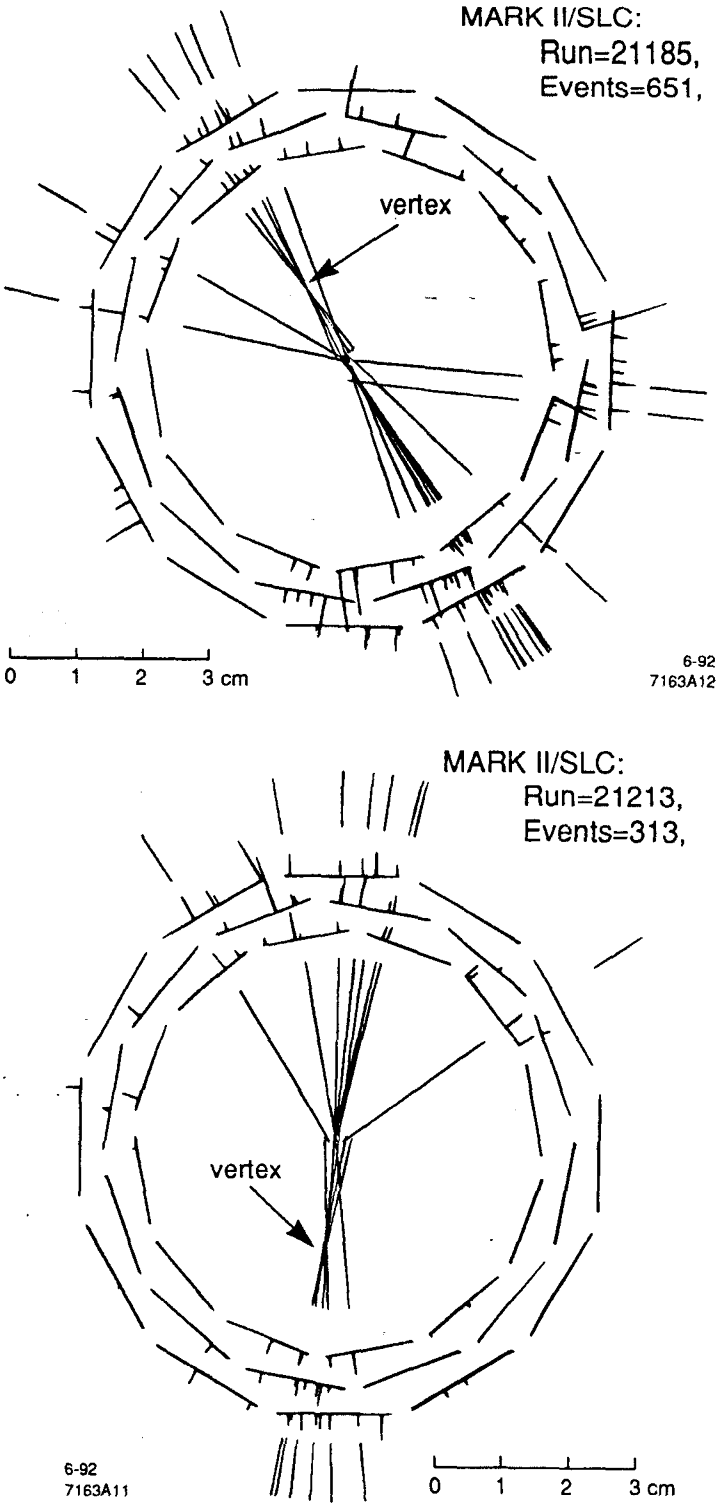

Figure 88 Two of the most spectacular bottom event candidates. Both events have a separated vertex that is over 1 cm from the Z^0 decay vertex. Only vertex quality tracks are shown.

increase slightly since the B hemispheres are tagged somewhat more efficiently. However, the latter effect is marginal; for instance, the purity of the tag increases from 79.5% to 83.0% as the generated lifetime for $b\bar{b}$ events doubles from 1 ps to 2 ps (see Figure 74).

6.4.1 Measured Lifetime from a Fit to the $\Sigma\delta$ Distribution

We can also determine the B lifetime through a fit to the entire untagged $\Sigma\delta$ distribution by maximizing the logarithm of the likelihood function. A maximum log likelihood fit is almost always statistically superior since it uses the entire shape of the distribution rather than just the mean of the distribution.[87] The likelihood fit can also be made less sensitive to fluctuations in the tails of the distribution, compared to the mean. The ability to perform a multi-parameter fit offers yet another advantage. For instance, both the lifetime and the purity can be extracted from a two-parameter likelihood fit, which would give us another handle on the performance of the impact parameter tag. However, our limited Z^0 data prevents us from taking advantage of this last feature. Because the vertex detectors allow precision measurements of the individual $\Sigma\delta$'s, we shall see that the statistical power between a one-parameter likelihood fit and the mean of the $\Sigma\delta$ distribution are nearly equivalent.

The probability distribution for the untagged $\Sigma\delta$ distribution used in the likelihood fit can be expressed as

$$F(\Sigma\delta) = \alpha_b F_b(\Sigma\delta, \tau_b) + \alpha_c F_c(\Sigma\delta) + \alpha_{uds} F_{uds}(\Sigma\delta) \tag{40}$$

where F_{uds}, F_c, and F_b are the normalized $\Sigma\delta$ probability distributions for *uds*, charm, and bottom jet hemispheres, respectively. The α_i's are the fraction of each quark flavor in the untagged sample. From Table 29 on page 136 we expect α_{uds}=0.073, α_c=0.119, and α_b=0.808. The logarithm of the likelihood function can be written as $\sum \log F(\Sigma\delta_i)$, where the sum runs over all 53 of the $\Sigma\delta_i$'s in the untagged sample. The lifetime is simply the value of τ_b that maximizes the log likelihood. Likewise, a multi-parameter fit maximizes $\sum \log F(\Sigma\delta_i)$ with respect to each parameter.

The probability distributions for *uds* and charm events are taken directly from the Monte Carlo distributions shown in Figure 82. The distribution for bottom hemispheres has a more complex shape since it evolves as a function of the B lifetime. We can approximate $F_b(\Sigma\delta,\tau_b)$ analytically as

$$\begin{aligned} F_b(x,\tau_b) &= [\alpha_1 E(x,\lambda_1) + \alpha_2 E(x,\lambda_2) + (1-\alpha_1-\alpha_2)\,\delta(x)] \\ &\otimes [(1-\beta)\,G(x,\sigma_c) + \beta T(x,\lambda_t)] \end{aligned} \tag{41}$$

where $E(x,\lambda_i)$ is an exponential decay function with decay length λ_i, $\delta(x)$ is the Dirac delta function, $G(x,\sigma_c)$ is a gaussian function of width σ_c, and $T(x,\lambda_t)$ is a two-sided symmetric exponential of decay length λ_t.† The symbol ⊗ denotes the convolution between two functions. The functions E, δ, G, and T are all normalized to one. The term

$$\alpha_1 E(x,\lambda_1) + \alpha_2 E(x,\lambda_2) + (1-\alpha_1-\alpha_2)\,\delta(x) \tag{42}$$

can be thought of as the "physics" function which describes the case of perfect track resolution and no beam motion. Of course there are subtle distinctions between the two distributions since tracks from charm or strange decays can cause $\Sigma\delta$ to be negative. The physics function is convoluted by the symmetric function

$$(1-\beta)\,G(x,\sigma_c) + \beta T(x,\lambda_t) \tag{43}$$

made up of a gaussian with exponential tails and can be considered a "pseudo-resolution" function.

$F_b(\Sigma\delta,\tau_b)$ has a total of seven free parameters: the two amplitudes of the exponential decay functions, α_1 and α_2, the two decay lengths, λ_1 and λ_2, the core gaussian width, σ_c, the decay length of the two-sided exponential function, λ_t, and the fractional area under the exponential tails of the resolution function, β. The evolution of $F_b(\Sigma\delta,\tau_b)$ as the lifetime increases can be checked by generating $b\bar{b}$ events for a number of discrete values of the B lifetime, spanning from 0.75 ps to 3.75 ps. From the Monte Carlo sample of 20,000 events, roughly 3500 $b\bar{b}$ events passed the hadronic event cuts. These events were generated with τ_b=1.24 ps. Rather than creating a new batch of MC events for each value of τ_b and running the entire collection through the full Mark II detector simulation, we reused the same 3500 MC $b\bar{b}$ events by rescaling each decay time by a constant factor to reflect the new lifetime distribution. The B decay lengths are subsequently rescaled by the same factor. The impact parameter for tracks from B decays is recomputed by moving the primary vertex by the change in decay length along the B hadron

---

† The symmetric exponential is of the form $T(x,\lambda_t) = \frac{1}{2\lambda_t}\exp(-|x|/\lambda_t)$.

direction. Tracks from *udsc* events or fragmentation tracks from $b\bar{b}$ events keep the same impact parameter.

At each lifetime, a binned maximum log likelihood fit is performed on the $\Sigma\delta$ distribution for bottom hemispheres to optimize the seven parameters in $F_b(\Sigma\delta,\tau_b)$. Each parameter is next approximated by a quadratic polynomial in τ_b so that the probability density $F_b(\Sigma\delta,\tau_b)$ will be a smooth function of the lifetime. The parameters' functional dependencies on τ_b are plotted in Figure 89. Not shown is the value for σ_c which is a constant equal to 160 μm. Because the impact parameters are only rescaled to reflect the change in generated B lifetime, the MC points are moderately correlated. The distributions include the same fragmentation tracks, the same B decay multiplicities, and the same B momenta. The statistics of the MC sample introduces a scaling error of ~2% for the parameters, but the basic lifetime evolution of $F_b(\Sigma\delta,\tau_b)$ is well described.

Any parametrization simpler than the one described above, for instance the convolution of an exponential decay function and a gaussian function, inadequately models the $\Sigma\delta$ distribution for B hemispheres. The delta function is justified because on average 8% of the hemispheres do not contain any tracks from the B hadron due to a combination of low B decay multiplicities and track finding inefficiencies. The rationale for demanding a second exponential decay function cannot be isolated to a particular source, but it does describe the $\Sigma\delta$ distribution more accurately, especially for small values of $\Sigma\delta$ since λ_2 is always about one-third the value of λ_1. The second exponential probably represents the combined effects of low momentum B hadron production, low multiplicity B decays, and enhanced impact parameters from tertiary charm decays. Although $\alpha_1 + \alpha_2$ is relatively constant at ~0.85, the amplitude of the second exponential $E(x, \lambda_2)$ diminishes rapidly as a function of τ_b. Hence the physics function does not evolve as a simple scaling of the lifetime. On the other hand, the pseudo-resolution function changes shape only slightly as a function of τ_b. It consists of a gaussian core of width 160 μm augmented with a two-sided exponential of decay length ~800 μm. The two-sided exponential covers 20-25% of the fractional area of the pseudo-resolution function.

Finally, we should note that the most important point of parametrizing the $\Sigma\delta$ distribution for bottom hemispheres is to arrive at a description of $\Sigma\delta$ which is analytic in τ_b. Although desired, it is not critical that we fully understand the origins of each term in Eqn. (41). Shown in Figure 90 is the semi-log plot of the optimized fit $F_b(\Sigma\delta,\tau_b)$ overlaid on the $\Sigma\delta$ distribution for B hemispheres generated

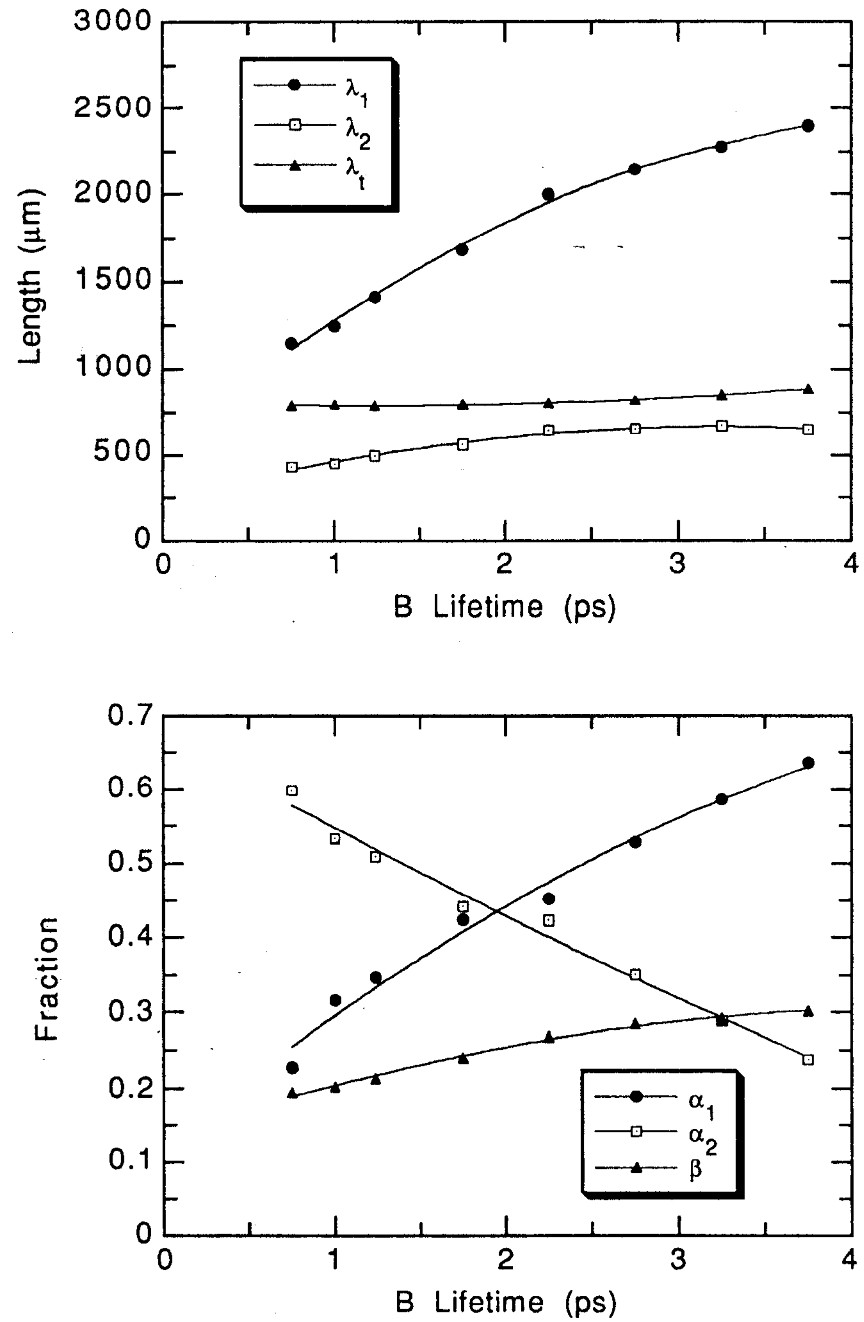

Figure 89 Parameters in Eqn. (41), which describe the shape of the $\Sigma\delta$ distribution for bottom hemispheres, as a function of the B lifetime. We use the quadratic approximation to the parameters in the likelihood fit of the data. Not shown is σ_c, which is relatively constant at ~160 μm.

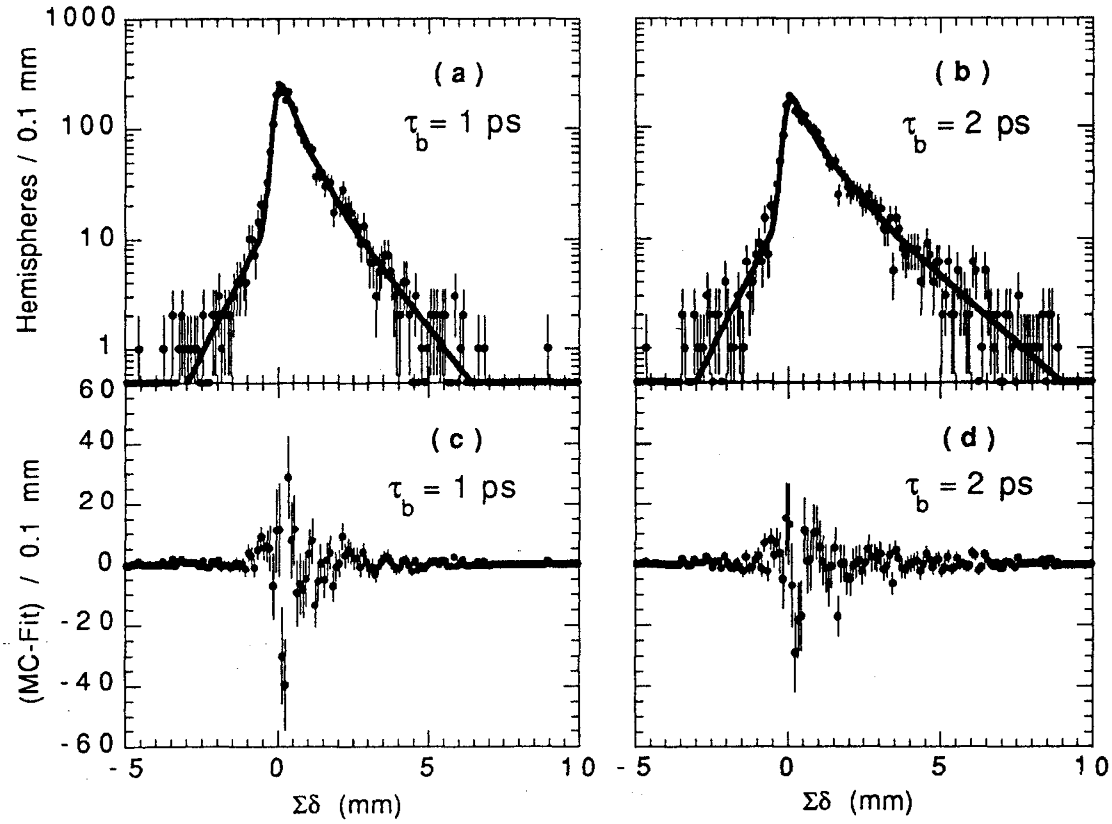

Figure 90 Monte Carlo Σδ distribution for B hemispheres (points) and likelihood fit (curve) using the parametrization in Eqn. (41) and values from Figure 89. For both a B lifetime of (a) 1 ps and (b) 2 ps, the fit accurately describes the MC distribution. Figures (c) and (d) show the difference between MC and fit values.

at two different lifetimes, 1 ps and 2 ps. The lower two plots present the difference between the MC and the fit. Both plots reveal that the fit accurately describes the Monte Carlo distribution over the entire range in Σδ.

6.4.2 Statistical Error: the Ensemble Method

Because of the limited size of the untagged sample, we choose τ_b to be the only free parameter in the log likelihood fit to the opposite hemisphere Σδ distribution. The quark flavor fractions in Eqn. (40) are assigned their Monte Carlo expectations. The purity α_b increases slowly with τ_b, and the ratio α_c/α_{uds} is fixed at 0.62. The software package MINUIT [86] performs the one-parameter lifetime fit and calculates the uncertainty. The fit yields

$$\tau_b = 1.68^{+0.47}_{-0.40} \text{ ps} \tag{44}$$

where the errors are statistical.

Performing a two-parameter log likelihood fit in which the lifetime and the purity are free parameters yields a lifetime of 1.16±0.36 ps and a purity of 116±17%. The value for the purity is unphysical and 2σ higher than the MC expectation, which suggests a deficiency in the number of hemispheres with $\Sigma\delta$ near the origin and pulls the lifetime down from the one-parameter likelihood fit for τ_b. Although the expected tag purity is relatively insensitive to the generated B lifetime, when treated as free parameters in the likelihood fit, the lifetime and the purity become extremely correlated. With such low statistics, the fit is sensitive primarily to the mean of the $\Sigma\delta$ distribution, and this quantity can remain invariant as long as the product of the fit lifetime and fit purity remains constant. Hence, the results of the two-parameter likelihood fit are not very reliable.

We need to apply caution when interpreting the accuracy of the statistical errors returned from the likelihood fit. Even though MINUIT accommodates asymmetric errors, the accuracy breaks down for low statistics. At the level of 53 hemispheres MINUIT underestimates the errors by about 20%. This deficiency emerges because the likelihood fit fails to account for statistical fluctuations in the B purity, the B decay multiplicity, the average B fragmentation, the number tracks from K_s^0 and Λ decays, to name a few. In a one-parameter likelihood fit with the lifetime as the only free parameter, MINUIT assumes that the statistical error arises solely from fluctuations in the decay times of B hadrons. Normally these other "hidden" variations are absorbed in the systematic uncertainties. However, as an example, the systematic uncertainty due to our knowledge of the mean bottom fragmentation from the LEP experiments is smaller than the statistical fluctuations of $\langle x_E \rangle_b$ in a sample of 53 untagged hemispheres. In the limit of large statistics, the systematic uncertainty in $\langle x_E \rangle_b$ overwhelms the uncertainty due to statistical fluctuations, hence the total error is properly estimated.

A procedure that calculates the statistical errors correctly for a small data set is the Monte Carlo method, often called the ensemble method. [87] In this method, Monte Carlo ensembles of untagged hemispheres are generated, each the same size as the untagged hemisphere sample in the Mark II data. The collection of ensembles possesses all the statistical fluctuations that affect the data. These not only include fluctuations in B decay times between ensembles, but also fluctuations in purity, B decay multiplicity, B momentum, and resolution tails.

The ensemble method requires Monte Carlo events to be generated for discrete values of the B lifetime. We used one set of 20,000 MC events with full detector simulation generated with τ_b=1.24 ps to construct ten batches of 20,000 events, each with a different value of τ_b in the range of 0.75 ps to 3.5 ps. This procedure was preferred over generating ten fully independent batches of 20,000 MC events due to the computational magnitude of that task. Since the purity in the tag is high, the same *udsc* events can be used for all ten batches without making the untagged $\Sigma\delta$ distributions between batches excessively correlated. The $b\bar{b}$ events are also recycled, but are modified in a way to reflect the B lifetime in each batch. We employ the same procedure used to study the lifetime evolution of $F_b(\Sigma\delta,\tau_b)$ in the previous section: impact parameters from B decay tracks are reevaluated by moving the primary vertex a distance along the B hadron direction so that the decay length scales with the decay time. This time, rather than rescaling all the decay times in a batch by the same factor, the decay times are rethrown using an exponential distribution with the appropriate lifetime. Reshuffling the decay times ensures that the collection of $b\bar{b}$ events in different batches are less correlated. Each set still has the same mean B decay multiplicity and the same mean B fragmentation $\langle x_E \rangle_b$. However, as seen in Table 30 on page 143, nearly half of the standard deviation in the $\Sigma\delta$ distribution for bottom is attributed to the exponential distribution of decay times.

The number of tagged hemispheres in each batch grows with lifetime from about 3000 to 4100. Hemispheres opposite the tag are divided into ensembles containing 53 hemispheres each; the number of ensembles range from 56 for τ_b=0.75 ps to 77 for τ_b=3.5 ps. The MINUIT package determines the B lifetime from a one-parameter likelihood fit to the $\Sigma\delta$ distribution of each MC ensemble, and the 68% confidence interval is drawn for the collection of ensembles at each discrete value of the generated B lifetime (Figure 91). The 1σ intervals for a specific lifetime describes the rms deviation in fit lifetimes expected for an ensemble generated with that lifetime. However, we wish to ask a very different question. We need to know over what range of generated B lifetimes $\tau_{b,gen}$ is it probable that an ensemble of 53 untagged hemispheres yields a maximum log likelihood fit lifetime $\tau_{b,MLL}$ that agrees with the value of 1.68 ps observed in the Mark II data. The answer is obtained by first connecting all the 68% confidence intervals to construct the 1σ contour, which is the shaded region in Figure 92. Next, a horizontal line is drawn at $\tau_{b,MLL} = 1.68\text{ps}$, and the intersection of the line with the 1σ contours projected onto the x-axis is the 68% confidence interval for the measured B lifetime.

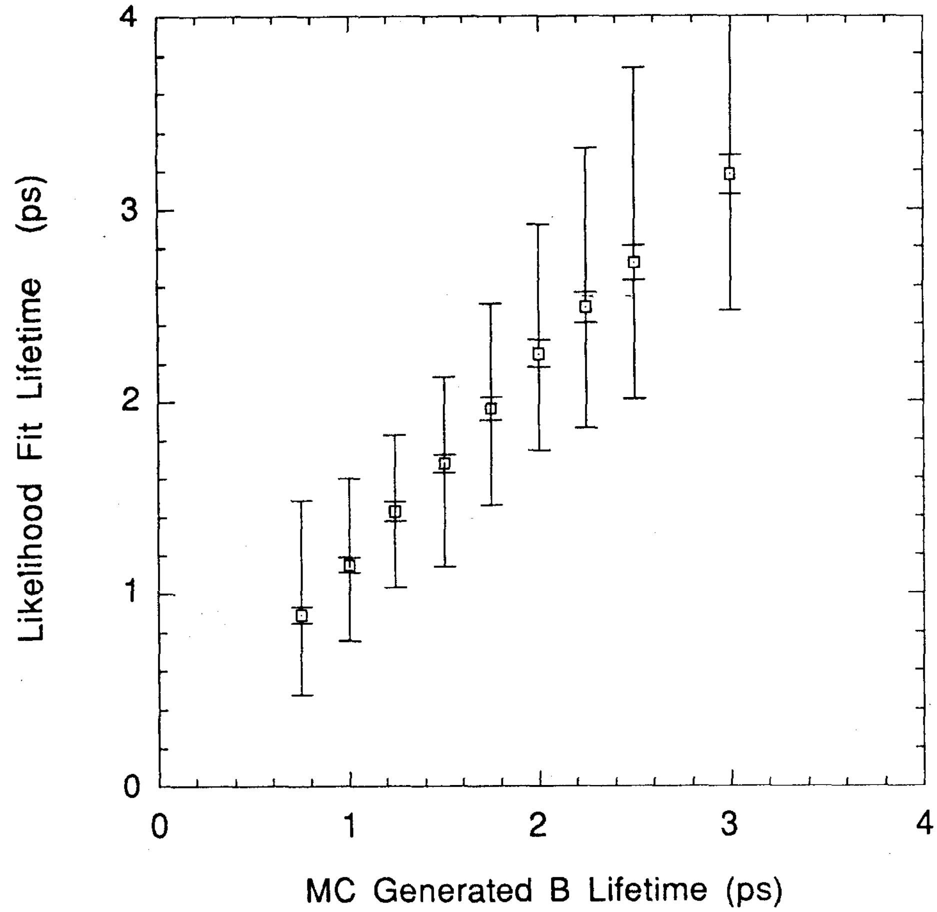

Figure 91 68% confidence intervals of the fit B lifetime from ensembles of MC untagged hemisphere samples constructed for a discrete set of generated B lifetimes in the range 0.75 ps to 3.5 ps. The data points (boxes) define the high statistics calibration curve between $\tau_{b,gen}$ and $\tau_{b,MLL}$, and are accurate to ~4%.

A calibration curve can be constructed to determine the most probable value for the measured B lifetime. The likelihood fit is applied to the $\Sigma\delta$ distribution for the entire untagged sample at each discrete value of the generated lifetime. The curve inside the shaded 1σ contour shows this relation between the MC generated lifetime $\tau_{b,gen}$ and the fit lifetime $\tau_{b,MLL}$. It is linearly approximated as

$$\tau_{b,MLL} = (0.114 \pm 0.018) + (1.047 \pm 0.011)\,\tau_{b,gen} \tag{45}$$

The data points on the calibration curve are not fully independent; only fluctuations in decay times are properly modeled. The other fluctuations (number of tagged *udsc* hemispheres, B decay multiplicities, B momentum, etc.) are the same

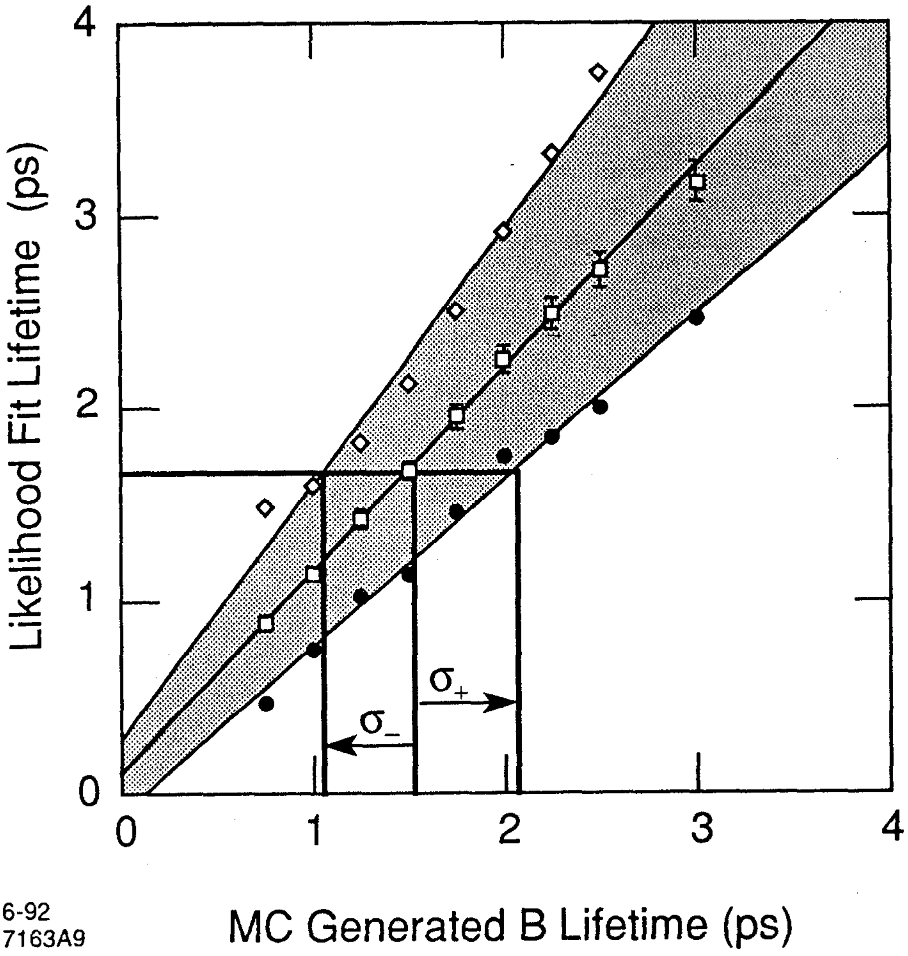

Figure 92 The shaded region is the $\pm 1\sigma$ contour, and the diagonal line in the interior is the calibration curve which relates the fit lifetime to the MC generated lifetime. A thick line, drawn horizontally at 1.68 ps, corresponds to the fit value measured from the Mark II untagged data. The intersection of this horizontal line with the calibration curve and the 1σ contour provides the corrected B lifetime and its 1σ errors. From the projections onto the x-axis, we measure $\tau_b = 1.53\ ^{+0.55}/_{-0.45}$ ps, where the error is statistical only.

for all the calibration points and will contribute to an overall uncertainty in the scale of ~2%. The χ^2 reflects this correlation between calibration points, and is 0.2 per degree of freedom.

Because the fit lifetime is not identically equal to the generated lifetime, the fitting procedure introduces some bias into the B lifetime measurement. The likelihood fit returns a value that is about 10-15% higher than the generated lifetime, and requires the calibration curve to correct this overestimate. The bias exists because all the fully simulated MC $b\bar{b}$ events, rather than just the untagged

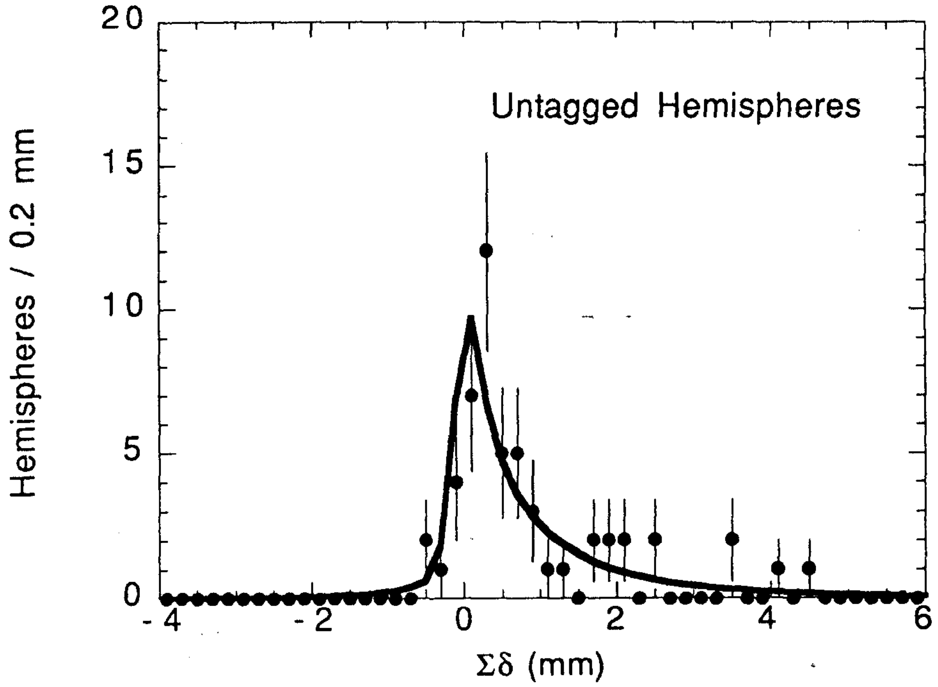

Figure 93 Σδ distribution for the 53 untagged hemispheres overlaid with the likelihood fit (curve). The fit accurately describes the positive tail of the distribution; for instance, 8.0 (6.8) hemispheres lie beyond 2 mm in the data (fit).

B hemispheres, are used to parametrize the Σδ distribution for bottom hemispheres, namely the function $F_b(\Sigma\delta,\tau_b)$. However, the mean of the Σδ distribution for untagged B hemispheres is approximately 8% larger than the mean for all B's. Although the decay times in the untagged bottom sample are bias-free, the thrust axis of tagged $b\bar{b}$ events are preferentially more perpendicular to the beam axis since the tagging efficiency for these events is higher. The average $|\sin\theta_{thrust}|$ for tagged B's is ~4% larger than that for all B hemispheres. The tagging efficiency is higher for two reasons. First, the decay length projected onto the *xy* plane increases, which leads to a corresponding increase in the impact parameters of tracks from B decays. Second, more tracks from B decays are included in the sum, since the event is better contained in the fiducial volume of the detector. Since both B jets in an event generally have equal but opposite polar directions, the same effects that increase the tagging efficiency will also increase the $\langle\Sigma\delta\rangle$ in the opposite hemisphere.

The median of the likelihood fits to the collection of ensembles at each generated MC lifetime can also be used instead of the full statistics likelihood fit. This leads to a relation between $\tau_{b,gen}$ and $\tau_{b,MLL}$ that differs by less than 4% from the relation expressed in Eqn. (45). This amount is negligible compared to the statistical accuracy of our lifetime measurement.

Finally, an analytic parametrization for $F_b(\Sigma\delta,\tau_b)$ which is simpler than the expression given in Eqn. (41) could have been used; however, the likelihood fit would have had an even larger lifetime bias. Although we can always compensate for the bias by constructing a calibration curve from the MC, it is usually safer to minimize the correction factor by choosing a more representative parametrization.

Using Figure 92, a horizontal line is drawn across at $\tau_{b,MLL} = 1.68\text{ps}$, which corresponds to the log likelihood value for the 53 hemispheres opposite the tag in the hadronic Z^0 data. The corrected lifetime and its statistical error occur at the intersection of the horizontal line with the calibration curve and the 1σ contours. From this plot, we measured the B lifetime to be

$$\tau_b = 1.53^{+0.55}_{-0.45}\ \text{ps} \tag{46}$$

The statistical error is asymmetric and roughly 32%. The fit shows good agreement with the tagged $\Sigma\delta$ distribution as demonstrated in Figure 93. The fit has a mean of 750 μm, which is about 15% lower than the mean of the distribution. This will lead to a larger value for the lifetime when we use $\langle\Sigma\delta\rangle$ as the lifetime estimator in the next section. The exponential tails are well described by the fit. The number of hemispheres with $\Sigma\delta$ beyond 2 mm is eight in the data and 6.8 in the fit. There are no hemispheres in the data with $\Sigma\delta \le -1$ mm and 0.9 in the fit.

6.4.3 Measured Lifetime from the $<\Sigma\delta>$

We can use the mean of the untagged $\Sigma\delta$ distribution instead of the likelihood lifetime fit $\tau_{b,MLL}$ as an alternate estimator of the B lifetime. The untagged $\langle\Sigma\delta\rangle$ is computed for each of the Monte Carlo ensembles that were constructed in the previous section. A plot analogous to Figure 92 relates the untagged $\langle\Sigma\delta\rangle$ to the generated B lifetime $\tau_{b,gen}$. The calibration curve is constructed from the $\Sigma\delta$ distribution mean of the entire untagged hemisphere sample, computed at each of ten discrete lifetime values between 0.75 ps and 3.5 ps. The relation between the untagged $\langle\Sigma\delta\rangle$ in microns and $\tau_{b,gen}$ in ps can be approximated by a second order polynomial:

$$\text{untagged } \langle\Sigma\delta\rangle = (85 \pm 12) + (507 \pm 14)\tau_{b,gen} + (34 \pm 4)\tau^2_{b,gen} \tag{47}$$

The calibration curve has a 2% uncertainty in its scale. The 1σ contours are constructed from the 68% confidence intervals from the collection of untagged ⟨Σδ⟩'s at each of the ten discrete lifetime values. The calibration curve and the 1σ contours are drawn in Figure 94.

In the Mark II data, the hemispheres opposite the tag possess a mean of $\langle \Sigma\delta \rangle = 855 \pm 153\mu\mathrm{m}$ which leads to a measurement of the B lifetime of

$$\tau_b = 1.72^{+0.73}_{-0.46}\ \mathrm{ps} \tag{48}$$

Using the geometric mean of the asymmetric errors, the statistical error is comparable to the likelihood fit error. Even though the two methods operate on the identical untagged sample, comparing the lifetime difference between the two different procedures for the MC ensembles, we expect an rms difference of ±0.22 ps. The measured lifetime difference of $\Delta\tau_b$=0.19 ps is within errors.

6.5 The Tagged Σδ Distribution

Yet another check on the B lifetime measurement utilizes the 53 tagged hemispheres. There is a significant overlap between the tagged and the untagged sample: 22 B jets are shared from the 11 double tagged events. However, that still leaves about 20 independent B hemispheres in the tagged sample. The collection of tagged hemispheres represents a biased sample of B hadrons, with an average decay time estimated by the MC to be roughly $2\tau_b$. The biased decay times is evident by the mean of the distribution, $\langle \Sigma\delta \rangle = 1500\mu\mathrm{m}$, which is nearly double the mean of the untagged distribution.

The B lifetime is measured by comparing the mean of the tagged Σδ distribution to the MC calculated mean, which rises as a function of τ_b. Again, the ensemble method is used to calculate the statistical error. The calibration curve and the 1σ contours generated from ensembles of MC tagged samples yield a B lifetime of

$$\tau_b = 1.46^{+0.53}_{-0.35}\ \mathrm{ps}. \tag{49}$$

Although this value is shorter than the lifetime obtained from the 53 hemispheres opposite the tag using the likelihood fit, the difference is not significant. The rms lifetime difference between the two methods for the collection of MC ensembles is about ±0.44 ps, indicating that the difference of 0.07 ps is well within the expected range.

Taking the geometric mean of the asymmetric error, the percentage error in the lifetime is on par with error from the untagged sample. However, the decay times

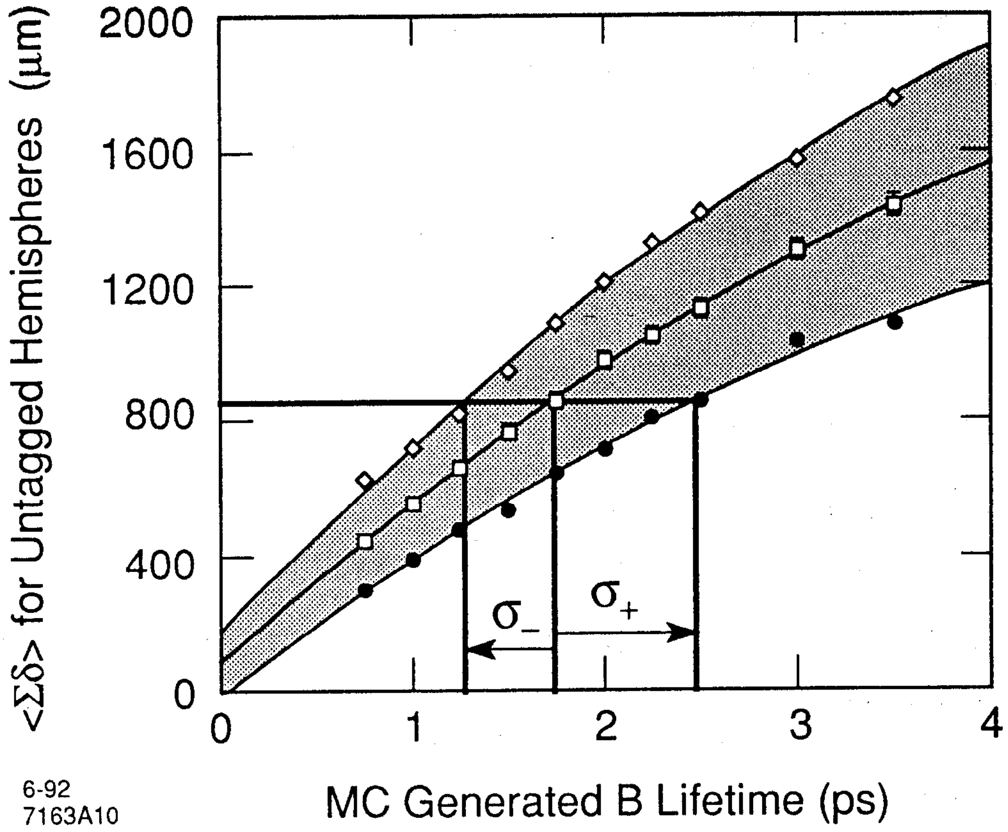

Figure 94 The 1σ contour (shaded region) and the calibration curve (fit to the boxes) convert the mean $\Sigma\delta$ for the untagged hemispheres into a measurement of the B lifetime. A thick line, drawn horizontally at 855 μm, corresponds to the $<\Sigma\delta>$ of the Mark II untagged sample. The measured B lifetime from the ensemble method is $\tau_b = 1.72\ ^{+0.73}/_{-0.46}$ ps, where the error is statistical only.

are highly biased since the tag efficiency is not a flat function of the decay time, as seen in Figure 75 on page 133. Any uncertainty in the tag efficiency, especially in the region of rapid change from 0 ps to 2 ps, will lead to a systematic uncertainty in the lifetime. Since we rely heavily on the MC to remove this decay time bias, we use the results from the tagged sample only as a consistency check.

6.6 The $\Sigma\delta$ Distribution from All Hadronic Events

There is one final subset of the hadronic data that we can examine, namely the entire hadronic set of 416 hemispheres, i.e. without any bottom enrichment scheme. This more than doubles the number of B jets but also causes a serious drop in purity since the fraction of hadronic Z^0 decays that produce bottom quarks is only 22%. The probability distribution for $\Sigma\delta$ can be written analogous to Eqn. (40) as

$$F(\Sigma\delta) = f_b F_b(\Sigma\delta, \tau_b) + f_c F_c(\Sigma\delta) + f_{uds} F_{uds}(\Sigma\delta) \tag{50}$$

where F_{uds}, F_c, and F_b are the probability distributions for *uds*, charm, and bottom jet hemispheres, respectively. The f_i's set to the branching fractions in the MC for each quark flavor after the event selection cuts: f_{uds}=0.592, f_c=0.181, and f_b=0.227.

The MC ensembles are constructed to include exactly 53 tagged hemispheres, so that the ensembles will have a total of 380 to 530 hemispheres, depending on the generated lifetime. Each ensemble undergoes the same likelihood fit as the data, and the results are used to compute the statistical error. Just like the previously discussed methods, a calibration curve is constructed to convert the likelihood fit lifetime $\tau_{b,MLL}$ to the MC generated lifetime $\tau_{b,gen}$. This time, the calibration curve contains very little bias compared to the one for untagged hemispheres because both the functional form $F(\Sigma\delta)$ and the MC ensembles are constructed from all hadronic events. Over the range of 1 ps to 3 ps, $\tau_{b,MLL}$ is within 3% of $\tau_{b,gen}$.

The maximum log likelihood fit on the data yields $\tau_{b,MLL} = 1.77\text{ps}$ which corresponds to a B lifetime measurement of

$$\tau_b = 1.77^{+0.88}_{-0.36}\ \text{ps} \tag{51}$$

The $\Sigma\delta$ distribution is described well by the fit (Figure 95) and measured value is in good agreement with the results from the tagged sample enriched with bottom hadrons. Again, the tails are well described by the fit. The largest deviation is near a $\Sigma\delta$ of 2 mm. Nevertheless, 26 hemispheres in the data and 19.9 in the fit have $\Sigma\delta \geq 2$ mm, which is not a significant difference. Eight in the data and 6.9 in the fit have $\Sigma\delta \leq -1$ mm.

The statistical performance using the geometric mean of the asymmetric error is slightly worse than the untagged case. It also relies more heavily on an accurate description of the background *udsc* distribution. For these reasons, as with the tagged sample, this measurement is used only as a consistency check.

Since the total number of hemispheres is significantly larger than the tagged sample, we can be assured of some confidence in a two-parameter likelihood fit which extracts both the *B* lifetime and the *B* fraction. This yields τ_b=1.8±0.5 ps and f_b=0.22±0.04, in agreement with expectations. Again, a word of caution: the quoted statistical errors are from MINUIT and hence are underestimated by about 15%.

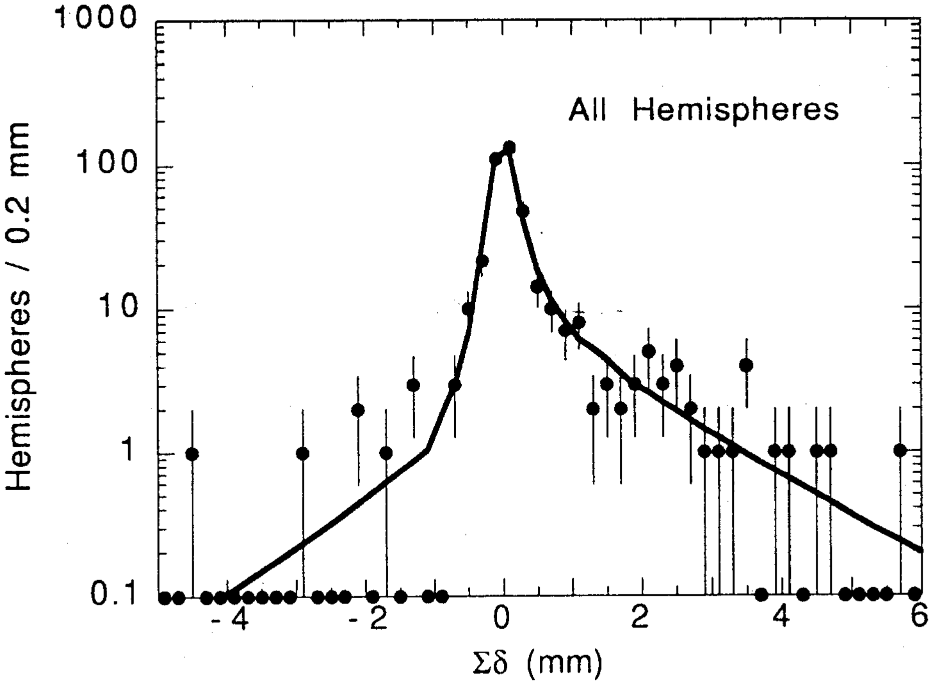

Figure 95 Σδ distribution for all 416 hemispheres overlaid with the likelihood fit (curve). The fit accurately describes the positive and negative tails of the distribution; for instance, 26 (19.9) hemispheres lie beyond 2 mm in the data (fit), and 8 (6.9) hemispheres lie below -1 mm.

In a similar fashion, we can employ $\langle \Sigma\delta \rangle$ as the lifetime indicator. A *B* lifetime of

$$\tau_b = 1.64^{+0.59}_{-0.44}\,\mathrm{ps} \qquad (52)$$

is required to generate the distribution mean of $\langle \Sigma\delta \rangle = 270\mu\mathrm{m}$. The result concurs with the lifetime measurement from the likelihood fit to the untagged Σδ distribution.

6.7 Summary of the Lifetime Measurements

Table 32 lists the lifetime measurements for all the methods. We have used the value $1.53^{+0.55}_{-0.45}$ ps from the likelihood fit to the untagged sample as our quoted B lifetime measurement. This measurement is consistent with the world average of 1.29±0.05 ps. We choose this method because the untagged sample does not contain a bias in decay times like the tagged sample, nor is it as sensitive as the all hemisphere sample to inaccuracies in the background *udsc* Σδ distribution. The other four methods serve as measurement checks.

Table 32 The B lifetime measurements for each of the five methods. We take the fit to the untagged distribution as our quoted value. The untagged, tagged, and all hadronic samples are highly correlated, so averaging the measured values improves the statistical performance by only ~10%. The measured τ_b differences between the fit to the untagged sample and the other methods are all within the rms deviation as predicted by the MC.

Sample	Method	B lifetime (ps)	Measured difference (ps)	MC rms deviation (ps)
53 hemispheres opposite the tag	Likelihood fit	$1.53^{+0.55}_{-0.45}$	≡ 0.00	—
	$\langle\Sigma\delta\rangle$	$1.72^{+0.73}_{-0.46}$	+0.19	±0.22
53 tagged hemispheres	$\langle\Sigma\delta\rangle$	$1.46^{+0.53}_{-0.35}$	−0.07	±0.44
All 416 hemispheres	Likelihood fit	$1.77^{+0.88}_{-0.36}$	+0.24	±0.69
	$\langle\Sigma\delta\rangle$	$1.64^{+0.59}_{-0.44}$	+0.11	±0.66

Also shown in Table 32 are the measured differences between the quoted value and the other methods, and rms lifetime differences between methods as observed in the MC ensembles. The tagged, untagged, and all hemisphere samples do not consist of independent sets of bottom jets, and the range in the MC rms lifetime differences, from ±0.22 ps to ±0.69 ps, strongly reflects the fraction of hemispheres in common. In all cases, the measured lifetime difference is within MC expectations of the rms lifetime difference.

Finally, averaging the lifetime measurements gains us only 10% in statistical power, since the measurements are so strongly correlated. This is true whether we average the measured lifetimes from the untagged and tagged collections, or from all three groups.

6.8 Other Consistency Checks

In this section we will study the measured B lifetime's sensitivity to variations in the impact parameter tag requirements and in the track quality cuts. We also want to ensure that the measurement is not dominated by a few hemispheres with unusually large values of $\Sigma\delta$. This could indicate an unfortunate statistical fluctuation in our small untagged sample, or unforeseen or poorly modeled tails in the impact parameter resolution function.

6.8.1 The Trimmed Mean

We have already shown that the tails and the mean of the $\Sigma\delta$ distribution in both the untagged sample and the entire set of 416 hadronic hemispheres are well described by the likelihood fit. A second way to ensure that one or two hemispheres are not dominating the measurement is to study the "trimmed" mean, which is the mean of the distribution after discarding an equal fraction of entries from both the left and right sides of the distribution. A trim of 0% is just the ordinary mean, whereas a trim of 100% gives the median of the distribution. The MC expects the trimmed mean of the $\Sigma\delta$ distribution for the untagged sample to decline as the trim factor increases; the median is roughly half the mean. We see no appreciable deviation between data and MC for any value of the trim, including small trims (Figure 96). This observation suggests that our value of τ_b is due to a systematic tendency of the entire distribution rather than a couple of outliers with unusually large values of $\Sigma\delta$. Since we are statistics limited, we do not truncate any of the hemispheres from our untagged sample.

The trimmed mean is significantly more important when the shape of the impact parameter distribution is resolution dominated rather than lifetime dominated. In this case, outliers in the tails of the resolution function will degrade the statistical power of the measurement unless a small fraction of the hemispheres are removed. This technique has been employed successfully numerous times in the past with a trim commonly set at 20%. [8][72]

Substantially more deviations exist for the trimmed mean of the 53 tagged hemispheres (Figure 97). The maximum difference between the data and the Monte Carlo predictions is 15% of the measured lifetime, although even this is no greater than expected with our small sample size. Again, the behavior for small trims is excellent. Thus unusually large fluctuations in the decay times of the B's or in the non-gaussian tails of the resolution function appear to be absent.

6.8.2 Sensitivity to the Track Cuts

Any unanticipated sensitivity of the lifetime measurement to the maximum allowed impact parameter δ_{max} can be another indication that the track resolution function is not well understood. The $\langle\Sigma\delta\rangle$ for the untagged sample should increase as the impact parameter cutoff relaxes since the tracks from bottom decays with the

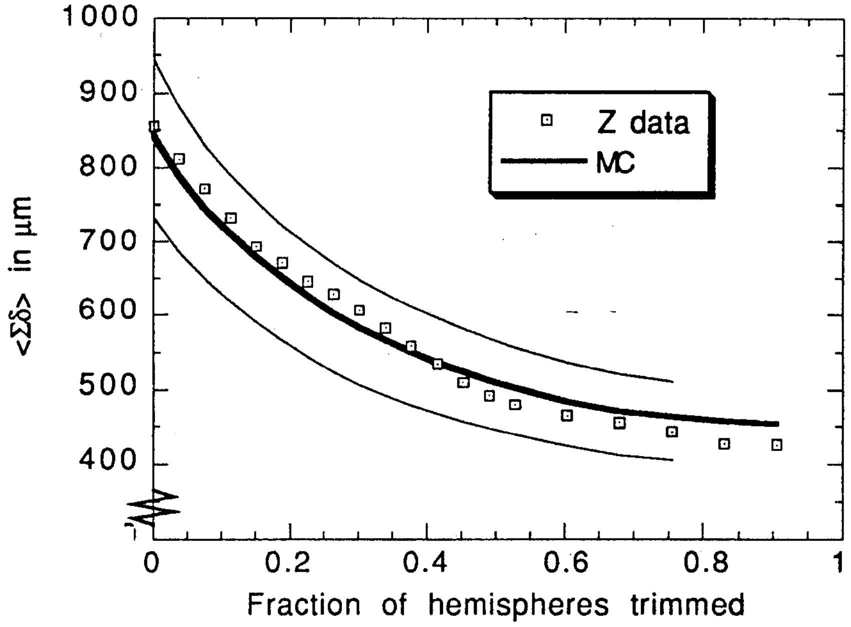

Figure 96 Trimmed mean for the untagged hemisphere sample. A trim of 0 (1) corresponds to the mean (median) of the Σδ distribution. The MC deviates from the data by less than ±15% of the MC lifetime (thin curves) over the entire trimmed range.

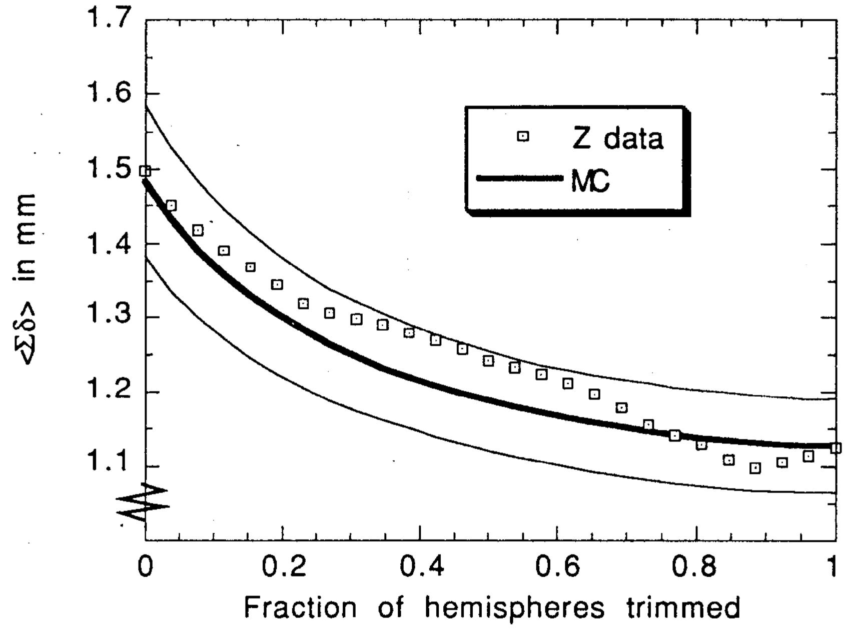

Figure 97 Trimmed mean for the tagged hemisphere sample. The MC deviates from the data by less than ±15% of the MC lifetime (thin curves) over the entire trimmed range.

largest impact parameters will enter the sum. However, the data is not sufficiently sensitive to δ_{max} since there are only two tracks with $|\delta|$ between 2 mm and 10 mm in the untagged sample. On the other hand, there are eighteen tracks with the magnitude of δ in that range if we consider all 416 hemispheres in the data. The $\langle\Sigma\delta\rangle$ as a function of δ_{max} is presented in Figure 98. The data follows the rise of $\langle\Sigma\delta\rangle$ predicted by the Monte Carlo, but the graininess of the data is still quite visible. This is not surprising since the negative tail of the inclusive impact parameter distribution was well modeled by the Monte Carlo as described in Section 4.5.3, and almost all problems with the resolution function should appear in both the positive and negative tails.

We can also examine any sensitivity that the minimum transverse momentum cut has on the lifetime measurement. We selected the minimum cutoff of $P_{xy}\sqrt{\sin\theta}$ to be 0.5 GeV in order to reduce the effects of multiple Coulomb scattering on the $\Sigma\delta$ distribution. This effectively removed about 10% of the tracks. The dependence on the cutoff from 0.25 GeV to 1.25 GeV for the untagged $\langle\Sigma\delta\rangle$ is shown in Figure 99. The $\langle\Sigma\delta\rangle$ in the data falls slightly faster than the MC predictions, but is still in accordance with the Monte Carlo expectations. The decline of $\langle\Sigma\delta\rangle$ reflects the loss of tracks from B decays in the sum as the cutoff increases.

6.8.3 Sensitivity to the Impact Parameter Tag

One final check on the measured lifetime investigates its sensitivity to variations in the impact parameter tag requirements. As discussed in Section 5.2, by modifying the number of required tracks from two to three and the impact parameter significance (δ/σ) from two to four, we displayed a spectrum of tagging efficiencies spanning 15% to 52%. The lifetime was calculated for each alteration of the bottom tag using the untagged $\langle\Sigma\delta\rangle$ as the lifetime estimator. Presented in Figure 100, nearly all the computed lifetimes are within 10% of our measurement using the canonical hemisphere tag of two or more tracks with impact parameters greater than 3σ. Only the tag with the lowest efficiency of 15% lies outside this window, but not surprisingly this tag also has the largest statistical error, since only fourteen bottom jets are expected to be tagged. All variations yield a measured lifetime that is consistent with the world average.

6.9 Systematics

To calculate the B lifetime, we need to determine the purity of the tagged sample and the shapes of the $\Sigma\delta$ distributions for bottom and background (*udsc*)

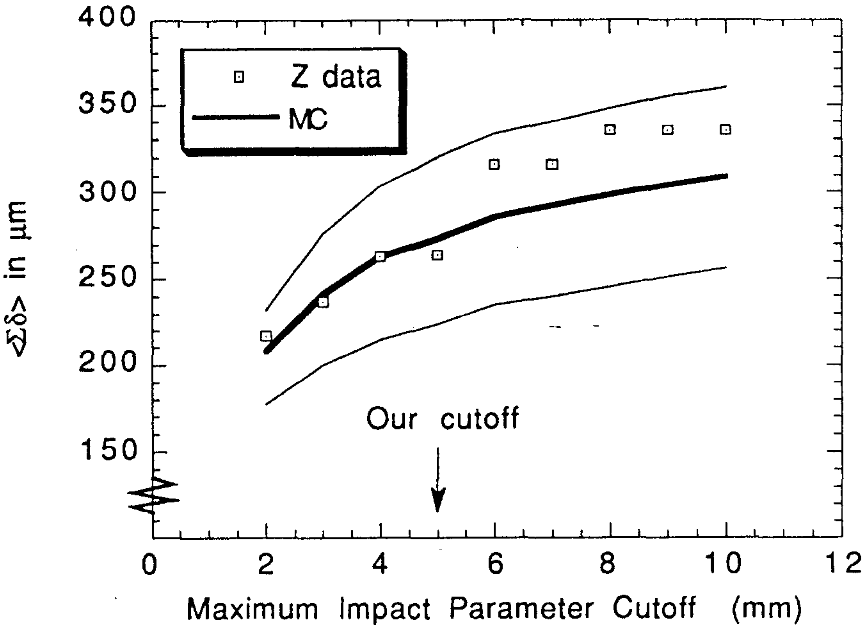

Figure 98 <Σδ> for all 416 hadronic hemispheres as a function of the maximum impact parameter cutoff, δ_{max}. The MC deviates from the data by less than ±30% of the MC lifetime (thin curves).

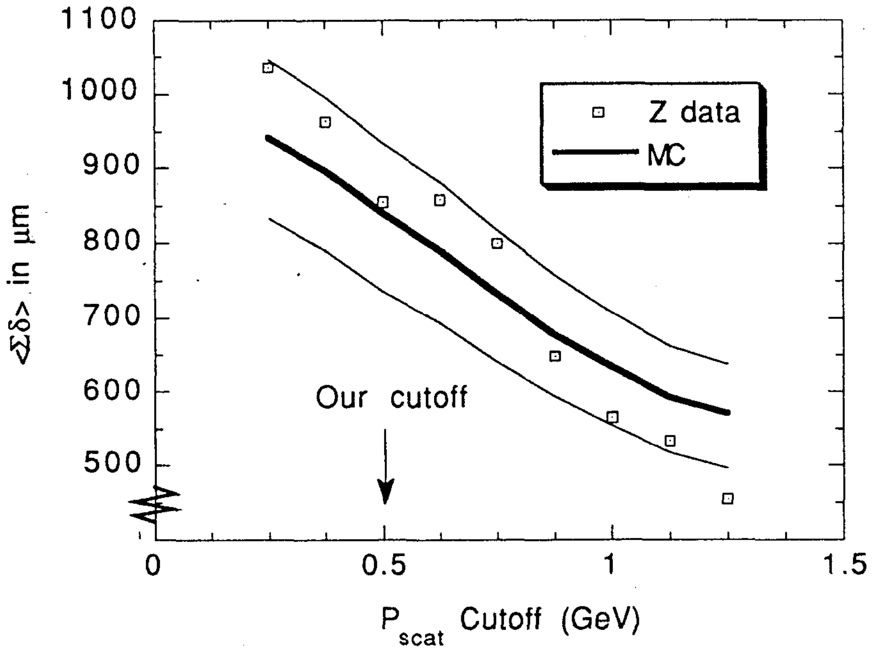

Figure 99 <Σδ> for the untagged hemisphere sample as a function of the minimum transverse momentum cutoff. The MC deviates from the data by less than ±15% of the MC lifetime (thin curves).

hemispheres from the Monte Carlo simulation. There are a variety of effects that cause uncertainties in these quantities which in turn generate systematic errors in the B lifetime. These systematic effects can be subdivided into two categories: uncertainties in the detector performance and uncertainties in the physical parameters of the Monte Carlo.

The impact parameter resolution and the track efficiency fall under the first category. These features have been investigated in great detail in Chapters 2 and 4, but our knowledge of the tracking performance is limited by low statistics; i.e. less than 3000 hadronic charged tracks were available to fine-tune the Monte Carlo detector simulation. The level of multiple Coulomb scattering is guided by the amount of material that a track passes through, and is subject to some uncertainty.

The physical parameters to the Monte Carlo determine the hadronic decay properties of the Z^0 boson. In particular, the B lifetime measurement is sensitive to the production and decay mechanism of B hadrons in $Z^0 \rightarrow b\bar{b}$ events. These input

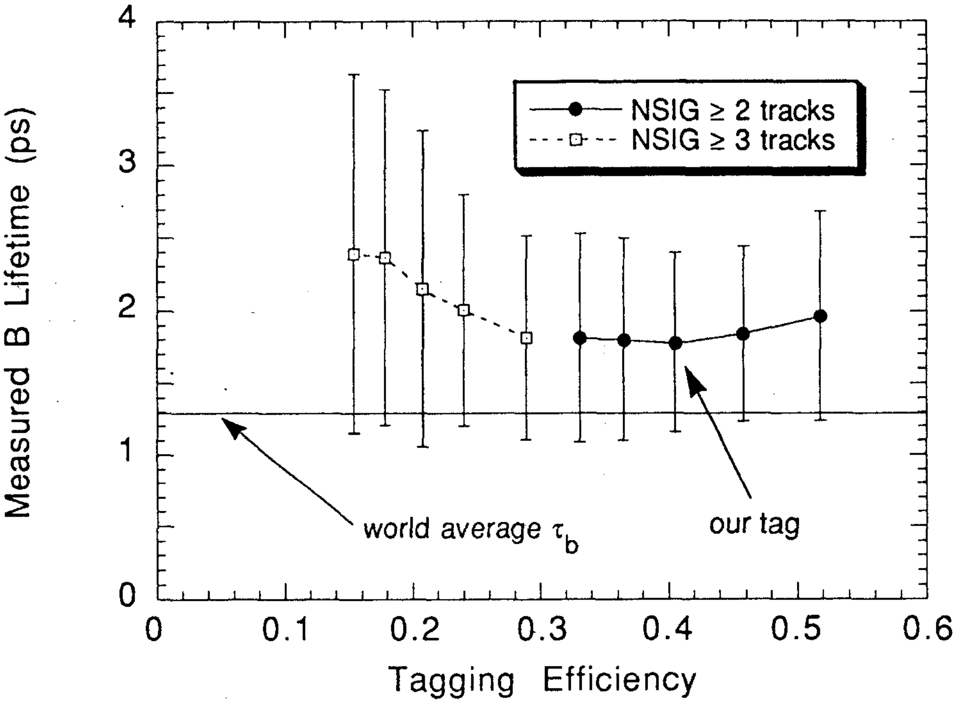

Figure 100 The B lifetime computed from the <Σδ> of the untagged hemisphere sample versus the tagging efficiency. The measured lifetime is relatively insensitive to the choice of tag. All values, including our tagging efficiency of 40%, agree with the world average of 1.29±0.05 ps.

parameters typically are obtained from prior experimental results from the LEP, CLEO, ARGUS, PEP, and PETRA collaborations. These parameters include the heavy flavor branching fractions, heavy flavor fragmentation, B decay multiplicity and momentum spectrum, and the average charm lifetime.

If the Monte Carlo accurately simulates the hadronic data, the measured B lifetime should be relatively stable under variations in the event cuts, track cuts, and B-tagging cuts. These checks were all performed in the previous section. In this section, we will determine the systematic error to the B lifetime by varying the detector performance and physics related parameters to within their tolerances.

6.9.1 Track Resolution

6.9.1.1 Symmetric Tails

Our largest source of systematic error is the uncertainty in track resolution. In Section 4.5, we discussed that the negative half of the impact parameter distribution provides a good measure of the tracking performance in hadronic events. However, our limited statistics prevents us from knowing the precise amount of added track smearing required in the Monte Carlo.

We explored the range of an extra symmetric gaussian and symmetric exponential tail smearing that can be applied to a given fraction of the Monte Carlo tracks while still compatible with the hadronic data. Two tests were applied to ensure agreement between the data and MC. First, the fraction of tracks with impact parameter $\delta \leq -1\text{mm}$ was forced to agree within 1σ. This test is most sensitive to the extra exponential smearing. Second, a likelihood fit to the negative δ region was required to agree within 2σ of the hadronic data and offers the most sensitivity to the extra gaussian degradation in the MC. The allowed range of extra smearing was presented in Table 25 on page 125. The optimal prescription called for 5% of the tracks to be smeared by a gaussian of width 175 μm, and 1% of the tracks to be smeared by a symmetric exponential distribution of decay length 1 mm.

As the track error increases, so does the number of tagged hemispheres. Proportionately more *udsc* hemispheres will be tagged than bottom hemispheres, which lowers the sample purity and reduces the mean of the untagged $\Sigma\delta$ distribution in the Monte Carlo. The number of tagged hemispheres in the allowed range of track degradation varies by ±6.1% relative to the preferred track resolution function. Since the sample is rich with bottom hadrons, the purity varies by only ±2.9% from its nominal value of 0.80. The variations in the computed Monte Carlo lifetimes using the untagged $\langle\Sigma\delta\rangle$ as the lifetime estimator range from –3.5% to

+4.7%, and to a large degree, follow the changes in purity: i.e. extra track smearing yields a smaller $\langle \Sigma\delta \rangle$ and hence a shorter MC lifetime. Since we use the calibration curve to compute the B lifetime (Figure 94 on page 168), a decrease in the MC lifetime leads to an equivalent increase in the measured B lifetime from the hadronic data. Thus the systematic error on the lifetime is $^{+3.5}_{-4.7}$ %.

Relying on the likelihood fit as the B lifetime estimator yields a slightly different systematic error. The Monte Carlo computed lifetimes in the allowed range still decreases with larger amounts of gaussian smearing, but they increase with added exponential smearing. The likelihood fit is fairly insensitive to very negative tails, and so it perceives the added symmetric exponential smearing as an enhancement of the very positive δ tail due to a longer lifetime. The MC lifetimes changes spanned -4.6% to +7.5%, which results in a systematic error on the B lifetime of $^{+4.6}_{-7.5}$ %. Since this range encompasses the range using the untagged $\langle \Sigma\delta \rangle$, we take this value as the systematic error. The hypothesis of no additional track errors corresponds to a 3σ deviation in the likelihood fit to the region $\delta \le 0$, and produces a shift in the measured B lifetime of 0.2% or -7.6% when using the likelihood fit or the untagged $\langle \Sigma\delta \rangle$, respectively, as the lifetime estimator. However, this shift is still within the bounds of the systematic error associated with uncertainties in tracking the resolution.

The B lifetime measurement is not terribly sensitive to the exact nature of a symmetric exponential tail smearing. Instead of the nominal treatment of randomly degrading 1% of the tracks by an exponential distribution of decay length 1 mm, we smeared 0.5% of the tracks with an exponential of decay length 2 mm. Since the tracks from K_s^0 and Λ generally have low momentum, we also smeared 2% of the low momentum tracks ($P_{xy} \le 1.5$ GeV) while keeping the more energetic tracks unaltered. In all three cases, there was no appreciable difference in the computed lifetime.

6.9.1.2 Asymmetric Tails

We have assumed that the uncertainty in the far tails of the impact parameter resolution function can be modeled by a symmetric exponential function. This is valid if the mechanism for generating tails is due to pattern recognition errors in track finding or hard scatters by the detector material. However, the assumption is false if the uncertainty in the tails of the resolution function is due to an uncertainty in the production of K_s^0 or Λ particles, since the δ distribution of the daughter tracks is highly asymmetric (refer to Figure 59 on page 100).

Approximately two-thirds of the tracks have a positive impact parameter, distributed roughly exponentially. Modifying the additional exponential tail smearing to mimic this asymmetry and satisfying the constraint on the fraction of tracks with $\delta \leq -1$ mm leads to an error in the measured B lifetime of $^{+2.9}_{-4.6}\%$. The corresponding systematic error had we chosen a symmetric exponential function is $^{+2.9}_{-2.0}\%$, where we are of course ignoring the systematics due to the extra gaussian smearing. Hence, the net increase in the systematic error is $^{+0.0}_{-4.1}\%$. The upper limit corresponds to no additional smearing, whereas the lower limit results from the maximum allowed tail smearing. The effects of an asymmetric track degradation are tempered somewhat, because although the purity drops more, the $\langle\Sigma\delta\rangle$ for untagged bottom hemispheres increases from the asymmetric smearing.

6.9.2 Multiple Coulomb Scattering

The amount of material that a charged particle passes through is documented in Table 22 on page 104. From the central core of the impact parameter significance δ/σ_δ in Figure 68 on page 116, we estimate the degree of multiple Coulomb scattering to about ±4%. We can examine the consequences of the allowing the multiple scattering to be in this range by degrading the track position proportionally to the calculated impact parameter resolution. The systematic effect on the measured B lifetime is only ±0.8%.

6.9.3 Tracking Efficiency

The tracking efficiency of the central drift chamber is known to about 2% due to the difficulty of normalizing the charged multiplicity in the chamber. The tracking efficiency in the vertex detector is known to better than 1%. By randomly removing tracks in the Monte Carlo, we observe the corresponding change in the B lifetime. The total systematic error is ±3%.

6.9.4 Heavy Quark Fragmentation

As seen in Figure 81 on page 146, the average momentum of B hadrons affects not only the tagging efficiency, but also the $\langle\Sigma\delta\rangle$ for bottom hemispheres. The LEP groups have measured the mean B fragmentation from the momentum spectrum of high P_T leptons to be $\langle x_E \rangle_b = 0.705 \pm 0.013$ (see Table 15 on page 83). The Monte Carlo was generated with a mean fragmentation of 0.68. We varied $\langle x_E \rangle_b$ in the Monte Carlo by reweighting $b\bar{b}$ events such that the shape of the fragmentation distribution for various reweights always conformed to the Petersen parametrization. A 3% variation in $\langle x_E \rangle_b$ translates to a systematic error of 4% in the B lifetime measurement.

The B lifetime measurement is very insensitive to the average charm quark fragmentation. LEP has measured the fragmentation $\langle x_E \rangle_c$ to be roughly 0.51±0.03 (see Table 16 on page 83). Even though our MC generated charm hadrons in $Z^0 \rightarrow c\bar{c}$ events with a mean x_E of 0.42, a reweighting of the events to agree with the LEP results causes a shift in the measured B lifetime of less than 1%.

6.9.5 Heavy Flavor Production

The fraction of $b\bar{b}$ events in hadronic Z^0 decays (f_b) has been measured quite accurately by the LEP experiments to be 0.213±0.010, which is in excellent agreement with the Standard Model prediction of 0.217. The branching fractions from the individual LEP experiments are listed in Table 12 on page 81. The 5% uncertainty translates into only a 1% systematic error on the B lifetime, primarily because the sample's high purity makes it relatively insensitive to shifts in f_b.

The fraction of $c\bar{c}$ events in hadronic Z^0 decays (f_c) is known only to within 15%; the LEP experiments have measured f_c to be 0.176±0.027. However since the charm component in the tagged sample is very small and $\langle \Sigma\delta \rangle$ for charm is only one-sixth the mean value for bottom hemispheres, a 15% uncertainty in f_c translates to only a 2% systematic uncertainty in the B lifetime.

While fixing the purity at 80%, any uncertainty in the makeup of background hemispheres in the tagged sample, i.e. the relative proportion of charm versus *uds* jets, has a negligible effect on the B lifetime. The charm component in the background can vary as much as 65±20%, yet the systematic error on the lifetime is under 1%.

As discussed in Section 3.1, bottom quarks will hadronize predominantly into B^0 and B^+ mesons. B_s meson and B baryon production is down substantially due to the difficulty to extract strange quarks and diquarks out of the vacuum. However, the experimental knowledge for the fraction of B_s and Λ_b in $b\bar{b}$ events is only rudimentary at best. The B_s meson has not yet been observed, and only recently have ALEPH [56] and UA1 [57] observed Λ_b. Extracted from the LUND Monte Carlo, the four bottom hadron species have slightly different charged multiplicities, tag efficiencies, and $\langle \Sigma\delta \rangle$'s (see Table 33). The B^0 meson has on average 0.4 more charged tracks than the B^+ meson, which leads to a slightly higher tagging efficiency and a larger mean for its $\Sigma\delta$ distribution. Although B baryons have the highest multiplicity, they have the lowest tagging efficiency and $\langle \Sigma\delta \rangle$.

Table 33 Variations in the properties of the B hadron species. The values are given by the LUND Monte Carlo.

Bottom Species	Production Rate	Charged Multiplicity	Tag Efficiency	$\langle\Sigma\delta\rangle$
B^+	39.8%	5.05	43.6%	830 μm
B^0	39.8%	5.44	46.2%	908 μm
B_s	11.6%	5.52	44.6%	833 μm
Λ_b	8.8%	5.69	35.7%	673 μm

All these differences contribute to systematic errors in the B lifetime. Although experimental evidence is not yet in hand, we can be reasonably assured that B_s is produced in the range 11.6±5%, and Λ_b in the range 8.8±5%. If the excess or deficit is compensated by equal proportions of B^0 and B^+ mesons, the systematic error in the lifetime is only ±1.3%. Most of this error is from deviations in the properties of Λ_b.

6.9.6 B Decay Multiplicity and Momentum Spectrum

More important than any relative differences between B^0, B^+, B_s, and B baryon decay properties is the absolute scale of the charged multiplicity for B hadrons, since the average $\Sigma\delta$ is roughly proportional to the number of B decay tracks included in the sum (Figure 80 on page 145). Equally significant is the momentum spectrum dn/dx, where $x=P/M_B$, and P is the momentum of B daughter particle in the rest frame of the B hadron. A harder spectrum will generate charged tracks with greater momentum and greater P_T with respect to the B direction in the lab frame. These factors will induce not only larger impact parameters, but also smaller calculated errors σ_δ, which will increase both the tagging efficiencies and the $\langle\Sigma\delta\rangle$ for bottom hemispheres.

These properties, B decay multiplicity and momentum spectrum, have been constrained using the ARGUS and CLEO measurements at the Υ_{4S} resonance. The charged multiplicity is 5.44±0.14 tracks, [77][78] and the momentum spectrum is obtained from the CLEO data.[82] The Υ_{4S} produces only $B_{u,d}$ mesons, but since $B_{u,d}$ mesons comprise ~80% of the B hadrons in $b\bar{b}$ events at the Z^0 resonance, we have examined the subset of $b\bar{b}$ events which contains only these mesons, and forced this collection to conform to the CLEO and ARGUS results. The LUND MC is then used to account for differences in the multiplicity and momentum distributions for B_s and B baryons and to extrapolate the systematic effect to all $b\bar{b}$ events.

We use a scheme for reweighting $b\bar{b}$ events that adjusts the B multiplicity and x distribution independently of each other. [81] The uncertainty in multiplicity results in a ±2.5% systematic error in the B lifetime. Uncertainties in the momentum spectrum arise primarily because the CLEO experiment has measured the x distribution accurately for $x > 0.04$. The uncertainty in multiplicity provides a reasonable upper limit for the uncertainty in the momentum spectrum in the region $x < 0.04$, which is completely unconstrained by data. If this region alone is used to produce a 1σ change in the multiplicity, the shift in τ_b is ±3.7%.

6.9.7 Charged Multiplicity

Neither the uncertainties in the charged multiplicity of *uds* events nor the uncertainties in the number of fragmentation tracks in charm or bottom events affects the B lifetime measurement. The LUND MC generates about 1.0 more charged tracks than the average LEP multiplicity of 20.94±0.20 tracks in hadronic events. [79] The Mark II observes a consistent value of 20.9±0.5 for the hadronic multiplicity, where the error is statistical only. Since the charm and bottom decay multiplicities are known to high accuracy, the difference between data and MC must arise from multiplicities from *uds* events or fragmentation tracks in charm and bottom events. Randomly eliminating a fraction of these tracks to change the multiplicity by ±1 results in <1% change in τ_b.

The Mark II has recently reported the number of fragmentation tracks from $b\bar{b}$ events to be 12.0±1.8±0.6. [80] Varying this quantity within its limits by throwing out randomly selected fragmentation tracks leads to a systematic error on the B lifetime of ±1%.

6.9.8 Average Charm Lifetime

Charm hadron lifetimes have been measured with great precision by the fixed target photo-production experiment E691 at Fermilab (refer back to Table 7 on page 27). However, because the D^0 and D^+ lifetimes differ by a factor of 2.5, uncertainties in the relative production of charm hadrons through $Z \to c\bar{c}$ events or tertiary charm decays in $b\bar{b}$ events will result in uncertainties in the average charm lifetime. These uncertainties affect the B lifetime measurement through two mechanisms. A larger charm lifetime will contribute to a higher charm background in the tagged sample, will increase the $\langle \Sigma\delta \rangle$ in bottom hemispheres due to the tertiary charm decays. Nevertheless, the systematic effect small. First, the charm background in the tagged sample is only ~15%. Second, the charm lifetime enhances the total $\Sigma\delta$ in bottom hemispheres due to the tertiary decay by only 20% on average.

The LUND Monte Carlo generates a pseudoscalar-to-vector meson ratio for charm in the ratio 1:3 which nets approximately 2.2 times more D^0 mesons than D^+ mesons due to the asymmetric decay of the vector mesons into charged and neutral pseudoscalars. Averaged over all charm hadrons the charm lifetime is 0.55 ps. CLEO [22] and ARGUS [26] have measured the pseudoscalar-to-vector ratio in B mesons to be approximately 0.3±0.1. ALEPH [33] has measured this ratio in direct charm production from $Z^0 \to c\bar{c}$ events to be 0.5±0.2. Although this ratio has a considerable range, the average charm lifetime changes by only 3-4%. The uncertainty in the average lifetime due to errors in the individual lifetime is only 2%. Added in quadrature, the total systematic error on the B lifetime from both direct charm production and tertiary charm decay is under 1%.

6.9.9 Monte Carlo Statistics

The shapes of the $\Sigma\delta$ distributions for *uds*, charm, and bottom hemispheres, as well as the calibration curves that related the log likelihood fit and the $\langle\Sigma\delta\rangle$ to the measured B lifetime were derived from a Monte Carlo sample size with full detector simulation of 20,000 events. The uncertainty in the calibration curves from Monte Carlo statistics is ~2%, which we take as a systematic error in the lifetime measurement.

6.9.10 Uncertainty in Tag Purity

Although uncertainty in the purity of the impact parameter tag affects the B lifetime measurement, we do not consider it as a separate systematic error. Rather, the error in the purity arises from systematic effects that have been previously discussed. By including the uncertainty in the tag purity, we would, in effect, be double counting the systematic errors that affect both the purity and the lifetime, since calculating the purity is only an intermediate step in measuring the B lifetime. Had we possessed a larger hadronic data set, we might have been able to fit for the purity in the untagged sample, thereby reducing the majority of the systematic errors in the B lifetime primarily to only those components that affect the uncertainty in the shape of the $\Sigma\delta$ distribution for bottom hemispheres.

Table 34 Summary of all the systematic errors that affect the B lifetime measurement, subdivided according to uncertainties in the detector performance versus uncertainties in hadronic event properties. The total systematic error is +9/–11% of the measured B lifetime.

Source	% Error
Detector Performance:	
Track resolution function	+4.6/–8.5
Multiple scattering	±0.8
Tracking efficiency	±3
Hadronic Event Properties:	
$Z^0 \rightarrow b\bar{b}$ fraction	±1
$Z^0 \rightarrow c\bar{c}$ fraction	±2
B fragmentation $\langle x_E \rangle$	±4
Relative production of $B_{u,d}$, B_s, and B baryon	±1.3
B decay multiplicity and momentum spectrum	±4.5
Average charm lifetime	±1
Charged multiplicity	±1
Monte Carlo statistics	±2

6.9.11 Summary of Systematic Errors

Table 34 lists the systematic errors that affect the B lifetime measurement. The errors are subdivided according to whether they are associated with the detector performance or with the hadronic event properties. Added in quadrature, the total systematic error is +9/-11%. The major source of error was due to uncertainties in the impact parameter resolution function, which resulted from our low statistics.

6.10 B Lifetime Summary

Using an impact parameter tag on hadronic event hemispheres, we tagged 53 hemispheres, of which 80% are expected to contain bottom hadrons. The hemispheres opposite the tagged ones provide a relatively unbiased sample of B hadrons. Performing a fit to the untagged $\Sigma\delta$ distribution, we measured the B lifetime to be

$$\tau_b = 1.53\,^{+0.55}_{-0.45} \pm 0.16 \text{ ps} \tag{53}$$

where the first error is statistical and the second is systematic.

"I can't tell you just now what the moral of that is, but I shall remember it in a bit." "Perhaps it hasn't one," Alice ventured to remark. "Tut, tut, child!" said the Duchess. "Everything's got a moral, if only you can find it."

– Lewis Carroll

7 Conclusions

In this thesis we have measured the B hadron lifetime using the Mark II detector at the Stanford Linear Collider. A precision vertex drift chamber and silicon strip detector allowed us to identify bottom events using an impact parameter tag. The vertex system resolved impact parameters to 30 μm for high momentum tracks, and 70 μm for tracks with a momentum of 1 GeV. Requiring a hemisphere to have at least two tracks that significantly miss the Z^0 decay vertex selects B hadrons with an efficiency of 40% and a sample purity of 80%. This method has a purity comparable to tags that require a high P_T lepton, but is considerable more efficient at identifying B hadrons. The LEP experiments typically identified 2-3% of the B hadrons using a high P_T lepton tag.

From 208 hadronic Z^0 decays that satisfied the event selection cuts, 53 hemispheres were tagged. 22 of these hemispheres came from 11 double-tagged events. Assuming a tagging efficiency and purity from the Monte Carlo, the results are consistent with a hadronic branching fraction $Z^0 \to b\bar{b}$ of 0.217, as predicted by the Standard Model.

The hemispheres opposite the tag (the untagged sample) are enriched in B hadrons and unbiased in B decay times. From a fit to the untagged $\Sigma\delta$ distribution, we measured the B lifetime to be

$$\tau_b = 1.53^{+0.55}_{-0.45} \pm 0.16 \text{ ps} \tag{54}$$

where the first error is statistical and the second is systematic. Our measurement is consistent with the current world average of 1.29±0.05 ps. The systematic error was dominated by our incomplete knowledge of the tracking resolution function due to limited event statistics. The B lifetime measured from the tagged sample and the entire hadronic sample without enrichment gave consistent results.

Although our measurement is statistically limited, the precision performance of the vertex detectors offers a unique opportunity to observe any potentially anomalous behavior of B hadron decays. The shape of the $\Sigma\delta$ distribution is dominated by the B decay time distribution and the variance in the B momentum and decay multiplicity, rather than the tracking resolution. We observed no long tails in the $\Sigma\delta$ distribution. Also, there was no measured correlation in the $\Sigma\delta$'s between the two hemispheres in tagged events, beyond that from the common thrust axis. In addition, none of the three-jet events were triple-tagged when the impact parameter tag was applied to the individual jets. None are expected, since the gluon jet rarely produces a $b\bar{b}$ pair. The absence of any anomalous behavior along with the agreement of our measurement of the B lifetime and estimate of the hadronic branching fraction $Z^0 \rightarrow b\bar{b}$ with the world average, provides strong evidence that the impact parameter tag is a robust method of identifying B hadrons.

Finally, an impact parameter tag offers another avenue for discerning any differences in lifetime between charged and neutral B hadrons, principally because the B semileptonic branching fraction is proportional to the lifetime. The average lifetime using high P_T leptons is expected to be equal to or greater than the average lifetime employing an impact parameter tag (Figure 14 on page 31). Since the world average B lifetime is dominated by the LEP results using high P_T leptons, we can use our measurement to obtain the ratio of the average B lifetime from the two techniques, $\langle\tau\rangle_{lepton}/\langle\tau\rangle_{impact}$, to be $0.84^{+0.38}_{-0.22}$. Taking the conservative approach by assuming this ratio is consistent with 1.0, we can constrain the B^0 and B^+ lifetimes to within a factor of five of each other (90% CL). We would need to resolve $\langle\tau\rangle_{lepton}/\langle\tau\rangle_{impact}$ to 4% in order to exclude a B^0/B^+ lifetime difference greater than a factor of 1.5. Reducing the systematic errors to this level would be a challenge.

It is hoped that future experiments will be able to incorporate an impact parameter tag to measure the B lifetime and other properties of B hadrons to a level that is competitive with methods using high P_T leptons.

References

[1] The JADE Collaboration, "Upper Limit on Beauty Lifetime and Lower Limit on Weak Mixing Angles", Phys. Lett. B114 (1982) 71.

[2] The MAC Collaboration, "Lifetime of Particles Containing b Quarks", Phys. Rev. Lett. 51 (1983) 1022.

[3] N. S. Lockyer *et al.* (Mark II Collaboration), "Measurement of the Lifetime of Bottom Hadrons", Phys. Rev. Lett. 51 (1983) 1316.

[4] The TASSO Collaboration, "Determination of the Average Lifetime of Bottom Hadrons", Phys. Lett. B149 (1984) 524.

[5] The JADE Collaboration, "Determination of the B Lifetime", Z. Phys. C31 (1986) 349.

[6] D. E. Klem *et al.* (DELCO Collaboration), "Measurement of the Average B Hadron Lifetime", Phys. Rev. Lett. 53 (1984) 1873.

[7] J. M. Brom *et al.* (HRS Collaboration), "Measurement of the Lifetime of Hadrons Containing the b Quark", Phys. Lett. B195 (1987) 301.

[8] The MAC Collaboration, "Determination of the Lifetime of Bottom Hadrons", Phys. Rev. Lett. 58 (1987) 640.

[9] D. E. Klem *et al.* (DELCO Collaboration), "Measurement of the Average Lifetime of Hadrons Containing Bottom Quarks", Phys. Rev. D37 (1988) 41.

[10] R. A. Ong *et al.* (Mark II Collaboration), "Refined Measurement of the B Hadron Lifetime", Phys. Rev. Lett. 62 (1989) 1236.

[11] The TASSO Collaboration, "Measurement of the Average Lifetime of B Hadrons", Z. Phys. C44 (1989) 1.

[12] The JADE Collaboration, "A Measurement of the Average Lifetime of B Hadrons Produced by e^+e^- Collisions at $\sqrt{s}$ = 36.3 GeV", preprint DESY 90-087, July 1990.

[13] S. R. Wagner *et al.* (Mark II Collaboration), "Measurement of the B^0 Meson Lifetime", Phys. Rev. Lett. 64 (1990) 1095.

[14] The DELPHI Collaboration, "Measurement of the Average Lifetime of B Hadrons", preprint CERN-PPE/91-131, August 1991. Submitted to Z. Phys. C.

[15] The OPAL Collaboration, "Observation of J/ψ Production in Multihadronic Z^0 Decays", preprint CERN-PPE/91-92, June 1991. Submitted to Phys. Lett. B.

[16] The ALEPH Collaboration, "Measurement of the B Hadron Lifetime", preprint CERN-PPE/90-195, December 1990. Submitted to Phys. Lett. B.

[17] The L3 Collaboration, "Measurement of the Lifetime of B Hadrons and a Determination of $|V_{cb}|$", L3 preprint #32, July 1991.

[18] The OPAL Collaboration, "Measurement of the Average B Hadron Lifetime in Z^0 Decays", preprint CERN-PPE/91-201, November 1991. Submitted to Phys. Lett. B.

[19] F. Weber (The ALEPH Collaboration), "A Measurement of Exclusive B^0 and B^+ Lifetimes", presented at the DPF91 conference in Vancouver, August 1991.

[20] N. R. Stanton (E653 Collaboration), "Beauty Pairs and Cahrm Semileptonic Decays from Fermilab E653", presented at the 3rd Topical Seminar on Heavy Flavours, San Miniato, Italy, June 1991.

[21] The ARGUS Collaboration, "A Measurement of $\tau(B^+)/\tau(B^0)$ from the Lepton and Dilepton Rates in Υ_{4S} Decays", preprint DESY-91-056, June 1991.

[22] The CLEO Collaboration, "Exclusive and Inclusive Semileptonic Decays of B Mesons to D Mesons", Phys. Rev. D43 (1991) 651.

[23] The ARGUS Collaboration, "Measurement of the Decay $B^- \to D^0 l^- \bar{\nu}$", preprint DESY 91-122, October 1991.

[24] The ARGUS Collaboration, "Measurement of the Lifetime Ratio $\tau(B^+)/\tau(B^0)$", Phys. Lett. B232 (1989) 554.

[25] The CLEO Collaboration, "Limits on $B^0\bar{B}^0$ Mixing and $\tau(B^0)/\tau(B^+)$", Phys. Rev. Lett. 58 (1987) 183.

[26] The ARGUS Collaboration, "Exclusive Semileptonic Decays of B Mesons to D Mesons", preprint DESY-92-029, February 1992.

[27] The DELPHI Collaboration, "A Measurement of the Partial Width of the Z^0 Boson into b Quark Pairs", preprint CERN-PPE/90-118, August 1990.

[28] The ALEPH Collaboration, "Heavy Flavour Production in Z Decays", Phys. Lett. B244 (1990) 551.

[29] The L3 Collaboration, "Measurement of $Z^0 \to b\bar{b}$ Decay Properties", Phys. Lett. B241 (1990) 416.

[30] The OPAL Collaboration, "A Study of Heavy Flavour Production using Muons in Hadronic Z^0 Decays", Phys. Lett. B263 (1991) 311.

[31] The L3 Collaboration, "Measurement of $Z^0 \to b\bar{b}$ Decays and the Semileptonic Branching Ratio Br $(b \to lX)$", Phys. Lett. B261 (1991) 177.

[32] R. Jacobsen *et al.* (Mark II Collaboration), "Measurement of the $b\bar{b}$ Fraction in Hadronic Z^0 Decays with Precision Vertex Detectors", Phys. Rev. Lett. 67 (1991) 3347.

[33] The ALEPH Collaboration, "Production and Decay of Charmed Mesons at the Z Resonance", preprint CERN-PPE/91-114, July 1991. Submitted to Phys. Lett. B.

[34] The OPAL Collaboration, "A Study of $D^{*\pm}$ Production in Z^0 Decays", Phys. Lett. B262 (1991) 341.

[35] P. Mattig, "QCD Measurements with Heavy Quarks at LEP", Heavy Flavour Physics Conf. at Orsay, June 1991. Preprint BONN-HE-91-19.

[36] Ian Shipsey, "B Physics with CLEO", preprint PU-91-654. Published in Les Rencontres (March 1991).

[37] The CLEO Collaboration, "Inclusive and Exclusive Decays of B Mesons to Final States Including Charm and Charmonium Mesons", preprint CLNS-91-1102 and CLEO-91-8.

[38] The DELPHI Collaboration, "DELPHI Results on Z^0 Decays into Heavy Flavours", preprint LAL-91-22, May 1991. Talk at the XXVIth Rencountres de Moriond, March 17-23, 1991.

[39] P. Roudeau, "Heavy Quark Physics at LEP", Lepton-Photon Conf 1991. Preprint LAL-91-49

[40] P. Colas, "B Physics at LEP", 14th Int'l Warsaw Mtg on Elementary Particle Physics, May 27-31, 1991. Preprint SACLAY-DPHPE-91-12, October 1991.

[41] R. J. Morrison, "Production and Decay of Heavy Flavors", Nuclear Phys. B (Proc. Suppl.) 16 (1990) 108.

[42] R. J. Morrison and M. S. Witherell, "D Mesons", preprint UCSB-HEP-89-01. To be published in Annual Rev. of Nucl. and Particle Science, Vol. 39.

[43] R. Ruckl, *Weak Decays of Heavy Quark States*, Proceedings of the International School of Physics (1984)

[44] J. L. Cortes *et al.*, "Mass Effects in Weak Decays of Heavy Particles", Phys. Rev. D25 (1982) 188.

[45] N. Cabibbo and L. Maiani, "The Lifetime of Charmed Particles", Phys. Lett. B79 (1978) 109.

[46] C. S. Kim and A. D. Martin, "On the Determination of V_{ub} and V_{cb} from Semileptonic B Decays", Phys. Lett. B225 (1989) 186.

[47] M. Bauer and B. Stech, "Exclusive D Decays", Phys. Lett. B152 (1985) 380;
M. Bauer, B. Stech, and M. Wirbel, "Exclusive Non-leptonic Decays of D, D_s, and B Mesons", Z. Phys. C34 (1987) 103.

[48] G. Altarelli *et al.*, Nucl. Phys. B208 (1982) 365.

[49] N. Isgur *et al.*, Phys. Rev. D39 (1989) 799.

[50] M. Wirbel, B. Stech, and M. Bauer, Z. Phys. C29 (1985) 637.

[51] J. C. Körner and G. A. Schuler, Z. Phys C38 (1988) 511.

[52] N. Isgur and M. Wise, Phys. Lett. B237 (1990) 527.

[53] S. Stone, "Semileptonic B Decays - Experimental", preprint HEPSY-4-91, October 1991. To be published in "B Decays".

[54] J. L. Rosner, "The Cabibbo-Kobayashi-Maskawa Matrix", preprint EFI-91-49, September 1991. To be published in "B Decays".

[55] The OPAL Collaboration, "A Study of K_s^0 Production in Z0 Decays", preprint CERN-PPE/91-86, May 1991. Submitted to Phys. Lett. B.

[56] ALEPH Collaboration, "Evidence for B Baryons in Z Decays", preprint CERN-PPE-91-229, December 1991. Submitted to Phys. Lett. B

[57] UA1 Collaboration, "First Observation of the Beauty Baryon Λ_b in the Decay Channel $\Lambda_b \to J/\psi\Lambda$ at the CERN proton-antiproton Collider", preprint CERN-PPE-91-202, November 1991. Submitted to Phys. Lett. B.

[58] C. Adolphsen *et al.*, "The Mark II Silicon Strip Vertex Detector", Nucl. Instr. Meth. A313 (1992) 63.

[59] J. P. Alexander *et al.*, "The Mark II Vertex Drift Chamber", Nucl. Instr. Meth. A283 (1989) 617.

[60] G. S. Abrams *et al.*, "The Mark II Detector for the SLC", Nucl. Instr. Meth. A281 (1989) 55.

[61] D. Durrett *et al.*, "Calibration and Performance of the Mark II Drift Chamber Vertex Detector", SLAC-PUB-5259, May 1990. Presented at the Novosibirsk Conf, 1990.

[62] G. Hanson, "The New Drift Chamber for the Mark II Detector at the SLAC Linear Collider", SLAC-PUB-3880, February 1986. Presented at the Vienna Wire Conf. 1986.

[63] R. Jacobsen *et al.*, "Recent Experience with Backgrounds at the SLC", SLAC-PUB-5471, May 1991. Presented at the IEEE Particle Accelerator Conf, S.F.

[64] H. Brafman *et al.*, IEEE Trans. Nucl. Sci. NS-25 (1978) 692;
T. Himel, Ph.D. thesis, SLAC-REP-223 (October 1979).

[65] J. Perl *et al.*, "Track Finding with the Mark II/SLC Drift Chamber", Nucl. Instr. Meth. A252 (1986) 616.

[66] R. L. Glückstern, "Uncertainties in Track Momentum and Direction due to Multiple Scattering and Measurement Errors", Nucl. Instr. Meth. 24 (1963) 381.

[67] W. Bartel *et al.*, (JADE Collaboration), Z. Phys. C33 (1986) 23.

[68] T. Sjöstrand, Comput. Phys. Commun. 39 (1986) 347.
T. Sjöstrand and M. Bengtsson, Comput. Phys. Commun. 43 (1987) 367.
M. Bengtsson and T. Sjöstrand, Nucl. Phys. B289 (1987) 810.

[69] G. S. Abrams *et al.* (Mark II Collaboration), "First Measurement of Hadronic Decays of the Z Boson", Phys. Rev. Lett. 63 (1989) 1558.
G. S. Abrams *et al.* (Mark II Collaboration), " Measurement of Charged Particle Inclusive Distributions in Hadronic Decays of the Z Boson", Phys. Rev. Lett. 64 (1990) 1334.

[70] A. Petersen *et al.*, Phys. Rev. D37 (1988) 1.

[71] C. Peterson *et al.*, Phys. Rev. D27 (1983) 105.

[72] P. Weber, "Separated Vertex Search and Measurement of the B Hadron Lifetime in e^+e^- Annihilation at $\sqrt{s}$ = 29 GeV", Ph. D. thesis, Department of Physics, University of Colorado, Boulder, Colorado, 1990.

[73] R. Fulton *et al.* (CLEO Collaboration), "Obervation of B Meson Semileptonic Decays to Noncharmed Final States", Phys. Rev. Lett. 64(1990) 16.

[74] H. Albrecht *et al.* (ARGUS Collaboration), "Observation of Semileptonic Charmless B Meson Decays", Phys. Lett. B234 (1990) 409.

[75] H. Albrecht *et al.* (ARGUS Collaboration), "Reconstruction of Semileptonic $b \rightarrow u$ Decays", Phys. Lett. B255 (1991) 297.

[76] H. A. Bethe, Phys. Rev. 89 (1953) 1256;
W. T. Scott, Rev. Mod. Phys. 35 (1963) 231;
V. L. Highland, Nucl. Instr. Meth. 129 (1975) 497;
G. R. Lynch and O. I. Dahl, Nucl. Instr. Meth. B58 (1991) 6.

[77] H. Albrecht *et al.* (ARGUS Collaboration), "Measurement of R and Determination of the Charged Particle Multiplicity in e^+e^- Annihilation at E_{cm} around 10 GeV", DESY-91-092, August 1991.

[78] B. Gittelman, S. Stone, *B Meson Decay*, published in A. Ali, P. Söding (editors) High Energy Electron-Positron Physics, World Scientific Publishing Co., (1988) 273.

[79] G. S. Abrams *et al.* (Mark II Collaboration), Phys. Rev. Lett. 64, (1990) 1334;
D. Decamp *et al.* (ALEPH Collaboration), Phys. Lett. B273 (1991) 181;
P. Abreu *et al.* (DELPHI Collaboration), Z. Phys. C50 (1991) 185;
B. Adeva *et al.* (L3 Collaboration), Phys. Lett. B259 (1991) 199;
P. D. Acton *et al.* (OPAL Collaboration), CERN-PPE/91-176.

[80] B. A. Schumm *et al.* (Mark II), "Measurement of the Charged Multiplicity of Events Containing Bottom Hadrons at E_{cm} = 91 GeV", SLAC-PUB-5727, January 1992.

[81] B. A. Schumm, MarkII/SLC Memo No. 268, August 1991, unpublished.

[82] Persis Drell and Dave Besson for the CLEO collaboration, private communication.

[83] Particle Data Group, "Review of Particle Properties", Phys. Lett. B239 (1990) VII.1;
I. Bigi and A. Sanda, Phys. Rev. D29 (1984) 1393.

[84] B. Andersson *et al.*, "Parton Fragmentation and String Dynamics", Phys. Rep. 97 (1983) 31.

[85] G. H. Trilling, LBL Physics Note TG360, 1982, unpublished.

[86] F. James and M. Roos, "MINUIT", Computer Physics Communications, 10 (1975) 343. Internal report CERN/DD/75/20.

[87] W. T. Eadie *et al.*, "Statistical Methods in Experimental Physics", North-Holland Publishing Co., 1971.

[88] *SLAC Linear Collider Conceptual Design Report*, SLAC-Report-229, June 1980.

[89] G. S. Abrams *et al.* (Mark II Collaboration), "Initial Measurements of the Z Boson Resonance Parameters in e^+e^- Annihilation", Phys. Rev. Lett. 63 (1989) 724.

[90] G. S. Abrams *et al.* (Mark II Collaboration), "Measurements of the Z Boson Resonance Parameters in e^+e^- Annihilation", Phys. Rev. Lett. 63 (1989) 2173.